THE MOON CHALLENGE

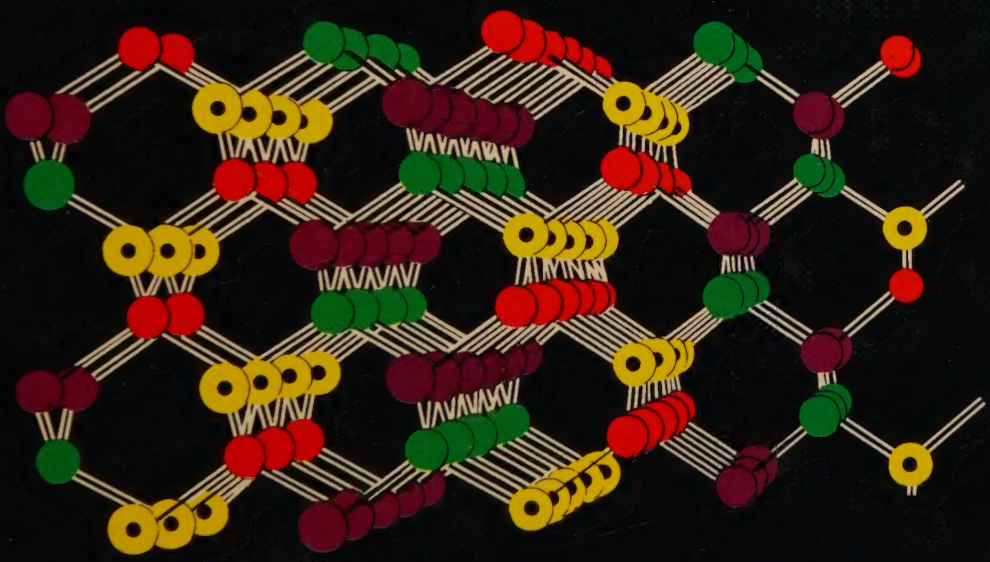

The MOCVD challenge
Volume 1: A survey of GaInAsP–InP for photonic and electronic applications

The MOCVD Challenge

Volume 1: A Survey of GaInAsP–InP for Photonic and Electronic Applications

M Razeghi

Laboratoire Central de Recherches, Thomson-CSF, Orsay, France

Adam Hilger, Bristol and Philadelphia

© IOP Publishing Ltd 1989

All rights reserved. No part of this publication may be reproduced, stored in a retrieval system or transmitted in any form or by any means, electronic, mechanical, photocopying, recording or otherwise, without the prior permission of the publisher. Multiple copying is permitted under the terms of the agreement between the Committee of Vice-Chancellors and Principals and the Copyright Licensing Agency.

British Library Cataloguing in Publication Data

Razeghi, M.
The MOCVD challenge
Vol 1: A survey of GaInAsP–InP for
photonic and electronic applications.
1. Semiconductors. Structures & physical properties
I. Title
537.6'22

ISBN 0-85274-161-8

US Library of Congress Cataloging-in-Publication Data are available

Consultant Editor: **Dr C Hilsum**, GEC

Published under the Adam Hilger imprint by IOP Publishing Ltd
Techno House, Redcliffe Way, Bristol BS1 6NX, England
242 Cherry Street, Philadelphia, PA 19106, USA

Typeset by Mathematical Composition Setters Ltd, Salisbury
Printed in Great Britain by J W Arrowsmith Ltd, Bristol

To my family

Contents

Foreword ix

Preface xi

Introduction 1

1 Growth Technology 3
- 1.1 Introduction 3
- 1.2 Metallorganic chemical vapour deposition 8
- 1.3 New non-equilibrium growth techniques 24

References 28

2 InP–InP System: MOCVD Growth, Characterization and Application 29
- 2.1 Introduction 29
- 2.2 Energy band structure of InP 29
- 2.3 Growth and characterization of InP using TEIn 32
- 2.4 Growth and characterization of InP using TMIn 51
- 2.5 Incorporation of dopants 57
- 2.6 Application of InP epitaxial layers 63

References 67

3 GaInAs–InP System: MOCVD Growth, Characterization and Application 69
- 3.1 Growth conditions 69
- 3.2 Optical and crystallographic properties, and impurity incorporation of GaInAs grown by MOCVD 76
- 3.3 Shallow p^+ layers in GaInAs grown by MOCVD by Hg implantation 96
- 3.4 GaInAs–InP heterojunctions, multiquantum wells and superlattices grown by MOCVD 99

3.5 Magnetotransport in GaInAs–InP heterojunctions grown by MOCVD 117
3.6 Applications of GaInAs–InP systems grown by MOCVD 153
References 159

4 GaInAsP–InP System: MOCVD Growth, Characterization and Application 165
4.1 Growth conditions 165
4.2 Characterization 173
4.3 Applications of GaInAsP–InP systems grown by MOCVD 204
References 259

5 MOCVD Growth, Characterization and Applications of III–V Semiconductor Strained Heterostructures 263
5.1 Growth procedure and characterization 263
5.2 Growth of GaInAs–InP multiquantum wells on $Gd_3Ga_5O_{12}$ garnet (GGG) substrate 269
5.3 Applications 275
5.4 Monolayer epitaxy of $(GaAs)_n(InAs)_n$–InP by MOCVD 284
References 289

6 MOCVD Growth of III–V Heterojunctions and Superlattices on Si Substrates and their Applications 290
6.1 Introduction 290
6.2 MOCVD growth of GaAs on Si 294
6.3 InP grown on Si 296
6.4 GaInAsP–InP grown on Si 300
6.5 Applications 304
References 319

Appendix Safety Information about Alkyls 321

Index 327

Foreword

More than 35 years have elapsed since Welker, in the Erlangen Laboratory of Siemens, discovered the semiconducting properties of III–V compounds. This immediately created a flurry of experimental and theoretical research, showing clearly that physicists and engineers were well aware that this new class of semiconductors might, in time, have important, maybe revolutionary, applications.

Yet, except for some very specialized, low-volume devices, such as Hall effect devices, many years were to pass before some of these materials, mostly GaAs and InP, began to be used in significant amounts in the information technology industry. And, at first, they were almost entirely used in devices which could not be made using the, by then, workhorse of the semiconductor industry, silicon. Injection lasers, made possible by the 'direct gap' character of most of the III–V compounds, or the Gunn effect, are typical examples.

The reasons behind this long lead time are clear: silicon technology was mature and comparatively easy to apply. III–V technologies, on the other hand, had to be developed almost from scratch. New types of 'compositional structures' were, in many cases, necessary for the full advantage of III–V compounds over silicon, in some applications, to be realized fully. The early semiconductor lasers, based on GaAs, could only operate in a pulsed mode, with a low duty factor, and at reduced temperature. 'Separate confinement' and later quantum wells made it possible to operate semiconductor lasers in continuous wave mode above room temperature. But that implied that not only the dopant concentration, but also the composition of the materials be varied in a controllable way over very short distances, for example in the GaAs–(Ga, Al)As system. And the same type of structures proved necessary to take full advantage of the specific properties of III–V compounds (direct gap, high electron mobility, etc) in microwave or digital applications.

All this was only made possible through the development of new technologies for the epitaxial growth of these materials. Liquid phase

epitaxy (LPE) first, molecular beam epitaxy (MBE) a little later, and finally metallorganic chemical vapour deposition (MOCVD) have been as important for III–V technology as diffusion has been for a long time for silicon.

This is so well recognized by the scientific and technical community that the very important IBM Europe Science and Technology Prize was awarded jointly to the three European scientists who had made decisive breakthroughs in developing these technologies: Mme Bauser for LPE, Mr Joyce for MBE, and Mme Razeghi for MOCVD. They were dubbed, on the occasion, the Queens and King of epitaxy!

Needless to say, when one of the Queens writes as thorough a treatise on this very subject, this is bound to become a major event. At a time when, at last, III–V compounds, mostly InP (covered in volume 1) and GaAs (covered in volume 2) based materials, are becoming of major importance to industry, this treatise will be a must for every scientist and engineer in the field.

Manijeh Razeghi has been recognized all over the world for her ability to achieve astonishingly brilliant results with MOCVD technologies. Simply reading the book may not be quite enough for every engineer to do fully as well as she does. But it is a necessary step in that direction.

Pierre Aigrain
Paris

Preface

The metallorganic chemical vapour deposition (MOCVD) growth technique has given a new insight into the physics of materials science. Over the last few years there has been a growing demand for a comprehensive survey to be published on the subject. My purpose in writing this book is therefore to introduce the reader to the MOCVD technique in all its complexity and to show its impact on the development and applications of III–V semiconductor materials worldwide.

Continued striving to improve the performance of heterojunctions and superlattices has motivated much research in the area of semiconductor materials science. A new material in turn generates new technology and new devices, thus creating a new urgency for investigation.

The ability to improve the performance of heterojunctions and superlattices with hyper-abrupt interfaces and low background doping density is the key ingredient to exploration of these new device concepts. Just as important, however, is an ability to fabricate devices reproducibly and economically, as this will play a major role in determining the rate at which the new device concepts can be implemented.

The evolution of MOCVD has fulfilled this requirement. It has allowed access to new device phenomena by producing multilayer heterostructures with extremely fine dimensional and compositional control. This control is especially important in optoelectronics and microwave devices, as it greatly affects both their optical and electronic properties.

A wide range of potentially useful new phenomena based on multiple layer epitaxy is thus becoming available and with imaginative implementation may be expected to lead to further novel device structures.

This series of books explores the growth and characterization of III–V semiconductor heterojunctions, multi-quantum wells and superlattices for fundamental physics and advanced photonic and electronic devices. This volume aims to be a state-of-the-art review of methods of producing very thin, accurately controlled epitaxial layers of $Ga_xIn_{1-x}As_yP_{1-y}$ binary, ternary and quaternary semiconductor multilayers and microstructures over

a large variety of substrates. A second volume, to follow, will similarly deal with GaAs and related compounds.

Volume 1 is organized as follows: Chapter 1 introduces the basic concepts and gives useful information for an understanding of the MOCVD growth technique.

The following three chapters demonstrate applications of the technique for the growth of InP, $Ga_xIn_{1-x}As$ and $Ga_xIn_{1-x}As_yP_{1-y}$ multilayer systems.

Chapter 5 considers in detail strained layers and their applications, whilst the final chapter is devoted to novel combinations of III–V compounds with existing silicon technology.

The material presented in this book is a distillation of my work at Thomson over the past few years and as such would not have been possible without the support and assistance of my colleagues. I wish to take this opportunity to give them my grateful thanks.

I wish to express my thanks to the management of Thomson-CSF: first and foremost President Alain Gomez, the president of Thomson SA, whose scientific and industrial ambition along with his encouragement have fired the enthusiasm of scientists within the company, and Professor P Aigrain, scientific consultant of Thomson, for his scientific assistance.

My work would not have been possible without the facilities and encouragement provided at Thomson Laboratories under the management of Drs E Spitz, P Leclerc, G Nuzillat, J P Duchemin and D Kaplan. To them I owe so much.

To all I give my heartfelt thanks: my fellow researchers at Thomson, especially B Vinter, Ph Maurel, F Omnes, M Defour, O Acher, G Timms, R Blondeau, B de Cremoux, J Nagle, C Weisbuch, A Fredrich, A Huber, J P Castera, P L Meunier, G Doriath and M Warnecke; and my international colleagues, Professors J P Chapelle, L Taurel, H Curien (University of Paris), M Rahmani (University of Teheran), J C Portal (INSA), D C Tsui (University of Princeton), G S Stillman (University of Illinois), A Yariv (University of Caltec), D Bimberg (University of Aachen), K von Klitzing (Stuttgart), Drs J C C Fan, J P Salerno (KOPIN), Professor R A Stradling (Imperial College, London), P D Decoster (University of Lille) and J Bok (University of Paris).

I am also grateful to D Leguen and J Antoine for their excellent technical assistance and to M Magis, M Vary, M Gaillot and B Cornell for their help in preparing the manuscript.

Finally my sincere thanks to Dr C Hilsum, chief scientist of GEC, who reviewed and edited my manuscript. His constructive criticism, suggestions and encouragement have made an invaluable contribution to the writing of this book. I am indebted to him.

M Razeghi
October 1988

Introduction

The secret of accomplishing meaningful basic or applied research on semiconductors is to have control over the preparation of the materials. This has proved particularly so for compound semiconductors, and for many compounds progress has been minimal for long periods because synthesis and purification were not mastered. The III–V compounds have not been exceptions, though their potential applications have drawn many scientists into their study, and a great deal of effort has been expended on developing growth techniques. Certainly we have progressed from the days when the preparation of GaAs was invariably accomplished by an explosion, but even 20 years after the discovery of GaAs and InP, the manufacture of pure crystals was best described as occasional. These problems had led many laboratories to study epitaxial deposition, because it was believed, correctly, that the lower temperature of preparation would give both higher purity and better control. A range of methods were tried, exploiting hydrides, chlorides, and, later, liquid phases. All were marginally successful, but the practice still remained an art. The introduction of metall-organic chemical vapour deposition in 1972 was not greeted universally with acclaim. Few workers were enthusiastic about its advantages over the established methods, and it was regarded as an unpleasant necessity for dealing with compounds incorporating aluminium. Acceptance came slowly, with the realization that the modern forms of device, with many layers containing a variegated selection of elements, could not be produced in numbers by the older methods. Today it is an established and standard technique, available throughout the world.

Science and engineering move forward through the concerted efforts of many people. The history of progress in GaAs and the other III–V compounds is studded with many distinguished names following the original discovery by Professor Heinrich Welker in 1952. Various scientists have made important discoveries on the long road since then, and their contributions must not be minimized. Nevertheless, one name stands out in the field of MOCVD, that of Dr Manijeh Razeghi. Her achievements in

material and device preparation are too many to list. That is why this is an unusual book. It sets out to describe growth, characterization and applications of heterojunctions, quantum wells and superlattices based on InP and its derivatives. It draws heavily, perforce, on Dr Razeghi's own work because she has contributed so much. It is a pleasure for me to acknowledge her success in this introduction.

C Hilsum
Wembley
August 1988

Chapter 1 Growth Technology

1.1 INTRODUCTION

During the past 10 years extensive theoretical and experimental studies on low-dimensional structures (LDS) of InP, GaAs and related compounds have been performed in two distinct contexts.

(1) Low-dimensional, meaning less than three dimensions: the properties of the two-dimensional electron or hole gas in different III–V semiconductor heterojunctions is now a mature, even ageing subject.

(2) Low in the sense of small: as in the physics of semiconductors, where the feature size of the sample is small compared with the intrinsic quantum length scale associated with carriers in semiconductors. This is given by the de Broglie wavelength, defined as $\lambda = h/p$ where h is Planck's constant and p the carrier momentum, typically given by $p^2/2m^* = kT$, where m^* is the effective mass of the carrier, k is Boltzmann's constant and T is the temperature.

Low-dimensional structures have also become essential elements in modern device technology.

Figure 1.1 shows the $x-y$ compositional plane for ternary and quaternary alloys lattice-matched to an InP substrate. Each corner has a binary III–V material. The mixture of binaries at each side gives the ternary III–III–V or III–V–V alloys, and the combination of binaries or ternaries inside gives the quaternary alloys. The broken curves represent equal energy gaps, and the full lines represent equal lattice parameters. Two systems are very interesting for optoelectronic and microwave devices.

One of them is ternaries and quaternaries lattice-matched to a GaAs substrate, for which the energy gap varies between 1.43 and 2.4 eV. In this system, all of the ternaries and quaternaries have an energy gap higher than GaAs binary crystal, so in heterostructures the electrons and holes are usually confined in the binary material.

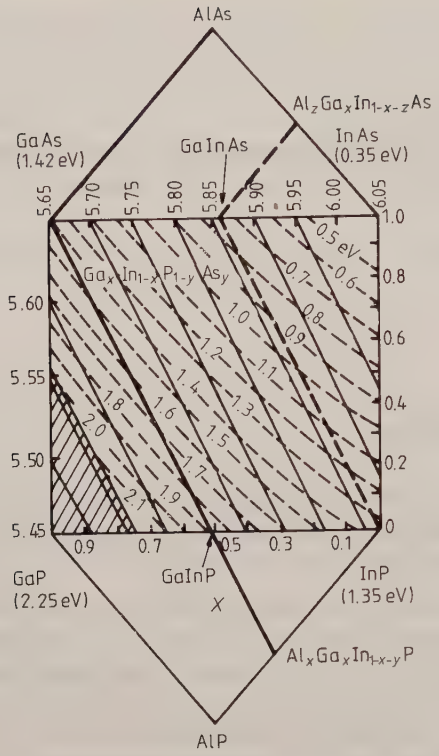

Figure 1.1 The $x-y$ compositional plane for quaternary III–V alloys at 300 K. The $x-y$ coordinate of any point in the plane gives the compositions. The full lines are lattice parameters. The broken curves are direct energy gap values.

The other system is composed of ternaries and quaternaries lattice-matched to an InP substrate, for which the energy gap varies between 0.75 and 1.35 eV. In this system all of the ternaries and quaternaries have an energy gap lower than InP, so electrons and holes are confined in the ternary or quaternary alloys.

There is now a need for a wide range of semiconducting materials, especially InP, GaAs and related compounds, to be grown as thin single-crystal films. Thickness has to be controlled, increasingly more accurately, and uniformity of thickness can be vital. Epitaxial layers as thin as 10 Å or less are now needed. Excellent homogeneity and purity are required. It is desirable to have no misfit dislocations present, and to have a very sharp boundary between the substrate and epitaxial layers. A major goal for solid state physics and solid state technology is the perfection of materials and substrate in which charge carriers have long lifetime, low scattering, high mobilities and controlled densities: such materials have allowed the elucida-

tion of the electronic structure of solids and the development of semiconductor electronic and photonic devices.

To grow heterojunctions, quantum wells (QW) and superlattices of InP- and GaAs-based materials, different growth techniques are available. In this chapter, we first describe briefly other methods currently used, then describe the metallorganic chemical vapour deposition method and finally discuss recent developments of new methods.

1.1.1 Liquid-phase epitaxy

Liquid-phase epitaxy (LPE) involves the precipitation of material from a supercooled solution onto an underlying substrate. The composition of the layer formed on the substrate depends mainly on the equilibrium phase diagram and to a lesser extent on the orientation of the substrate.

Growth of InP–GaInAsP has been started mainly by LPE, the LPE reactor consisting of a horizontal furnace system and a sliding graphite boat. There are basically three parameters that influence growth in LPE: the melt composition, the growth temperature and the growth time. The first reported growth apparatus was developed by Nelson [1].

The advantages of LPE for the growth of InP-based materials are simplicity of equipment, higher deposition rates and elimination of parasitic reactions due to use of reactive gases and their reactive products, which are often toxic and explosive.

The limitations of LPE technology are non-uniformity of the layer thickness, roughness of surface morphology and smaller wafer sizes. Owing to the high growth rate and melt-back effect, it is very difficult to grow multiquantum-well (MQW) or superlattice (SL) structures with $L_z \leqslant 100$ Å using LPE technology. Figure 1.2 shows a schematic diagram of an LPE reactor.

1.1.2 Vapour-phase epitaxy

The vapour-phase epitaxy (VPE) method was first demonstrated by Tietjen and Amick for the growth of GaAsP alloys. The growth of InP-based materials can be obtained in a fused-silica reactor composed of two zones set at different temperatures by using a multi-element furnace that surrounds the reactor. Hydrogen is often used as a carrier gas, and arsine (AsH_3) and phosphine (PH_3) as arsenic (As) and phosphorus (P) sources. Pure indium and gallium metal can be used as group III element sources. In the first zone of the reactor, called the source zone, held at a temperature T_S lying in the range 750–800°C, the gaseous species to be transported are

synthesized, following the reaction

$$In + HCl \rightarrow InCl + \tfrac{1}{2}H_2$$
$$PH_3 \rightarrow \tfrac{1}{4}P_4 + \tfrac{3}{2}H_2.$$

In the second zone, called the deposition zone, with a temperature T_D in the range 650–750°C, growth occurs via the reaction

$$\tfrac{1}{4}P_4 + InCl + H_2 \rightarrow InP + HCl.$$

VPE is a thermodynamic equilibrium growth technique (like LPE).

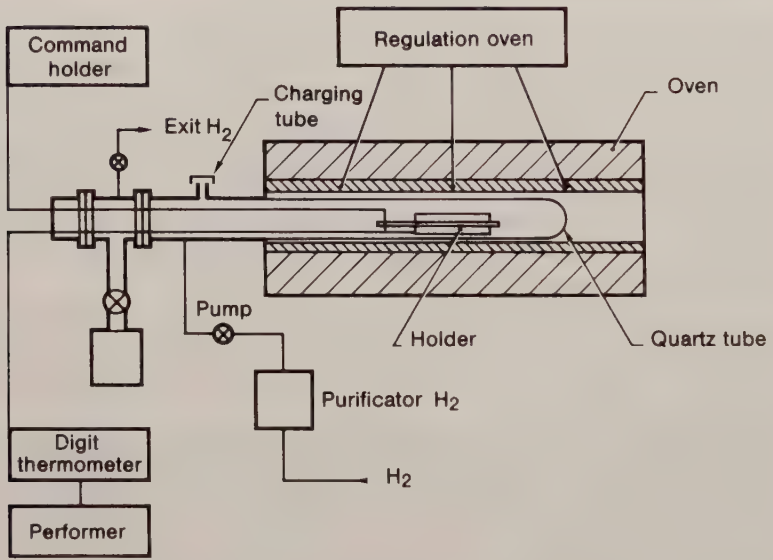

Figure 1.2 Principles of an LPE system.

The advantages of VPE over LPE are a high degree of flexibility in introducing dopant into the material as well as control of composition gradients by accurate flow metering.

Disadvantages include potential for hillock and haze formation, and interfacial decomposition during the preheat stage. It is very difficult to grow MQW or SL structures with $L_z \leqslant 50$ Å using VPE technology. One of the major advantages of VPE over LPE is the possibility of localized epitaxy. This means that if one grows InP-based material on an InP substrate consisting of a stripe of SiO_2 or Si_3N_4, there is monocrystal growth on the substrate, but no growth on the oxide (SiO_2 or Si_3N_4) surface, which could be important for monolithic integrated circuits on InP substrates. Figure 1.3 shows a schematic illustration of a VPE reactor.

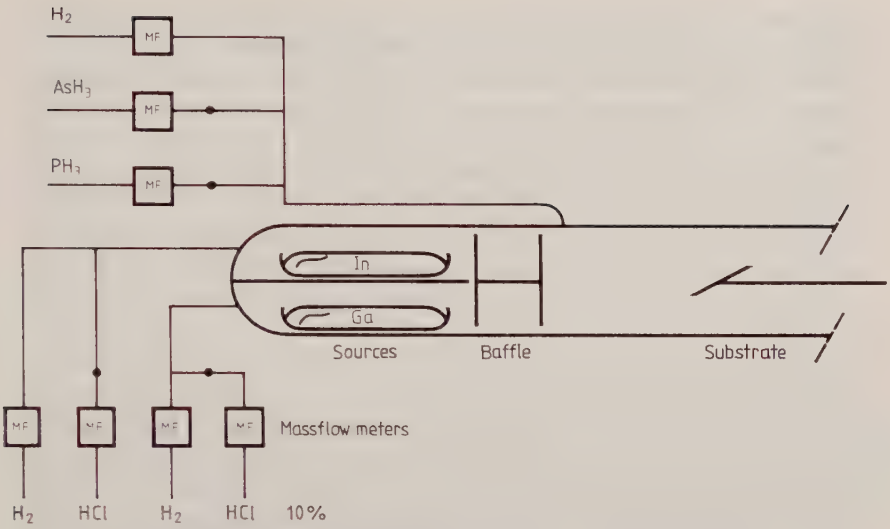

Figure 1.3 Schematic illustration of a VPE reactor.

1.1.3 Molecular beam epitaxy

The molecular beam epitaxy (MBE) process involves the reaction of one or more thermal beams of atoms and molecules of the III–V elements with a crystalline substrate surface held at a suitable temperature under ultra-high-vacuum (UHV) conditions. In 1958, using multiple beams, Gunther [3] described the growth of III–V materials; his films were grown on glass substrates and hence were polycrystalline. In 1968, Davey and Pankey [4] and Arthur [5] grew monocrystalline GaAs films by MBE.

Since MBE is essentially a UHV evaporation technique, the growth process can be controlled *in situ* by the use of equipment such as pressure gauge, mass spectrometer and electron diffraction facility located inside the MBE reactor. The MBE growth chamber can contain other components for surface analytical techniques, including reflection high-energy electron diffraction (RHEED) (the first information about the dynamics of film growth by MBE was obtained by Neave and Joyce [6] by studying RHEED oscillations), Auger electron spectroscopy (AES) (another non-destructive analytical method for characterization of the initial substrate surface, verification of surface accumulation of dopant elements during epitaxial growth, and determination of the change in the relative ratio of the constituent elements of reconstructed surface structures), X-ray photoelectron spectroscopy (XPS), low-energy electron diffraction (LEED), electron spectroscopy for chemical analysis (ESCA), secondary-ion mass spectroscopy (SIMS) (a powerful tool for surface and bulk material-composition analysis for pre- and post-deposition analysis during MBE growth) and

ellipsometry, which can all be used as *in situ* surface diagnostic techniques during MBE growth, due to the UHV growth conditions.

MBE has attracted much interest as an excellent crystal growth technology, especially for GaAs-based multilayer structures, because of its extremely precise control over layer thickness and doping profile, and the high uniformity of the epitaxial layer over a large area of a substrate ($>$ 3 inch diameter).

The disadvantages of MBE are that it is expensive, and that difficulties have been reported with p-type doping by Zn [7] and with the growth of phosphorus-bearing alloys such as InP and GaInAsP. Figure 1.4 shows an MBE reactor.

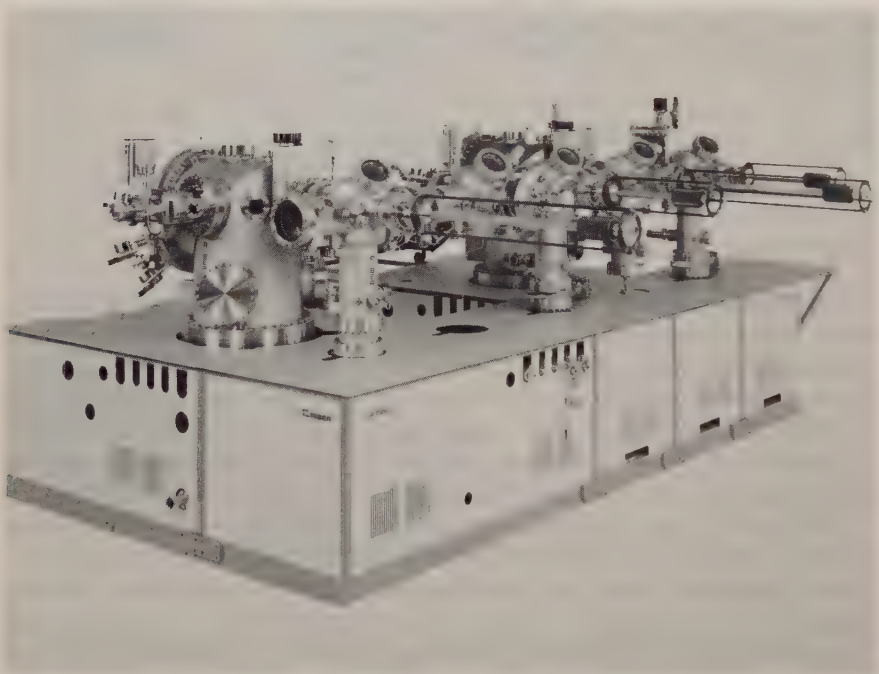

Figure 1.4 Photograph of an MBE reactor.

1.2 METALLORGANIC CHEMICAL VAPOUR DEPOSITION

Metallorganic chemical vapour deposition (MOCVD) has established itself as a unique and important epitaxial crystal growth technique yielding high-quality low-dimensional structures (LDS) for fundamental semiconductor physics research and useful semiconductor devices, both electronic and photonic. The growth of semiconductor III–V compounds results by

introducing metered amounts of the group III alkyls and the group V hydrides into a quartz tube that contains a substrate placed on radiofrequency (RF) heated carbon susceptor. The hot susceptor has a catalytic effect on the decomposition of the gaseous products and the growth therefore takes place primarily at this hot surface. MOCVD is attractive because of its relative simplicity compared to other growth methods. It can produce heterostructures, multiquantum wells (MQW) and superlattices (SL) with very abrupt switch-on and switch-off transitions in composition as well as in doping profiles in continuous growth by rapid changes of the gas composition in the reaction chamber.

The technique is attractive in its ability to grow uniform layers, its low background doping density and sharp interfaces, and in the potential for commercial applications. MOCVD can prepare multilayer structures with thicknesses as thin as a few atomic layers.

The main disadvantage of the MOCVD growth technique is the use of a high quantity of poisonous gases such as AsH_3 and PH_3. By comparison to MBE, it is very difficult to do *in situ* characterization during MOCVD growth (see figure 1.5).

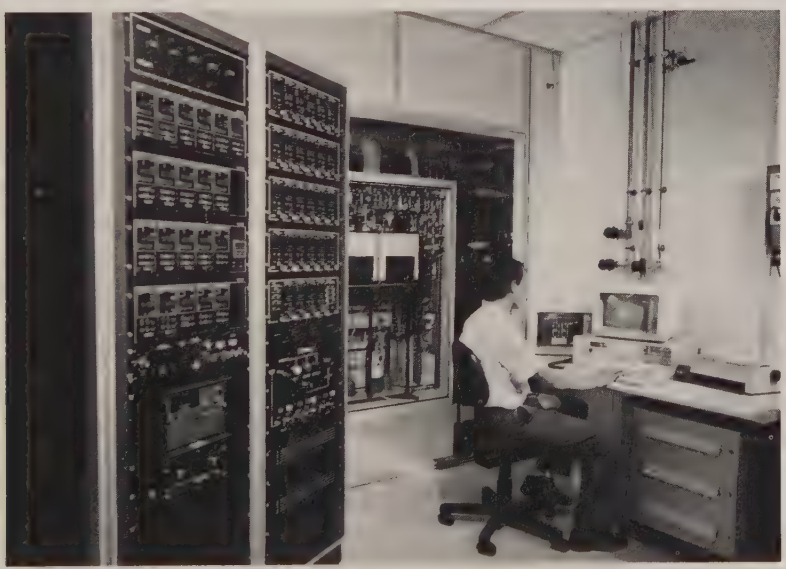

Figure 1.5 Photograph of an MOCVD reactor.

1.2.1 Experimental details

The InP-based semiconductor alloys defined to have an energy gap $E_g \leqslant 2.0$ eV discussed in this book are listed in table 1.1, together with properties relevant to their crystal growth and some of their physical parameters. They

all melt at high temperatures and have a strong tendency to decompose well below their melting points. In consequence, controlled melt growth of these compounds is difficult and most efforts have been directed towards vapour growth as a means for producing high-quality heterojunctions, quantum wells and superlattices.

Table 1.1 Some of the physical parameters of InP-based materials lattice-matched to InP (lattice parameter 5.869 Å).

Compound	Energy gap (eV)	Refractive index n	Electron effective mass, m_e^*	Heavy-hole effective mass, m_h^*
InP	1.35	3.45	0.08	0.56
$Ga_{0.25}In_{0.75}As_{0.5}P_{0.5}$	0.95	3.52	0.053	0.5
$Ga_{0.40}In_{0.60}As_{0.85}P_{0.15}$	0.80	3.55	0.045	0.5
$Ga_{0.47}In_{0.53}As$	0.75	3.56	0.041	0.5

Elemental vapour-phase epitaxy usually requires growth temperatures within the range 700–900°C. It has been recognized increasingly that high-temperature growth thermodynamically favours the formation of a multitude of impurity–defect complexes which act as electron traps and pin the Fermi level far from both the conduction and valence band edges of these compounds, and hence the material exhibits compensating properties. The lower growth temperature (500–630°C) for LP-MOCVD of InP-based materials, a feature shared with MBE, has stimulated substantial interest in this preparative route as a potential way of either eliminating or controlling detrimental impurities and defects. This control is particularly important where the material is the active medium in optoelectronic devices.

A review by Ludowise [8] presented practical information about the apparatus and technique as well as more fundamental details concerning the interrelation of the several parameters that control deposition and material quality.

LP-MOCVD was first applied to the growth of InP using the metal alkyl triethylindium ($(C_2H_5)_3In$, TEIn) and phospine (PH_3) as the source of phosphorus by Duchemin *et al* [9]. A review by Razeghi [10] described advances in the field prior to 1985. The developments since then for the growth of InP-based materials for optoelectronic and microwave devices form the basis of the present chapter.

1.2.2 Reactor design

The most important part of the growth apparatus is the deposition chamber. There are two basic reactor types, a vertical design originated by

Manasevit and Simpson [11], in which the gas flow is perpendicular to the substrate surface, and the horizontal version developed by Bass [12], in which the gas flow is parallel to the substrate surface. Both types have been used successfully at low and atmospheric pressures using several different substrate heating methods involving radiofrequency induction, resistance, radiant and laser heating. Figure 1.6 shows schematic drawings of vertical and horizontal reaction chambers (after Ludowise [8]).

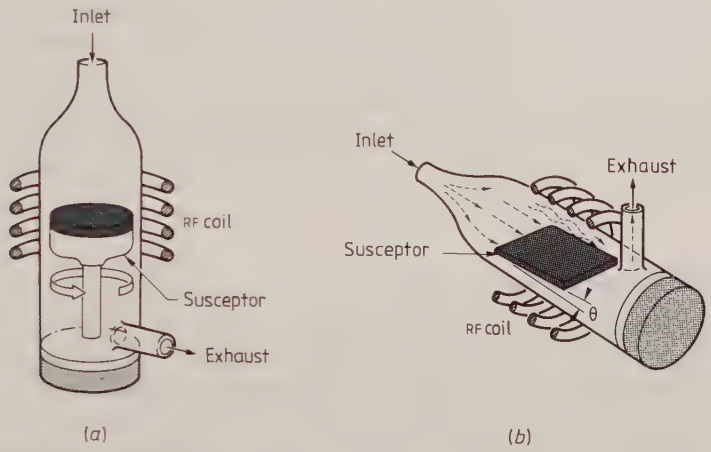

Figure 1.6 Schematic drawings of (*a*) vertical and (*b*) horizontal reaction chambers (after [8]).

The advantages of a low-pressure MOCVD process are:

(1) elimination of parasitic nucleations in the gas phase;
(2) reduction of out-diffusion (i.e. the solid-state diffusion of impurities from the substrate through active layers or from one active layer to another);
(3) reduction of autodoping (i.e. the doping of an epitaxial layer by volatile impurities that originate from the substrate);
(4) improvement of the interface sharpness and impurity profiles;
(5) lower growth temperature;
(6) thickness uniformity and compositional homogeneity; and
(7) elimination of memory effect.

The presence of vortices (behind the susceptor) and dead volumes (sharp corners in reactor inlet) will act as sources of unwanted materials which cannot be removed easily. So during the growth of a sharp heterojunction or a steep doping profile, by switching a flow with another chemical composition, the original composition is still present in the vortices and trapped gases. The slow out-diffusion from these parts will smear out the doping or

heterojunction profiles. This is called the memory effect. We can eliminate such trapped gases by rapid evacuation, i.e. working at low pressure.

In relation to reactor design, the main advantage of the horizontal reactor is considered to be the uniform gas flow achieved over a slightly angled susceptor (7–15°), which leads to uniform deposition as the reactants are depleted from the gas flow.

The most important feature in the growth of III–V semiconductor materials is the arrangement for mixing the gases in order to inhibit the pre-reaction between the constituent gas flow. The reactor design has concentrated on introducing the gases to the reactor separately. Good mixing between the metal alkyls and hydrides through a delivery tube near to the heated substrate is vital. So the use of a carrier gas (H_2 or N_2) which eliminates the pre-reaction enables good mixing to take place and allows the efficient gas mixer designed for III–V semiconductor growth to be utilized.

1.2.3 Growth procedure

The exact chemical decomposition pathways in MOCVD are not yet clearly understood. The nature of the reactions is in part determined by the dynamics of the gas, i.e. the velocity and temperature profiles in the vicinity of the susceptor and the subsequent concentration and thermal gradients that are established. The reaction pathways, of course, are also strongly influenced by the choice of precursor chemicals.

The MOCVD growth of InP, GaAs and related compounds can be explained by the rapid transport of reactive species from the pipeline to the deposition zone by forced flow (in this case, the control of flow dynamics, flow mixing and the adjustment of the flow to geometrical effects and temperature changes are essential). Then the transport of reactive species takes place in the deposition zone to the hot substrates by diffusion (knowledge about development of concentration profiles, the effect of thermal gradients on diffusion and the effect of annihilation or creation of molecular species on diffusion is crucial).

Since the growth rate in MOCVD is limited by mass transport of the group III growth component, flow dynamics coupled with diffusion govern the deposition rates and thereby the gas-phase depletion. A profound knowledge of flow patterns and concentration profiles in the reactor is essential for optimization of reactor construction. In this respect two important factors are homogeneous growth on large surface areas and minimization of gas memory effects, which is essential in the growth of InP-based heterojunctions and superlattices with sharp interfaces. To achieve these, the flow regime must be laminar with no turbulence in order to achieve control over the growth process, and it must develop its pattern in a controlled way when

it enters the reactor. Also when the gas is heated to the process temperature, no instabilities due to natural convection (buoyancy) in the boundary layer must occur. The term 'boundary layer' is used here to define the regions of rapidly increasing compositional, thermal or momentum gradients perpendicular to the substrate.

1.2.4 Flow patterns

One of the important factors in the MOCVD reactor is the flow pattern. We can specify the macroscopic gas movements in the MOCVD reactor (figure 1.7) as follows:

(1) laminar flow versus turbulence;
(2) diffusion versus free convection (buoyancy).

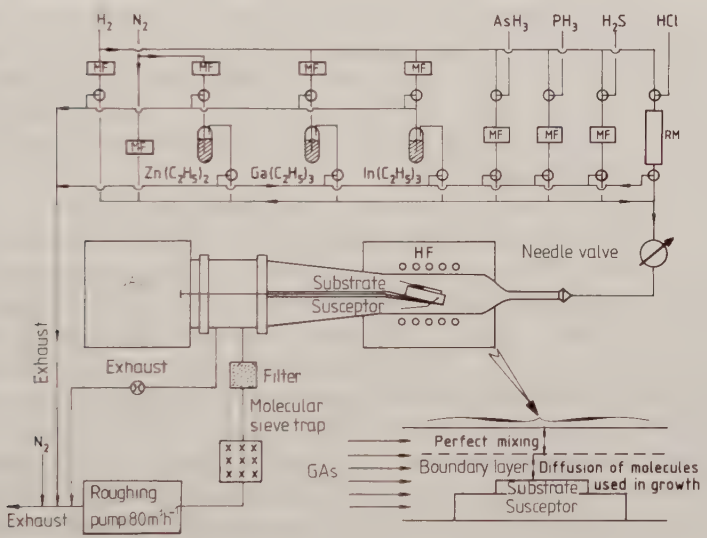

Figure 1.7 Schematic diagram of an MOCVD reactor and tube cross section showing laminar and mixed flow zones.

In order to specify the circumstances in which the different types of flow occur, we need to introduce the concept of the Reynolds number for the first case and the Rayleigh number for the second case.

The Reynolds number R_e (dimensionless) of reactor flow is

$$R_e \simeq \rho \bar{V} d/\eta$$

where d is the diameter of the tube (m), $\bar{V}$ the average flow-rate ($m\,s^{-1}$), ρ the density ($kg\,m^{-3}$) and η the dynamic viscosity ($kg\,m^{-1}\,s^{-1}$) of the gas.

When R_e is small (less than 100) the flow regime is laminar. In laminar flow, the velocity at a fixed position is always the same. Each element of the reactive species travels smoothly along a simple well defined path [13]. Each element starting at the same place follows the same path.

When R_e is high, the flow becomes turbulent, and none of these features is retained. The flow develops a highly random character with rapid irregular fluctuations of velocity in both space and time. In this case, an element of gas flow follows a highly irregular distorted path. Different elements starting at the same place follow different paths, since the pattern of irregularities is changing all the time [14].

The Rayleigh number R_a (dimensionless) of reactor flow is

$$R_a \simeq g\alpha C_p \rho^2 h^3 \Delta T/\eta K$$

where α is the coefficient of thermal expansion (K^{-1}), g the gravitational constant ($9.81\,m\,s^{-2}$), C_p the specific heat ($J\,kg^{-1}\,K^{-1}$), ρ the density ($kg\,m^{-3}$), h the free height above the susceptor (m), $\Delta T = T$(susceptor) $- T$(reactor wall), η the dynamic viscosity ($kg\,m^{-1}\,s^{-1}$) and K the thermal conductivity ($J\,m^{-1}\,s^{-1}\,K^{-1}$). When $R_a \leqslant 1700$, the gas is stable; for $R_a > 1700$, free convection occurs.

At high Rayleigh number, free convection occurs, which affects the mass transfer, growth rate and homogeneity. Usually convection occurs between hot substrate and cold reactor wall. The cause of convection is the action of the gravitational field on the density variations associated with temperature variations. The heavy cold gas is situated above the light hot gas. If the former moves downwards and the latter upwards, there is a release of potential energy which can provide kinetic energy for motion. There is thus the possibility that the equilibrium will be unstable.

From the kinetic gas theory, it follows that both the dynamic viscosity η and the thermal conductivity K are independent of reactor pressure. But the density ρ is pressure-dependent, which means that $R_e \propto \rho$ and $R_a \propto \rho^2$. So, the consequence is that lower pressures stabilize the convection behaviour of the gas flows, and laminar flows are more easily obtained.

For more details on models of flow dynamics, the reader is referred to the book by Tritton [15].

In conclusion, for the growth of high-quality III–V semiconductor materials, with sharp interfaces, and to avoid parasitic reactions in the gas phase and condensation at the inlet of the deposition zone of the reactor, giving variations from day to day and from system to system, the following remarks on reactor design are crucial.

(1) Laminar flows free of convection should exist by:
   (a) using a horizontal reactor,

(b) working at low pressure and
(c) decreasing the reactor diameter.

(2) No temperature gradient should be present across the susceptor.

(3) Eliminate the memory effect:
(a) the geometry of the reactor is such that no vortices can develop;
(b) no dead volumes are present inside the reactor; and
(c) elimination of sharp corners in reactor inlet, where the laminar flow can go by without having a strong interaction, and also behind the susceptor.

1.2.5 Starting materials

Alkyls of the group II and III metals, and hydrides of the group V and VI elements, are usually used as precursor species in MOCVD. Dilute vapours of these chemicals are transported at or near room temperature to a hot zone where a pyrolysis reaction occurs. For example, gallium arsenide is formed by heating trimethylgallium ($(CH_3)_3Ga_2$) or triethylgallium ($(C_2H_5)_3Ga_2$) and arsine over a suitable substrate, usually a single crystal of GaAs or Si, at a temperature around 600°C:

$$(C_2H_5)_3Ga_2 + AsH_3 \xrightarrow{H_2} GaAs + nC_2H_6$$
$$(CH_3)_3Ga_2 + AsH_3 \xrightarrow{H_2} GaAs + nCH_4. \qquad (1.1)$$

Problems may arise through the use of group III alkyls with group V hydrides because reactions may occur between the two species in the cold gas during transport to the hot growth zone.

When the alkyl radical is big, such as triethyl ($(C_2H_5)_3$), the temperature of decomposition is low, and in this case the growth temperature will be low, but there is the possibility of parasitic reaction in the gas phase. When the alkyl radical is small, such as trimethyl ($(CH_3)_3$), it becomes more stable, and the temperature of decomposition is high. The reaction described by equation (1.1) can be generalized for the III–V compounds to

$$R_3M + EH_3 \rightarrow ME + 3RH \qquad (1.2)$$

where M is the group III element, such as Al, Ga or In, E is the group V element, such as Sb, P or As, and $R = CH_3$ or C_2H_5. This is a simplified form of the reaction and it ignores any intermediate steps that may occur. If more than one reaction occurs, such as

$$xR_3M + (1-x)R_3M' + EH_3 \rightarrow M_xM'_{1-x}E + 3RH$$

$$x(C_2H_5)_3In_2 + (1-x)(C_2H_5)_3Ga_2 + AsH_3 \xrightarrow{H_2} In_xGa_{1-x}As + nC_2H_6$$

or

$$x\mathrm{R_3M} + (1-x)\mathrm{R_3M'} + y\mathrm{EH_3} + (1-y)\mathrm{E'H_3} \xrightarrow{\mathrm{H_2}} \mathrm{M_xM'_{1-x}E_yE'_{1-y}} + n\mathrm{RH}$$

$$x(\mathrm{C_2H_5})_3\mathrm{In} + (1-x)(\mathrm{C_2H_5})_3\mathrm{Ga} + y\mathrm{AsH_3} + (1-y)\mathrm{PH_3} \xrightarrow{\mathrm{H_2}} \mathrm{In_xGa_{1-x}As_yP_{1-y}} + n\mathrm{C_2H_6}$$

the alloy composition x and y is determined by the relative rates of the two reactions, which in turn depend upon a number of factors including gaseous diffusion, unknown intermediate steps, thermodynamics (sometimes) and reactor gas dynamics.

In general, the reaction of alkyl and hydride inside the reactor can be described as

$$\mathrm{R_3M} + \mathrm{EH_3} \rightarrow \mathrm{R_3M{-}EH_3}.$$

The strength of the M–E bond is a measure of the stability of the complex $\mathrm{R_3M{-}EH_3}$. Ludowise [8] proposed four cases for the progression of this reaction: (a) no reaction occurs; (b) formation of a volatile compound; (c) formation of a non-volatile compound; and (d) progression to additional reactions which produce non-volatile compounds. Cases (a) and (b) are the trivial cases since vapour transport still proceeds as desired. When non-volatile products are formed (cases (c) and (d)), the carrier gas can be depleted of one or more reactants, resulting in a lowered growth rate or shifted alloy composition. Two examples are the reaction of TEIn and $\mathrm{AsH_3}$ or TEIn and $\mathrm{PH_3}$. At the relatively low concentrations ($\leqslant 10^{-4}$ mole fraction) and high gas velocities used in an MOCVD reactor, the reactions may only progress a few per cent towards completion before the reactants reach the pyrolysis zone. The observation of a particular reaction depends upon the specifics of the reactor geometry. This may account for the current disagreement over the severity or even the existence of a reaction between trimethylindium (TMIn) and $\mathrm{PH_3}$ or $\mathrm{AsH_3}$.

The alternative for MOCVD growth of III–V compounds involves using adducts. An adduct is a compound formed between a group III alkyl such as $\mathrm{MR_3}$, which acts as an electron-acceptor molecule (Lewis acid), and a group V alkyl such as $\mathrm{ER_3}$, which acts as an electron-donor molecule (Lewis base), according to

$$\mathrm{MR_3} + \mathrm{ER_3} \rightarrow \mathrm{R_3MER_3}$$

e.g.

$$(\mathrm{CH_3})_3\mathrm{In} + (\mathrm{CH_3})_3\mathrm{P} \rightarrow (\mathrm{CH_3})_3{-}\mathrm{In}{-}\mathrm{P}{-}(\mathrm{CH_3})_3.$$

The idea of using adducts as precursors for both the group III and group V elements was proposed by Harrison and Tompkins [16] for the growth of

InSb and GaAs. Benz *et al* [17] used TMIn ($(CH_3)_3In$) and TMP ($(CH_3)_3P$) for the growth of InP material.

Later, Dietze *et al* [18] and Moss and Evans [19] developed methods for generating adducts within the reactor. Since the group V alkyls are, in general, stronger Lewis bases than the corresponding hydrides, the stable adducts can be used conveniently to inhibit case (d) reactions of the group III alkyl with group V hydrides. Adducts have a vapour pressure significantly lower than either of the individual components, however, and tend to be solids at room temperature. Adducts are less pyrophoric, are easier to handle than the alkyls and may be easier to purify. Because adducts are low-vapour-pressure solids, heated valves, lines and other equipment are often used to avoid condensation within the reactor. For more details on adducts, the reader is referred to the review by Moss and Evans [19].

Table 1.2 lists the vapour pressures and some other physical properties of most of the commonly used alkyls. The chemical names are usually abbreviated to a four-letter acronym; for example, trimethylgallium becomes TMGa. All of the group III alkyls are pyrophoric and react vigorously on contact with air or water. The alkyls are colourless liquids at room temperature except for the white solids TMIn and Cp_2Mg. The alkyls are monomeric in the vapour except for TMAl, which is dimeric. Because of their reactivity with oxygen, the alkyls must be handled under an inert atmosphere or vacuum. A number of commercial vendors supply the alkyls in electronic-grade purity. Rigorous handling procedures and cleanliness measures are necessary to preserve the level of purity. With the exception of a few workers who have used fractional distillation to improve the purity, most laboratories use the as-received materials.

The compounds used as sources of the group III and group V elements in this book are listed in table 1.3. Their vapour pressures as a function of temperature are given in figure 1.8. Their chemical properties are given in tables 1.4–1.8.

Triethylindium (TEIn), trimethylindium (TMIn) and triethylgallium (TEGa) have been used as group III sources. The hydrides, pure arsine (AsH_3) and pure phosphine (PH_3), have been used as group V sources. Diethylzinc (DEZn) is used for p-type doping and the sulphides, H_2S or silane (SiH_4), have been used for n-type doping. Pure hydrogen (H_2) and pure nitrogen (N_2) have been used as the carrier gas. The presence of N_2 is necessary to avoid the parasitic reaction between TEIn and AsH_3 or PH_3. The presence of H_2 is necessary to avoid the deposition of carbon. TEIn, TMIn and TEGa are contained in stainless-steel bubblers, which are held in controlled temperature baths at 31 and 0 °C, respectively. An accurately metered flow of nitrogen (N_2) for TEIn and purified H_2 for TEGa and TMIn is passed through the appropriate bubbler. To ensure that the source material remains in the vapour form, the saturated vapour that emerges from the bottle is immediately diluted by a flow of H_2.The mole fraction,

Table 1.2 Physical properties of some organometallics used in MOCVD[a].

Compound	Formula	Abbreviation	Melting point (°C)	Boiling point (°C)	$\text{Log}_{10}P$(mmHg) (T in kelvins)	Range (°C)
Group II sources						
Diethylberyllium	$(C_2H_5)_2Be$	DEBe	12	194	$7.59-2200/T$	
Dimethylberyllium	$(CH_3)_2Be$	DMBe				
Bis(cyclopentadienyl)magnesium	$(C_5H_5)_2Mg$	Cp_2Mg	176		$25.14-2.18 \ln T-4198/T$	
Group IIB sources[b]						
Dimethylzinc	$(CH_3)_2Zn$	DMZn	−42	46	$7.802-1560/T$	
Diethylzinc	$(C_2H_5)_2Zn$	DEZn	−28	118	$8.280-2190/T$	
Dimethylcadium	$(CH_3)_2Cd$	DMCd	−4.5	105.5	$7.764-1850/T$	
Group III sources						
Trimethylaluminium	$(CH_3)_3Al$	TMAl	15.4	126	$7.3147-1534.1/(T-53)$	17–100
Triethyaluminium	$(C_2H_5)_3Al$	TEAl	−58	194	$10.784-3625/T$	110–140
Trimethylgallium	$(CH_3)_3Ga$	TMGa	−15.8	55.7	$8.07-1703/T$	
Triethylgallium	$(C_2H_5)_3Ga$	TEGa	−82.3	143	$8.224-2222/T$	50–80
Trimethylindium	$(CH_3)_3In$	TMIn	88.4	133.8	$10.520-3014/T$	
Triethylindium	$(C_2H_5)_3In$	TEIn	−32	184	1.2	44
					3	53
					12	83

Group IV sources						
Tetramethylgermanium	$(CH_3)_4Ge$	TMGe	−88	43.6	139	0
Tetramethyltin	$(CH_3)_4Sn$	TMSn	−53	78	$7.495-1620/T$	
Tetraethyltin	$(C_2H_5)_4Sn$	TESn	−112	181		
Group V sources						
Trimethylphosphorus	$(CH_3)_3P$	TMP	−85	37.8	$7.7329-1512/T$	
Triethylphosphorus	$(C_2H_5)_3P$	TEP	−88	127	$7.86-2000/T$	18–78.2
Trimethylarsenic	$(CH_3)_3As$	TMAs	−87.3	50–52	$7.7119-1563/T$	
Triethylarsenic	$(C_2H_5)_3As$	TEAs	−91	140	15.5	37
Trimethylantimony	$(CH_3)_3Sb$	TMSb	−86.7	80.6	$7.7280-1709/T$	
Triethylantimony	$(C_2H_5)_3Sb$	TESb	−98	116	17	75
Group VI sources[c]						
Diethylselenium	$(C_2H_5)_2Se$	DESe	–	108.00		
Dimethyltellurium	$(CH_3)_2Te$	DMTe	−10	82.00	$7.97-1865/T$	
Diethyltellurium	$(C_2H_5)_2Te$	DETe	–	137–138	$7.99-2093/T$	

[a] After Ludowise [8]. [b] Used as p-type dopants. [c] Used as n-type dopants.

Table 1.3 Starting materials.

Group III sources	Group V sources	p-type dopant sources	n-type dopant sources
$Ga(C_2H_5)_3$	AsH_3	$(C_2H_5)_2Zn$	SH_2
$Ga(CH_3)_3$			SiH_4
$In(C_2H_5)_3$	PH_3		
$In(CH_3)_3$			

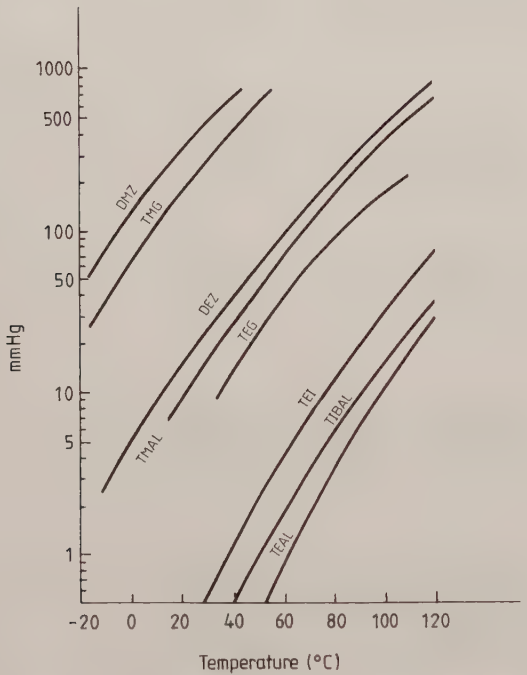

Figure 1.8 The vapour pressure of alkyl sources of group III as a function of temperature.

and thus the partial pressure, of the source species is lower in the mixture and is prevented from condensing in the stainless-steel pipework. The gas piping is made primarily of $\frac{1}{4}$ or $\frac{1}{8}$ inch stainless steel, and Swagelock or VCR fittings can be used. Commercially available alkyls are delivered in stainless-steel containers provided with valves and an inlet diptube assembly (see the appendix) to allow the bubbling of carrier gas, which is high-purity palladium-diffused hydrogen. Flows are monitored by mass flow controllers. These containers are connected by stainless-steel tubes and supported in thermostatically controlled baths in the range -40 to $+150^{\circ}C$. For safety information, see the appendix.

Table 1.4 Chemical properties of triethylindium.

Acronym	TEIn
Formula	$(C_2H_5)_3In$
Formula weight	202.01
Metallic purity	99.9999 wt% (min) indium
Appearance	Clear, colourless liquid
Density	1.260 g ml^{-1} at 20°C
Melting point	−32°C
Vapour pressure	1.18 mmHg at 40°C 4.05 mmHg at 60°C 12.0 mmHg at 80°C
Behaviour towards organic solvents	Completely miscible, without reaction, with aromatic and saturated aliphatic and alicyclic hydrocarbons. Forms complexes with ethers, thioethers, tertiary amines, phosphines, arsines and other Lewis bases
Stability to air	Ignites on exposure (pyrophoric)
Stability to water	Partially hydrolysed; loses one ethyl group with cold water
Storage stability	Stable indefinitely at ambient temperatures when stored in an inert atmosphere

Table 1.5 Chemical properties of triethylgallium.

Acronym	TEGa
Formula	$(C_2H_5)_3Ga$
Formula weight	156.91
Metallic purity	99.9999 wt% (min) gallium
Appearance	Clear, colourless liquid
Density	1.0586 g ml^{-1} at 20°C
Melting point	−82.3°C
Vapour pressure	16 mmHg at 43°C 62 mmHg at 72°C 760 mmHg at 143°C
Behaviour towards organic solvents	Completely miscible, without reaction, with aromatic and saturated aliphatic and alicyclic hydrocarbons. Forms complexes with ethers, thioethers, tertiary amines, tertiary phosphines, tertiary arsines and other Lewis bases
Stability to air	Ignites on exposure (pyrophoric)
Stability to water	Reacts vigorously, forming ethane and Et_2GaOH or $[(Et_2Ga)_2O]_x$
Storage stability	Stable indefinitely at room temperatures in an inert atmosphere

Table 1.6 Chemical properties of trimethylindium.

Acronym	TMIn
Formula	$(CH_3)_3In$
Formula weight	159.85
Metallic purity	99.999 wt% (min) indium
Appearance	White, crystalline solid
Density	1.586 g ml^{-1} at 19°C
Melting point	89°C
Boiling point	135.8°C at 760 mmHg 67°C at 12 mmHg
Vapour pressure	15 mmHg at 41.7°C
Stability to air	Pyrophoric, ignites spontaneously in air
Solubility	Completely miscible with most common organic solvents
Storage stability	Stable indefinitely when stored in an inert atmosphere

Table 1.7 Chemical properties of diethylzinc.

Acronym	DEZn
Formula	$(C_2H_5)_2Zn$
Formula weight	123.49
Metallic purity	99.9999 wt% (min) zinc
Appearance	Clear, colourless liquid
Density	1.198 g ml^{-1} at 30°C
Melting point	−30°C
Vapour pressure	3.6 mmHg at 0°C 16 mmHg at 25°C 760 mmHg at 117.6°C
Behaviour towards organic solvents	Completely miscible, without reaction, with aromatic and saturated aliphatic and alicyclic hydrocarbons. Forms relatively unstable complexes with simple ethers, thioethers, phosphines and arsines, but more stable complexes with tertiary amines and cyclic ethers
Stability to air	Ignites on exposure (pyrophoric)
Stability to water	Reacts violently, evolving gaseous hydrocarbons, carbon dioxide and water
Storage stability	Stable indefinitely at ambient temperatures when stored in an inert atmosphere

Table 1.8 Chemical properties of trimethylgallium.

Acronym	TMGa
Formula	$(CH_3)_3Ga$
Formula weight	114.82
Metallic purity	99.9999 wt% (min) gallium
Appearance	Clear, colourless liquid
Density	1.151 g ml^{-1} at 15°C
Melting point	−15.8°C
Vapour pressure	64.5 mmHg at 0°C 226.5 mmHg at 25.0°C 760 mmHg at 55.8°C
Behaviour towards organic solvents	Completely miscible, without reaction, with aromatic and saturated aliphatic and alicyclic hydrocarbons. Forms complexes with ethers, thioethers, tertiary amines, tertiary phosphines, tertiary arsines, and other Lewis bases
Stability to air	Ignites on exposure (pyrophoric)
Stability to water	Reacts violently, forming methane and Me_2GaOH or $[(Me_2Ga)_2O]_x$
Storage stability	Stable indefinitely at ambient temperatures when stored in an inert atmosphere

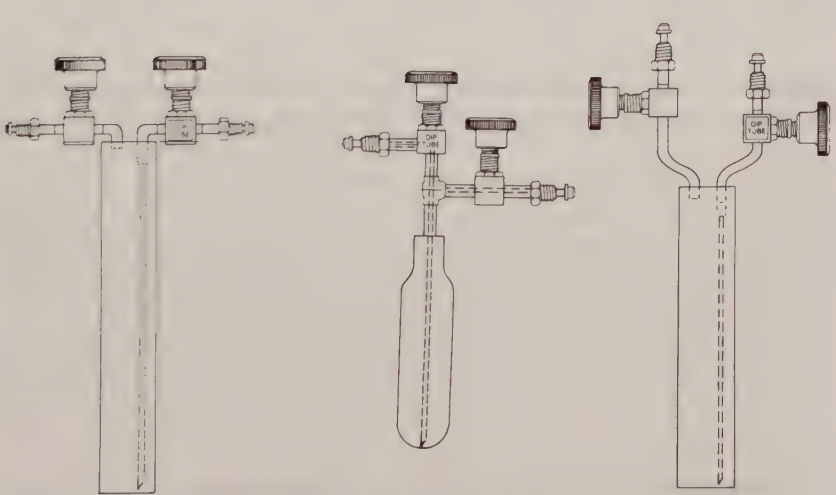

Figure 1.9 The commercially available stainless steel alkyl containers with valves and an inlet dip-tube assembly.

Figure 1.9 shows different alkyl containers.

The-flow rates of the hydrides, H_2 and N_2, are controlled by mass flow controllers within 0.2%. The metal alkyl or hydride flow can be injected either into the reactor or into the waste line by using the three-way valves (see the appendix). In each case, the source flow is first switched into the waste line to establish the flow-rate and then switched into the reactor.

1.3 NEW NON-EQUILIBRIUM GROWTH TECHNIQUES

1.3.1 Chemical beam epitaxy

For the growth of InP-based material with MBE, on the one hand, and for doing *in situ* characterization with MOCVD, on the other, there have been several modifications to the conventional non-equilibrium MBE and MOCVD growth techniques in the past few years. These have enhanced their versatility and increased their potential for the growth of InP and related compounds with extremely thin layers and abrupt interfaces.

In the case of MOCVD, the use of low-pressure MOCVD for the growth of InP was made by Duchemin *et al* [9]. It was shown that for silicon growth the use of low pressure reduced the absorption of hydrogen on the growing surface, thus permitting the growth of good-quality silicon at a lower temperature than is possible at atmospheric pressure. Fraas [20] reported that epitaxial GaAs, GaAsP and GaInAs films with good surface morphologies and electrical properties could be grown by reacting combinations of triethylgallium (TEGa), triethylindium (TEIn), arsine and phosphine in a high-vacuum system.

In the case of MBE, Panish [21] replaced the conventional condensed sources for the group V elements, usually As and P, with sources that decompose AsH_3 and PH_3, and called it gas-source molecular beam epitaxy (GSMBE).

Vodjdani [22] and Tsang [23] replaced the group III elements such as In and Ga used as the condensed source in conventional MBE by simple organometallic compounds. This extension of GSMBE was called metallorganic molecular beam epitaxy (MOMBE), chemical beam epitaxy (CBE) or metallorganic chemical beam deposition (MOCBD).

The CBE reactor (figure 1.10) employed the gas-handling system of MOCVD and the growth chamber of MBE. The main advantages of this combination by comparison to the conventional MBE are:

(1) The capability to grow high-quality InP-based material [24, 25].
(2) Elimination of oval defects even at high growth rates.
(3) High-quality InP-based material at high growth rates.
(4) The flexibility of source changes.

Figure 1.10 Photograph of a CBE reactor.

(5) The versatility of using different alkyl and hydride sources.
(6) Good homogeneity and composition uniformity over large areas of substrate, due to a single group III (and group V if desired) beam.

The main advantages of the above combination compared to MOCVD growth techniques are:

(1) Use of at least 100 times less AsH_3 and PH_3 for the growth of GaAs- and InP-based materials.
(2) Elimination of parasitic reaction in the gas phase, because of UHV conditions.
(3) The possibility of using different *in situ* surface diagnostic techniques.
(4) Improvement of homogeneity and composition uniformity and reproducibility of InP-based materials over large areas of substrate.
(5) *In situ* etching and removal of oxide during the growth of InP on a Si substrate.
(6) Reduction of memory effect during p-type doping.
(7) Reduction of boundary-layer thickness on the hot substrate surface.
(8) Compatibility with other high-vacuum thin-film processing techniques such as plasma etching, metal evaporation, ion beam etching and ion implantation.
(9) The possibility to do localized epitaxy.

No deposition was observed on a SiO_2 film [26, 27]. This is in contrast with conventional MBE or MOCVD where polycrystalline GaAs deposits on the SiO_2 masked region. It was found that monocrystalline GaAs was grown on the bare substrate with narrow-stripe patterns and that the growth

did not take place on the large SiO_2 covered areas. This phenomenon had already been observed with VPE. The growth mechanism that causes this remarkable feature is not clear at present; this feature may be due to a surface-catalysed growth process.

1.3.2 Atomic layer epitaxy

For future integrated circuits (IC) with monolayer controlled multilayer structure, one needs a more advanced epitaxial technique, which has atomic scale, high uniformity of thickness and composition, and perfect selective epitaxy, and is free from any defects such as spitting, dislocations, or hillocks. Atomic layer epitaxy (ALE) is a new growth technique with control at the monolayer level. ALE was originally proposed by Suntola [28, 29], who described a novel mode of evaporative deposition for preparing thin films of zinc sulphide. ALE operates by growing complete layers on top of each other, there being two basic variants based on evaporative deposition, relying on heated elemental source materials, or chemical vapour deposition, relying on sequential surface exchange reactions between compound reactants. By definition, ALE is based on chemical reactions at the solid surface of a substrate, to which the reactants are transported alternately as pulses of neutral molecules or atoms, either as chopped beams in high vacuum, or as switched streams of vapour possibly with an inert carrier gas. The incident pulse reacts directly and chemically only with the outermost atomic layer of the substrate. The film therefore grows stepwise, a single monolayer per pulse, provided that at least one complete monolayer coverage of a constituent element, or of a chemical compound containing it, is formed before the next pulse is allowed to react with the surface.

1.3.3 Metallorganic atomic layer epitaxy

In this technique (MO-ALE) alkyls and hydrides are used for the starting materials. Nishizawa *et al* [30] and Doi *et al* [31] used MO-ALE for the growth of GaAs layers and they showed the GaAs to be p-type, with hole concentrations of $10^{19}\,cm^{-3}$ and mobilities of $60–200\,cm^2\,V^{-1}\,s^{-1}$. Kobayashi *et al* [32] introduced a small amount of AsH_3 during the TEGa exposure step. They call this technique flow-rate modulation epitaxy (FME). They succeeded in the growth of n-type GaAs having carrier concentrations of $10^{14}–10^{16}\,cm^{-3}$ and mobilities as high as $42\,000\,cm^2\,V^{-1}\,s^{-1}$ at 77 K. Additional AsH_3 introduction with TEGa suppresses carbon contamination and explains the gas properties [33].

1.3.4 Chloride atomic layer epitaxy

In this technique, chloride and hydride are used as starting materials. GaAs

layers grown by GaCl-ALE are n-type with a carrier concentration of 6×10^{15} cm^{-3} and mobility of 16 000 cm^2 V^{-1} s^{-1} at 77 K. Matsumoto and Usui [34] showed using photoluminescence at 5 K that the layers are compensated by a carbon acceptor. The electron trap EL_2 was not detected in the GaCl-ALE sample. This is in contrast with conventional VPE or MOCVD samples which exhibit EL_2 in the concentration range 10^{14}–10^{15} cm^{-3}.

The greatest advantage of ALE, especially digital ALE (where the thickness grown is insensitive to any analogue quantities such as source gas pressure, growth temperature and growth time), is to obtain large-diameter integrated-circuit wafers with monolayer control of thickness and composition.

1.3.5 Migration-enhanced epitaxy

Rapid migration of the evaporated materials on the growing surface is essential to the growth of high-quality epitaxial layers. In conventional MBE growth of GaAs and AlAs layers, migrating materials on the growing surface are Ga–As and Al–As molecules rather than Ga and Al atoms, respectively, because these layers are grown under arsenic-stabilized conditions. The migration of these molecules on the surface is very slow, especially at low temperatures. Therefore, lowering the substrate temperature considerably deteriorates the crystal quality of grown layers.

Horikoshi [35] proposed a new mode of MBE growth which makes it possible to grow high-quality GaAs and AlAs layers at very low substrate temperatures ($\sim 200^\circ$C) by enhancing the migration of the materials evaporated on the growing surface. This method has been termed migration-enhanced epitaxy (MEE). It is based on the very rapid migration of Ga and Al atoms on the growing surface, and on the alternate supply of Ga(Al) atoms and arsenic molecules to the growing surface. RHEED intensity observations revealed that Ga and Al atoms migrate on the GaAs surface much more rapidly than Ga–As and Al–As molecules, and that they migrate very actively even at temperatures as low as 200°C. They showed that high-quality GaAs and AlAs could be grown at very low temperatures by alternately supplying Ga(Al) atoms and arsenic molecules to the substrate surface. Applying the MEE method, 1–2 μm thick GaAs layers were grown at a substrate temperature of 200°C. These layers showed efficient photoluminescence (PL) from the band-edge excitons at 4.2 K. AlAs–GaAs single-quantum-well structures with 3–6 nm widths were also grown at 200°C by MEE. These structures showed PL due to electronic transitions between quantized levels in the wells, indicating a reasonable quality of AlAs [35].

REFERENCES

[1] Nelson H 1963 *RCA Rev.* **19** (24) 603
[2] Tietjen J J and Amick J A 1966 *J. Electrochem. Soc.* **113** 724
[3] Gunther K G 1958 *Patent* 2937816
[4] Davey J E and Pankey T J 1968 *J. Appl. Phys.* **39** 1941
[5] Arthur J R 1968 *J. Appl. Phys.* **39** 4032
[6] Neave J H, Joyce B A, Dobson P J and Norton N 1983 *Appl. Phys.* A **31** 1
[7] Noyanuma M and Takahashi K 1975 *Appl. Phys. Lett.* **27** 342
[8] Ludowise M I 1985 *J. Appl. Phys.* **58** R31
[9] Duchemin J P, Bonnet M, Koelsch F and Huighe D 1979 *J. Electrochem. Soc.* **126** 1134
[10] Razeghi M 1985 *Semicond. Semimet.* **22** 299
[11] Manasevit H M and Simpson W I 1971 *J. Electrochem. Soc.* **118** C291
[12] Bass S J 1975 *J. Cryst. Growth* **31** 172
[13] Prandtl L and Tietgens O C 1934 *Applied Hydro- and Aeromechanics* (New York: McGraw-Hill)
[14] Shapiro A H 1961 *Shape and Flow* (London: Heinemann)
[15] Tritton D J 1977 *Physical Fluid Dynamics* (Wokingham: Van Nostrand Reinhold)
[16] Harrison B C and Tompkins E H 1962 *Inorg. Chem.* **1** 951
[17] Benz K W, Renz H, Wiedlein J and Pilkuhn N H 1981 *J. Electron. Mater.* **10** 185
[18] Dietze W T, Ludowise M J and Copper C B 1981 *Electron. Lett.* **17** 698
[19] Moss R H and Evans J S 1981 *J. Cryst. Growth* **55** 129
[20] Fraas L M 1981 *J. Appl. Phys.* **52** 6939
[21] Panish M B 1980 *J. Electrochem. Soc.* **127** 2729
[22] Vodjdani N 1982 *Thèse de Doctorat 3eme Cycle* Université Paris XI
[23] Tsang W T 1984 *Appl. Phys. Lett.* **45** 1234
[24] Panish M B and Hamm R A 1986 *J. Cryst. Growth* **78** 445
[25] Tsang W T 1986 *Appl. Phys. Lett.* **48** 511
[26] Cho A Y and Ballamy W C 1975 *J. Appl. Phys.* **46** 783
[27] Takahashi K 1984 *Proc. Research and Development Association for Future Electron Devices* Tokyo, paper I-2
[28] Suntola T, Atron J, Pakkala A and Linfors S 1980 *SID 80, Digest* 108
[29] Suntola T 1984 *16th Int. Conf. on Solid State Devices and Materials* Tokyo, Extended Abstract, p 647
[30] Nishizawa J and Kurabayashi T 1986 *J. Crystallogr. Soc. Japan* **28** 133
[31] Doi A, Aoyagi Y and Namba S 1986 *Appl. Phys. Lett.* **48** 1787
[32] Kobayashi N, Makimoto T, and Horikoshi Y 1985 *Japan J. Appl. Phys.* **24** L962
[33] Makimoto T, Kobayashi N and Horikoshi Y 1986 *Japan J. Appl. Phys.* **25** L513
[34] Matsumoto T and Usui A 1986 *Fall Meeting Japan. Soc. Appl. Phys.* Abstracts
[35] Horikoshi L 1986 *The Physics and Fabrication of Microstructures* (Les Houches)

Chapter 2 InP–InP System: MOCVD Growth, Characterization and Application

2.1 INTRODUCTION

The early work on InP was stimulated by the need for long-wavelength lasers as light sources adapted to lower loss and lower dispersion at $\lambda = 1.3–1.55\ \mu m$ in silica fibres. Future telecommunications systems will require narrow-spectrum 1.55 μm lasers and very sensitive detectors, and this is driving significant research on the technology of InP and related compounds. For microwave devices, with the exception of mobility, which is higher in GaAs, the other characteristics favour InP over GaAs in terms of superior Gunn device performance. The development of these devices has been the direct result of basic research on InP and related compounds. Knowledge of the band structures, electrical properties, optical properties and carrier recombination mechanisms has led a number of physicists to conclude that multilayers of InP and related compounds are the best candidates for a number of future optoelectronic and microwave devices.

2.2 ENERGY BAND STRUCTURE OF InP

InP (indium phosphide) has the zinc blende crystal structure. Its lattice may be considered as two interpenetrating face-centred-cubic sublattices, one made up of indium atoms and the other of phosphorus atoms.

Figure 2.1 shows the Brillouin zone (see e.g. Kittel [1] for the theory of band structure in crystals) of the InP crystal (zinc blende lattice), and indicates the most important symmetry points and symmetry lines, such as

the centre of the zone ($\Gamma = (2\pi/a)(0, 0, 0)$), the $\langle 1\,1\,1 \rangle$ axes (Λ) and their intersections with the zone edge ($L = (2\pi/a)(\frac{1}{2}, \frac{1}{2}, \frac{1}{2})$), the $\langle 1\,0\,0 \rangle$ axes (Δ) and their intersections ($X = (2\pi/a)(0, 0, 1)$), and the $\langle 1\,1\,0 \rangle$ axes (Σ) and their intersections ($K = (2\pi/a)(\frac{3}{4}, \frac{3}{4}, 0)$).

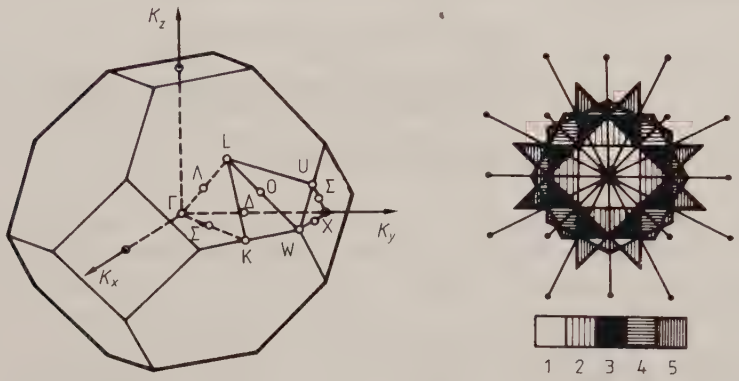

Figure 2.1 First Brillouin zone for InP-based materials (zinc blende lattice), including important symmetry points and lines.

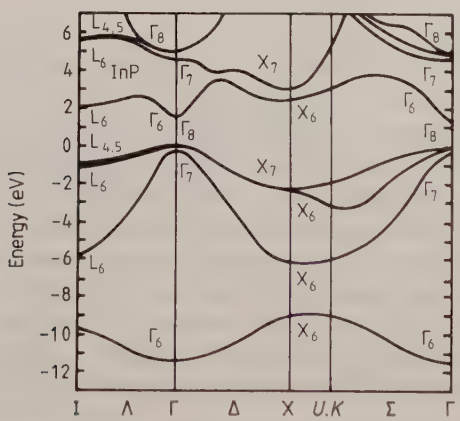

Figure 2.2 The energy band structure of InP.

The E–k diagram of InP is shown in figure 2.2. Around an extremum, the energy E varies with $k - k_0$ parabolically, where k_0 is the value of k at the extremum. The expression relating E has the simplest form for the Γ point minimum. The relation is

$$E - E_\Gamma = \hbar^2 k^2 / 2m_e^*. \tag{2.1}$$

The constant m_e^* is the effective mass of an electron [2]. The E–k relation

for the minima lying on the Λ or Δ directions is of the form

$$E - E_L = \frac{\hbar^2}{2}\left(\frac{\Delta k_\parallel^2}{m_\parallel^*} + \frac{\Delta k_\perp^2}{m_\perp^*}\right) \tag{2.2}$$

where $\Delta \boldsymbol{k} = \boldsymbol{k} - \boldsymbol{k}_L$, $m_\parallel$ is the effective mass for the ⟨1 1 1⟩ direction and $m_\perp$ that for a perpendicular direction.

InP and related compounds have a covalent bond structure. When a covalent bond is produced between two unlike atoms, such as In and P, it is called a heteropolar bond. In InP semiconductor crystals, the bond orbitals are constructed from sp^3 hybrids (see figure 2.3) (a linear combination of p orbitals and s orbitals is called an sp hybrid; the 3 indicates that there is three times the probability of finding an electron in a p state than in an s state). Indium has the electronic configuration $4d^{10}5s^25p^1$ and P has the electronic configuration $3s^23p^3$. After hybridization there are two atoms, and hence eight electrons, per primitive unit cell in the InP crystal. There are one 5s level and three 5p levels in the In atom and one 3s level and three 3p levels in the P atom, each giving rise to a bond in the crystal. This gives a total of four bonds arising from the atomic energy levels containing the valence electrons of InP. These four bonds are called the valence bonds of the band structure of InP. We now consider the allocation of the eight valence electrons of InP among the four valence bonds, since there are two primitive unit cells of the InP lattice. There are a total of eight electrons to put into four valence bonds. Considering, for example, the (1 0 0) and (1 1 1) directions near the centre of the Brillouin zone, the point in K space (reciprocal lattice) at which a valence electron has the highest energy is the Γ point at the centre of the Brillouin zone. We therefore say that the valence-band maximum occurs at the centre of the Brillouin zone. At $T = 0$, all the valence-band states are occupied by electrons, and all the higher bands of the InP band structure are empty. At temperatures above absolute zero, a few electrons will be thermally excited from the highest valence band into the next vacant higher band.

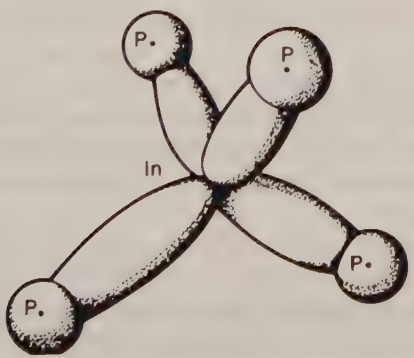

Figure 2.3 sp^3 hybrid bond orbitals.

The next empty band above the highest valence band is called the conduction band, because electrons thermally excited into it will find empty states available for the electrical conduction process. The conduction-band minimum is at the Γ point at the zone centre (the conduction-band minimum is often called the conduction-band edge, and the valence-band maximum is called the valence-band edge). The minimum energy gap E_g is the energy difference between the conduction-band minimum (E_c) and the valence-band maximum (E_v), so the magnitude of E_g of the energy gap in InP is given by

$$E_g = E_c - E_v. \tag{2.3}$$

The valence bands are characteristically threefold near the edge, with the heavy hole (hh) and light hole (lh) bands degenerate at the centre, and a band spin–orbit hole (soh) split off by the spin–orbit splitting Δ;

$$E_v(\text{hh}) \equiv -\hbar^2k^2/2m^*_{\text{hh}} \tag{2.4}$$

$$E_v(\text{lh}) \equiv -\hbar^2k^2/2m^*_{\text{lh}} \tag{2.5}$$

$$E_v(\text{soh}) \equiv -\Delta - \hbar^2k^2/2m^*_{\text{soh}}. \tag{2.6}$$

The values of the mass parameters of InP are given in table 2.1.

Table 2.1 Effective masses of electrons and holes in InP crystal.

Electron effective mass	m^*_e/m_0	0.073
Heavy hole	m^*_{hh}/m_0	0.40
Light hole	m^*_{lh}/m_0	0.078
Split-off hole	m^*_{soh}/m_0	0.15
Spin–orbit splitting	Δ (eV)	0.11

2.3 GROWTH AND CHARACTERIZATION OF InP USING TEIn

High-quality InP layers have been grown by MOCVD. TEIn and PH_3 are used for In and P sources, respectively. A mixture of H_2 and N_2 is used as carrier gas. The presence of H_2 is necessary to avoid the deposition of carbon, and the presence of N_2 is necessary to avoid the parasitic reaction between TEIn and PH_3.

The InP layers can be grown at 76 Torr and low temperature, between 500 and 650°C, by using TEIn and phosphine (PH_3) in a $H_2 + N_2$ carrier gas. The growth rate depends linearly upon the TEIn flow-rate and is independent of the flow-rate of PH_3 within the range 200–800 $cm^3\,min^{-1}$ (figure 2.4), of the substrate temperature and of the substrate orientation,

which suggests that the epitaxial growth is controlled by the mass transport of the group III species.

Razeghi and Duchemin [3] have studied the growth of InP layers by using 100% H_2 and $H_2 + N_2$ mixtures as the carrier gas. The best morphology and the highest PL intensity were obtained by using 50% H_2 and 50% N_2.

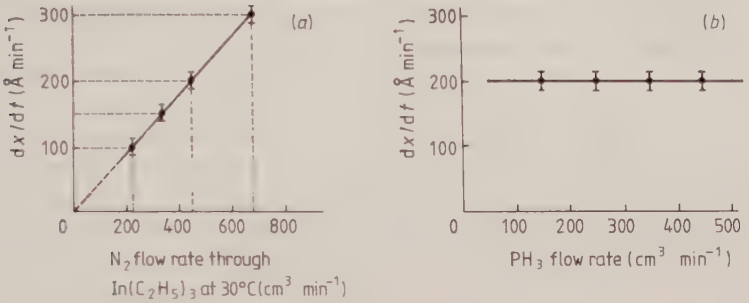

Figure 2.4 Variation of the growth rate of InP with (*a*) TEIn flow ($T_G = 550°C$, PH_3 flow 300 $cm^3\,min^{-1}$, total flow 6 $l\,min^{-1}$) and (*b*) PH_3 flow ($T_G = 550°C$, N_2 flow-rate through TEIn 450 $cm^3\,min^{-1}$).

Table 2.2 Optimum growth conditions.

Growth temperature (°C)	N_2–TEIn bubbler flow ($cm^3\,min^{-1}$)	PH_3 flow ($cm^3\,min^{-1}$)	Total flow ($l\,min^{-1}$)	Growth rate (Å min^{-1})
550	450	260	6	200 ± 10
	225	200	6	100 ± 10
650	450	520	6	220 ± 10
	225	400	6	110 ± 10

Using Ar instead of N_2 gives InP layers with the same surface quality. Table 2.2 lists the optimum growth conditions for MOCVD growth of InP at 550 and 650°C that were used for this study. The InP layers grown by MOCVD are less compensating at lower growth temperature. Figure 2.5 shows that the carrier concentration of InP is $N_D - N_A = 6 \times 10^{14}\ cm^{-3}$ when grown at 520°C and $6 \times 10^{15}\ cm^{-3}$ at 650°C if all other growth conditions remain the same.

2.3.1 Preparation of substrates

Semi-insulating or n^+ substrates are supplied by MCP Crystacomm Metals Research or Sumitomo in the form of ingots or polished wafers. Wafers are sliced 2° off $(1\,\bar{1}\,0)$ and chemically etched for 10 s at room temperature in a

15% bromine–methanol solution in order to remove 20 μm from each side. The wafers are then mechanochemically polished in a solution of 1.5% bromine in methanol, removing 80–100 μm more. The substrates are finally cleaned in methanol and rinsed in isopropyl alcohol. The substrates are etched again, just before use, by dipping in 1% bromine in methanol at room temperature for 1 min, rinsing in warm isopropyl alcohol, and drying. An n^+ Sn-doped substrate and a semi-insulating Fe-doped substrate are generally used for each experiment.

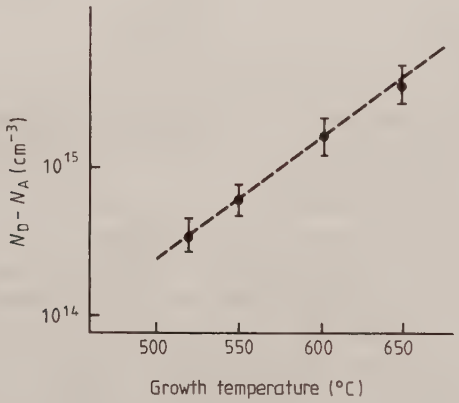

Figure 2.5 Variation of residual carrier concentration of InP layers grown by MOCVD as a function of growth temperature.

Pretreatment of the substrates prior to epitaxial growth is critical. The optimum pretreatment procedure is as follows:

(1) Dipping in H_2SO_4 for 3 min with ultrasonic agitation.
(2) Rinsing in deionized H_2O.
(3) Rinsing in hot methanol.
(4) Dipping in 3% Br in methanol at room temperature for 3 min (ultrasonic bath).
(5) Rinsing in hot methanol.
(6) Dipping in H_2SO_4 for 3 min.
(7) Rinsing in deionized H_2O.
(8) Rinsing in hot methanol.

After this pretreatment, it is possible to keep the substrate for one or two weeks without repeating this treatment prior to growth.

2.3.2 Orientation effects

Growth of InP layers has been carried out on (1 0 0) substrates misoriented

up to 4° towards (1 1 0). At the low growth temperature (550°C), the surfaces of the grown layers are generally mirror-smooth to the naked eye whether the substrates were accurately oriented or not, but at high growth temperature the best-quality InP layers were obtained by using (1 0 0) substrates 2° off towards (1 $\bar{1}$ 0). The density of surface defects is higher on (1 0 0)-oriented substrates compared to 2° off material. Saxena *et al* [4] reported a similar investigation on GaAs substrates.

Most epitaxial growth of III–V semiconductors has been performed on either (1 0 0) or (1 1 1) crystal faces. Shaw [5] has studied the chloride VPE growth of GaAs on (1 0 0), (1 1 1), (1 1 2), (1 1 3) and (1 1 5) GaAs substrates and concluded that the best morphologies in the 700–800°C temperature range are obtained on (1 1 3)A substrates. Olsen *et al* [6] reported the chloride VPE growth of InP on InP substrates at 700°C on (1 0 0), (1 1 1), (3 1 1) and (5 1 1) both exact and 2° off towards (1 1 0) orientation. They found the best morphology and highest PL intensity for the (3 1 1)B 2° off substrate orientation.

Razeghi *et al* [7] have performed a study of MOCVD simultaneous growth on nine InP substrates with orientations of (1 0 0), (1 1 1) and (1 1 5) placed adjacent to each other within the reactor for a growth temperature of 650°C. Table 2.3 indicates relative PL intensity I, PL halfwidth $\Delta h\nu$, growth rate dx/dt, net carrier concentration evaluated by C–V measurements and relative surface appearance of MOCVD InP grown on InP substrates of various orientations at 650°C. The relative PL intensity is a measure of the radiative recombination efficiency within the material, whereas the PL halfwidth is a measure of crystalline quality and impurity incorporation (see §2.4).

Table 2.3 Relative PL intensity I, relative surface appearance and carrier concentrations of the InP grown on InP substrates by MOCVD[a].

Orientation	$N_D - N_A$ (cm^{-3})	Surface quality[b]	I	$\Delta h\nu$ at 300 K (MeV)
InP(Sn)(1 0 0) 2° 1 $\bar{1}$ 0	3×10^{17}	E	16	60
InP(Fe)(1 0 0) exact	3×10^{17}	G	9	60
InP(Fe)(1 0 0) 2° 1 $\bar{1}$ 0	3×10^{17}	VG	16	60
InP(Fe)(1 0 0) 3° 1 $\bar{1}$ 0	3×10^{17}	VG	16	60
InP(Sn)(1 0 0) 4° 1 $\bar{1}$ 0	3×10^{17}	VG	16	60
InP(S)(1 1 1B) 2°	2×10^{17}	VG	45	60
InP(S)(1 1 5B) 2°	2×10^{17}	E	180	95
InP(Fe)(1 1 1B) exact	3×10^{17}	G	10	60
InP(Sn)(1 0 0) exact	3×10^{17}	VG	8	60

[a] Growth rate 220 ± 10 Å min^{-1}.
[b] E, excellent; VG, very good; G, good.

Table 2.4 presents S, Si, Cr, Fe, Mg and Mn distributions measured by secondary-ion mass spectroscopy (SIMS) in these layers. All of the layers were doped by H_2S, and C–V measurements give $N_D - N_A \simeq 2 \times 10^{17}$ cm^{-3} for all of them.

The SIMS analyses were performed using a Cameca IMS3F instrument [8]. The surface of the sample was scanned with a focused oxygen primary-ion beam. The scanned area was 250×250 μm for the working conditions, and the analysed region was 60 μm in diameter.

The precision of measurements is 50% for each impurity element. Analysis of a large number of epilayers is necessary for any given set of growth conditions in order to specify accurately the contribution of each impurity source and its relation to the substrate in MOCVD layer growth.

Table 2.4 S, Si, Cr, Fe, Mg and Mn distributions measured by SIMS in the InP layers grown by MOCVD at 650°C[a].

Reference layer	S	Si	Cr	Fe	Mg	Mn
InP(S)						
(1 1 1)	3×10^{17}	5×10^{16}	4×10^{14}	2×10^{14}	2×10^{14}	4×10^{14}
(1 1 5)	6×10^{17}	5×10^{16}	4×10^{14}	2×10^{15}	1×10^{14}	5×10^{14}
(1 0 0) 2°	3×10^{17}	5×10^{16}	4×10^{15}	1×10^{16}	2×10^{14}	5×10^{14}
InP(Fe)						
(1 0 0) 2°	6×10^{16}	3.5×10^{16}	3×10^{15}	2×10^{14}	4×10^{14}	7×10^{14}
(1 0 0) 3°	8×10^{16}	3×10^{16}	5×10^{14}	2×10^{15}	1×10^{15}	1×10^{15}
(1 0 0) 4°	1.5×10^{16}	5×10^{16}	5×10^{14}	2×10^{14}	2×10^{14}	5×10^{15}
InP(Sn)						
(1 0 0) 2°	2×10^{17}	7×10^{16}	5×10^{15}	2×10^{14}	2×10^{16}	5×10^{14}

[a] All layers doped by H_2S ($N_D - N_A \simeq 2 \times 10^{17}$ cm^{-3}).

2.3.3 Source-purity effects

The importance of source purity is illustrated in table 2.5, where we have listed the range of 300 K and 77 K mobilities and carrier concentrations with a variety of source materials under optimum growth conditions, as defined in table 2.2. The purity of undoped InP grown by MOCVD depends very strongly on the particular source of TEIn and PH_3 used in the growth. Dapkus *et al* [9] reported a similar investigation for GaAs layers grown by MOCVD using TMGa and AsH_3 and showed a similar dependence on source purity.

Table 2.5 Effect of source purity on carrier concentration and 300 K and 77 K mobility on InP layers. Different batches are indicated by producer and batch number.

Sources				
TEIn	PH_3	$N_D - N_A$ (cm^{-3})	μ(300 K) ($cm^2 V^{-1} s^{-1}$)	μ(77 K) ($cm^2 V^{-1} s^{-1}$)
α-Ventron (I)	Matheson (I)	6×10^{14}	5300	85 000
α-Ventron (I)	Air Liquide (I)	3×10^{16}	3400	42 000
Sidercom	Matheson (I)	1.3×10^{16}	3000	25 000
α-Ventron (II)	Matheson (I)	7×10^{15}	3990	58 000
α-Ventron (II)	Air Liquide (I)	7×10^{16}	3550	35 000
Texas-Alkyle	Phoenix	3×10^{15}	4500	65 000
α-Ventron (III)	Matheson (II)	5×10^{15}	5500	95 000
SMI	Matheson (II)	10^{14}	5500	150 000

2.3.4 Material characterization

(a) Photoluminescence

Photoluminescence is the optical radiation emitted by a physical system resulting from excitation to a non-equilibrium state by irradiation with light. Three processes can be distinguished: creation of electron–hole pairs by absorption of the exciting light, radiative recombination of electron–hole pairs, and escape of the recombination radiation from the sample. Photoluminescence (PL) is very useful for the assessment of semiconductor materials. Impurities and native defects that are present in concentrations as low as about 1×10^{15} cm^{-3} can be detected without destruction of the sample, and any surface irregularities are unimportant. By calibrating with known impurity concentrations, it is possible to calculate any unknown carrier concentration from the halfwidth of the spectral line associated with a particular impurity. From the lineshapes and halfwidths as a function of temperature, it is possible to distinguish between simple and complex centres, and between simple donors and acceptors if the effective masses of the electrons and holes are different. By simple donors and acceptors are meant those centres which give rise to luminescence lines whose lineshapes can be fitted by the effective-mass theory for hydrogenic levels. A simple centre is defined as an impurity that sits on the In or P lattice site and which contributes only one additional carrier to the system. The activation energy of a single carrier bound to the substitutional impurity is small and close to that calculated from the hydrogenic model.

Figure 2.6 shows the PL spectrum measured at 6.6 K of an undoped InP layer grown by MOCVD using TEIn α-Ventron and PH_3 from Matheson. The PL was excited by using the 5145 Å line of an Ar^+ laser and was analysed with a Ge photodiode.

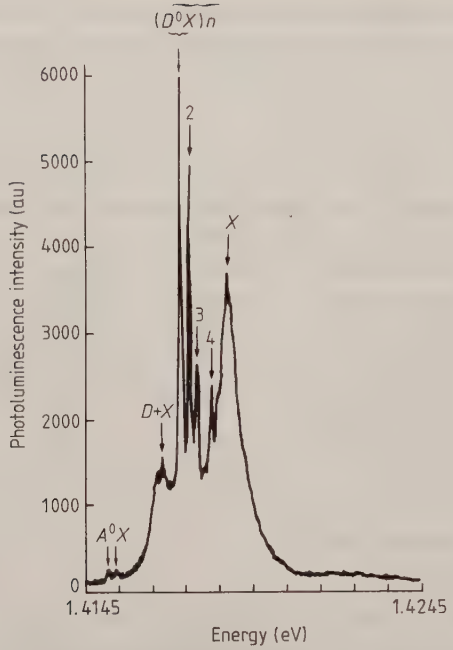

Figure 2.6 Photoluminescence spectrum of InP undoped layer grown by MOCVD.

Similar to GaAs, several elementary recombination mechanisms may occur and cause near-band-gap emission lines: free excitons (X: 1.4181 eV), excitons and shallow impurities (D^0X: 1.4169 eV; A^0X: 1.4147 eV). Silicon is the dominant donor and Zn the acceptor in the undoped InP samples grown by MOCVD, using TEIn.

(b) Study of impurity redistribution in the InP layer by SIMS

In SIMS analysis the surface of the sample under study is bombarded by a beam of energetic ions (O_2^+, Ar^+ or Cs^+ generally). A fraction of the sputtered species are ions. The secondary ions provide information about the sample composition. A mass spectrometer selects the mass of the ions of interest. The secondary-ion intensity measurements are carried out by an electron multiplier.

The analyses at Thomson are performed with a Cameca IMS3F [10, 11], which has the essential characteristics required for semiconductor analysis, such as high trace sensitivity (parts-per-billion range), high mass resolution ($M/\Delta M = 10\,000$), high depth resolution (nanometre range), wide dynamic range in depth profiling (5 in current use, 7 in special conditions), mass-separated primary-ion beam, simultaneous depth profiling of several elements and caesium gun equipment. The use of Cs^+ ion bombardment in

conjunction with negative secondary-ion detection in an ultra-high-vacuum environment has dramatically increased the usefulness of SIMS, particularly for III–V compound technology [12]. Therefore SIMS, with its excellent sensitivity and depth resolution (30–100 Å), provides doping profiles and positions.

The replacement in the primary- and secondary-ion optics of the stainless-steel apertures by tantalum ones was one of the modifications. As a result of this the background of Cr diminished by a factor of 100 and a lower limit of detection of about 5×10^{12} atoms cm^{-3} was obtained in InP for these elements. This sensitivity is necessary for a better evaluation of InP, because Fe and Cr are deep-acceptor-level elements in InP. In the analysis of InP, the surface is scanned with a focused mass-filtered oxygen-ion beam ($I_p \sim 1.5$ μA at 10 keV). The scanned area is 250×250 μm and the analysed region is 150 μm in diameter [13]. An offset target voltage of -50 V was applied to avoid possible interference with ionized hydrocarbons. Ion-implanted samples were the standard for quantitative calibration of the instrument. The statistical results of various experiments show that the quantitative results of SIMS are given with an accuracy of ±20% at a concentration level of 1×10^{16} atoms cm^{-3}. Below this level, results are less accurate: ±50% at 1×10^{14} atoms cm^{-3}. Depth measured on a bevel has a precision estimated at 10%. The detection limits of the impurities that were measured are Mg, Cr, Mn: 5×10^{12} atoms cm^{-3}; Fe: 1×10^{13} atoms cm^{-3}; and Si: 7×10^{13} atoms cm^{-3}.

Figure 2.7 shows typical SIMS depth profiles of Mg, Si, Cr, Fe and Mn in an InP layer grown on semi-insulating Fe-doped InP substrate by MOCVD under standard growth conditions. Each sample was analysed in two different areas about 10 mm apart. Generally, analysis of two clean areas gives reproducible and representative results for the material.

Accumulation of impurities such as Mg, Fe, Cr, Mn and Si was detected by SIMS at the interface between substrate and epilayer. A similar phenomenon was observed in GaAs epilayers grown by MOCVD [14]. The accumulation of these impurities may have different origins such as:

(1) Incorporation of impurity from the ambient gas phase during preheating.
(2) Incorporation of impurity from exposure to air.
(3) Contamination of the substrate by chemical etching before growth.
(4) Incorporation of impurity during *in situ* HCl etching.
(5) Out-diffusion of impurities from substrate to epilayer.
(6) The effect of substrate orientation on impurity redistribution.

To determine the origin of these impurities, Razeghi and Duchemin [3] performed the following experiment. An InP epilayer 3 μm thick was grown on an InP substrate under the conventional procedure. The wafer was

removed from the reactor. After 30 min exposure to air, the wafer was transferred again into the reactor and a second epilayer 3.5 μm thick was grown under the same growth conditions.

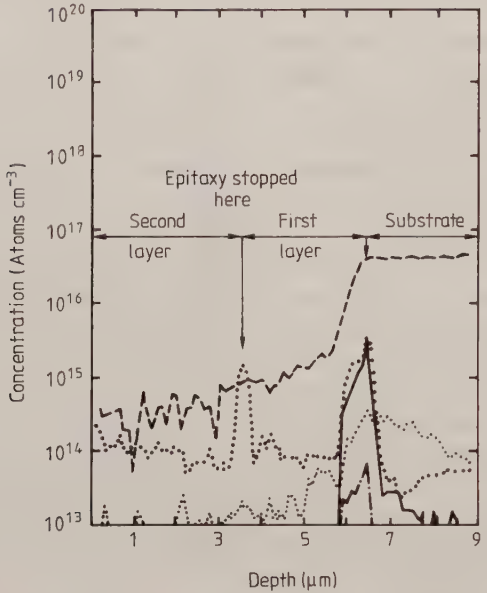

Figure 2.7 Depth profiles of Mg (—), Si (. . . .), Cr (. . . .), Fe (— — —) and Mn (— · —) in an MOCVD InP layer grown on an InP(Fe) substrate. Epitaxy was stopped, the wafer was taken out of the reactor and a second layer was grown on the first.

Figure 2.7 shows the 'pile-up' of impurities at the epilayer–substrate interface where peaks in the concentration of Mg, Cr, Mn, Fe and Si were analysed. At the epilayer–epilayer interface, the only concentration change was some increase in the Si level, which may be due to the heating of the susceptor. These experiments indicate that exposure to air and heating under $H_2 + N_2 + PH_3$ pressure under conventional growth conditions do not account for the accumulation of impurities.

In order to examine the possibility of contamination of the substrate by pregrowth chemical treatment, Razeghi [16] grew an InP epilayer 10 μm thick under conventional growth conditions. She cut the sample into two parts. On one part, Razeghi did the pregrowth chemical etching to remove 2 μm of epilayer.Then the sample was placed into the reactor and another 2 μm InP was grown under the conventional growth conditions. Figure 2.8 shows the impurity profile of the sample after regrowth. One can observe similar accumulations of impurities at the epilayer–substrate interface and epilayer–epilayer interface. These results show clearly that the majority of

impurities result from the chemical etching, even though very pure reactants were used (e.g. 'suprapure' Merck H_2SO_4, Fe (10^{-6}%), Cr (10^{-7}%) and Mg (10^{-6}%)).

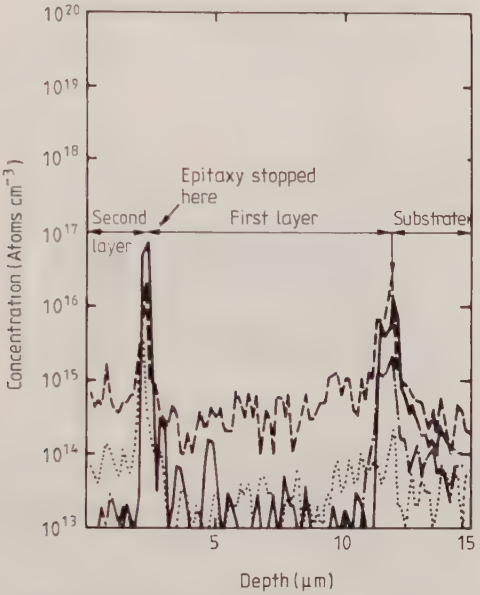

Figure 2.8 Depth profiles of Mg (—), Cr (. . . .), Fe (— — —) and Mn (— · —) in an MOCVD InP layer grown on an InP(S) substrate. The first layer was partly removed by controlled chemical etching. A second layer was grown on the chemically treated first epilayer.

In order to evaluate the effect of some growth parameters such as *in situ* HCl etching prior to layer growth on impurity redistribution, the second part of the 10 μm thick InP epilayer was again placed in the reactor and Razeghi *et al* did *in situ* HCl etching for 1 min at 550°C. After that, they grew 2 μm InP on the sample. Figure 2.9 shows the SIMS impurity profiles of the sample. The considerable peaks of Si, Fe, Mg, Mn and Cr at the epilayer–epilayer interface show the impurities incorporated from the HCl.

In situ HCl etching without PH_3 flow created the same interface contamination with an enhanced impurity redistribution in the layer for Fe and Cr which occurred as shown in figure 2.10. It is possible that in this case a surface with a large degree of non-stoichiometry and a large density of defects (phosphorus vacancies) accelerates impurity diffusion.

To evaluate the effect of doping elements of substrates, Razeghi and Duchemin [3] have performed a study of MOCVD growth simultaneously on three InP substrates doped respectively with Fe, Sn and S placed adjacent to each other within the reactor for growth under conventional growth conditions.

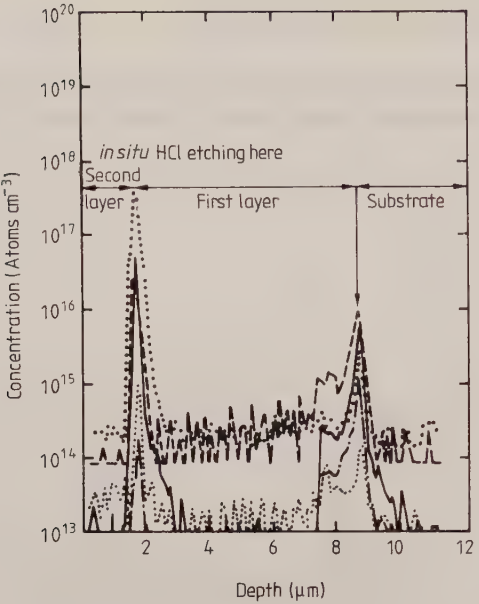

Figure 2.9 Depth profiles of Mg (—), Si (. . . .), Cr (— — —), Fe (. . .) and Mn (— · —) in an MOCVD InP layer grown on an InP(S) substrate. The first layer was partly removed by *in situ* HCl etching in PH_3/H_2 flow.

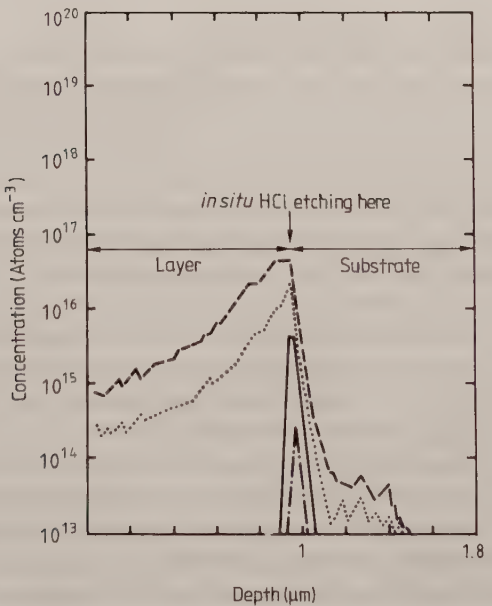

Figure 2.10 Depth profiles of Mg (—), Cr (. . . .), Fe (— — —) and Mn (— · —) in an MOCVD InP layer grown on an InP(S) substrate. The substrate was *in situ* HCl etched without PH_3 in H_2.

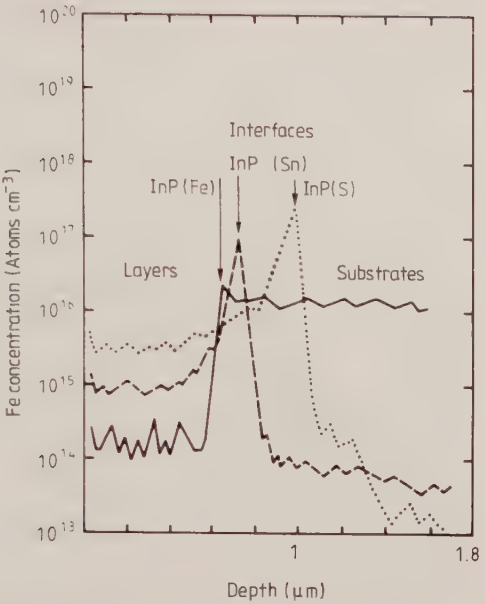

Figure 2.11 Depth profiles of Fe in MOCVD on InP(Fe) (—), InP(S) (. . .) and InP(Sn) (— — —) substrates (same run).

Figure 2.11 shows the Fe profiles. One can observe that the Fe concentration and the Fe accumulation at the Fe-doped substrate–epilayer interface and in the layer are about 10 times lower than in the case of Sn- or S-doped substrates. The result are similar for Mg, Mn and Si. The different levels of the same elements in the layers grown in the same run are most probably due to the substrate quality. The degree of non-stoichiometry on the surface and in the substrates could influence chemisorption, the crystal quality of layers, the formation of vacancies and consequently the impurity redistribution. Layers grown on Fe-doped substrates often present lower impurity peaks at the interface and lower impurity density in epitaxial layers. Nevertheless, similar results have also been obtained on S- and Sn-doped substrates from different growths and different suppliers [17].

In order to estimate the effect of substrate orientation on the impurity redistribution, growth of InP layers has been carried out on Fe-doped substrates oriented 2°, 3° and 4° off (1 0 0) towards (1 1 0) (from the same InP ingot) [3].

The three samples were prepared simultaneously and layers were grown in the same run under conventional growth conditions. Figure 2.12 shows the Fe depth profiles of layers. No significant difference in Fe redistribution due to misorientation of InP substrate can be observed. Similar results were found concerning Mg, Cr, Si and Mn.

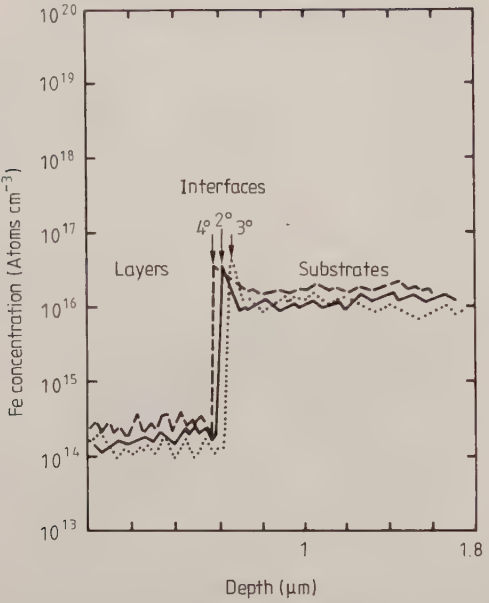

Figure 2.12 Depth profiles of Fe in MOCVD InP on InP(Fe) semi-insulating substrates oriented (1 0 0) off 2° (—), 3° (. . . .) and 4° (— — —) towards (1 1 0).

(c) Carrier concentration measurements

When a metal is brought into intimate contact with a semiconductor, the difference between the conduction band of the semiconductor at the interface and the Fermi level in the metal is established. The energy difference is called the built-in voltage eV_{bi} and serves as a boundary condition on the solution of the Poisson equation in the semiconductor, which proceeds in exactly the same manner as in p–n junctions. Energy band diagrams of a Schottky barrier on an n-type semiconductor under different biasing conditions, viz. (*a*) thermal equilibrium, (*b*) forward bias and (*c*) reverse bias, are shown in figure 2.13 [19].

A depletion region is established by the combined effect of the built-in voltage (V_{bi}) and applied reverse bias (V_{aR}) or applied forward bias (V_{aF}), and the electron density distribution $n(X)$ at the edge of the depletion region is as illustrated in figure 2.13(*d*). The plot of space-charge density $\rho(X)$ as a function of depth for uniform material illustrates the presence of positive fixed ionized donor charge eN_d in the semiconductor and an accumulation of electrons in the metal (figure 2.13(*e*)). Under the abrupt approximation that $\rho \simeq qN_d$ for $X \leqslant X_d$ and $\rho \simeq 0$ and $dV/dX \simeq 0$ for $X > X_d$, where X_d is the depletion width, N_d can be given by

$$N_d = \frac{2}{q\varepsilon_s}\left(-\frac{1}{d(1/C^2)/dV}\right). \tag{2.7}$$

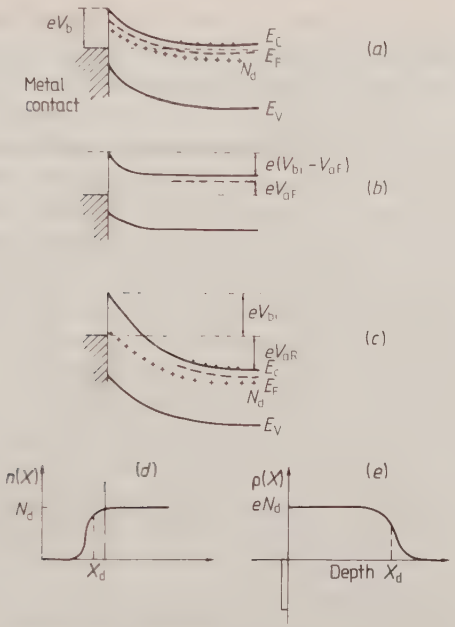

Figure 2.13 Energy band diagram of a Schottky barrier on an n-type semiconductor under different biasing conditions: (*a*) thermal equilibrium; (*b*) forward bias; (*c*) reverse bias; (*d*) electron density distribution $n(X)$ at the edge of the depletion region; (*e*) space-charge density plotted as a function of depth.

If N_d is constant throughout the depletion region, one should obtain a straight line by plotting $1/C^2$ versus V.

For determining the carrier concentration in InP and related compounds, the conventional non-destructive, capacitance–voltage ($C-V$) method is usually used. The main disadvantage of the $C-V$ method is that the maximum depth that can be profiled is limited by electrical breakdown at high reverse bias, and this can be restrictive in highly doped materials where the depletion depths are small. Originally this was overcome by alternate chemical etching and profiling with a temporary mercury barrier, but this process is time-consuming and tedious. Ambridge *et al* [20–22] used an electrolyte to make the barrier and to remove material electrolytically so both processes can be carried out in the same electrochemical cell and controlled electronically, using automatic equipment to perform the repetitive etch/measure cycle and generate a profile plot. The etch depth can be measured continuously by integrating the etch current and applying Faraday's law. The basic principles of electrochemical $C-V$ profiling are documented in a number of original papers by Ambridge *et al* [22] and a review paper by Blood [23]. This method is destructive, but the profile can, in principle, be measured to unlimited depth. The requirements for the

electrolyte are rather demanding, calling for satisfactory barrier and dissolution properties on n- and p-type material. Actually, a versatile instrument manufactured by Polaron Equipment Ltd, Watford, UK (sometimes called the 'Post Office Plotter' or POP) is available commercially.

Figure 2.14 shows a schematic diagram of the electrochemical cell used in the profiles. The semiconductor sample is held against a sealing ring, which defines the contact area, by means of spring-loaded back-contacts. The etching and measuring conditions are controlled by the potential across the cell and this is established by passing a DC current between the semiconductor and the carbon electrode to maintain the required overpotential measured potentiometrically with reference to the saturated calomel electrode (SCE). The AC signals are measured with respect to a Pt electrode located near the semiconductor surface to reduce the series resistance of the electrolyte. The capacity associated with the charged depletion zone in the semiconductor material is then determined. When the contact is illuminated with photons of energy greater than the band gap of the semiconductor, the reverse current is increased, due to the flow of holes or electrons from the semiconductor into the electrolyte in n- or p-type material, respectively. This causes a change in the voltage for zero current which is of opposite sign for n- and p-type material and can therefore be used to indicate the material type. Material is dissolved when an anodic current is drawn by a flow of holes from the InP, whereas a cathodic current causes deposition of material from the electrolyte (which is HCl for InP) onto the semiconductor surface. In order to etch n-type material the holes are generated by illumination under reverse bias. Smooth removal of n-type material is achieved when the anodic current depends upon the illumination intensity but not upon the potential. For a reverse-bias $C-V$ measurement on p-type material, the potential is switched from an anodic to a cathodic value, and, to avoid contamination of the sample surface by the cathodic reaction promoted by electrons from the conduction band, it is important that the cathodic potential is such that the reverse current during the measurement is very small.

To calculate the depth etched (X_e), one can use Faraday's law of electrolysis [23] for the total charge transferred by integrating the etch current I:

$$X_e = (M/qFDS) \int I \, dt \tag{2.8}$$

where M is the molecular weight and D the density of the semiconductor, F the Faraday constant, S the dissolution surface and q the charge transferred per molecule dissolved. For InP, $q = 6$. The depletion depth (X_d) can be obtained from

$$X_d = \varepsilon\varepsilon_0 S/C \tag{2.9}$$

by measurement of C at 3 kHz ($\simeq 0.14$ V peak-to-peak), and $N(X_d)$ is

derived from

$$N(X_d) = -\frac{C^3}{e\varepsilon\varepsilon_0 S^2}\left(\frac{\Delta C}{\Delta V}\right)^{-1} \tag{2.10}$$

where $\Delta C/\Delta V$ is measured by modulation at 30 Hz ($\simeq 0.28$ V peak-to-peak) at a low fixed reverse bias.

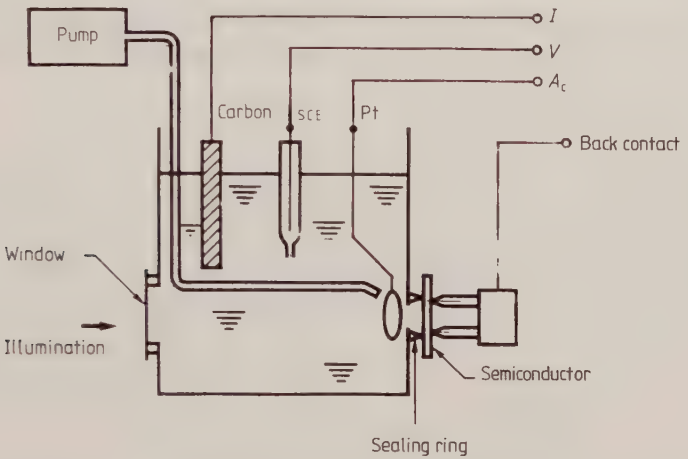

Figure 2.14 Schematic diagram of the electrochemical cell used in the profiles.

Figure 2.15 shows a typical electrochemical profile of an n-type InP grown by MOCVD using the 3 mm sealing ring and HCl electrolyte. Figure 2.15(*a*) shows the electrochemical (polaron) profile for InP over an Sn-doped InP substrate ($N_D - N_A = 10^{18}$ cm^{-3}), establishing uniform doping through the layer thickness and an abrupt change in carrier concentration.

Figure 2.15(*b*) shows the carrier concentration profile evaluated from C–V measurements for InP over a semi-insulating InP substrate, exhibiting uniform doping through the layer thickness and an abrupt change in carrier concentration. The C–V measurements and polaron profile give the concentration of shallow dopants ($N_D - N_A$), which agrees with the carrier concentration deduced from Hall effect measurements.

(d) Hall mobility measurements

All of the devices using InP-based materials require an exact specification in terms of carrier concentration and thickness, and top performance often depends on material quality. Use of the Hall effect is extremely common to determine carrier density and mobility between room temperature and 2 K. In many cases mobility is used as a simple figure of merit for quality of

starting materials such as hydride (PH_3 or AsH_3) and alkyl (TEIn or TMIn). Hall data can yield excellent quantitative information on the electrically active impurities in a semiconductor.

The total mobility in InP material results from the combination of different scattering processes such as:

(1) defect scattering—impurity (neutral or ionized) scattering and crystal defects;

(2) lattice scattering—inter-valley scattering, intra-valley optic (polar or non-polar) scattering, intra-valley acoustic (piezoelectric or deformation potential) scattering; and

(3) carrier–carrier scattering.

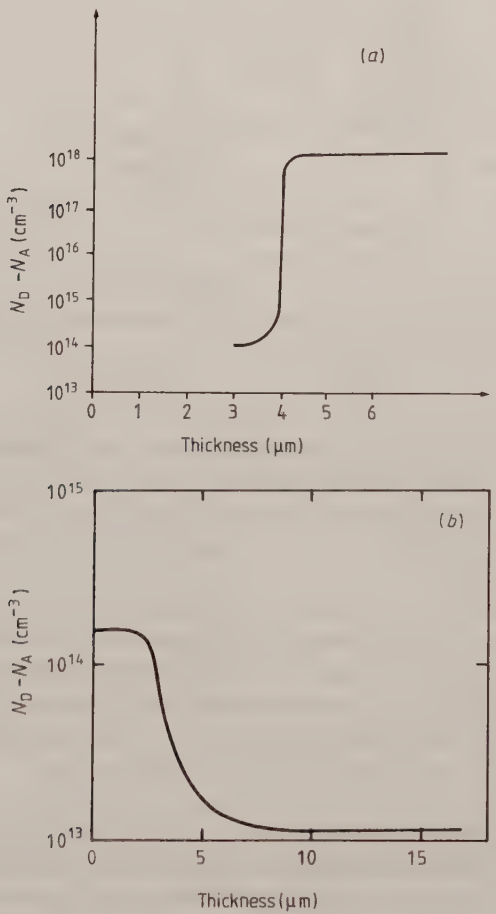

Figure 2.15 Carrier concentration profiles from (*a*) polaron profile and (*b*) $C-V$ measurements for InP (TEIn) layer on semi-insulating InP substrate.

The lack of a centre of symmetry in InP-based materials leads to piezoelectric behaviour and through this the phonons can scatter the electrons. The most important defect scattering is charged-impurity scattering, in which the electron scatters off the long-range Coulomb potential. Neutral centres can also interact in a complex manner but this is generally only important in the highest-purity samples at low temperatures. The dependence of mobility from ionized impurities (μ_i) on temperature and impurity density can be given by [19]

$$\mu_i \simeq (m^*)^{-1/2} N_I^{-1} T^{3/2} \tag{2.11}$$

where N_I is the ionized-impurity density.

The lattice is in constant motion even at absolute zero, the quantized normal modes of its vibration being known as phonons. The contractions and dilatations of the lattice in the presence of phonons create potential fluctuations of various origins which interact with and scatter the electron. The interaction may be through local band structure perturbations, known as deformation potential scattering, involving either acoustic phonons or non-polar optic phonons.

The temperature dependence of the mobility due to deformation potential acoustic phonon scattering is

$$\mu_A \simeq (m^*)^{-5/2} T^{-3/2}. \tag{2.12}$$

In polar semiconductors such as InP, the lattice vibrations give rise to an electrostatic potential on which the carriers can scatter. For acoustic phonons, this mechanism is known as piezoelectric scattering. Above 200 K polar optical phonon scattering dominates the mobility.

For making Hall measurements the Van der Pauw clover-leaf [24] geometry is most commonly used. This pattern is ideal and simple for making Hall measurements on epitaxial layers in which the layer thickness is orders of magnitude less than the lateral dimension of the sample.

Figure 2.16 shows the typical Hall mobility as a function of temperature for InP layers grown by MOCVD. From these data and the measured carrier density, one can usually estimate the net donor density $N_D - N_A$, the compensation ratio $K = N_A/N_D$ and the donor ionization energy E_d.

If we assume that all common donor species in InP and related compounds are hydrogenic with binding energy E_d given by

$$E_d = 13.6 \times \frac{m^*}{m_0} \frac{1}{\varepsilon_r^2} \quad \text{(eV)} \tag{2.13}$$

with $m_e^* = 0.08 m_0$, $m_p = 0.5 m_0$ and $\varepsilon_r = 12.4$ (ε_r is the relative dielectric constant), we obtain for donor impurities $E_d(\text{donor}) \simeq 7$ meV and for acceptor impurities $E_d(\text{acceptor}) \simeq 40$ meV. This shows that for InP and related compounds the donors are all shallow and the acceptors rather deep.

This means that for temperatures between, say, 4 and 400 K, the Fermi-energy movement is not sufficient to change the charge state of the deeper compensating acceptors.

Hall mobilities of epitaxial InP layers grown on semi-insulating substrates were measured in a magnetic field of 4000 G by a conventional Van der Pauw technique. In table 2.6 we give the measured mobility at 300 and 77 K in undoped InP, using pure starting materials (TEIn from α-Ventron and PH_3 from Matheson).

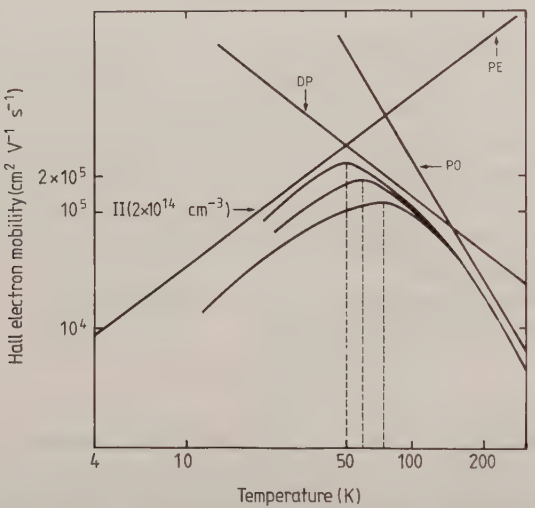

Figure 2.16 Electron Hall mobility as a function of temperature, for MOCVD InP on InP substrate.

Table 2.6 Average measured values of mobility for InP epilayer.

		300 K		77 K	
Sample no.	Thickness (μm)	$N_D - N_A$ (cm^{-3})	μ_H ($cm^2 V^{-1} s^{-1}$)	$N_D - N_A$ (cm^{-3})	μ_H ($cm^2 V^{-1} s^{-1}$)
119	2.5	2×10^{15}	5350 ± 2%	1.5×10^{15}	59 800
151	2.5	5×10^{15}	5240 ± 2%	3.6×10^{15}	56 700
127	3.3	5.7×10^{15}	4950 ± 2%	5.7×10^{15}	53 320
43	4	10^{14}	5500 ± 2%	10^{14}	150 000

(e) Deep-level transient spectroscopy

This is a method for obtaining information about defects giving rise to electrically active deep energy levels. Conventional deep-level transient

spectroscopy (DLTS) can, in a Schottky-barrier junction, only detect majority-carrier traps. It is easy, however, to resolve different traps and derive their concentrations. The DLTS measurements show that there are two electron traps in InP layers grown by MOCVD (see table 2.7) [25].

Table 2.7 Electron traps in InP epilayer.

Activation energy, E (meV)	Capture cross section, S (cm^{-2})
E_5, 433	3×10^{14}
E_6, 661	8×10^{14}

2.3.5 Interfaces

The surface of InP layers and the epitaxial layer–substrate interface have been studied by Auger electron spectroscopy. Figure 2.17 shows the Auger spectrum for such an interface eroded by sputtering. Here it can be seen that there are no impurities at the interface. Figure 2.17 indicates the Auger spectrum for the surface of the InP epilayer and shows the presence of O and C as well as P and In. The number of dislocations in the epilayer is the same as in the substrate, and it is not possible to see the interface between the substrate and the epilayer after normal chemical etching.

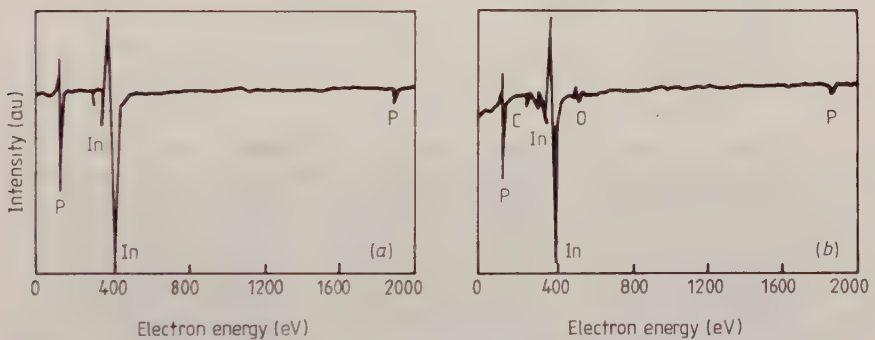

Figure 2.17 Auger spectrum for (*a*) the InP epilayer–substrate interface and (*b*) the surface of the epilayer.

2.4 GROWTH AND CHARACTERIZATION OF InP USING TMIn

TEIn is liquid and its vapour pressure is low (see chapter 1). In MOCVD at low pressure, one has to be careful, and a small change of pressure inside or outside the TEIn container produces secondary sources of TEIn in the gas

panel. In this case it is very difficult to control the growth rate and quality of the epitaxial layer.

Trimethylindium is solid under 80°C, and its vapour pressure is higher than that of TEIn. Therefore one can maintain the temperature of TMIn sources lower than room temperature, avoiding the condensation of TMIn in the gas panel, and also eliminate the problem of secondary sources of TMIn in the gas panel. So Razeghi *et al* [26] decided to use TMIn instead of TEIn for the growth of InP and related compounds. In that case one can use pure H_2 as a carrier gas (see chapter 1). Essentially for these reasons the results of growth using TMIn are generally better than those from TEIn.

High-quality InP epilayers have been grown by MOCVD using trimethylindium (TMIn) (Alfa product) and PH_3 (Matheson) for In and P sources, respectively. Pure hydrogen is used as the carrier gas. The growth temperature is 550°C and growth pressure is 100 mbar. Details on optimized growth conditions determined during these investigations are indicated in table 2.8.

All the InP layers have been grown on (1 0 0)-oriented Sn- and Fe-doped InP substrates. The main characteristics of the different samples are summarized in table 2.9.

Table 2.8 Optimized conditions of InP growth using TMIn.

Growth temperature	(°C)	550
Total H_2 flow	($l\,min^{-1}$)	6
H_2 through TMIn bubbler	($cm^3\,min^{-1}$)	50
PH_3 flow	($cm^3\,min^{-1}$)	100
Growth rate	($Å\,min^{-1}$)	300

Table 2.9 Some of the characteristics of InP epilayers using TMIn.

Sample no.	A	B	C	D	E
Thickness (μm)	5	8	10	5	3.5
$N_D - N_A$ (cm^{-3})	7×10^{13}	2×10^{14}	3×10^{13}	6×10^{13}	10^{14}
μ(300 K)($cm^2\,V^{-1}\,s^{-1}$)	5500	4500	6000	5500	5000
μ(50 K)($cm^2\,V^{-1}\,s^{-1}$)	150 000	100 000	200 000	145 000	110 000

Figure 2.18(*a*) shows the transition region after chemical etching of an InP epilayer grown by MOCVD using TMIn. The etch-pit density (EPD was the same in the substrate as in the confinement InP layers, and the interfaces are defect-free. The surface photographs of InP layers on InP substrates of various orientations are shown in figure 2.18(*b*).

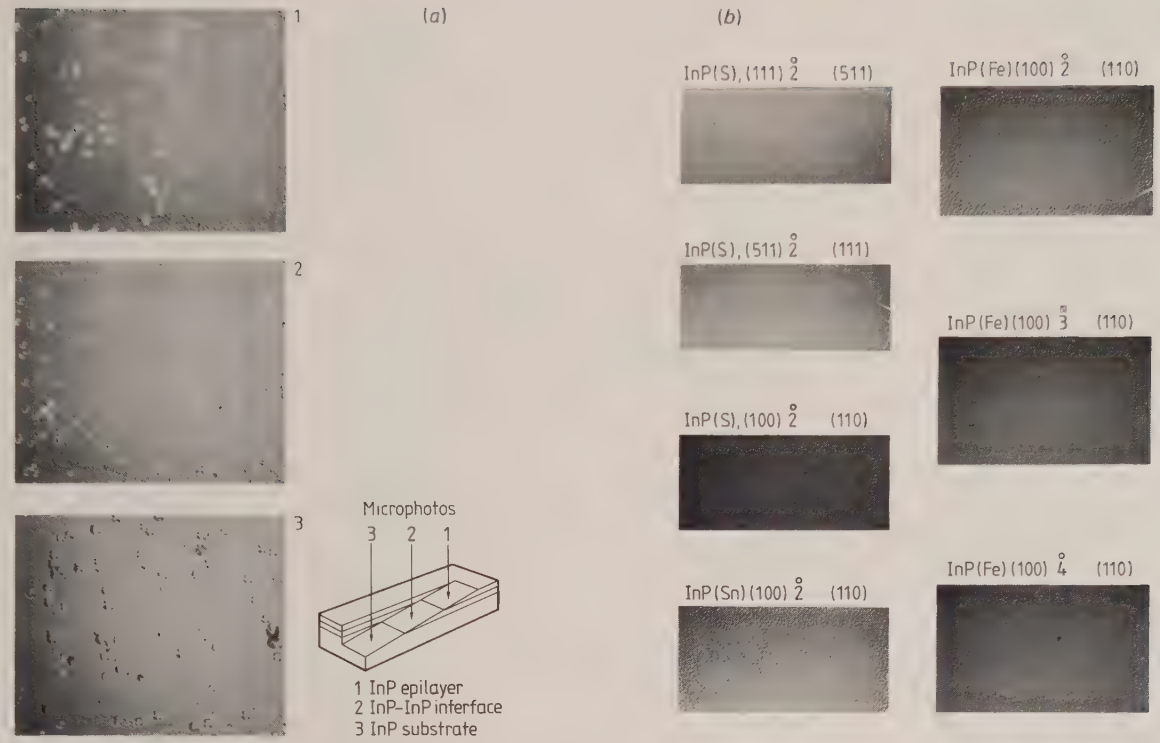

Figure 2.18 (*a*) Transition region after chemical etching of an InP–InP epilayer grown by MOCVD. (*b*) Optical surface photographs of InP layers on InP substrates of various orientations as indicated.

Figure 2.19 indicates the electrochemical polaron profile of an InP layer using TMIn. A carrier concentration as low as 3×10^{13} cm^{-3} has been measured, which is the purest InP epilayer yet grown by any growth technique.

Electrical measurements were performed, using the classical Van der Pauw technique, with ohmic contacts produced by evaporation and annealing of Au–Ge. The maximum mobility was generally found between 50 and 55 K, and exceeded 100 000 cm^2 V^{-1} s^{-1}, proving the high quality of the samples under study. At the same time, the residual doping level was found to be very low, generally less than 10^{14} cm^{-3}.

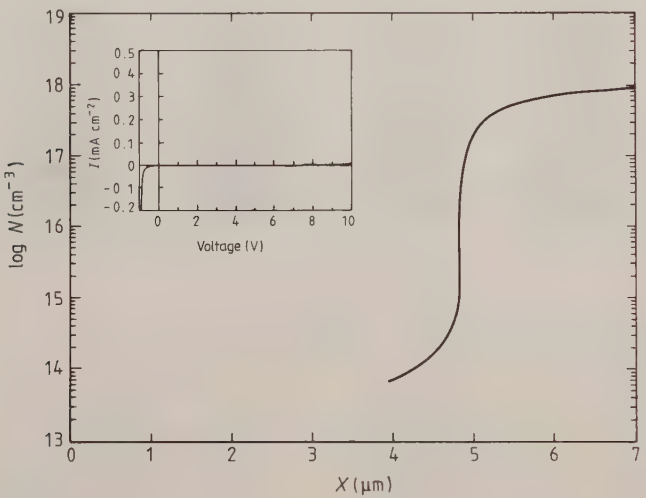

Figure 2.19 Typical electrochemical polaron profile of an InP epilayer grown by MOCVD: TMIn + PH_3, $\mu(77\ K) \simeq 150\,000$ cm^2 V^{-1} s^{-1}, $dx/dt \sim 300$ Å min^{-1}.

Photoluminescence measurements were performed at 2 K, using a dye laser as the source of excitation. The excitation energy was tuned just above the band gap of InP, at about 1430 meV, with a slit width of 50 μm.

Figures 2.20–2.22 show the near-gap photoluminescence (NGPL) spectra of samples A, B and C. All of them exhibit different lines identified as free exciton (X), exciton bound to neutral donor (D^0X) and charged donor (D^+X), donor–valence band recombination (D^0–h) and exciton bound to acceptor (A^0X). The positions in energy of all of the peaks and their identification are summarized in table 2.10.

The free-exciton line is located at about 1418.8 meV, in good agreement with previous work on the subject. Various components of the bound-exciton (D^0X) recombination, identified as $(D^0X)_n$ with $n = 1, \ldots, 5$, have been observed. They are more complicated, since an additional electron is

present, making the donor neutral before binding the exciton. The different components $(D^0X)_n$ result from different angular momentum states of the $j = \frac{3}{2}$ hole [27]. The states of the complex are generally described by those of the hole in a central potential, with a pair of electrons in the singlet state. Their linewidths are less than 0.1 meV, thus necessitating a very sensitive optical system.

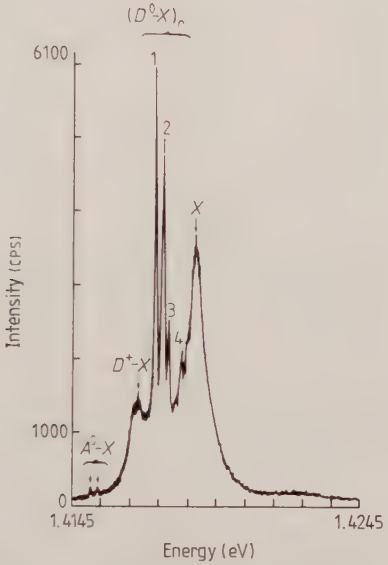

Figure 2.20 Near-gap photoluminescence (NGPL) at 2 K of an InP (TMIn) epilayer grown by LP-MOCVD (sample A). $E_{exc} = 1.426$ eV, $I_{exc} = 4$ mW.

In two of them (A and B), two very weak lines due to an exciton bound to the acceptor (A^0X), located at 1414.2 and 1414.4 meV, appear. We have summarized in table 2.11 the intensity ratio of X/D^0X and A^0X/D^0X lines for the three samples. In all cases, the acceptor-bound exciton line appears very weak compared to the other recombination processes. The sample therefore should be very little compensated.

For sample C (figure 2.22), the sensitivity of detection was multiplied by 100 in the region of the A^0X peak, with no trace of an acceptor. This further demonstrates the purity of the sample, and can explain the exceptionally high mobility measured ($\mu(50\text{ K}) = 200\,000\text{ cm}^2\text{ V}^{-1}\text{ s}^{-1}$).

On the other hand, the free-exciton peak (X) appears more intense than the donor-bound exciton peak (D^0X). This is the first time that such a fact has been observed, in any InP crystal, thus confirming the very low concentration of donors ($3 \times 10^{13}\text{ cm}^{-3}$) determined by a polaron profile.

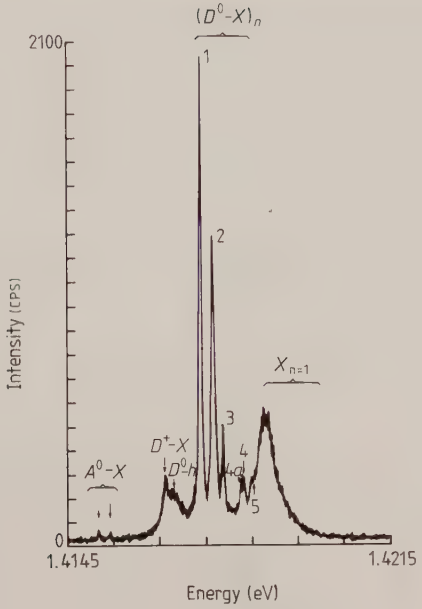

Figure 2.21 Low-temperature NGPL spectrum at 2 K of an InP (TMIn) epilayer grown by MOCVD (sample B). $E_{exc} = 1.426$ eV, $I_{exc} = 8$ mW.

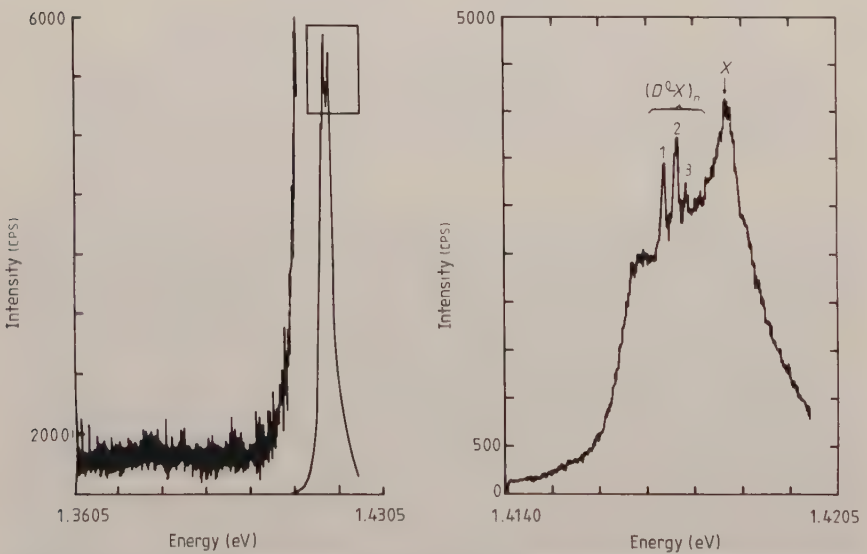

Figure 2.22 Low-temperature photoluminescence spectrum at 2 K of an InP (TMIn) epilayer grown by MOCVD (sample C). $I_{exc} = 6.6$ mW. Inset: detail of NGPL spectrum at 2 K. $E_{exc} = 1.43$ eV, $I_{exc} = 4$ mW.

Table 2.10 Positions in energy of all of the PL recombination lines in an InP epilayer

Type of recombination	Energy (meV)
X	1418.8
D^0X, $n=1$	1417.3
D^0X, $n=2$	1417.6
D^0X, $n=3$	1417.8
D^0X, $n=4$	1418.3
D^0X, $n=5$	1418.5
D^+X	1416.6
D^0–h	1416.8
A^0X	1414.2
A^0X	1414.4

Table 2.11 The ratio of PL intensity of X/D^0X and A^0X/D^0X in InP epilayers grown by MOCVD.

Sample no.	A	B	C
X/D^0X	5.8×10^{-1}	2.8×10^{-1}	1.25
A^0X/D^0X	2.0×10^{-2}	3.0×10^{-2}	no acceptor

Residual donors in a high-purity InP layer grown by MOCVD were identified in 1987 by magnetophotoluminescence (MPL) and photothermal ionization spectroscopy (PTIS) measurements at the University of Illinois by Professor Stillman's group. The donors identified in two samples from MPL and PTIS are 88% Si and 12% S. (For the experimental details, the reader should consult the original reference [28].)

2.5 INCORPORATION OF DOPANTS

2.5.1 p-Type

InP layers grown by MOCVD can be doped p-type by using diethylzinc (DEZn). Figure 2.23 shows the variation of net carrier concentration as a function of H_2 flow through the DEZn bubbler (-15°C) (growth temperature 650°C). When the flow rate of DEZn is kept constant, the free-carrier concentration varies exponentially with $1/T$, as shown in figure 2.24, where T is growth temperature.

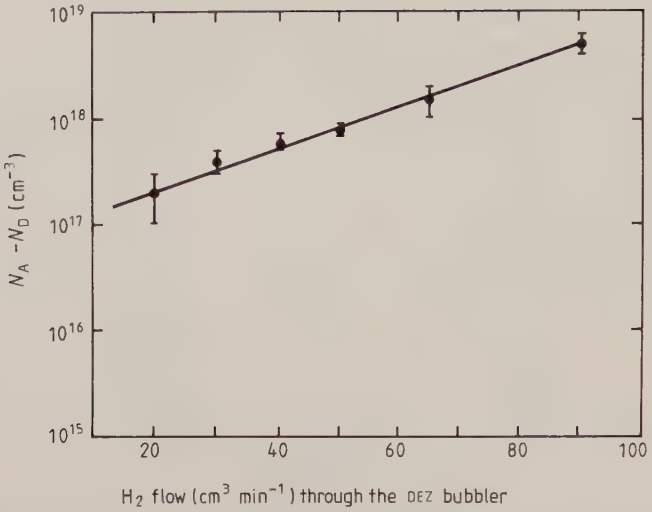

Figure 2.23 Variation of acceptor level $N_A - N_D$ in InP with DEZn flow-rate ($T_G = 650^\circ$C, total flow 7 l min^{-1}).

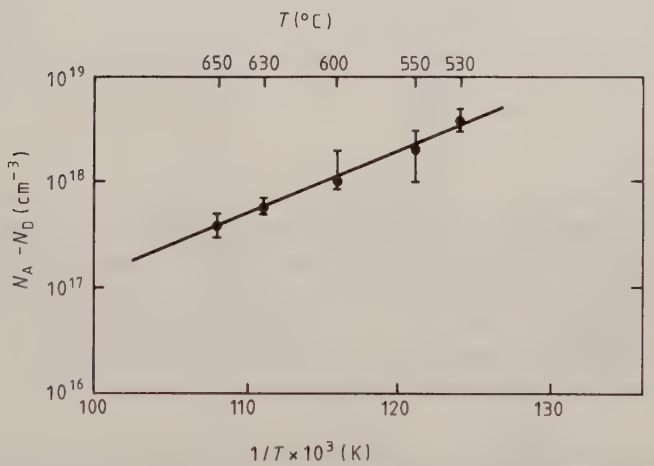

Figure 2.24 Variation of acceptor level in InP with growth temperature: $N_A - N_D \propto \exp(-E_i/kT)$ ($E_i \simeq 10$ meV, 30 cm^3 min^{-1} H_2 flow through DEZn bubbler).

The incorporation of dopants during growth on InP using doping species such as DEZn can be explained by using a model described by Duchemin [29]. If we assume that all the DEZn arriving at the hot surface is decomposed, then the Zn concentration becomes limited by the diffusion of the DEZn through the boundary layer to the hot surface. After decomposition there are two possible limiting cases:

(1) In the simplest case, all of the decomposed material is incorporated into the growing layer. Thus here the impurity concentration is independent of temperature and inversely proportional to the growth rate. This behaviour is observed for the doping of silicon by germanium using germane (GeH_4) [30].

(2) The second case is that in which only a small fraction of the secondary form (Zn) of the dopant is incorporated into the growing layer. Here the major part of the dopant is vaporized and is then lost by diffusion away from the substrate. As the temperature is raised, more of the dopant is vaporized, and the doping concentration decreases. Here, then, the doping concentration decreases as the temperature increases but is independent of the growth rate. This behaviour is typical of the doping of InP by zinc (figure 2.25).

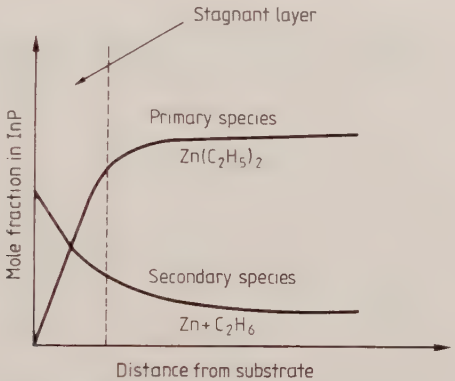

Figure 2.25 Total decomposition of DEZn (primary species) with partial incorporation of Zn (secondary species).

2.5.2 n-Type

Epilayers of InP and related compounds grown by MOCVD can be doped n-type using H_2S or SiH_4. When the flow-rate of H_2S is kept constant, the free-carrier concentration varies exponentially with $1/T$ as in the case of DEZn. The free-carrier concentration in the epilayer decreases when the growth temperature increases. Figure 2.26 shows the variation of $N_D - N_A$ as a function of H_2S flow rate.

The decomposition of the H_2S (primary species) is the rate-limiting step; after decomposition, most of the secondary species (S) is incorporated into the growing layer (figure 2.27).

A typical polaron electrochemical profile (using a 0.1 cm^2 area and 0.5 M HCl) of an InP Gunn-diode structure (n^+-n-n^+) grown by MOCVD is shown in figure 2.28. Using H_2S for n^- doping, the interfaces between the layers are sharp. Figure 2.29 presents a SIMS profile for a similar Gunn-diode structure of InP.

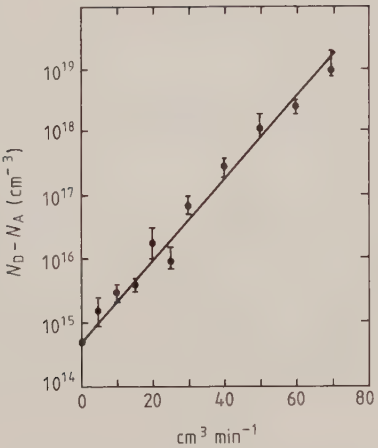

Figure 2.26 Variation of donor level $N_D - N_A$ in InP layers with H_2S in H_2 ($T_G = 550°C$, $dx/dt = 200$ Å min^{-1}).

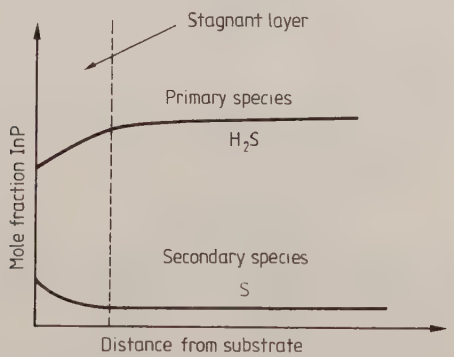

Figure 2.27 Partial decomposition of H_2S (primary species) with incorporation of S (secondary species).

Sulphur has been widely used as an n-type dopant for DH layers grown by MOCVD for laser applications. There have been indications in the literature [31–33] that, at high growth temperature, significant sulphur diffusion can occur, which will seriously degrade doping interfaces.

In the case of SiH_4, when the flow rate is kept constant, the free-carrier concentration increases with increasing growth temperature. At higher temperature, the decomposition of the SiH_4 is more efficient. We found that for high doping levels of about 10^{18} cm^{-3} (such as used in lasers) it is better to use H_2S. Using H_2S the epitaxial layers are less compensated. Silicon in III–V compounds is amphoteric, and incorporation in InP depends on the ratio of III/V elements. But the diffusion coefficient of Si is less than that of S, so for modulation doping it is better to use Si.

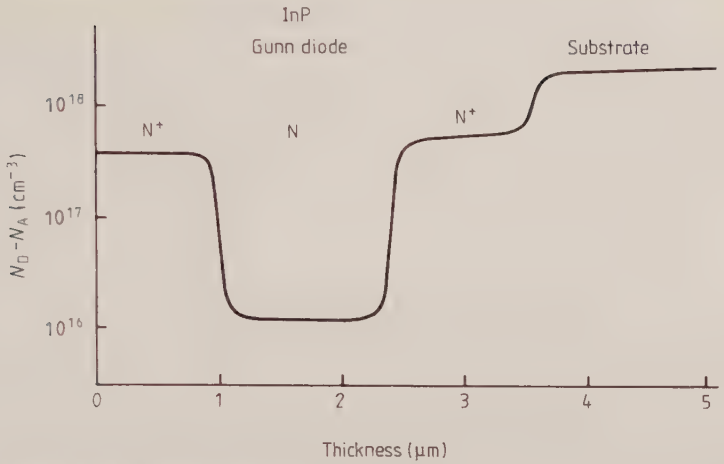

Figure 2.28 Electrochemical profile of an InP Gunn-diode structure.

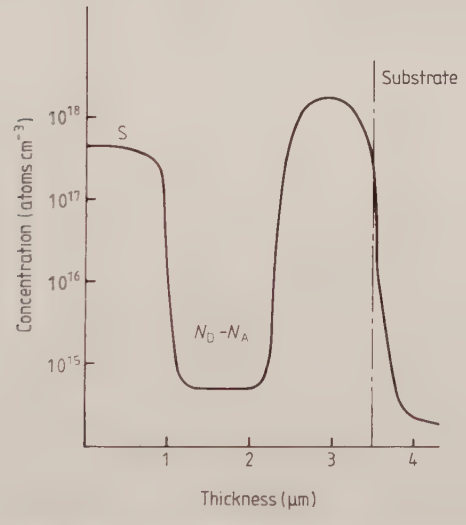

Figure 2.29 SIMS profile for Gunn-diode structure of InP by MOCVD.

In order to examine these topics and to identify a satisfactory n-type dopant for Gunn-diode InP and modulation-doped GaInAs–InP layers grown by MOCVD, Razeghi [34] examined the electrical properties of epitaxial layers doped with SiH_4. Figure 2.30 shows electrochemical profiles of typical doping interfaces for InP doped with S and Si, indicating that the interfaces of S-doped layers do not differ significantly from those doped with Si.

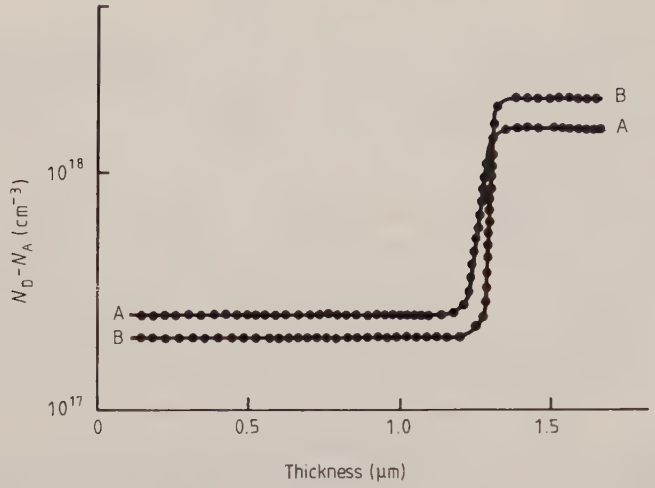

Figure 2.30 Electrochemical profiles of typical doping interfaces for InP doped with S (A) and Si (B): LP-MOCVD; full circles indicate values with light; full curves indicate values without light.

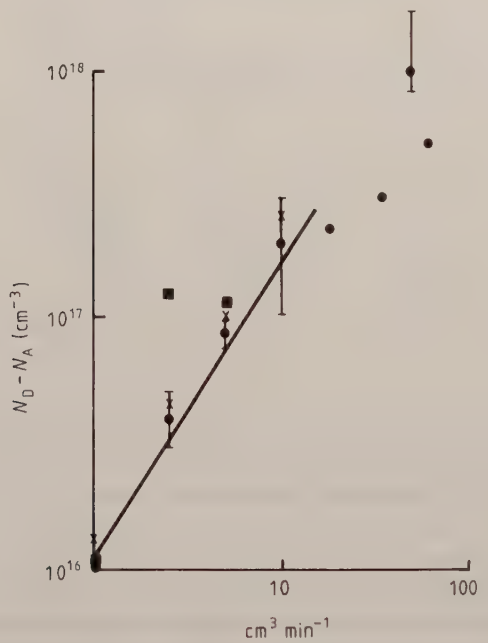

Figure 2.31 Variation of donor level in an InP layer with SiH_4 flow-rate: MOCVD InP; (X) C–V, (•) electrochemical profile, (■) Hall mobility (250 PPM SiH_4 in H_2) ($T_G = 550^\circ C$, $dx/dt = 200$ Å min^{-1}, $N_D - N_A = 66$, 57 and 47% for $\mu = 2600$, 1400 and 2700 cm^2 V^{-1} s^{-1}, respectively).

For the same carrier concentration, the measured Hall mobility is lower in Si-doped InP layers than in the S-doped one (figure 2.31). The results show that the Si-doped InP layers are compensated. Autocompensation was not present in the S-doped samples. Also, with S it is generally simpler to obtain highly doped InP layers. There is a satisfying agreement between the results of Razeghi [34] and those obtained by Giles *et al* [32] using chloride-process VPE growth of InP layers.

2.6 APPLICATION OF InP EPITAXIAL LAYERS

InP is an excellent candidate for microwave diodes. Microwave diodes can be made with operating frequencies covering the range from about 0.1 to 200 GHz with corresponding wavelengths from 300 cm to 1.5 mm.

The applications in this frequency range are numerous, including radar for both military and civil applications. For example, communication via satellites is made at 12 GHz for broadcasting and at 20–30 GHz for communication. But communication flow is increasing so rapidly that new channels are necessary, and the use of frequencies up to 100 GHz is anticipated in the near future.

2.6.1 Gunn diodes

The Gunn diode [35] is a transferred-electron device. Coherent microwave output is generated when a DC electric field in excess of a critical threshold value of several thousand volts per centimetre is applied across an n-type sample of GaAs or InP. Hilsum [36] and Ridley and Watkins [37] predicted that such oscillations should be observed because of an intrinsic negative differential resistance. To understand this effect, consider the energy–momentum diagrams for GaAs and InP in figure 2.32, the two most important semiconductors for transferred-electron devices. Figure 2.32 shows that the band structures of GaAs and InP are similar. The energy separation between the two valleys is ΔE, which is about 0.31 eV for GaAs and 0.53 eV for InP. An applied electric field induces transfer of conduction-band electrons from the low-energy, high-mobility valley to higher-energy, low-mobility satellite valleys.

As a consequence the electrons are slowed down and accumulate in domains which are propagated along the sample. The propagation time, which is proportional to the sample length, determines the frequency.

Figure 2.33 shows the measured room-temperature velocity–field characteristics for GaAs and InP. The threshold field ε_T defining the onset of negative differential resistivity is 3.2 kV cm^{-1} for GaAs and 10.5 kV cm^{-1} for InP. The peak velocity V_P is about 2.2×10^7 cm s^{-1} for high-purity GaAs and 2.5×10^7 cm s^{-1} for high-purity InP. In order to have the

electron-transfer mechanism, the following conditions are necessary:

(1) In the absence of a bias electric field, most electrons are in the lower conduction-band minimum, or $kT \leqslant \Delta E$.

(2) In the lower conduction-band minimum, the electrons must have high mobility, small effective mass and low density of states; whereas in the upper satellite valleys, the electrons must have low mobility, large effective mass and high density of states.

(3) The energy separation between the two valleys must be smaller than the semiconductor band gap so that avalanche breakdown does not set in before electrons are transferred into the upper valleys.

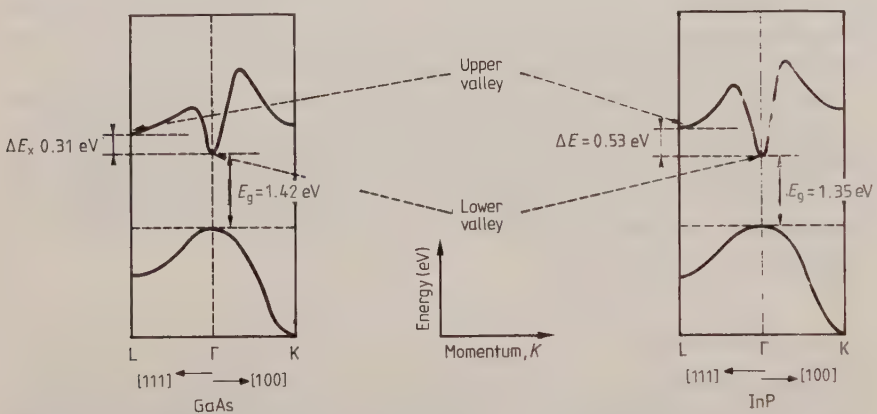

Figure 2.32 Band structures of InP and GaAs.

High-power and high-efficiency InP Gunn diodes made from layers grown by MOCVD have been developed in the millimetre-wave range. Gunn diodes processed using the integral heat-sink technique have delivered up to 100 mW continuous-wave (CW) output power with 2.5% efficiency at 94 GHz, while average power levels in excess of 90 mW were obtained at 94 GHz [38].

Gunn diodes, which are well known as low-noise devices, are better adapted for communications receivers than are avalanche diodes. Until recently, gallium arsenide had been the only material for such applications. But since its introduction a few years ago, indium phosphide has been recognized to be a very attractive material for making millimetre-wave oscillators [39–41].

The cut-off frequency is approximately 200 GHz at 3 dB for InP compared with 100 GHz for GaAs. The key characteristic necessary to obtain high efficiency is a high peak-to-valley ratio V_P/V_V of the electron velocity as a function of applied electric field. The peak-to-valley ratio is significantly higher in InP than in GaAs (4 for InP versus 2.4 for GaAs).

Other InP properties compared to those in GaAs which aid in obtaining higher power output are higher threshold field, higher electric breakdown field and higher thermal conductivity. For these reasons, indium phosphide offers significant advantages over gallium arsenide for high power and efficiency at millimetre wavelengths.

Until recently, the output power and efficiency obtained using InP represented only a modest improvement over GaAs. Recent progress in 94 GHz InP Gunn-device development at Thomson's laboratory [28] showed that higher output power and efficiency can be obtained from InP in the millimetre range.

Thomson have developed a microwave diode structure whose performance is claimed to outclass any other device reliable enough to be used in professional equipment. In the CW mode output power up to 103 mW was measured at 94 GHz with 2.5% efficiency. This device is based on a three-layer n^+-n-n^+ structure where Si (from silane) was used as the dopant [42]. This dopant allows precise control of doping profiles. High-quality non-intentionally doped and Si-doped epitaxial InP material was reproducibly obtained by low-pressure metallorganic chemical vapour deposition.

The device structure consists of an n^+ buffer layer with carrier densities of $10^{18}\,cm^{-3}$ followed by an active layer doped in the 10^{16} to $1.5 \times 10^{16}\,cm^{-3}$ range and a contact layer in the $10^{18}\,cm^{-3}$ range.

Excellent results have been obtained from wafers ranging in active layer thickness from 0.9 to 1 μm. A typical 94 GHz InP Gunn-device doping profile is shown in figure 2.34.

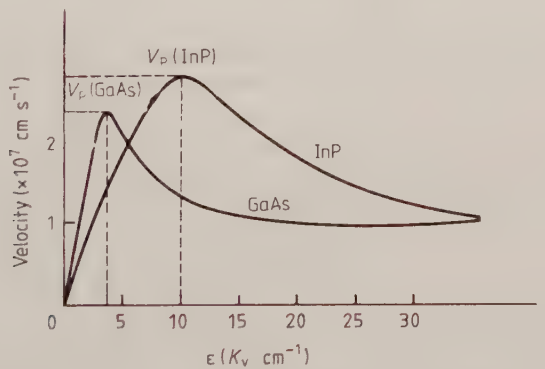

Figure 2.33 Room-temperature velocity–field characteristics for GaAs and InP.

The grown wafers are 2.5×4 cm and are processed using the integral heat-sink technique. This technique consists of various epitaxial layers, alloyed Au–Ge, Ti, Pt and Au contacts and an electroplated 40 μm gold

heat-sink to reduce thermal resistance and facilitate chip bonding and packaging. On the epilayer side of the as-grown wafers, channels are etched 10–20 μm deep, spaced 3 mm apart to provide a depth gauge when the substrate side is thinned. The entire epilayer side is then metallized with Au–Ge, Ti, Pt and Au. The Au heat-sink is electroplated 40 μm thick. The wafer is then turned over and uniformly thinned to 10 μm with a lap and chemical polish technique until the channels on the other side are exposed (see figure 2.34).

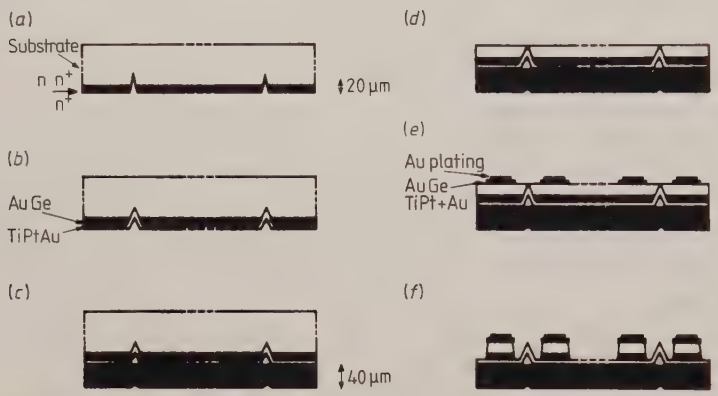

Figure 2.34 The various sequences of Gunn-diode technology. (*a*) Etched channels in the epilayer side; (*b*) Au–Ge, Ti, Pt, Au metallization; (*c*) Au heat-sink; (*d*) substrate removed to expose channels; (*e*) metallizations (30–60 μm diameter, Au-plated); (*f*) etched mesas.

A total substrate thickness less than 10 μm is required at 94 GHz in order to minimize significant resistive loss created by the substrate. Au–Ge, Ti, Pt and Au contacts are formed on this new thinned substrate surface. Mesas of 30–60 μm diameter are defined using a light-sensitive $FeCl_3$ etch.

A low-inductance bond was obtained by using two 100 μm gold ribbons stitch-bonded from the metallized ceramic across the mesa. The best result, however, was obtained using a star pattern top bond. In both cases the reduced parasitic inductance allowed the diode to operate at a higher frequency with no power loss.

The thermal resistance of these 94 GHz InP Gunn devices with 60 μm diameter mesa ranges between 40 and 45 °C W^{-1}. The working temperature of the active layer is less than 200 °C.

Both CW power level and efficiency of these devices were studied over a temperature range of -40 to $+60$ °C. A power shift of 0.005 dB $°C^{-1}$ and a frequency shift of 3.5 MHz $°C^{-1}$ have been observed.

Amplitude-modulated (AM) noise (-140 dB_c Hz^{-1} single-sideband (SSB) at 10 kHz from carrier) and frequency-modulated (FM) noise (-60 dB_c Hz^{-1}

SSB at 10 kHz from carrier) at 94 GHz were found to be similar to those obtained with gallium arsenide [38].

REFERENCES

[1] Kittel C 1971 *Introduction to Solid State Physics* (New York: Wiley)
[2] Kane E O 1966 *Semicond. Semimet.* **1** 75
[3] Razeghi M and Duchemin J P 1983 *J. Cryst. Growth* **64** 76
[4] Saxena R, Cooper C, Ludowise M, Hikido S and Borden P G 1981 *J. Cryst. Growth* **55** 58
[5] Shaw D 1968 *J. Electrochem. Soc.* **115** 405
[6] Olsen G, Zamerowski J and Hawrylo F 1982 *J. Cryst. Growth* **59** 654
[7] Razeghi M, Blondeau R, Bouley J C, Decremoux B and Duchemin J P 1984 *Proc. 9th IEEE Int. Laser Conf.*
[8] Huber A, Morillot G, Bonnet M, Merenda P and Bessonneau G 1982 *Appl. Phys. Lett.* **41** 638
[9] Dapkus P, Manasevit H and Hess K 1981 *J. Cryst. Growth* **55** 10
[10] Lepareux M 1980 *Rev. Tech. Thomson-CSF* **12** 225
[11] Huber A 1986 *Rev. Tech. Thomson-CSF* **18** 1
[12] Magee C 1979 *J. Electrochem. Soc.* **126** 660
[13] Huber A M, Morillot G, Hersee S D and Kazmierski K 1984 *Proc. Third Conf. on Semi-insulating III–V Materials* Oregon (Nantwich: Shiva) p 466
[14] Huber A M, Morillot G, Bonnet M, Meranda P and Bessonneau G 1982 *Appl. Phys. Lett.* **41** 638–9
[15] Razeghi M and Duchemin J P 1983 *J. Vac. Sci.* B **1** 262
[16] Razeghi M 1983 *Rev. Tech. Thomson-CSF* 1983 **15** 1
[17] Huber A M, Razeghi M and Morillot G 1984 *Gallium Arsenide and Related Compounds, 1984* (Inst. Phys. Conf. Ser. 74) p 223
[18] Razeghi M, Poisson M A, Larivain J P and Duchemin J P 1983 *J. Electron. Mater.* **12** 371
[19] Sze S M 1982 *Physics of Semiconductor Devices* (New York: Wiley)
[20] Ambridge T, Elliott C R and Faktor M M 1973 *J. Appl. Electrochem.* **3** 1–15
[21] Ambridge T and Faktor M M 1974 *J. Appl. Electrochem.* **4** 135–42
[22] Ambridge T and Faktor M M 1975 *J. Appl. Electrochem.* **5** 319–28
[23] Blood P 1985 *Semicond. Sci. Technol.* **1** 7–27
[24] Van der Pauw J 1958 *Philips Res. J.*
[25] Lim H, Sagres G, Bastide G, and Gouskov L 1982 *J. Appl. Phys.* **53** 3085
[26] Razeghi M, Maurel P, Defour M, Omnes F, Neu G and Kozacki A 1988 *Appl. Phys. Lett.* **52** 117
[27] Dean P J and Skolnick M S 1983 *J. Appl. Phys.* **54** 346
[28] Bose S S, Lee B, Kim N H and Stillman G E 1987 *Appl. Phys. Lett.* **51** 937
[29] Duchemin J P 1977 *Rev. Res. Thomson-CSF* **9** 1
[30] Duchemin J P 1977 *Rev. Res. Thomson-CSF* **9** 2
[31] Benz K, Hagleko H and Bosch R 1982 *J. Physique* **43** C5
[32] Giles P, Davies P and Hardell N 1984 *J. Cryst. Growth* **65** 351

[33] Störmer H J, Dingle R, Gossard A, Weigmann W and Sturge M 1979 *Solid State Commun.* **29** 705
[34] Razeghi M 1985 *Semiconductors and Semimetals* ed W T Tsang (New York: Academic) ch 5
[35] Gunn J B 1963 *Solid State Commun.* **1** 88
[36] Hilsum C 1962 *Proc. IRE* **50** 185
[37] Ridley B K and Watkins T B 1961 *Proc. Phys. Soc. Lond.* **78** 293
[38] Poisson M A 1984 *Proc. Int. Conf. on GaAs and Related Compounds* Biarritz
[39] Corlett R 1975 *Indium Phosphide CW Transferred Electron Amplifiers* (Inst. Phys. Conf. Ser. 24) ch 2
[40] Crowley J D 1980 *Electron. Lett.* **16** 705
[41] Hamilton R J 1976 *IEEE Trans. Microwave Theor. Tech.* **MTT-24** 775
[42] Razeghi M, Blondeau R, Decremoux B and Duchemin J P 1985 *Appl. Phys. Lett.* **46** 131

Chapter 3 GaInAs–InP System: MOCVD Growth, Characterization and Application

A useful material for long-wavelength optical communication devices is $Ga_{0.4}$-$In_{0.53}As$, lattice-matched to InP. Moreover, its high mobility and large drift velocity make this material very promising for use in high-frequency field-effect transistors (FET) [1], optical-fibre communication, satellite transmission, radar linkage, direct satellite broadcasting, use in supercomputers and high-speed signal processing [2, 3]. This chapter describes MOCVD growth, characterization and applications of $Ga_{0.4}$-$In_{0.53}As$–InP heterojunctions (HJ), multiquantum wells (MQW) and superlattices (SL), which show mobility values comparable with the best reported values obtained on epitaxial growth by other techniques.

3.1 GROWTH CONDITIONS

Layers of GaInAs can be grown at 76 Torr and low temperature, between 500 and 650°C, using TEIn or TMIn, TEGa and AsH_3 in an $H_2 + N_2$, or H_2 in the case of TEIn, carrier gas. Figure 3.1 shows that the growth rate depends linearly upon the TEIn + TEGa flow-rate and is independent of that of AsH_3 within the range 60–90 $cm^3\,min^{-1}$, which suggests, as in the case of InP, that epitaxial growth is controlled by mass transport of the group III species. Uniform-composition $Ga_{0.47}In_{0.53}As$ over a large area of 10 cm^2 of InP substrate has been obtained (figure 3.2). The epitaxial-layer quality is sensitive to the alloy composition, as in the case of GaInAs grown by other techniques.

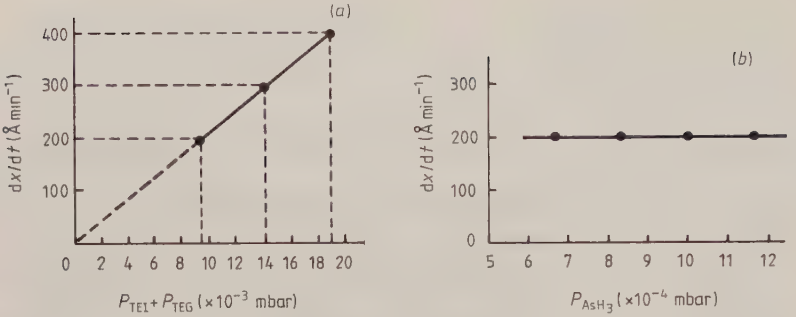

Figure 3.1 Variation of the growth rate dx/dt of $Ga_{0.47}In_{0.53}As$–InP with (*a*) TEIn + TEGa flow-rate and (*b*) AsH_3 flow-rate ($T_G = 550^\circ C$; $P_{TEIn} + P_{TEGa} = 9.4 \times 10^{-3}$ mbar; total flow-rate $\sim 6\,l\,min^{-1}$).

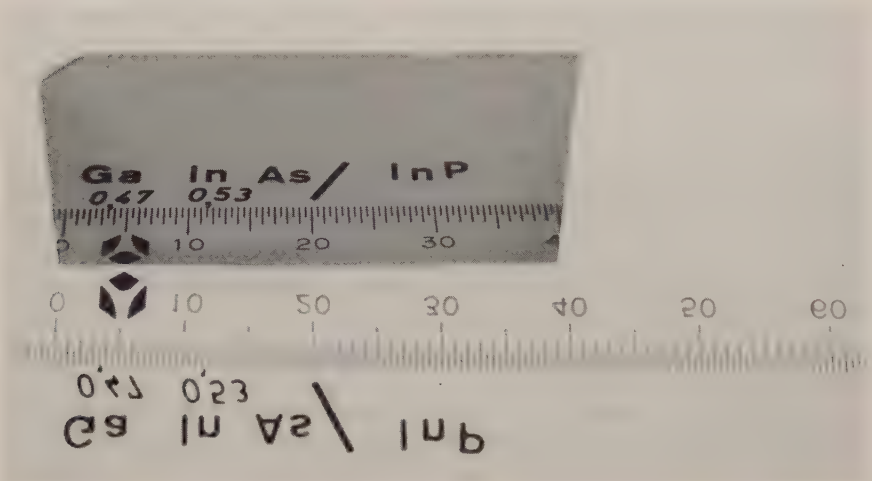

Figure 3.2 Surface quality of typical GaInAs–InP layers grown by MOCVD.

The surface morphology of GaInAs–InP layers depends on the pretreatment of the substrate and is independent of the lattice mismatch, even in the case of a GaAs layer on an InP substrate with a lattice mismatch of 10^{-2} or more. $Ga_{0.47}In_{0.53}As$/InP layers with an excellent surface morphology and state-of-the-art electron mobility can be grown under the following reactor conditions:

Growth temperature	550°C
Total flow	7 l min^{-1}
N_2–TEIn bubbler flow	450 cm^3 min^{-1}
H_2–TEGa bubbler flow	180 cm^3 min^{-1}
AsH_3 flow	90 cm^3 min^{-1}
Growth pressure	76 Torr.

Under these conditions, the growth rate is 270 Å min^{-1}. InP–GaInAs interfaces can be obtained by turning off the phosphine flow and turning on both the TEGa and AsH_3. GaInAs–InP interfaces can be obtained by turning off the AsH_3 and TEGa flow and turning on the PH_3 flow. The growth rate is small (1 to 5 Å s^{-1}), and it takes less than 1 s for a gas flow to reach its new steady state.

The thickness of epilayer is measured by a bevel stain technique (solution) and the composition calculated either from the PL wavelength or from the value of the lattice parameter as measured by single-crystal x-ray diffraction. The x-ray measurement yields the strained (s) value of the lattice mismatch

$$(\Delta a/a)_s = (a_{InP} - a_{GaInAs})/a_{InP} \tag{3.1}$$

by means of

$$(\Delta a/a)_s = \Delta\theta \cos\theta \tag{3.2}$$

where a is the lattice parameter, θ the average diffraction angle and $\Delta\theta$ is half the angular difference between the $K_{\alpha 1}$ x-ray peak for the substrate and $K_{\alpha 1}$ for the epitaxial layer.

The unstrained (un) value of lattice mismatch $(\Delta a/a)_{un}$ that is necessary to calculate the true composition of the epitaxial layer is related to the strained value by

$$(\Delta a/a)_s = (1 + 2c_{12}/c_{11})(\Delta a/a)_{un} \tag{3.3}$$

where c_{11} and c_{12} are the elastic constants of $Ga_xIn_{1-x}As$ [4]. The variation of growth rate dx/dt, lattice mismatch $\Delta a/a$ and PL wavelength of GaInAs layers over an area of 10 cm^2 of an InP substrate is less than 5% (figure 3.3).

Razeghi and Duchemin [5] have studied the growth of GaInAs layers by using 100% H_2 and mixtures of $H_2 + N_2$ as the carrier gas. The highest PL intensity and the best mobility were obtained by using 60% H_2 and 40% N_2. Razeghi and Duchemin [5] have performed a study of MOCVD growth of GaInAs simultaneously on six InP substrates with orientations of (1 0 0), (1 1 1) and (1 1 5) placed adjacent to one another within the reactor at a growth temperature of 550°C, similar to the study on InP described earlier in chapter 2.

Table 3.1 indicates relative PL intensity, PL halfwidth $\Delta h\nu$, growth rate dx/dt and electron carrier concentration measured by a C–V method. Measurements by DLTS show that there are no detectable electron traps in GaInAs layers grown by MOCVD [6].

The photoluminescence (PL) intensity and PL halfwidth of GaInAs layers over InP substrates grown by MOCVD depend directly on the purity of the starting material.

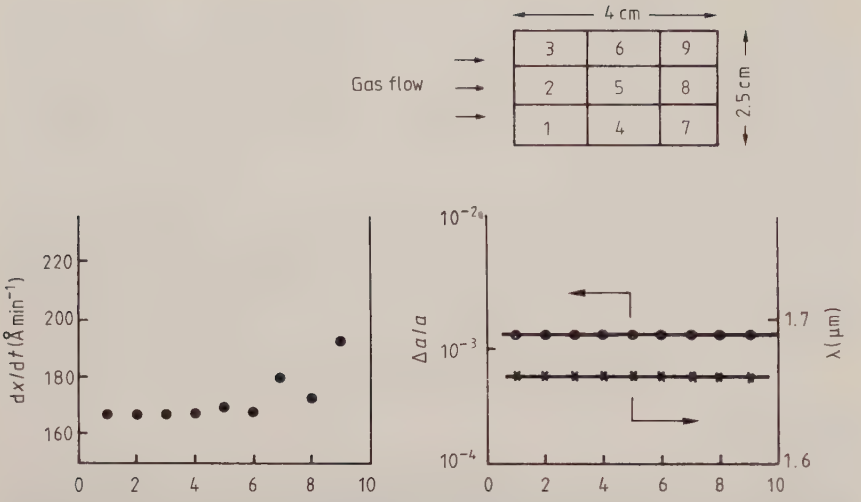

Figure 3.3 Variation of PL wavelength (X), lattice mismatch $\Delta a/a$ (•) and growth rate dx/dt over an area of 10 cm^2 for a GaInAs–InP epitaxial layer; the layer thickness is 5 μm.

Table 3.1 PL intensity *I*, PL halfwidth $\Delta h\nu$ and *C–V* carrier concentrations of GaInAs grown on InP substrates by MOCVD.

Orientation	$N_D - N_A$ (cm^{-3})	dx/dt (Å min^{-1})	$\Delta a/a$	*I* (au)	$\Delta h\nu$ (meV) at 300 K
InP(Sn)(1 0 0) 2°	5×10^{14}	260 ± 10	$+1 \times 10^{-3}$	1	45
InP(S)(1 0 0) 2°	6×10^{14}	260 ± 10	$+1 \times 10^{-3}$	0.5	60
InP(Fe)(1 0 0) 2°	3×10^{14}	260 ± 10	$+1 \times 10^{-3}$	2	40
InP(Sn)(1 0 0)	6×10^{14}	260 ± 10	$+1 \times 10^{-3}$	0.2	60
InP(S)(1 1 1) 2°	5×10^{14}	260 ± 10	$+1 \times 10^{-3}$	3	50
InP(S)(1 1 5) 2°	5×10^{14}	260 ± 10	$+1 \times 10^{-3}$	10	80

Figure 3.4 presents a typical absorption spectrum [7] at 1.5 K, the light beam being perpendicular to the interface. The absorption edge occurs around 807 meV and is characteristic of free-exciton absorption. The corresponding luminescence spectrum exhibits two lines around 805 and 788 meV, which are likely to be due, as in bulk GaInAs grown by LPE [8, 9], to donor–valence band and donor–acceptor recombination processes, respectively. These optical results show that the quality of the bulk material is good.

The Hall mobilities were measured in a magnetic field of 4000 G on cloverleaf samples cut from epitaxial wafers. Ohmic contacts were formed

by evaporating approximately 2500 Å of 12% Ge in Au, then annealing for 4 min at 460°C under nitrogen. This procedure yielded contacts that were ohmic at 300 and 77 K.

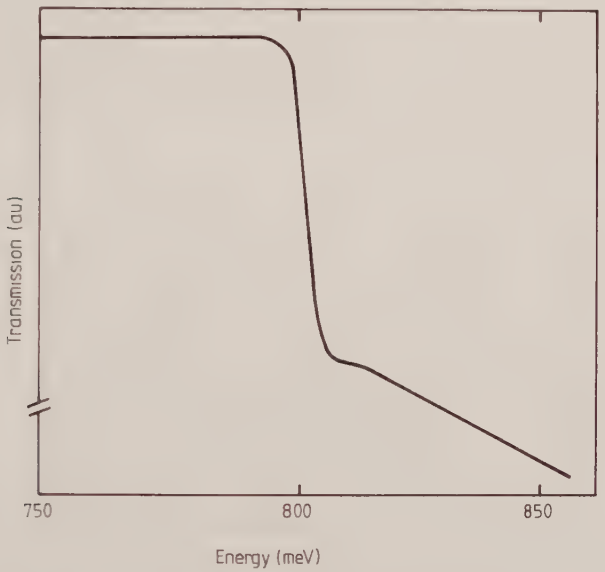

Figure 3.4 Transmission spectrum measured for a $Ga_{0.47}In_{0.53}As$–InP heterojunction at 1.5 K (from [163]).

Typical values as a function of the thickness of the layer, composition, electron carrier concentration and temperature are summarized in table 3.2. The electron carrier concentration remained roughly constant between 300 and 77 K. The mobilities and doping of nominally undoped $Ga_{0.47}In_{0.53}As$ grown at a substrate temperature between 550 and 650°C are also shown in table 3.2. The mobilities increase and the backgrounds (all n-type) decrease at lower growth temperature. The increased mobility in $Ga_{0.47}In_{0.53}As$ is comparable to the best reported mobility achieved by LPE, VPE and MBE for this composition. In table 3.2, the change of mobility at 77 K with temperature shows that the material is apparently less compensated at 550 than at 650°C.

Compensation and mismatch effects would reduce the mobility for a particular electron concentration. The effect of mismatch on mobility is pronounced. The variation of Hall mobility with lattice mismatch for a particular electron concentration ($N_D - N_A \simeq 5 \times 10^{15}$) is plotted in figure 3.5. The mobility is independent of the lattice mismatch in the range $(\Delta a/a)_s \leqslant \pm 2 \times 10^{-3}$, although Razeghi and Duchemin [5] have found a serious decrease for values of mismatch in the range $(\Delta a/a)_s \geqslant \pm 5 \times 10^{-3}$.

In general, layers that are in tension (positive mismatch) have lower mobilities than those in compression with the same, but negative, mismatch [10].

The variation of Hall mobility as a function of temperature is shown in figure 3.6. The best mobility obtained was 12 000 $cm^2 V^{-1} s^{-1}$ at 300 K and

Table 3.2 Typical mobility for GaInAs/InP grown by MOCVD as a function of layer thickness, composition, electron carrier concentration and growth temperature.

GaInAs layer	T_G(°C)	Thickness (μm)	$N_D - N_A$ (cm^{-3})	μ($cm^2 V^{-1} s^{-1}$) 300 K	77 K	$\Delta a/a$ strained
1	550	6	1.8×10^{15}	11 800	48 000	$+5 \times 10^{-3}$
2	550	3.4	2.7×10^{15}	9 732	32 150	-4.9×10^{-3}
3	550	1	4.8×10^{15}	8 700	41 000	$+2.6 \times 10^{-3}$
4	650	0.78	1.2×10^{16}	8 100	17 600	$+4 \times 10^{-4}$
5	650	1.21	1.1×10^{16}	9 020	21 000	$+10^{-4}$
6	550	0.9	4.2×10^{15}	9 000	37 300	-10^{-3}
7	550	0.66	2.5×10^{15}	11 900	60 000	$+10^{-4}$
8	550	0.6	2×10^{14}	12 000	100 000	$+10^{-4}$
9	530	1	2×10^{14}	13 000	130 000	$+10^{-4}$

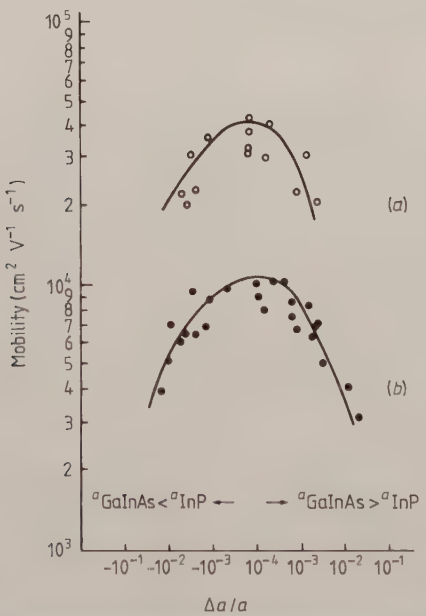

Figure 3.5 Variation of the measured Hall mobility with lattice mismatch for an electron concentration $N_D - N_A \simeq 2.5 \times 10^{15}$ at (*a*) 77 and (*b*) 300 K (from [164]).

700 000 $cm^2 V^{-1} s^{-1}$ at 2 K, with electron carrier concentration of $N_D - N_A \simeq 2.5 \times 10^{14}$ cm^{-3}, for a thickness of 0.5 μm.

The carrier concentration profile evaluated from $C-V$ measurements and the electrochemical profile for GaInAs layers over an InP substrate exhibit uniform doping along the layer thickness and an abrupt change in the carrier concentration (figure 3.7). GaInAs layers grown by LP-MOCVD can be doped n-type by using H_2S or SiH_4, and p-type by using DEZn.

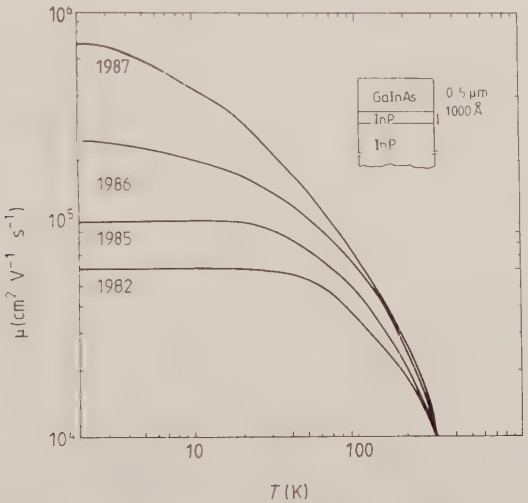

Figure 3.6 Variation of the measured Hall mobility as a function of temperature.

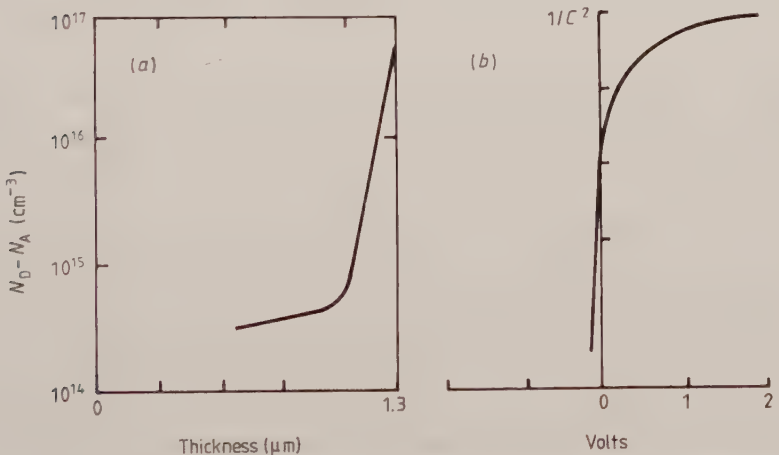

Figure 3.7 (*a*) Carrier concentration profile evaluated by $C-V$ measurements and (*b*) electrochemical profile (shown for a $Ga_{0.47}In_{0.53}As$ layer on an Sn-doped substrate) (from [165]).

For the same growth temperature and the same flow-rate of DEZn, the hole carrier concentration of GaInAs layers is higher than that of InP. Figure 3.8 shows the electrochemical profile of a GaInAs–InP DH layer for FET applications. The growth conditions and DEZn flow-rate for InP and GaInAs layers are the same, and we can see that the interfaces are sharp and that $N_A - N_D$ is higher for GaInAs than for InP.

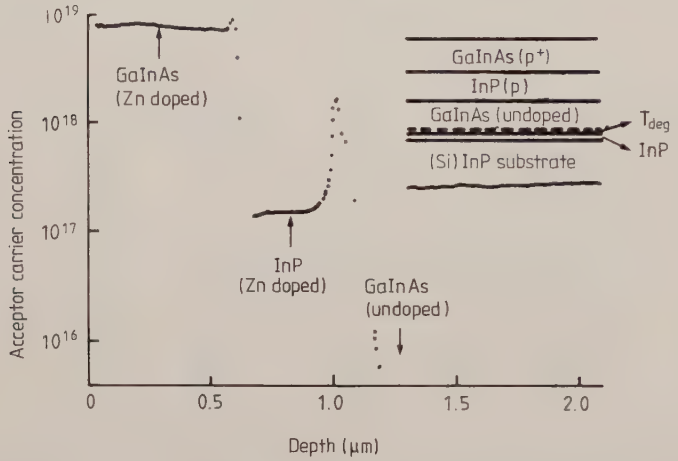

Figure 3.8 Electrochemical profiles of typical doping interfaces for GaInAs–InP doped with DEZn for FET applications.

3.2 OPTICAL AND CRYSTALLOGRAPHIC PROPERTIES, AND IMPURITY INCORPORATION OF GaInAs GROWN BY MOCVD

Goetz *et al* [11] have performed a comparative study of some crystallographic and optical properties of n- and p-type $Ga_xIn_{1-x}As/InP$, $0.44 < x < 0.49$, grown by liquid-phase epitaxy (LPE), vapour-phase epitaxy (VPE) and metallorganic chemical vapour deposition (MOCVD). Three different substitutional acceptors were chemically identified as C, Zn and Si, and their binding energies determined. The presence and concentration of these acceptors in nominally undoped material depend on the crystal growth process and its parameters. X-ray measurements and photoluminescence spectra reveal clearly and in mutual agreement inhomogeneities of the composition and deviations of the $Ga_xIn_{1-x}As$ composition from the composition at lattice match. The energy of the direct band gap as a function of the Ga concentration and the bowing parameter (see chapter 1) were derived with great precision and yielded values different from earlier experimental work. Details of the photoluminescence and absorption spectra such as free- and bound-exciton lines and pair bands were identified

and provided relevant exciton and acceptor binding energies and the LO-phonon energy.

3.2.1 Sample preparation

The LPE layers were grown in a conventional horizontal sliding system within a lamp-heated furnace, which permits fast changes in temperature. After baking the In melt for about 20 h at 800°C and the In + GaAs + InAs melt for about 10 h at 660°C, growth was carried out at temperatures of about 640°C by a step cooling technique with a temperature step of 3°C. PH_3 was added to the H_2 ambient to avoid substrate degradation at elevated temperatures [12]. Nominally undoped n-type layers with a thickness of up to 8 μm exhibited carrier concentrations in the low 10^{15} cm^{-3} range and mobilities of up to 11 000 cm^2 V^{-1} s^{-1} at 300 K and 43 000 cm^2 V^{-1} s^{-1} at 77 K (table 3.3). The p-type $Ga_{0.47}In_{0.53}As$ layers were grown from a Zn-doped solution with Zn mole fractions equal to 5×10^{-7} or more, leading to p doping levels lower than 10^{16} cm^{-3}.

The VPE material was grown using the In/Ga–AsH_3–HCl–H_2 system [13]. An In/Ga alloy source (Ga concentration 6%, source temperature 700°C) was used for the generation of metal chlorides; it was shown earlier that this method has the advantage of improved control of film composition compared to the commonly used two-source system. High-purity HCl was generated by decomposition of $AsCl_3$ in a separate furnace (730°C) and freeze-out of the arsenic. The deposition temperature was between 680 and 715°C. Partial pressures of the chlorides were adjusted at 7.5×10^{-3} bar and of AsH_3 at 1.2×10^{-2} bar in the deposition zone. Undoped n-type layers with a thickness of up to 5.6 μm exhibited carrier concentrations in the low 10^{15} cm^{-3} range and mobilities of up to 9700 cm^2 V^{-1} s^{-1} at 300 K and 29 000 cm^2 V^{-1} s^{-1} at 77 K (table 3.3).

Razeghi *et al* [14] have grown MOCVD undoped n-type layers at 550°C with a thickness of 0.7 μm exhibiting carrier concentrations of 2×10^{14} cm^3 and mobilities of 12 000 cm^2 V^{-1} s^{-1} at 300 K, 155 000 cm^2 V^{-1} s^{-1} at 77 K and 700 000 cm^2 V^{-1} s^{-1} at 2 K. The details are indicated in table 3.3.

3.2.2 Electrical, crystallographic and optical experiments

Carrier concentrations and mobilities were measured by the conventional Van der Pauw technique (table 3.3). Double-crystal x-ray diffraction was used to assess the lattice mismatch and the Ga concentration x_{Ga} of the epitaxial films. Figure 3.9 shows diffraction spectra of VPE, LPE and MOCVD samples.

The strain due to the lattice mismatch between layer and substrate leads to a tetragonal distortion of the layer lattice with two different lattice constants $a_\parallel$ (parallel to the interface) and $a_\perp$ (in the growth direction) [15, 16] and eventually to an inclined growth of the layer relative to the substrate

Table 3.3 Sample parameters (x_{Ga} is the Ga concentration, $\Delta\theta$ is the width of the x-ray peaks and I_{lum} is the luminescence intensity in relative units of the exciton line at 2 K and 30 mW cm^{-2} excitation density).

Sample	Method	Thickness (μm)	x_{Ga}	$\Delta\theta$ (arcsec)	I_{lum} (au)	Doping	n, p (10^{15} cm^{-3}) 300 K	n, p (10^{15} cm^{-3}) 77 K	μ(cm^2 V^{-1}s^{-1}) 300 K	μ(cm^2 V^{-1}s^{-1}) 77 K
8.81	LPE	6.8	0.485	61	25	und	n = 80	–	1 800	–
69.81	LPE	3.7	0.472	39	40	und	n = 1.7	–	11 000	43 000
86.81	LPE	4.1	0.462	61	–	Zn	p = 14	–	170	450
105.81	LPE	2.7	0.475	65	33	und	n = 1.8	–	10 000	36 000
107.81	LPE	8.2	0.473	44	5	und	n = 6.0	–	8 000	–
108.81	LPE	5.1	0.473	119	–	Zn	p = 4.4	–	169	–
113.81	LPE	2.5	0.481	33	–	Zn	n = 3.8	–	4 800	–
128.81	LPE	1.2	0.486	58	–	Zn	n = 16	–	5 200	–
129.81	LPE	0.9	0.464	54	13	und	n = 40	–	6 800	–
8.82	LPE	1.1	–	–	15	und	n = 2.4	3.1	9 600	29 000
9.82	LPE	6.1	0.471	46	24	und	n = 5.9	4.4	7 200	23 000
16.82	LPE	0.5	–	–	–	und	p = 4.0	–	110	–

17.82	LPE	0.6	0.475	43	24	und	n =	4.0	–	5 800	–
34.82	LPE	0.6	0.475	72	2.4	und		–		–	–
M 23	LPE	11.0	–	–	57	und	n =	5.0	–	10 000	31 000
M 65	LPE	5.5	0.473	33	-	Zn	p =	1.6	–	137	–
J 32	VPE	2.0	0.472	65	3.8	und	n =	2.6	2.9	9 800	27 000
J 37	VPE	3.0	0.457	144	1.8	und	n =	4.6	4.1	9 500	26 000
J 39	VPE	5.0	0.458	147	2.9	und	n =	4.7	4.2	9 700	29 000
JQ 49	VPE	0.8	0.441	272	1.4	und	n =	2.8		9 300	–
JQ 51	VPE	1.1	0.447	188	1.3	und	n =	2.4	–	8 500	–
JQ 55	VPE	0.7	0.457	251	0.8	und	n =	2.8	–	8 200	-
JQ 62	VPE	1.4	0.456	232	0.1	und	n =	0.67	–	9 000	–
P 79	VPE	5.6	0.457	586	1.2	und	n =	17	13	6 200	15 000
PS 82	VPE	3.3	0.451	337	0.4	und	n =	3.4	2.9	9 400	27 000
58	MOCVD	0.9	0.477	–	1.0	und	n =	4.2	–	9 000	37 000
59	MOCVD	0.9	–	–	0.2	und	n =	5.1	–	8 600	33 000
85	MOCVD	6.0	0.431	344	5.8	und		–	–	12 000	48 500
235	MOCVD	0.7	–	–	39	und	n =	2.0	–	12 000	55 000
365	MOCVD	1.0	0.462	70	7.0	und	n =	200	–	7 500	–
131	MOCVD	0.6	0.47	30	–	und	n =	0.2	0.2	12 600	155 000

surface with a misorientation angle α [17, 18]. Goetz *et al* [11] determined the three quantities $(\Delta a_{\parallel}/a)_s$, $(\Delta a_{\perp}/a)_s$ and α from the x-ray double-crystal diffractometer measurements in the conventional way (described in [15–18]) by using the (1 1 3) and (1 1 5) Cu K_α Bragg reflections in different geometries (InP substrate: (0 0 1) oriented). They found $(\Delta a/a)_s$ for MOCVD samples in the range -2.6 to $+3.7 \times 10^{-3}$. In agreement with Kawamura and Okamoto's results [18], $(\Delta a_{\parallel}/a)_s$ was at least one order of magnitude smaller (coherent growth). Within experimental error (± 10 arcsec) they did not find any misorientation α. The Ga concentration x_{Ga} (table 3.3) was determined from a_f, the lattice constant of the strain-free epilayer, by applying Vegard's law [19]; a_f was estimated from $(\Delta a/a)_s$ using the relation $(\Delta a_f/a)_s \simeq 0.5 \times (\Delta a_{\perp}/a)_s$. This relation follows from equation (3.3), assuming $c_{11} \simeq c_{12}$ in $Ga_{0.47}In_{0.53}As$ [9].

3.2.3 Results and discussion

Figure 3.10 shows typical photoluminescence spectra of nominally undoped n-type LPE, VPE and MOCVD samples at $T = 2$ K. Part of the information gained from these spectra is similar and in agreement with that gained from x-ray experiments. The width of the edge luminescence bands and their intensities are governed largely by the quality of the crystal. Clearly the MOCVD material has a much more homogeneous composition, and a more perfect surface, leading to a lower surface recombination velocity: in the LPE and MOCVD (no. 235) spectra the dominating near-band-gap line is considerably more intense and has a linewidth of about 2–3 meV ($P_{laser} = 30\ mW\ cm^{-2}$), much narrower than in VPE material (4–5 meV) (for details see table 3.3).

In §3.2.4, we shall show that the dominant high-energy line (figure 3.10) is due to bound excitons. Figure 3.10 reveals that already small variations of the Ga concentration lead to a considerable shift of the band gap and thus of the luminescence lines. In §3.2.5, we use this sensitive feature to derive the dependence of the gap energy at $T = 2$ K from the composition in the range $x_{Ga} = 45$–49%. Down to 25 meV below the exciton line, further bands can be seen. They will be identified as donor–acceptor pair recombinations (§3.2.6).

The mobility of sample 235 increases to $90\,000\ cm^2\ V^{-1}\ s^{-1}$ at 2 K, indicating the presence of a two-dimensional electron gas at the GaInAs/InP interface. The luminescence of such samples differs strongly from the luminescence of the MOCVD layer shown in figure 3.10 which has a 77 K mobility of $33\,000\ cm^2\ V^{-1}\ s^{-1}$. The intensity is higher by more than one order of magnitude, and the near-gap spectrum does not show any indication of recombination of donor-bound electrons with holes bound to Si, Zn and C acceptors. An example of such a remarkable spectrum is given in figure 3.11.

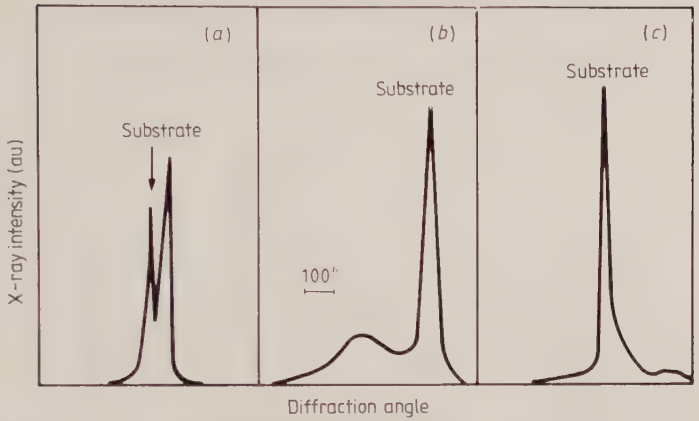

Figure 3.9 X-ray double-crystal diffraction pattern of (*a*) LPE, (*b*) VPE and (*c*) MOCVD $Ga_xIn_{1-x}As$ on an InP substrate. The LPE layer is better matched to the substrate lattice and shows less compositional fluctuations (smaller width of layer x-ray peak). Layer thicknesses: (*a*) 3.7 μm; (*b*) 1.4 μm; (*c*) 0.7 μm.

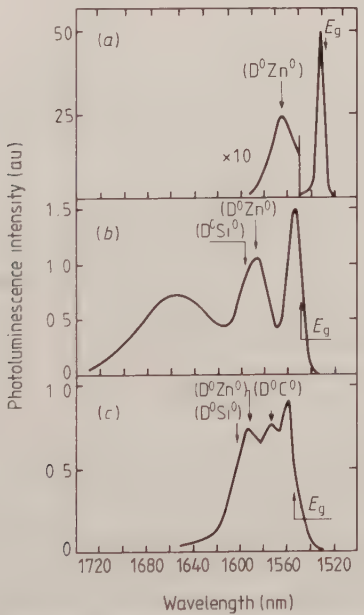

Figure 3.10 Typical photoluminescence spectra of nominally undoped ($n = 2$ to 5×10^{15} cm^{-3}) LPE (*a*), VPE (*b*) and MOCVD (*c*) $Ga_xIn_{1-x}As$. Small changes in the Ga concentration x cause considerable shifts of the emission lines. $T = 2$ K, $P = 30$ mW cm^{-2}.

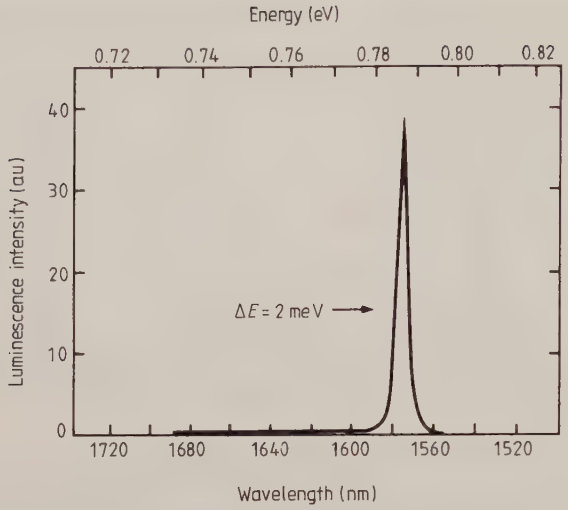

Figure 3.11 Photoluminescence spectrum of a very-high-mobility MOCVD $Ga_xIn_{1-x}As$ layer. The emission intensity and linewidth are comparable to the spectra of the LPE layers (figure 3.10). No impurity bands occur. $T = 2$ K, $P = 30$ mW cm^{-2}. $x = 0.447$.

3.2.4 Exciton line

Similar to GaAs, several elementary recombination mechanisms may occur and cause near-band-gap emission lines: free excitons (X), excitons bound to shallow impurities (D^0X, D^+X, A^0X) and donor–valence band recombinations (D^0h). Since only one rather broad near-band-gap line was observed under any circumstances, we estimated roughly the relative spectral positions at which these recombinations should be found in $Ga_{0.47}In_{0.53}As$. Table 3.4 shows the resulting values. The donor and free-exciton binding energies E_D and E_X used in this calculation were determined from the usual hydrogenic model:

$$E_{D,X} = [(\mu/m_0)/\varepsilon_0^2] \times 13.6 \text{ eV} \tag{3.4}$$

where $\mu = m_e$ (conduction-band effective mass) or $1/\mu = 1/m_e + \frac{1}{2}(1/m_{hh} + 1/m_{lh})$ (exciton reduced mass), respectively. Using a dielectric constant $\varepsilon_0 = 13.7$ (linear interpolation between $\varepsilon_0(GaAs) = 12.56$ and $\varepsilon_0(InAs) = 14.74$) and the effective masses $m_e/m_0 = 0.041$, $m_{hh}/m_0 = 0.47$ and $m_{lh}/m_0 = 0.050$ (derived by Alavi *et al* [20] from magnetoabsorption measurements) the effective-mass donor and free-exciton binding energies of three shallow acceptors (identified as C, Zn and Si) are determined as $E_C = 13$ meV, $E_{Zn} = 22$ meV and $E_{Si} = 25$ meV. According to Haynes' rule the coefficients a, a', β, β' and β'', which are a measure of the localization energy of the exciton, have a value of about 0.1. The resulting relative

spectral positions of the different recombination lines (table 3.4) are displayed in figure 3.12. Two typical examples of near-gap lines (2 and 5 meV halfwidth) are superimposed. It is obvious from this comparison that the observed peaks are caused by a superposition of several of these recombination processes. Rather broad linewidths are typical of ternary and quaternary semiconductors and are attributed to compositional inhomogeneities and to alloy clustering [21].

Table 3.4 Predicted spectral positions of several near-band-gap emission lines in $Ga_{0.47}In_{0.53}As$. E_g is the energy of the fundamental gap; E_X, E_D and E_A are the free-exciton, donor and acceptor binding energies, respectively.

Recombination process	Theoretical emission energy using $a, a', \beta, \beta', \beta'' \simeq 0.1$	
X	$E_g - E_X$	$= E_g - 2.0$ meV
D^0X	$E_g - (E_X + aE_D)$	$= E_g - 2.3$ meV
D^+X	$E_g - (E_D + a'E_D)$	$= E_g - 3.3$ meV
A_1^0X	$E_g - (E_X + \beta E_{A_1})$	$= E_g - 3.3$ meV
A_2^0X	$E_g - (E_X + \beta' E_{A_2})$	$= E_g - 4.2$ meV
A_3^0X	$E_g - (E_X + \beta'' E_{A_3})$	$= E_g - 4.5$ meV
D^0h	$E_g - E_D$	$= E_g - 3.0$ meV

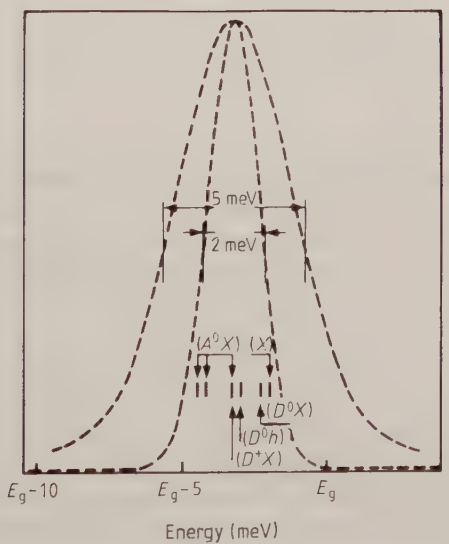

Figure 3.12 Theoretically derived positions of several near-band-gap emission processes relative to E_g (compare table 3.4). Typical near-band-gap emission lines with widths of 2 and 5 meV are superimposed.

The excitonic nature of the dominant high-energy peak is proved by its excitation and temperature dependence. Whereas the impurity band shows a sublinear increase due to saturation effects at higher laser powers, typical of pair bands, the near-band-gap peak increases linearly with excitation over four orders of magnitude (figure 3.13). Detailed balance calculations show that this is the expected excitation dependence of bound-exciton recombination processes [22].

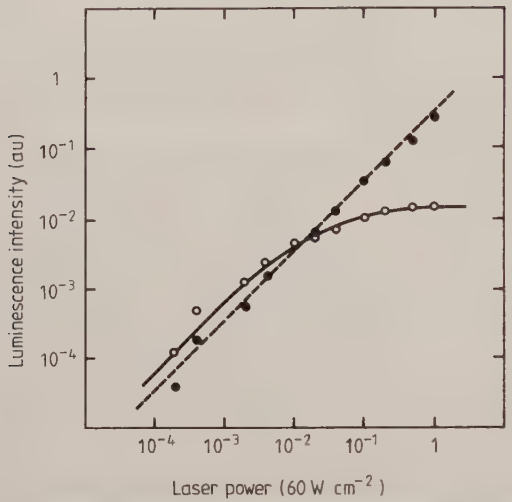

Figure 3.13 Integrated intensity of the pair emission band (○) and the exciton line (•) as a function of the laser power density for an undoped $Ga_{0.47}In_{0.53}As$ sample at $T = 1.6$ K.

The thermal activation energies of the exciton line are determined from the integrated intensity shown in figure 3.14 versus the reciprocal temperature. Figure 3.14 shows that there are two competing ionization mechanisms with different activation energies. The measured temperature dependence is fitted with a theoretical expression derived by Bimberg *et al* [23]:

$$I_T/I_0 = [1 + C_1 \exp(T_1/T) + C_2 \exp(T_2/T)]^{-1}. \tag{3.5}$$

Here I_T and I_0 are the emission intensities at the temperatures T and $T = 0$ K, respectively, c_1 and c_2 are ratios of degeneracies, and $k_B T_1$ and $k_B T_2$ are activation energies. Excellent agreement between the measured points and equation (3.5) is achieved with the parameters given in the figure. The resulting activation energies are $k_B T_1 = 1.6 \pm 0.1$ meV and $k_B T_2 = 11.6 \pm 2$ meV. In a hydrogenic model the thermal activation is equal to three-quarters of the binding energy (the ratio between the $n = 1$ and $n = 2$ binding energies of a Rydberg series). Thus the activation energy

of $k_B T_1 = 1.6$ meV yields a binding energy of 2.1 meV, in excellent agreement with the theoretical binding energy of the free exciton (2.0 meV) derived above. The second activation energy in figure 3.14 (although less precise) is almost one order of magnitude larger and can be unambiguously identified with the excitation of a bound hole.

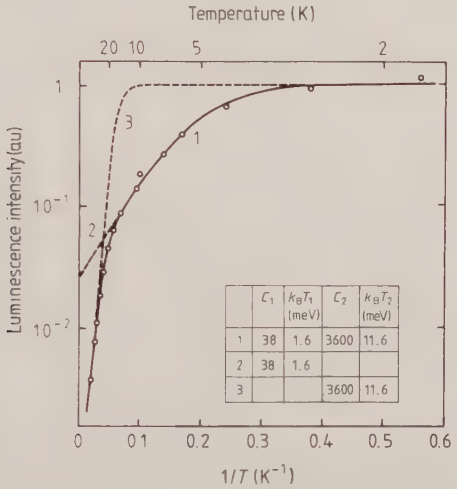

Figure 3.14 Integrated intensity of the exciton line for $Ga_xIn_{1-x}As$ as a function of $1/T$. The open circles are experimental points. The broken and full curves are theoretical fits with equation (3.5) assuming either one (broken) or two (full) activation energies $k_B T_{1,2} = 1.6$, 11.6 meV, respectively.

Absorption measurements confirm the excitonic nature of the near-band-gap fundamental absorption edge. In figure 3.15 an absorption spectrum (circles) is fitted with a theoretical expression of the absorption coefficient (full curve) based on Elliott's [24] theory of allowed, direct transitions between non-degenerate parabolic energy bands, including exciton effects in the approximation of the hydrogenic model:

$$\alpha(h\omega) = A\left[\sum_{n=1}^{\infty} 2\frac{R}{n^3}\,\delta\left(h\omega - E + \frac{R}{n^2}\right) + \frac{U(h\omega - E_g)}{1 - \exp\{-2\pi[R/(h\omega - E_g)]^{1/2}\}}\right] \tag{3.6}$$

where A contains the transition-matrix element, R is the excitonic Rydberg and $U(x) = 1$ for $x \geqslant 0$ and $U(x) = 0$ for $x < 0$. The first term in equation (3.6) describes transitions into the discrete states of the exciton and the second term transitions into the continuum. The temperature broadening of

the lineshape has been taken into account by convoluting equation (3.6) with a Lorentzian.

The best agreement between theory and the experimental spectrum is found for the width $\Gamma = 2.7$ meV, $E_g = 0.813$ eV and $E_{gx} = 0.811$ eV (figure 3.15). So again we find for the free-exciton binding energy a value of $E_X = 2$ meV in agreement with the photoluminescence results and the hydrogenic model.

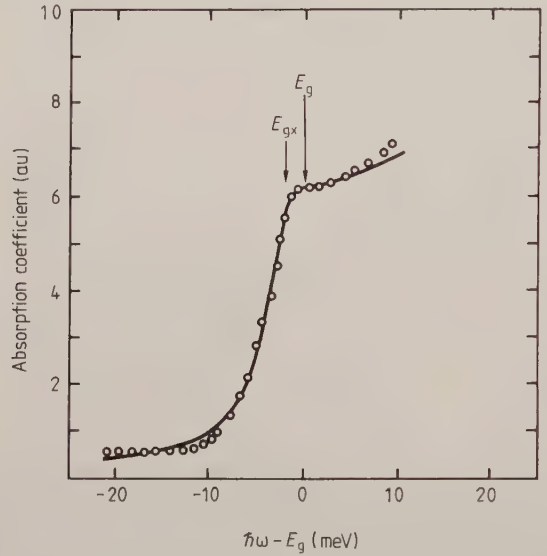

Figure 3.15 Absorption spectrum of an undoped LPE $Ga_xIn_{1-x}As$ layer at $T = 77$ K. The open circles are experimental points. The full curve is a theoretical one from equation (3.6) (parameters given in the text). E_{gx} is the position of the exciton energy gap derived from the fit. $x = 0.472$.

Careful examination of the absorption in figure 3.15 reveals a faint shoulder in the ascent of the absorption coefficient, 2–3 meV below the main edge. This shoulder might be caused by a bound exciton.

At high excitation intensity several additional lines appear in the photoluminescence spectrum (figure 3.16) separated from each other and the exciton line by 32 meV, respectively. The donor–acceptor pair emission band at 0.793 eV is completely saturated at these laser intensities (compare figure 3.13). The additional bands can be attributed to LO-phonon replicas of the exciton line. The LO-phonon energy of 32 ± 0.5 meV is in good agreement with earlier values by Shah *et al* [25], who fitted spectra of hot carriers with a value of 34 meV, by Pinczuk *et al* [26], who found 33.8 meV (Raman effect measurements), and by Brodsky and Lucovsky [27], who found two LO phonons with the energies of 32.9 and 29.1 meV (infrared reflectivity).

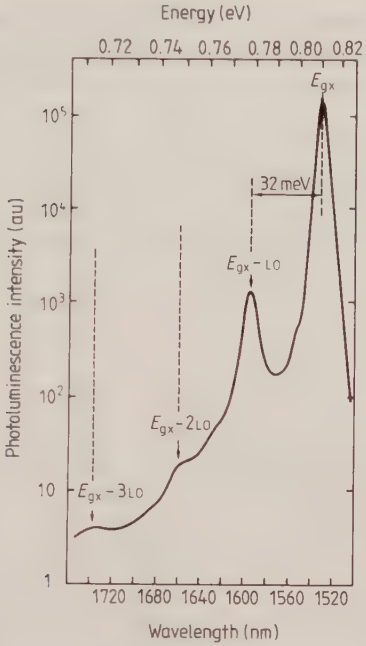

Figure 3.16 Low-temperature photoluminescence spectrum of the LPE sample of figure 3.15 at high excitation density: several LO-phonon replicas of the exciton line appear; the donor–acceptor band at 0.793 eV is completely saturated and hardly visible. $Ga_xIn_{1-x}As$ (undoped), $T = 2$ K, $P = 60$ W cm^{-2}.

3.2.5 Determination of $E_g(x_{Ga})$ near $x_{Ga} = 47\%$

A small mismatch between the lattice constants of the layer and the InP substrate ($\Delta a/a$) or corresponding small deviations of the Ga concentration (x_{Ga}) from the optimum value for complete lattice match (46.8%) lead to considerable change in the band gap. For a series of LPE and VPE samples, Goetz *et al* [11] derived the band gap at $T = 2$ K from the exciton emission-line position using figure 3.12 by adding the binding energy of 2.1 meV. In figure 3.17 the resulting values are displayed as a function of the Ga concentration x_{Ga} which was determined from the x-ray measurements described in §3.2.4

The varying error bars for x_{Ga} are due to varying compositional fluctuations in the layers and were extracted from the width of the x-ray layer peaks. The straight line in figure 3.17 is a fit to the experiment with the expression

$$E_g(x) = E_g^{InAs} + (E_g^{GaAs} - E_g^{InAs})x - Cx(1-x) \qquad (3.7)$$

with $E_g^{InAs} = 0.4105$ eV and $E_g^{GaAs} = 1.5192$ eV ($T = 2$ K) [28]. The bowing

parameter $C = 0.475$ describes the deviation of $E_g(x)$ from linearity between the two extremes E_g^{InAs} and E_g^{GaAs}. Thus equation (3.7) can be rewritten

$$E_g(x)|_{2\ K} = 0.4105 + 0.6337x + 0.475x^2. \tag{3.8}$$

For $x_{Ga} = 0.468$, the composition of optimum lattice match, equation (3.8) yields a gap energy of $E_g = 0.811$ eV ($T = 2$ K), which is probably the most precise value reported. This value is smaller than the value given by Towe [29]: $E_g = 0.821$ eV.

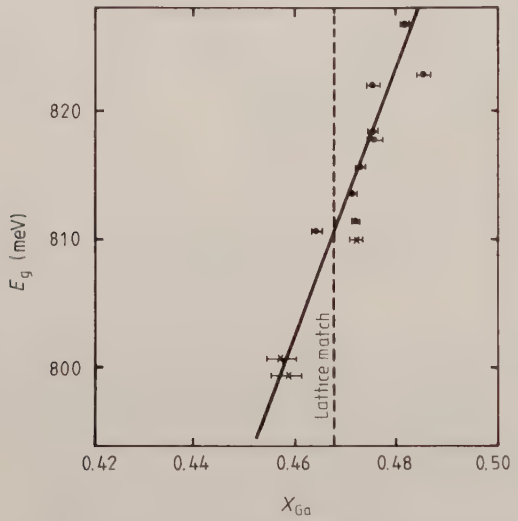

Figure 3.17 Band-gap energy at $T = 2$ K for $Ga_xIn_{1-x}As$ as a function of the Ga concentration X_{Ga} of several LPE (•) and VPE (X) samples. The error bars are due to the compositional inhomogeneities. The full line is a fit with equation (3.7).

3.2.6 Donor–acceptor pair recombination

Three bands are observed (8, 17 and 20 meV) below the near-band-gap line and are identified as donor–acceptor pair transitions (figure 3.18). Figure 3.18 shows a spectrum of an MOCVD sample in which all three acceptors occur simultaneously. In order to determine the binding energies of the acceptors, Goetz *et al* [11] tried to fit the pair bands with a theoretical lineshape as derived by Lorentz *et al* [30] for GaP:

$$I(R) \sim R^4 \exp\left[-(4\pi/3)N_D R^3\right] \exp(-2R/a_D). \tag{3.9}$$

This expression describes the intensity of saturated distant pair emission as a product of the number of 'isolated' pairs and the transition probability

for radiative recombination of the electrons and holes. R is the distance between donor and acceptor and is connected with the emission energy $\hbar\omega$, the band-gap energy E_g and the donor and acceptor binding energies E_D and E_a by

$$\hbar\omega = E_g - (E_A + E_D) + e^2/(\varepsilon_0 R). \tag{3.10}$$

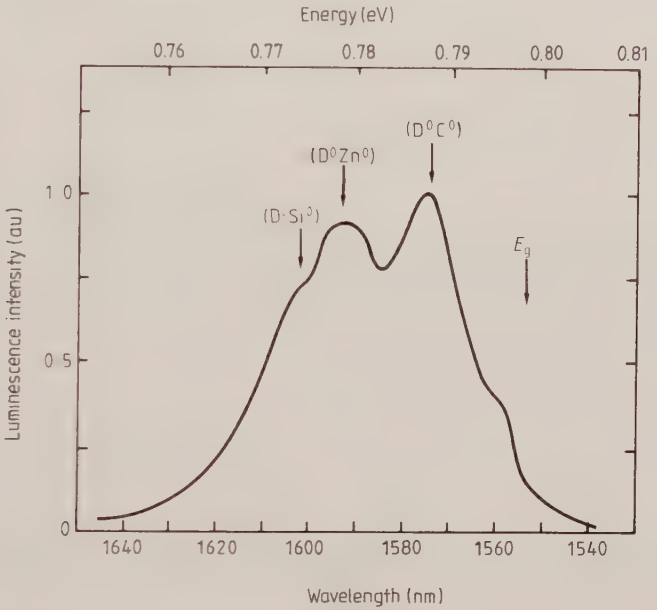

Figure 3.18 Photoluminescence spectrum of an undoped MOCVD $Ga_xIn_{1-x}As$ sample at $T = 1.8$ K. Three pair bands due to C, Zn and Si acceptors are resolved. The near-band-gap exciton line appears only weakly. $x = 0.457$.

Here the last term (Coulomb interaction term) takes into account the electrostatic interaction between the ionized donor and acceptor in the final state of the transition. The factor R^4 in equation (3.9) accounts for the number of donor sites per unit energy range; the first exponential (nearest-neighbour factor) describes the probability that an acceptor has no donor nearer than R, and the second exponential describes the overlap of the hole and electron, assuming that this overlap is predominantly determined by the effective Bohr radius a_D of the donor-bound electron. Further parameters are the donor concentration N_D and the static dielectric constant ε_0.

It turned out, however, that equation (3.9) yields lineshapes that are much narrower than the observed pair bands. As in the case of the exciton line, considerable broadening, familiar in solid solutions, has to be taken into account: microscopic fluctuations of the composition lead to a

variation of the impurity energy levels. Figure 3.19 shows an experimental pair spectrum (circles) and a theoretical lineshape according to equation (3.9) (full curve). The broadening effect is taken into account by convoluting equation (3.9) with a Gaussian distribution of width σ (broken curve). The donor concentration N_D is set equal to the carrier concentration at room temperature. For the donor Bohr radius a_D and the donor binding energy E_D we assume hydrogenic values with $a_D = (\varepsilon_0 m_0/m_e) \times 0.53$ Å ($\varepsilon_0 = 13.7$, $m_e/m_0 = 0.041$, §3.2.4) and $E_D = 3.0$ meV (according to equation (3.1)), respectively. For the gap energies E_g we use the values determined in §3.2.5. E_A and σ serve as fitting parameters. The acceptor binding energies derived from fits on 25 samples are $E_{A_1} = 13 \pm 1$ meV, $E_{A_2} = 22 \pm 1$ meV and $E_{A_3} = 25 \pm 1$ meV. Goetz *et al* [11] identify these acceptors as $A_1 = C$, $A_2 = Zn$ and $A_3 = Si$. The shallowest acceptor C occurs nearly exclusively in MOCVD samples (figure 3.10). Furthermore secondary-ion mass spectrometry (SIMS) analysis shows that the LPE and VPE samples contain Zn and Si. So the two other bands must be attributed to these impurities. Comparison with GaAs (figure 3.20) suggests that Zn is the shallower one.

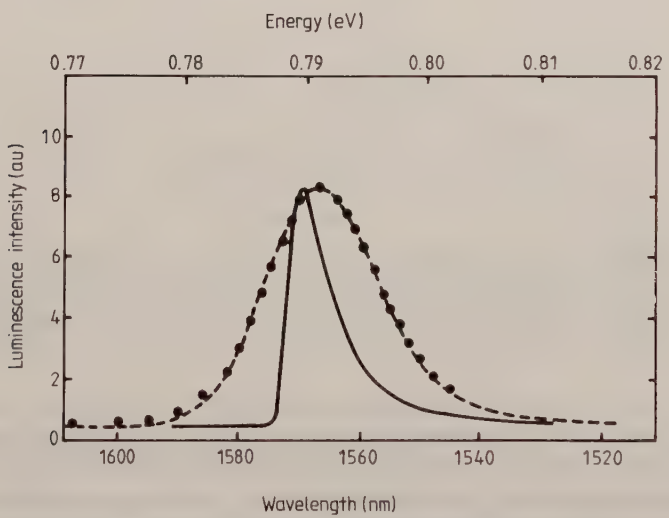

Figure 3.19 Pair band of an undoped $Ga_xIn_{1-x}As$ layer at $T = 2$ K (circles). Good agreement with the theoretical lineshape (equation (3.9)) is achieved by convoluting (3.9) (full curve) with a Gaussian of width 7.6 meV (broken curve).

3.2.7 Zn-doped samples

Zn-doped samples (figure 3.21) show one broad intense band in the spectral region where Goetz *et al* [11] found donor–Zn acceptor pair emission in

undoped samples, in agreement with the earlier LPE results [31]. The near-band-gap exciton line appears only very weakly. They found another weak emission 32 meV below the intense pair band, which can be identified as a LO phonon replica of this band. The spectra suggest that these samples are strongly compensated and have impurity concentrations orders of magnitude larger than the free-carrier concentration.

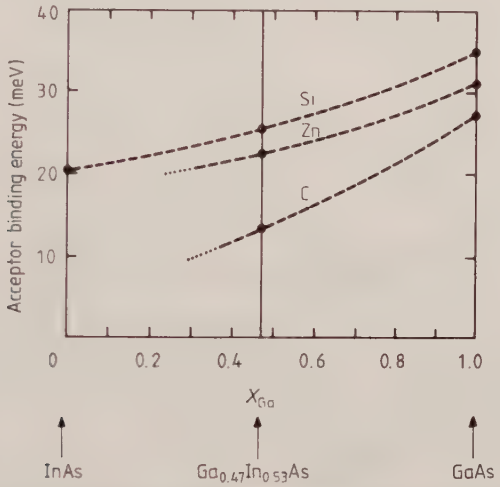

Figure 3.20 Si, Zn and C acceptor binding energies in GaAs and InAs (from [12]) and their respective values for $Ga_{0.47}In_{0.53}As$ determined here.

3.2.8 Deep Fe and intrinsic defect levels in $Ga_{0.47}In_{0.53}As/InP$

Only a few reports exist on deep traps in $Ga_{0.47}In_{0.53}As$ [32–35]. Among these only Yagi *et al* [33] and Rao and Bhattacharya [34] report on layers grown on semi-insulating InP:Fe substrates. Rao and Bhattacharya [34] tentatively proposed the existence of a trap 0.56 eV above the valence band, in contrast to our results. Yagi *et al* [33] observed an intense luminescence band at 0.66 eV for liquid-phase epitaxy layers grown on both Sn- and Fe-doped substrates. The luminescence intensity was found to depend strongly on lattice mismatch.

Goetz *et al* [36] have used low-temperature photoluminescence and deep-level transient spectroscopy (DLTS) to identify and characterize a deep Fe trap in high-purity undoped n-type and slightly Sn- and Zn-doped ($n \leqslant 10^{17}$ cm^{-3}) $Ga_xIn_{1-x}As$ ($x \approx 0.47$), epitaxially grown on InP. The InP substrate material was either semi-insulating Fe-doped or n-type S-doped. Results on samples grown by LPE, VPE and MOCVD (see previous section) are compared with each other and related to the different growth processes.

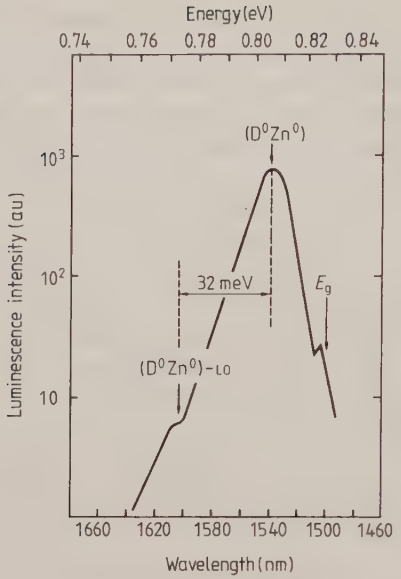

Figure 3.21 Photoluminescence spectrum of a lightly Zn-doped p-type $Ga_xIn_{1-x}As$ layer at $T = 2$ K. A strong donor–Zn acceptor pair emission with its LO-phonon replica can be seen.

Figure 3.22(*a*) shows typical deep-level photoluminescence spectra taken at 2 K and an excitation density of 60 W cm^{-2} of pure LPE, VPE and MOCVD samples all grown on InP:Fe substrates. The intensity of the bands shown in figure 3.22(*a*) is 3–5 orders of magnitude weaker than the near-gap emission band (not shown in figure 3.22(*a*); see previous section) [11]. The spectra exhibit two bands at 0.66 eV and at about 0.70 eV. The intensity of these bands from the 2.7 μm thick sample no. 105.81 is much larger than the intensity from the 6.8 μm thick sample no. 8.81. The precise position of the 0.70 eV band cannot be derived exactly due to the superposition with phonon sidebands of the near-gap emission. The 0.66 and 0.70 eV bands are absent in the luminescence spectra of InP:Fe substrates. More than 40 layers grown on Fe-doped InP substrates have been investigated and almost every one shows these bands. One can conclude that the luminescence definitely originates from the $Ga_{0.47}In_{0.53}As$ layers. No dependence of the luminescence intensity on doping or lattice mismatch is observed. Thus the new bands are not shallow-impurity- or interface-related.

The 0.66 eV band is completely absent in layers grown on S-doped InP substrates (figure 3.22(*b*)) whereas the 0.70 eV band is also present in the spectra of these layers. The spectra of the two samples nos P768 and 78.84 in figure 3.22(*b*) can be compared quantitatively with each other. In both cases two layers were grown under identical conditions from the same melt,

but on different substrates, as indicated. The insets of figure 3.22(*b*) show nicely the 0.66 eV band, which is extracted by subtraction of the spectra of the layers grown on different substrates.

The deep trap emission bands of the MOCVD layers are always extremely weak, broad and structureless. MOCVD layers of larger thickness do not show the bands at all (sample no. 59 in figure 3.22(*a*) has a thickness of 0.7 μm, whereas no. 365 has a thickness of 1.1 μm).

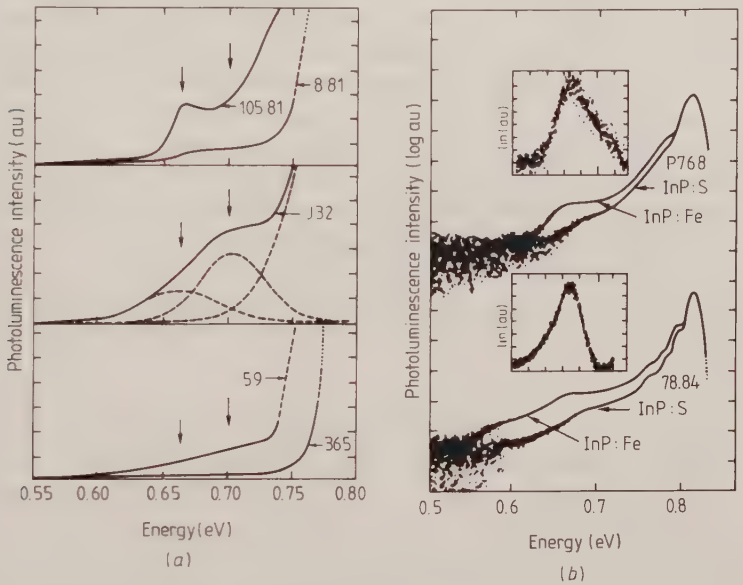

Figure 3.22 (*a*) Typical deep-level photoluminescence spectra of pure LPE, VPE and MOCVD GaInAs–InP samples. The arrows denote the positions of the 0.66 and 0.70 eV bands. The broken curves are Gaussians. (*b*) Near-gap and deep-level photoluminescence spectra of LPE samples from different laboratories grown on InP:Fe and InP:S, respectively. The emission band at 0.66 eV is absent in the layers grown on InP:S. The insets show the 0.66 eV band alone, extracted from the spectra by subtraction of the $Ga_{0.47}In_{0.53}As$/InP:S spectra (multiplied by a scaling factor) from the $Ga_{0.47}In_{0.53}As$/InP:Fe spectra, respectively. For both (*a*) and (*b*), $T = 2$ K, $P = 60$ W cm^{-2}.

Obviously there exists one Fe-related trap with an energy depth of 150 meV and another centre that is not related to Fe at a depth of 110 meV. The Fe centre is definitely introduced by out-diffusion from the substrate during the growth process. This conclusion is based on a comparison of a series of samples grown (a) at identical temperatures but with increasing thickness and (b) at increasing temperature but with similar thickness. With decreasing growth temperature and/or increasing layer thickness the 0.66

eV luminescence intensity drops. The 0.70 eV band is most likely due to an intrinsic defect of $Ga_{0.47}In_{0.53}As$. It is very weak in layers of high crystallographic perfection (monitored by x-ray experiments) showing high mobilities. In LPE layers grown at a temperature as low as 500°C and VPE layers the 0.70 eV luminescence intensity is comparatively large.

DLTS measurements were performed on metal–insulator–semiconductor (MIS) structures fabricated on p-type LPE samples. SiO_2 is deposited by chemical vapour deposition at 350°C. Aluminium is used as insulator contact. The carrier concentration of the $Ga_{0.47}In_{0.53}As$ layer is $p = 1.4 \times 10^{17}\ cm^{-3}$. The DLTS measurements reveal one trap only (figure 3.23) due to the inherently lower resolution of this method. The sign of the DLTS signal shows that this trap is correlated with the valence band. An Arrhenius plot yields an activation energy of 150 meV, in excellent agreement with the position of the 0.66 eV band found in photoluminescence. Depth profiles of this level agree with the above interpretation. Similar results were obtained on MOCVD-grown GaInAs layers.

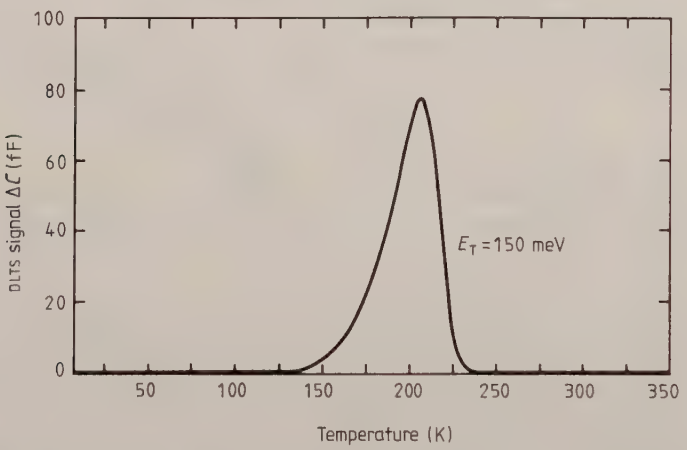

Figure 3.23 DLTS spectrum of a MIS structure on a p-type LPE $Ga_{0.47}In_{0.53}As$:Zn layer grown on an InP:Fe substrate. $p = 1.4 \times 10^{17}\ cm^{-3}$.

The dependence of the integrated luminescence intensity of the 0.66 eV band on laser power and temperature has been studied in detail. The intensity increases linearly with increasing excitation power over three orders of magnitude up to $100\ W\,cm^{-2}$. No saturation effects can be observed at higher laser powers. With increasing temperature the 0.66 eV band disappears at 40–50 K and the 0.70 eV band remains visible. The temperature dependence of the luminescence intensity of the 0.66 eV band discloses two competing ionization mechanisms with different activation

energies. The measured temperature dependence is fitted using equation (3.5). The resulting activation energies are $k_B T_1 = 2.5 \pm 0.5$ meV and $k_B T_2 = 100 \pm 20$ meV. In a hydrogenic model the thermal activation is equal to three-quarters of the binding energy (the ratio between the $n = 1$ and $n = 2$ binding energies of a Rydberg series). Thus the activation energy of $k_B T_1 = 2.5$ meV yields a binding energy of 3.3 meV, which is in reasonable agreement with the theoretical binding energy $E_D = 3.0$ meV of a hydrogenic shallow donor [11]. The second activation energy can be unambiguously identified with the excitation of a bound hole of the 150 meV deep trap. From these results we conclude that at the lowest temperatures the 0.66 eV band is due to a shallow donor–Fe acceptor transition:

$$D^0 + Fe^{3+} \rightarrow D^+ + Fe^{2+} + h\omega_{photon}$$

is a model of the underlying process. At higher temperatures the band is due to a free electron–Fe acceptor transition. The emission energies of these two transitions differ by less than the already small shallow donor binding energy of 3 meV. This does not lead to a perceptible difference in the spectral position of the rather broad ($\simeq 40$ meV) and featureless 0.66 eV band.

So, a deep Fe-related trap at $E_v + 150$ meV in $Ga_{0.47}In_{0.53}As$/InP:Fe layers and an intrinsic trap at a depth of 110 meV in $Ga_{0.47}In_{0.53}As$ layers grown on both InP:Fe and InP:S substrates are observed and characterized using photoluminescence and DLTS. The Fe trap is absent in layers grown on Fe-free InP substrates and is obviously caused by Fe diffusing out of the substrate during the growth process. The lower growth temperature of the MOCVD samples (550°C) leads to a lower out-diffusion compared to LPE (640°C) and VPE ($\simeq 700$°C) samples.

3.2.9 Comparison of transport, optical and crystallographic properties

High mobility of the electrons is advantageous for a number of devices like the two-dimensional electron-gas field-effect transistor (TEGFET). This study shows that decreasing acceptor-related luminescence—monitored by the intensity of acceptor-related luminescence—causes increasing mobilities, in particular at 77 K and lower, where ionized-impurity scattering is most important. The link between decreasing acceptor concentration and increasing mobility is most striking for the MOCVD layers. Layers that no longer contain C as monitored by the luminescence spectra show a really dramatic increase of mobility at temperatures below 77 K, indicating two-dimensional (2D) electron conduction at the interface. Layers grown with Air Liquide starting material, showing lower mobilities and strong impurity lines in the luminescence spectra, still exhibit indications of 2D mobility. The same layers show a luminescence yield improved by almost two orders of

magnitude, indicating more perfect control of morphology and interfaces by MOCVD.

Double-crystal diffractometry, transport, low-temperature photoluminescence and absorption measurements of high-purity n-type and lightly Zn-doped p-type $Ga_xIn_{1-x}As/InP$ layers ($x \simeq 0.47$) grown with different epitaxial techniques (LPE, VPE, MOCVD) are presented. The MOCVD samples have properties superior to the LPE samples. Peaks related to free and bound excitons are found in the photoluminescence and absorption spectra of the undoped samples. The binding energy of the exciton is determined as 2.1 ± 0.1 meV, in agreement with a hydrogenic theory. LO-phonon replicas of the exciton line establish a LO-phonon energy of 32 ± 0.5 meV. The exact dependence of the energy gap at $T = 2$ K from the solid-solution composition in the range $x_{Ga} = 45–49\%$ is determined and yields a bowing parameter $C = 0.475$. A gap value of $E_g = 0.811$ eV at optimum lattice match is found. Data on donor–acceptor pair transitions observed in the photoluminescence spectra are combined with secondary-ion mass spectrometry data to identify different acceptors: C, Zn and Si. Their binding energies are 13 ± 1.22, 22 ± 1 and 25 ± 1 meV, respectively. C is the dominant acceptor in most MOCVD samples, but is hardly present in the LPE and VPE samples, whereas Si and Zn are unintentionally both present in LPE, VPE and most MOCVD samples. The Zn-doped p-type samples show only a weak exciton line but a broad donor–Zn acceptor pair transition band with a LO-phonon replica.

3.3 SHALLOW p^+ LAYERS IN GaInAs GROWN BY MOCVD BY Hg IMPLANTATION

For some devices, especially for structures like junction FET, thin and abrupt $p^+–n$ junctions are required. Diffusion is a widely practised technique in realizing p-type layers. Zn- and Cd-diffused junctions have been obtained, but thin p-type layers are difficult to realize, since these dopants have high diffusion constants. It has been shown [37, 38] that Be and Cd ion implantation can also give p-type layers, but due to diffusion during annealing, it is not possible to have thin p-type layers. For example, after an anneal at 675°C for 25 s, a 100 keV Be implantation gives a junction depth of approximately 1 μm [39]. The classical acceptor impurities in III–V materials are Be, Zn and Cd. All these impurities show a relatively high diffusion. We have tried to look for other acceptor impurities that would diffuse slowly; Favenec *et al* [40] have investigated how mercury behaves in terms of the type of dopant, electrical activity and diffusion.

Growth of 1 μm depth of $Ga_{0.47}In_{0.53}As$ layers has been obtained on ⟨1 0 0⟩ S- and Fe-doped substrates. All epitaxial layers were unintentionally doped. The mercury beam came from a Penning source. An energy of

700 keV (Hg^{2+}) has been used with a maximum beam intensity of 100 nA cm^{-2}. The implantation was performed at room temperature and the samples were tilted 7° from the ⟨1 0 0⟩ axis. The projected range of 700 keV Hg^{2+} ions was about 1200 Å. After implantation the samples were annealed capless in a flowing high-purity 0.4% PH_3/H_2 mixture. All the anneals were performed at 700°C for 10 min. Annealing did not modify the chemical surface, and the mirror-like aspect was retained.

The surface carrier concentration N_s of mercury-implanted layers was measured by the Hall effect. N_s is the result of Hall experiments and is a good approximation of the surface carrier concentration. All implanted layers were found to be p-type after annealing. The results are summarized in figure 3.24, which is a plot of N_s as function of the implantation dose φ ranging from 10^{12} to 10^{14} ions cm^{-2}. For low doses, $N_s = \varphi$, indicating the full electrical activity of the implanted species. For higher doses, only a part of the mercury dopant is electrically activated. For an Hg^+ dose of 10^{14} ions cm^{-2}, we have obtained 3×10^{14} holes cm^{-2}.

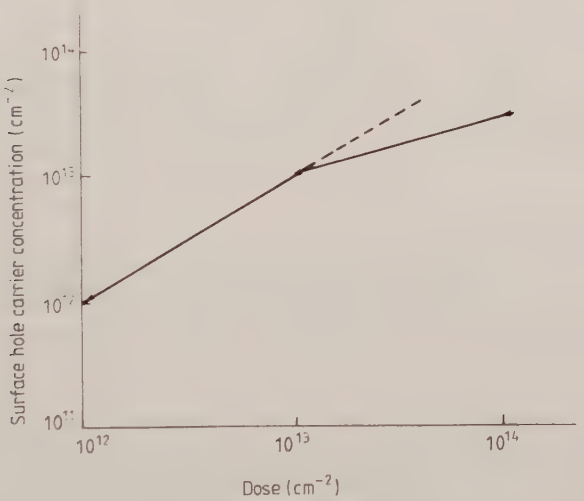

Figure 3.24 Surface carrier concentration plotted against mercury (Hg^+) dose.

Figure 3.25 shows typical results of the in-depth hole carrier distribution obtained by Hall measurements on a mesa etched Hall pattern in conjunction with chemical stripping of thin layers. The electrical profile has a similar shape for Hg^+ doses of 10^{13} and 10^{14} ions cm^{-2}. Near the surface a highly p^+-doped layer was obtained, and the hole carrier concentration should be about 10^{19} holes cm^{-3}. Hole concentration decreases as a function of depth. The junction is located at 2000 ± 200 Å for an Hg^+ dose of 10^{13} ions cm^{-2} and at 2300 ± 200 Å for an Hg^+ dose of 10^{14} ions cm^{-2}.

These electrical profiles show that impurities do not diffuse towards the bulk, but that there is a high surface pile-up after annealing at 700°C. Electrical profiles are the only indication of the non-diffusion of mercury in GaInAs. Unfortunately, it was not easy to measure how the mercury and the matrix elements interfered. On InP layers, SIMS analysis showed that mercury diffuses towards the surface and does not diffuse towards the bulk after a 700°C anneal. The diffusion of mercury impurities can be expected to be equivalent in InP and InGaAs.

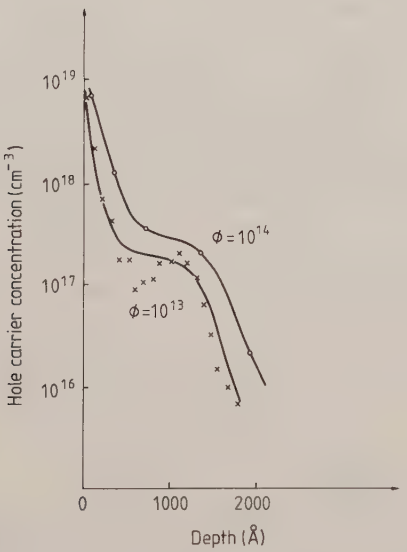

Figure 3.25 Hole carrier distribution for Hg^+ doses of $\varphi = 10^{13}$ and 10^{14} ions cm^{-2}.

A few p^+–n diodes were made from Hg-implanted epilayers grown on n^+ InP substrates. The structure was Au–Zn/Au/implanted p^+-GaInAs/8000 Å n(10^{16})-GaInAs/n^+-InP substrate/Au–Ge. Mesa diodes of area 3×10^{-4} cm^2 were fabricated. Figure 3.26 shows the current–voltage characteristic of a p^+–n diode. I–V characteristics show a soft reverse breakdown at about 8 V. This soft breakdown can be due to tunnelling, as was previously shown by Ito *et al* [41] in the case of GaInAs homojunction diodes with carrier concentrations of more than 10^{15} cm^{-3}. The leakage current is 5×10^{-3} A cm^{-2} at $V_R = -1$ V. Capacitance–voltage (C–V) data for the diodes yielded a linear plot of C^{-2} against V_R, indicating abrupt junctions.

So, mercury behaves as an acceptor dopant impurity in GaInAs and does not diffuse towards the bulk, whereas other acceptor impurities (Be, Zn, Cd) do. Mercury implantation should be a suitable method to obtain shallow p^+–n junctions on $Ga_{0.47}In_{0.53}As$.

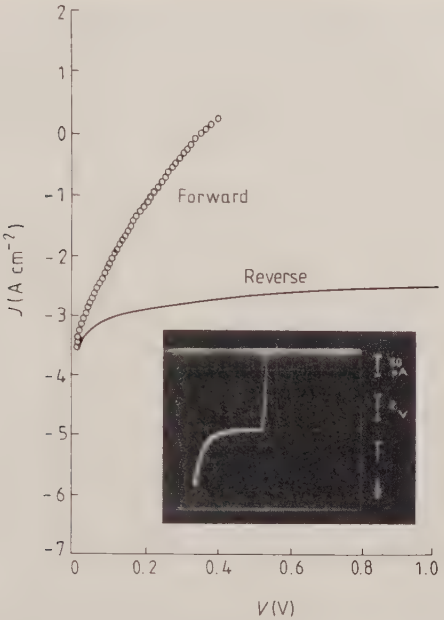

Figure 3.26 Semilogarithmic plot of $I-V$ characteristics of Hg-implanted n-GaInAs diode (dose = 10^{13} cm^{-2}). Inset is linear plot of $I-V$ characteristic.

3.4 GaInAs–InP HETEROJUNCTIONS, MULTIQUANTUM WELLS AND SUPERLATTICES GROWN BY MOCVD

3.4.1 Introduction

In 1970 Esaki and Tsu [42] envisaged solid-state superlattice semiconductors in which two materials with different electronic properties are interleaved in thin layers by periodically depositing two semiconducting materials, in contrast to natural superlattices (like SiC, which possesses various polytypical forms [43]), whose formation is difficult to control and is not well understood. The man-made superlattice can be achieved with predetermined prescriptions in terms of thickness, carrier concentration, strength of the periodic potential and number of periods. The superlattice potential subdivides the Brillouin zone of the bulk semiconductor into mini-zones, resulting in allowed mini-bands of electron transmission separated by forbidden bands. These mini-bands are relatively narrow on both energy and wavevector scales. The superlattice structure determines the mini-bands, which in turn dictate the transport and optical properties. Superlattices consisting of thin semiconductor layers were predicted to have

interesting physical properties such as the following:

(1) Quantum size effect (QSE). This effect occurs when the quantum-well thickness is of the order of the electron de Broglie wavelength. QSE becomes a dominant feature, changing the bulk, three-dimensional, behaviour into a quasi-two-dimensional one [44].

(2) Quantum tunnelling. Tunnelling phenomena across barriers open the way to many fascinating effects, the most eagerly expected being the Bloch oscillator. Esaki and Tsu [42] predicted Bloch oscillations in a compositional superlattice before superlattices existed. The superlattice should generate microwave radiation with wavelengths of less than 1 mm [42].

Experimentally the quantization of energy levels in superlattices was shown directly by the optical measurements of Dingle *et al* [44] and Chang *et al* [45]. The two-dimensionality of carrier transport in quantum wells (QW) and superlattices has been demonstrated in n-doped GaAs–GaAlAs superlattices by magnetoresistance quantum oscillations. Increase of two-dimensional carrier mobility by modulated doping, which separates donor atoms and charge carriers, was proposed and demonstrated by Störmer *et al* [46].

(3) Optical modulation devices. GaAs–GaAlAs superlattices show large non-linear optical effects associated with saturation of the room-temperature exciton resonances and also large electroabsorptive effects around the band-gap energy [47]. A new type of optoelectronic device, SEED (self-electro-optic effect device), was demonstrated using this effect [48]. It relies on modulation and detection within the same device and one possible mode of operation gives optical bistability at very low powers.

Another recent advance is the ability to grow strained layers, superlattices in which the crystal lattices of the two materials are not very closely matched. In that case there is a built-in strain in each layer.

3.4.2 Growth technique

Semiconductor multilayers and superlattices of III–V, II–VI and IV compounds can be grown by LPE, VPE, MBE and MOCVD.

Multiple-layer lasing structures with GaInAsP ($\lambda = 1.1\ \mu m$) layers as thin as 150 Å, separated by InP layers, have been reported using LPE [49].

The first semiconductor strained superlattices ($GaAs–GaAs_xP_{1-x}$) were grown using VPE [50, 51]. MBE is the most highly developed technique for multiple- and thin-layer crystal growth. Composition modulations down to alternate single atomic-layer thicknesses can be produced with MBE.

There have been a number of reports [44, 52–57] of excellent MBE growth of heterojunctions and superlattices of III–V and II–VI compounds. MBE has been used for growing semiconductor superlattices such as GaAs–GaAlAs, InAs–GaSb, InP–InGaAs, GaSbAs–GaSbAlSb, Ge–GaAs, Si–SiGe, CdTe–HgTe and PbTe–PbGeTe.

The disadvantages of MBE are that it is an expensive and complex process, and that there are difficulties with the growth of phosphorus-containing materials.

The evolution of MOCVD as a technique for the growth of high-quality layered semiconductor structures (e.g GaAs–GaAsP, GaAs–GaInAs, GaInAs–InP, GaInAsP–InP and GaAs–GaAlAs) has opened the way to the use of superlattice effects in new devices with many potential commercial applications. One of the major advantages of MOCVD is the ability to control solid composition easily in such systems as $Ga_xIn_{1-x}As_yP_{1-y}$–InP. The MOCVD growth of GaInAsP–InP superlattices, quantum wells (as thin as 8 Å) and heterojunctions exhibiting two-dimensional electron-gas behaviour was first reported by Razeghi *et al* [58].

High-quality $InP/Ga_{0.47}In_{0.53}As$ heterojunction, multiquantum-well and superlattice layers have been obtained using TEIn (or TMIn) and TEGa for In and Ga sources and pure AsH_3 and PH_3 for group V arsenic and phosphorus elements. Pure H_2 or a mixture of H_2 and N_2 is used as carrier gas. The growth temperature was between 500 and 650°C and the growth pressure was 76 Torr. The quality of epitaxial layers depends on the purity of the starting material. The highest purity of TEIn has been supplied by SMI. Highest purities of TEGa and TMIn have been obtained from α-Ventron (see chapter 2). Good-quality AsH_3 has been achieved using a passivated Matheson product. The growth conditions and characterization of these layers grown by MOCVD have been reported in detail elsewhere [59].

3.4.3 Structural characterization of GaInAs–InP quantum wells grown by MOCVD

Many high-quality $InP/Ga_{0.47}In_{0.53}As$ heterostructures such as modulation-doped heterojunctions (MDH), multiquantum wells (MQW) and superlattices (SL) have been grown. We describe now the different characterizations of these structures.

X-ray diffraction is of much use, particularly in the case of superlattices, to ensure the reproducibility of the wells and the barriers. Figure 3.27 exhibits the x-ray (4 0 0) diffraction pattern of a 10-period $Ga_{0.47}In_{0.53}As$/InP superlattice, with InP barriers of about $L_B = 250$ Å and $Ga_{0.47}In_{0.53}As$ wells of $L_z = 200$ Å [60]. A synchrotron beam of wavelength $\lambda = 1.2834$ Å is used as the x-ray source. Satellites corresponding to the artificial crystalline periodical $L_B + L_z$ introduced during growth have been resolved up to $n = \pm 5$. This is rarely observed and underlines the excellent structural quality of the sample under study. The $n = 0$ satellite, attributed to the (4 0 0) Bragg diffraction of the mean parameter of the superlattice, appears at the position of the InP substrate peak. This indicates that the lattice parameter of the ternary alloy is well adapted to that of the substrate.

From the angle $\Delta\theta = 360''$ between two adjacent satellites, we deduce,

using the classical expression

$$L_B + L_z = (\lambda/2)\Delta\theta \cos\theta$$

that the superperiodicity is $L_B + L_z = 410$ Å; this corresponds quite well to the expected value from the growth parameters.

The hyperfine structure observed in figure 3.27 near the substrate peak may be attributed to the interaction between incident and reflected waves through the $L = 5000$ Å epilayer (Pendellosung oscillations). If we use the classical equation

$$\delta\theta = (\lambda/2L) \cos\theta$$

with $L = 5000$ Å, we find $\delta\theta = 30''$, in good agreement with experimental results shown in figure 3.27. Such behaviour has rarely been observed in III–V superlattices.

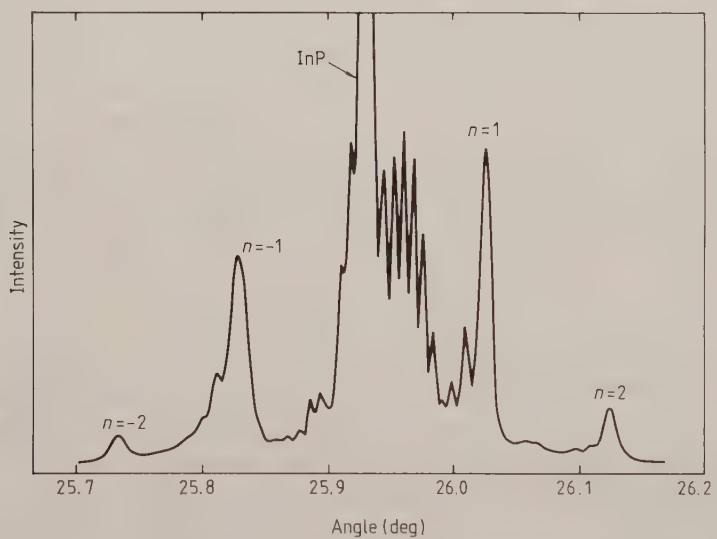

Figure 3.27 X-ray diffraction pattern of a 10-period $Ga_{0.47}In_{0.53}As/InP$ superlattice grown by MOCVD. $L_B(InP) = 250 \pm 20$ Å, $L_z(GaInAs) = 200 \pm 20$ Å.

SIMS analyses are performed for quantitative determination of impurities accumulated at the substrate–epilayer interfaces. The analyses are carried out on a modified Cameca IMS3F. The surfaces of the epitaxial layers are scanned with a focused mass-filtered oxygen-ion beam ($I_p = 1.5$ A at 10 keV). The scanned area is 250×250 μm and the analysed region is 150 μm in diameter.

Figure 3.28(*a*) exhibits the SIMS profiles of the four majority species (In, Ga, As and P) in a 25-period $Ga_{0.47}In_{0.53}As/InP$ superlattice with well and

barrier thicknesses of 150 Å. The In concentration appears almost constant, because it is the only element present in the barriers as well as in the wells. The signals of the other species are clearly oscillating with the change in chemical composition of the layers, thus evidencing the abruptness of the interface and the perfect control of compositions and of thicknesses.

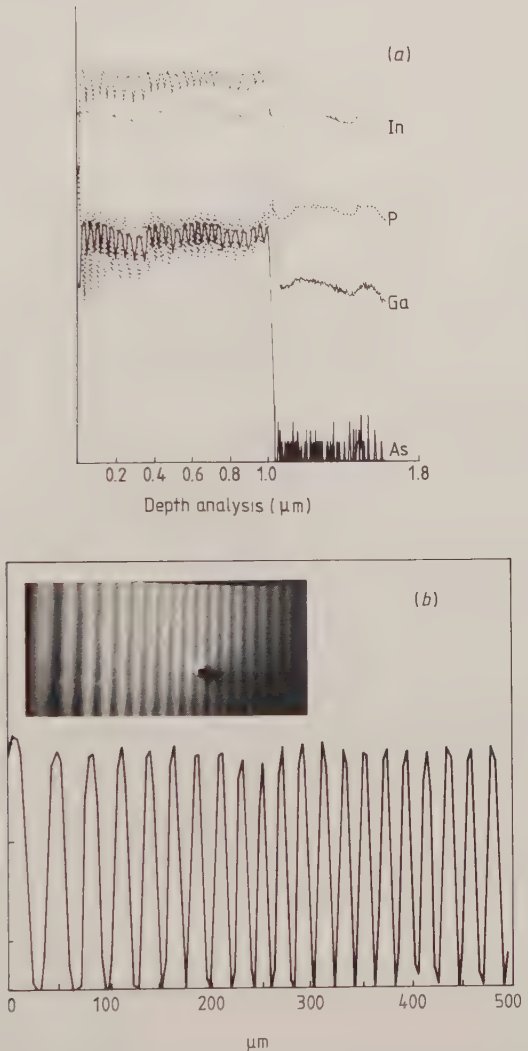

Figure 3.28 (*a*) Ga (— — —), In (. . . .), As (—) and P (• • •) SIMS profiles of a 25-period $Ga_{0.47}In_{0.53}As/InP$ superlattice ($L_z = 150$ Å, $L_B = 150$ Å) grown by MOCVD. (*b*) Phosphorus signal relative to the Auger spectrum of a $Ga_{0.47}In_{0.53}As/InP$ superlattice grown by MOCVD.

Auger spectra have been performed on chemical bevels. The samples are chemically etched by using a methanol–bromine solution (15% Br), in order to obtain a bevel with a mean amplification coefficient of 2100 (measured with a Talysurf). This means that a change of 1 μm along the surface corresponds to a change of 4.75 Å depth (z direction). By scanning the incident electron beam along the bevel, the phosphorus profile of a GaInAs–InP supperlattice has been obtained. It is shown in figure 3.28(*b*). There again the modulation of composition is clearly evidenced, thus confirming the abruptness of the interfaces.

The etch-pit density (EPD) is also performed on a chemical bevel. The defects are revealed in an H_3PO_4–HBr solution. The etch speed of the acid solution varies with the orientation of the atomic planes. Around a dislocation, the atomic plane appears slightly disoriented so that it is etched at a higher speed. For a fixed developing time, the etched thickness is greater around the defects than in the rest of the crystal; etch patterns appear that allow us to determine the density of dislocations.

We show in figure 3.29 the etch-pit density photograph of a $Ga_{0.47}In_{0.53}As$/InP heterojunction. The epitaxial layers, with a density of dislocations of about 10^4 cm^{-2}, equal to that of the substrate, show a crystalline quality at least corresponding to that of the InP substrate. No defects are evidenced at the interface.

Edge-on transmission electron microscope (TEM) characterization has been performed on a 40-period GaInAs–InP superlattice grown by MOCVD [61]. Figure 3.30 shows that the thickness of the layers is not regular and there are some dark point defects in the layers. These irregularities are due to the fact that the MOCVD reactor was operated manually, and there was a pyrolysis oven for PH_3. After elimination of the PH_3 pyrolysis oven and automatization of the MOCVD reactor, the thickness homogeneity of the superlattices was improved as shown on figure 3.30. The dark-field images at atomic resolution of the same superlattices are shown in figure 3.30. It is clear from this photograph that the interfaces between these layers are perfectly smooth and flat. Looking carefully at the InP/GaInAs interface (figure 3.30) we can see atomic steps every 80 Å, which can be attributed to the 2° misorientation of the InP substrate. The results show that perfect interfaces on an atomic scale can be grown by MOCVD.

3.4.4 Optical properties of GaInAs–InP quantum wells

(a) Photoluminescence

Quantum-well (QW) luminescence has been extensively studied in the GaAs–GaAlAs system and has provided significant information about the structural properties of heterostructure devices and about the 2D nature of elementary excitations. QW made of ternary or quaternary materials such as

GaInAs or GaInAsP imbedded in InP [62] or InAlAs [63] barrier material have been much less studied. Standard growth conditions were used, leading to a growth rate of about 2.5 Å s^{-1} and well defined interfaces by rapid switching of gas composition. Razeghi *et al* [64] studied multiple single-well samples, i.e. samples with a stack of quantum wells with different thicknesses grown under the same conditions. Three main subjects are addressed in what follows: (i) the origin and properties of luminescence lines; (ii) the observation of the excited states of the quantum wells by photoluminescence excitation spectroscopy (PLE) and the determination of QW parameters from these data; and (iii) the carrier-capture properties of thin quantum wells.

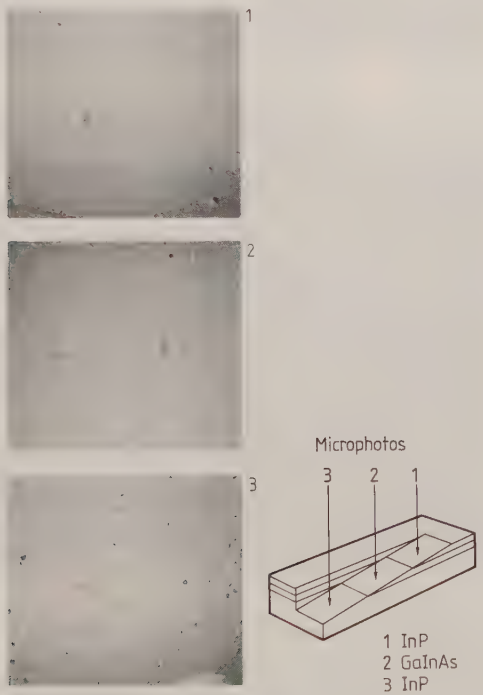

Figure 3.29 Etch-pitch density photograph of a $Ga_{0.47}In_{0.53}As/InP$ heterojunction grown by MOCVD.

A typical spectrum for a five-well structure is shown in figure 3.31. The well thicknesses indicated ('nominal') are those deduced from the growth rate as extrapolated for thin layers from the measured growth rate of thick layers. The remarkable features are the sharpness of lines, even for QW with an 8 Å nominal thickness ($\Delta E \simeq 9$ meV) at 5 K. The progress in sample quality can be traced by comparing these spectra with those obtained before

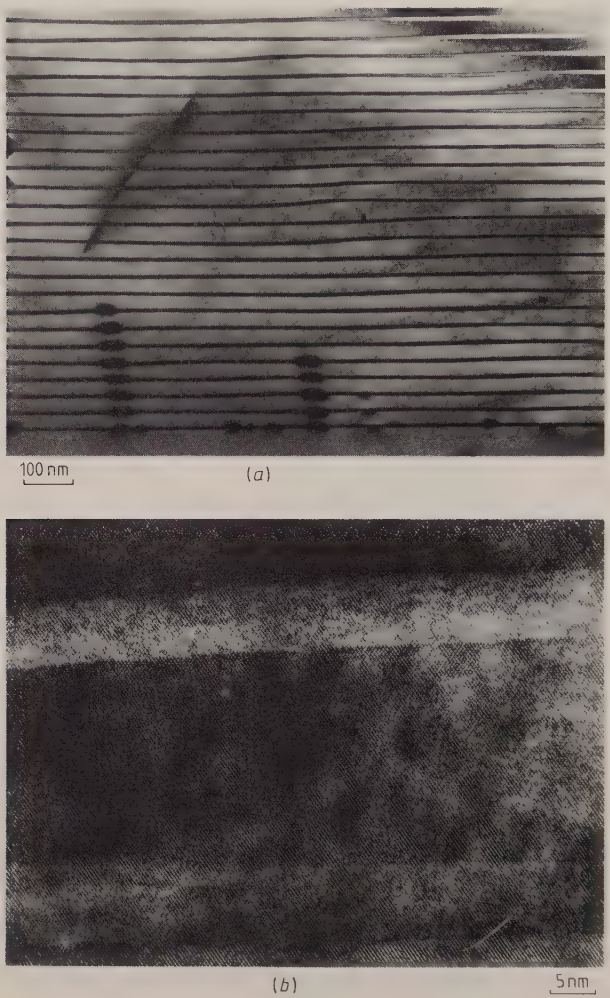

Figure 3.30 (*a*) Transmission electron micrograph of an LP-MOCVD $Ga_{0.47}In_{0.53}As/InP$ superlattice. (*b*) Dark-field image at atomic resolution of the same superlattice. (*c*) TEM of a $Ga_{0.47}In_{0.53}As/InP$ superlattice grown by an automatic MOCVD reactor.

by Razeghi *et al* [62]. Extremely large shifts of luminescence due to the quantum confinement effect of QW are observed, up to 0.320 eV for the nominal 8 Å QW.

The growth of layers with different thicknesses has allowed us to assess the origin of the variation in energy while scanning across the sample (figure 3.31). The recombination energy in an alloy QW can be approximated by

$$E = h\nu = E_0(x, y) + E^{e}_{conf} + E^{h}_{conf} \tag{3.11}$$

(*c*)

---

where $E_0(x, y)$ is the alloy band gap (dependent on local composition), and E^{e}_{conf} and E^{h}_{conf} are the confining energies for the electron and hole ground states, respectively. The small shift between the quantized electron–hole levels and luminescence line position due to exciton binding has been neglected here. Variations of $h\nu$ according to equation (3.11) can have two origins: (i) a variation in $E_0(x, y)$ due to alloy *macroscopic* variations of composition across the sample; and (ii) a change of the confining energies in a quantum well due to a *macroscopic* variation of QW thickness (originating in a non-uniform growth rate across the wafer). In case (i), one expects a similar shifting of the QW energies across the wafer, independent of the thickness of the quantum well under observation. In case (ii), if v_1 and v_2 are the two growth rates at two points 1 and 2, and remembering that $E \sim L^{-2}$ in the infinitely deep-well limit, one finds

$$\Delta E \simeq L^{-3}\Delta L = L^{-2}(v_2 - v_1)/v_2. \tag{3.12}$$

In this case, the energy shift between two points on the wafer depends on the well thickness. The *constant shift* observed for all the QW in those samples which display energy shifts across the wafer allows us to conclude that this is due to the macroscopic variations of the alloy composition across the sample.

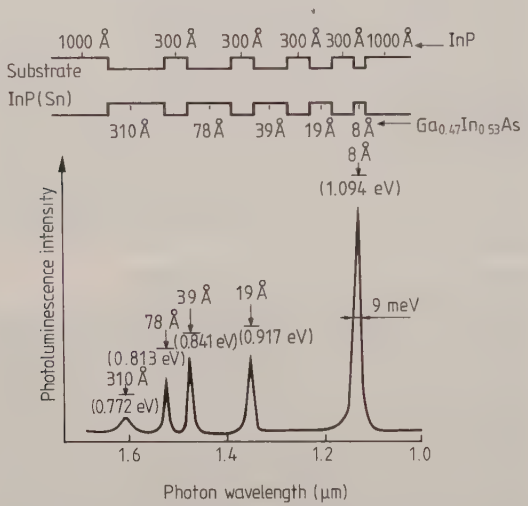

Figure 3.31 Photoluminescence spectrum of a multi-well LP-MOCVD GaInAs–InP sample at 5 K excited by an He–Ne laser in the InP overlayer.

It is not possible with the present level of understanding to decide the nature of the luminescent level at low temperatures. Comparing with GaAs–GaAlAs quantum wells, where the dominance of free-exciton-mediated recombination has been established through spin orientation and lineshape analysis [65], one could tentatively ascribe the same origin to the luminescence line in the GaInAs–InP system: the 2D exciton binding energy should be about 4 times larger than in 3D (as was recently well established in the GaAs–GaAlAs system by Maan *et al* [66], i.e. should be 10 meV.

The observed linewidth of the luminescence lines (and excitation spectra) is surprisingly small. A model of PLE spectra in GaAs–GaAlAs has described this linewidth as being caused by the spatially varying well thickness of the *microscopic* island-like topology of the interface due to a layer growth mode [67, 68]: assuming a half-monolayer height for the islands and a correlation length greater than or approximately equal to the exciton Bohr radius a_B, one expects variations of the exciton absorption or recombination energy given by $\Delta E \simeq L^{-3} a/2$. An $a/2$ fluctuation in interface position yields $\Delta E \simeq 42$ meV for a 20 Å thick sample, much above

the observed linewidth. It is possible to conclude that the previous model, although very successful in the case of GaAs–GaAlAs, does not apply to the GaInAs–InP case. One can therefore describe the interface as rather fuzzy. However, the observation of a narrow, well defined, intense luminescence peak, even for thicknesses down to 8 Å (nominal), leads us to emphasize the very good uniformity of this fuzzy well, i.e. very small deviations from the average thickness are allowed over macroscopic (here larger than a_B) distances.

(b) Excitation spectra

Excitation spectra have been recorded for a number of GaInAs–InP quantum wells. Figure 3.32 shows a typical PLE spectrum for a three-well structure of GaInAs–InP grown by MOCVD. A remarkable feature compared to the GaAs–GaAlAs case is that one cannot observe pairs of absorption peaks due to each confined electron level associated with either the heavy- or light-hole level. One can rather observe two series of peaks, one at lower energies and rather sharp, the other quite broad and more rightly described as a bump. Razeghi *et al* [64] tentatively ascribed these two series as due to heavy hole–electron and light hole–electron transitions. The different shapes of these transitions might be due to the different non-parabolicities of the two hole bands due to the strong valence-band mixing recently evidenced in the GaAs–GaAlAs case [69].

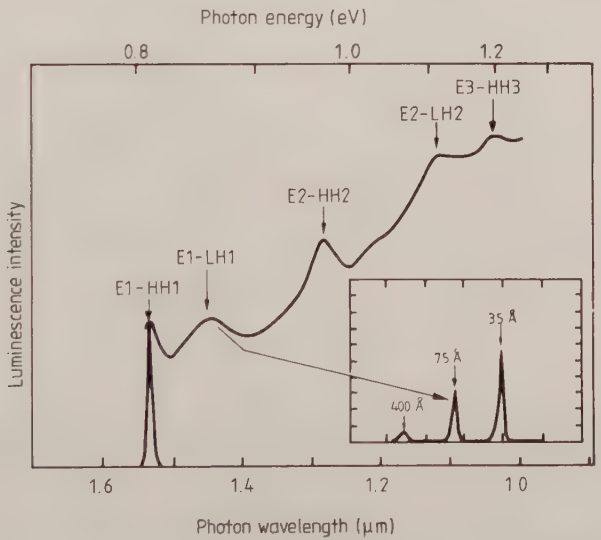

Figure 3.32 Excitation spectrum for a 75 Å GaInAs–InP quantum well at 5 K.

From these measurements one can try to evaluate the various parameters entering equation (3.11). It should be remarked that the situation is much more complicated than in the GaAs–GaAlAs case, as E_0 is not known so precisely and the various band parameters (mainly the hole masses) are also not too well determined. We therefore only produce here a preliminary fit of the experimental results taking all the unknowns as fitting parameters. Using a standard quantum-well calculation of energy levels, we introduce, in a simple iterative form, the non-parabolicity of the energy bands. No provision is taken for the mixing of the valence bands, which are considered fully uncoupled (figure 3.33). Neglecting exciton effects, which are small on the scale of confining energies, the best-fit parameters are

$E_0 = 0.742$ eV
$L = 39$ Å $\quad L = 78$ Å
$m_e = 0.041 m_0$
$m_{hh} = 0.5 m_0$ (has no influence on the fit down to m_{hh}, which is certainly not the case)
$m_{lh} = 0.042 m_0$
$Q = \Delta E_C / \Delta E_g = 0.5$.

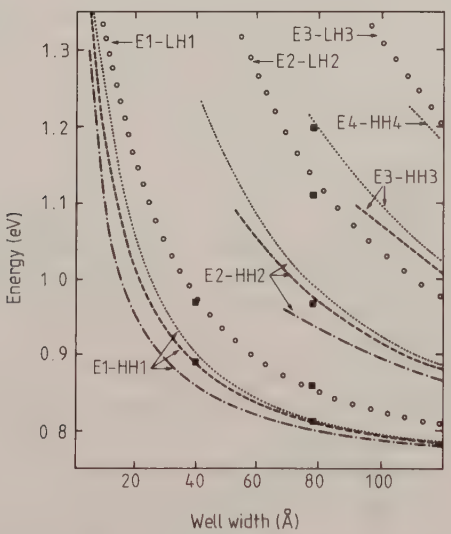

Figure 3.33 Fit of the transitions observed in excitation spectra for two wells with 75 and 35 Å nominal thickness. Fitting parameters: $E_0 = 0.742$ eV, $m_e = 0.041 m_0$, $m_{hh} = 0.5 m_0$, $m_{lh} = 0.042 m_0$, $L = 39$ Å, $L = 78$ Å. The various E–HH transition curves correspond to $Q = \Delta E_C / \Delta E_g = 0.3$ (— · —), 0.5 (— — — —) and 0.7 (. . . . .). Only one curve is traced for E–LH transitions (○), as this parameter has a negligible influence on transition energies.

As dramatically pointed out by Miller *et al* [70] in the GaAs–GaAlAs case, it can be observed that such optical measurements of interband transitions do not lead to an accurate determination of the relative band offsets: the change in the confining energies induced by a change in Q can easily be corrected by a change in other fitting parameters, here mainly E_0 and L. A more detailed knowledge of sample structure and band parameters is therefore needed before a more careful calculation can lead to a better precision in Q.

3.4.5 Room-temperature excitons in GaInAs–InP superlattices grown by MOCVD

Excitonic absorption at room temperature in GaAs–GaAlAs multiquantum wells has attracted a great deal of interest because of the novel physical properties and the potential usefulness in optoelectronic devices. Wood *et al* [71] have shown that the application of an electric field perpendicular to the quantum-well layers can cause a strong shift in the absorption edge, and that this shift can be used to make an optical modulator. Room-temperature excitonic absorption in GaInAs–AlInAs was first reported by Wood *et al* [71]. Razeghi *et al* [72] have made the first observation of room-temperature excitonic absorption in $Ga_{0.47}In_{0.53}As$–InP superlattices grown by MOCVD. Figure 3.34 shows the low-temperature photoluminescence spectrum of a GaInAs–InP multilayer grown by MOCVD. The details of the structure are shown in figure 3.34. It can be seen that the GaInAs

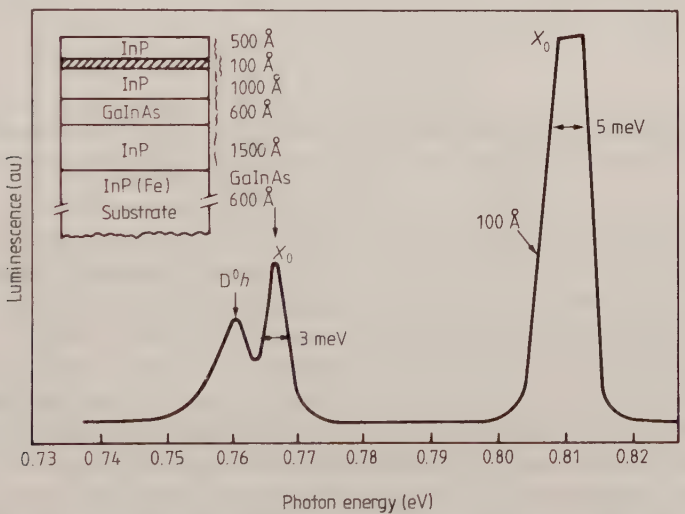

Figure 3.34 Photoluminescence spectrum of GaInAs–InP multilayer at 6 K. Inset: schematic representation of a GaInAs–InP multilayer grown by MOCVD. $P_{exc} = 0.8\ W\ cm^{-2}$.

quantum well of 100 Å thickness has a linewidth of 5 meV, while the GaInAs of 600 Å thickness has a linewidth of 3 meV, which can be attributed to free-exciton recombination, and the peak with energy 0.769 eV may be due to recombination of excitons bound to shallow impurities [73]. The excitonic nature of the dominant high-energy peak of the 100 Å quantum well is proved by photoluminescence excitation spectroscopy (PLE). Figure 3.35 shows the PLE spectrum of a GaInAs–InP quantum well of 100 Å thickness at 6 K. The PLE spectrum exhibits a series of peaks, which can be attributed to the heavy hole–electron and light hole–electron transitions as shown in figure 3.35.

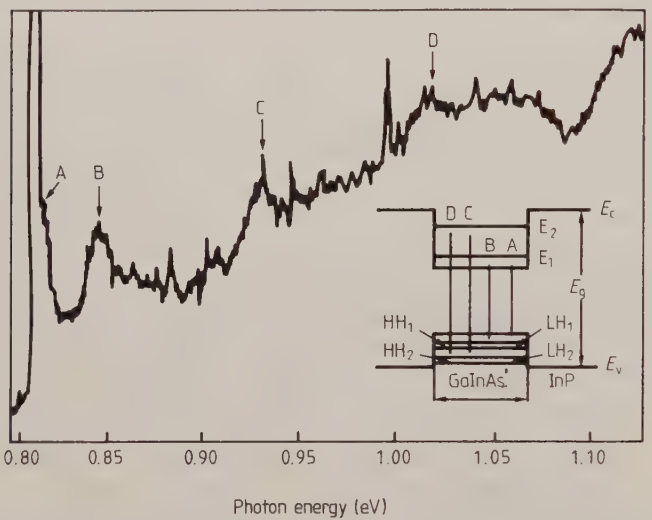

Figure 3.35 PLE spectrum of a GaInAs–InP quantum well of 100 Å thickness at 6 K. Transitions: A, E_1–HH_1; B, E_1–LH_1; C, E_2–HH_2; and D, E_2–LH_2. Inset: energy levels in a GaInAs–InP quantum well.

By comparing photoluminescence (PL) and PLE spectra taken at 6 K in figure 3.35, we find that the energy of the E_1–HH_1 sub-band transition, as determined by PLE, coincides with the peak energy of the (e, h) emission in the PL spectrum. Such a coincidence is only rarely observed as it can only occur in highly pure materials with very little disorder from alloying or interfaces. Usually luminescence is due to both intrinsic and extrinsic recombination processes, but PLE probes only intrinsic states. This coincidence of luminescence and PLE spectra shows that the PL of the GaInAs quantum well of 100 Å thickness under study is intrinsic and can be attributed to free-exciton recombination. Figure 3.36 shows the optical absorption spectrum of a GaInAs–InP superlattice at room temperature. The superlattice consists of 40 periods of approximately 100 Å thick

GaInAs wells and 200 Å thick InP barriers. The room-temperature absorption spectrum exhibits the step-like behaviour characteristic of the two-dimensional density of states and excitonic features at the onset of the steps. Furthermore, the 5 K photoluminescence spectrum of that superlattice shows a halfwidth of 6 meV, evidencing a good layer-to-layer reproducibility (see figure 3.36).

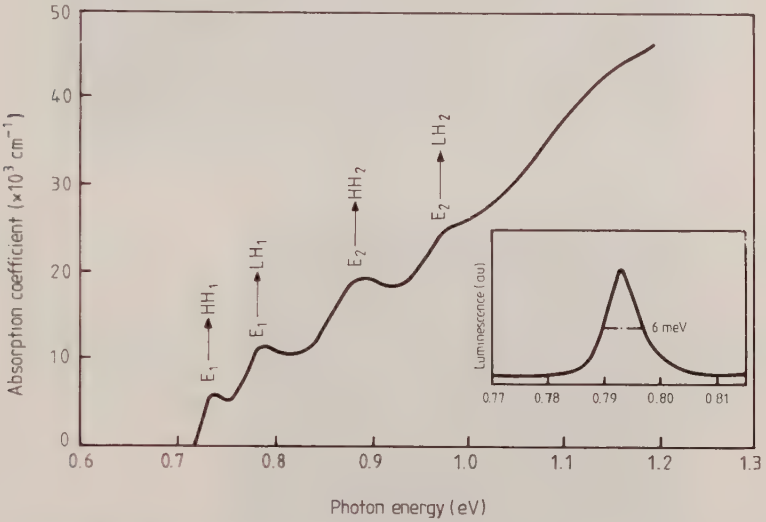

Figure 3.36 Room-temperature absorption spectrum of a GaInAs–InP superlattice consisting of 40 periods of 100 Å thick GaInAs wells and 200 Å thick InP barriers. Inset: photoluminescence spectrum of the same superlattice; $T = 5$ K, $P_{exc} = 0.8$ W cm^{-2}.

3.4.6 Negative differential resistance at room temperature from resonant tunnelling in GaInAs/InP double-barrier heterostructures

The principle of resonant tunnelling is shown schematically in figure 3.37. Quasi-bound states in a quantum well confined by two narrow barriers can be brought into coincidence with the Fermi energy of the doped region outside one barrier by the application of a voltage bias. There is a resonant increase in the tunnelling probability and hence current under these conditions. Further bias destroys the alignment and a negative differential resistance follows. In figure 3.38, we show current–voltage simulations for resonant tunnelling through 3 and 6 nm wide GaInAs wells bounded by 3 nm InP barriers. The model [74] used includes transport by tunnelling and thermionic emission. Depletion effects on the low-voltage side of the barrier have also been included. The position of the negative differential resistance reflects the energies of the bound states in the wells. A conduction-band offset of 530 meV has to be assumed [75].

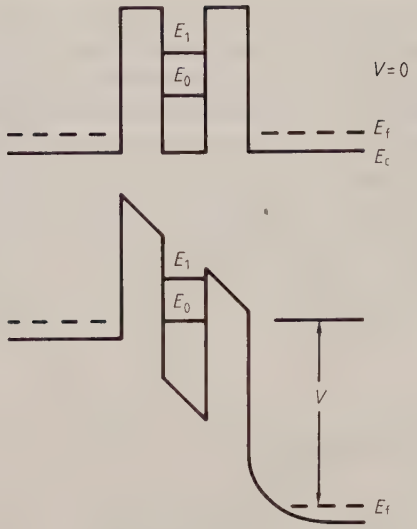

Figure 3.37 Conduction-band profile for a double-barrier resonant-tunnelling structure.

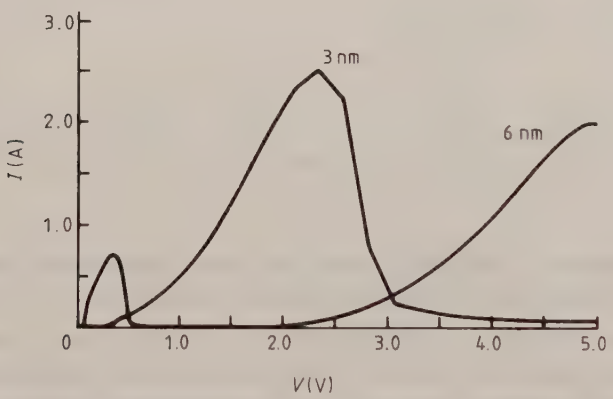

Figure 3.38 Resonant-tunnelling current–voltage simulations for 3 and 6 nm wide wells [166].

The layers in order of growth were as shown in figure 3.39. Boothroyd and Stobbs [76] have performed 'edge-on' transmission electron microscopy (TEM) characterization on a resonant-tunnelling structure of GaInAs–InP, viz. a 28 Å $Ga_{0.47}In_{0.53}As$ layer sandwiched between two InP layers of 36 Å thickness grown under the same conditions. Figure 3.39 shows 'edge-on' transmission electron microscopy characterization of this

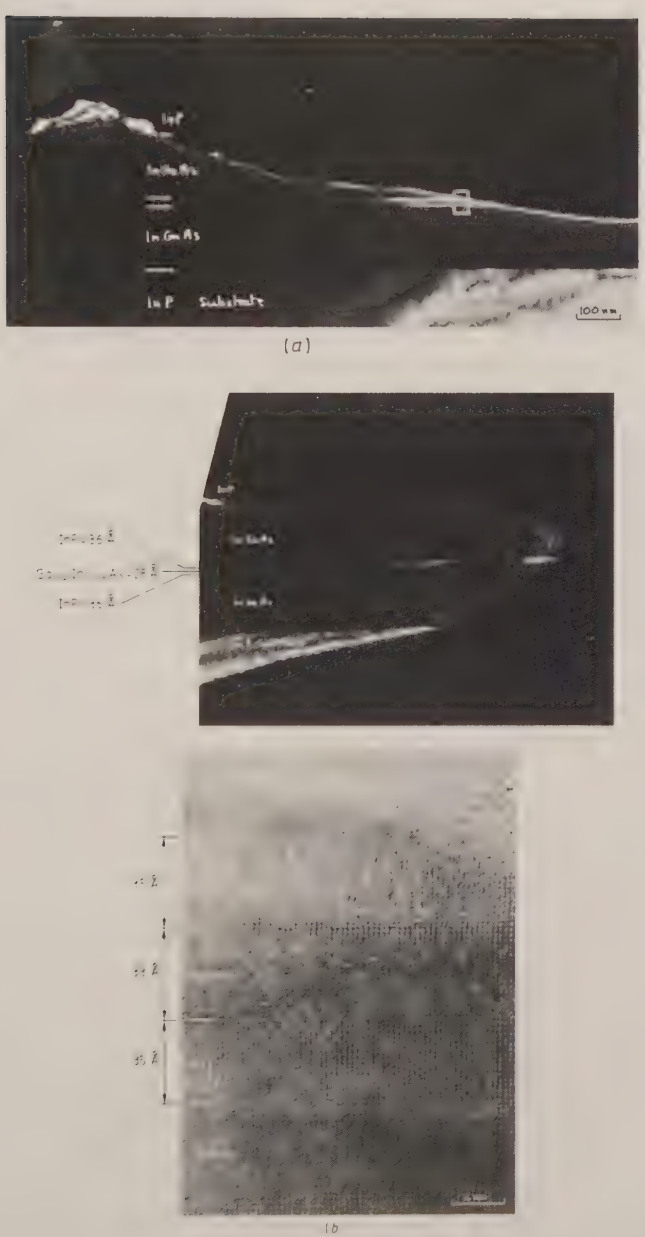

Figure 3.39 Edge-on transmission electron micrograph for a double-barrier resonant-tunnelling GaInAs–InP structure grown by MOCVD.

sample. The figure shows that the thickness of the triple layer is generally regular. The dark-field images at atomic resolution of another resonant-tunnelling structure, i.e. a 33 Å GaInAs layer sandwiched between two InP layers of 35 Å thickness grown by MOCVD, show that very thin epitaxial layers of GaInAs–InP of accurately controlled thickness and composition can be prepared by MOCVD. The material was processed into mesa diodes of 100 μm diameter with ohmic contacts to back and front formed using Au–Ge: Au metallization and transient alloying.

For those samples which in TEM showed a marked variability of barrier and well thickness (see for example figure 3.39) no negative-differential-resistance effects were observed. For a wafer which TEM indicated to have more uniform layering, and a well thickness within 10% of that specified, negative-resistance effects were observed.

The results achieved with pulsed I–V measurements are shown in figure 3.40. The presence of a thermionic emission contribution to the current at room temperature reduces the peak-to-valley ratio from the high values expected on the basis of resonant tunnelling alone. It is also possible that interface roughness and alloy scattering in the GaInAs contribute to the reduction of the peak-to-valley ratio, since inhomogeneities will destroy the coherence needed for resonant tunnelling. The voltage at which the negative differential resistance occurs agrees with the model calculations shown in figure 3.38.

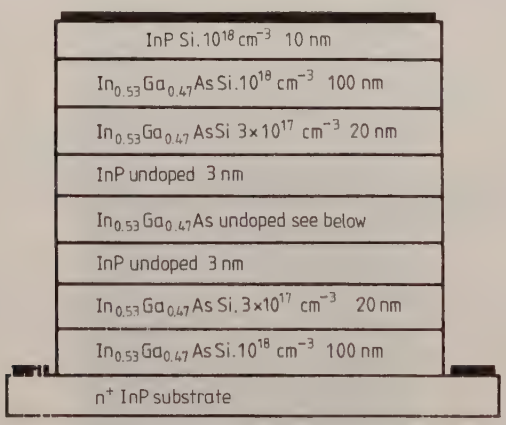
InP Si. 10^{18} cm^{-3} 10 nm
$In_{0.53}Ga_{0.47}As$ Si. 10^{18} cm^{-3} 100 nm
$In_{0.53}Ga_{0.47}As$ Si 3×10^{17} cm^{-3} 20 nm
InP undoped 3 nm
$In_{0.53}Ga_{0.47}As$ undoped see below
InP undoped 3 nm
$In_{0.53}Ga_{0.47}As$ Si. 3×10^{17} cm^{-3} 20 nm
$In_{0.53}Ga_{0.47}As$ Si. 10^{18} cm^{-3} 100 nm
n^+ InP substrate

Sample	Well thickness
539	3 nm
540	3
546	6

Figure 3.40 Double-barrier structure grown by MOCVD. Well widths of samples are shown.

3.5 MAGNETOTRANSPORT IN GaInAs–InP HETEROJUNCTIONS GROWN BY MOCVD

3.5.1 Shubnikov–de Haas and quantum Hall effects

The study of the Shubnikov–de Haas and quantum Hall effects (QHE) is one of the most useful and direct ways of characterizing semiconductor heterostructures. At low temperatures a two-dimensional gas of carriers bound in a heterostructure acts like a metal with a small Fermi energy, typically of order 10–100 meV. The magnetic field causes a quantization of the free-carrier states into a ladder of Landau levels (see [77]). Changing the magnetic field sweeps the level through the Fermi energy, causing oscillations in the magnetoresistance, known as the Shubnikov–de Haas effect. Since the cyclotron motion induced by the field is in the plane perpendicular to its direction, this means that a two-dimensional system is sensitive only to the component of the field parallel to the surface normal, so that rotation of the sample relative to the field can be used to provide a direct proof of the two-dimensional nature of any system under investigation. In the presence of a magnetic field, the energy of the Landau levels will increase linearly with field:

$$E(n_L, n) = (n_L + \tfrac{1}{2})\hbar\omega_c + E_n \tag{3.13}$$

where the Landau quantum number n_L takes integer values 0, 1, 2, 3, ... and E_n is the bottom of the sub-band n.

The degeneracy of a state with given quantum numbers n_L and n will also be proportional to the field. It is given by $2eB/h$.

By increasing magnetic field, the Fermi energy will therefore remain approximately constant, and the Landau levels will be swept upwards through the Fermi energy. The density of states at the Fermi energy will thus vary, and the electrical conductivity, which depends upon the density of states within approximately kT of the Fermi energy, will show oscillations periodic in inverse magnetic field.

The density of states for a two-dimensional electron gas (2DEG) in a magnetic field is shown in figure 3.41. We can calculate the oscillation periodicity from the degeneracy of the Landau levels; this derivation requires only that the separation of the levels is large relative to their broadening, or that the broadening is symmetric.

The conductivity of the 2DEG in a high magnetic field is approximately proportional to the product of the number of electrons within about kT of the Fermi energy and the scattering rate. Both these quantities are proportional to the density of states at the Fermi energy, and so the conductivity is essentially proportional to the square of the density of states at the Fermi energy. The conductivity will therefore be a minimum when the Fermi energy lies between two Landau levels, so that an integral number of levels

are completely filled. This occurs when the electron density n satisfies

$$n = N(2eB/h) \qquad N = 1, 2, 3, \ldots \tag{3.14}$$

where N is the number of filled levels, as the degeneracy of a Landau level is $2eB/h$. Conductivity minima will thus be seen when

$$B = \frac{1}{N}\frac{nh}{2e} = \frac{B_F}{N} \tag{3.15}$$

where B_F is the fundamental field, and so the minima form a series periodic in $1/B$. For a general field direction at an angle θ to the normal to the 2DEG, the oscillation periodicity depends only upon $B\cos\theta$, and the two-dimensional electron concentration is given by

$$\begin{aligned} n &= (2e/h)B_F \cos\theta \\ &= (4.836 \times 10^{10})B_F \cos\theta \text{ cm}^{-2} \end{aligned} \tag{3.16}$$

where B_F is in tesla.

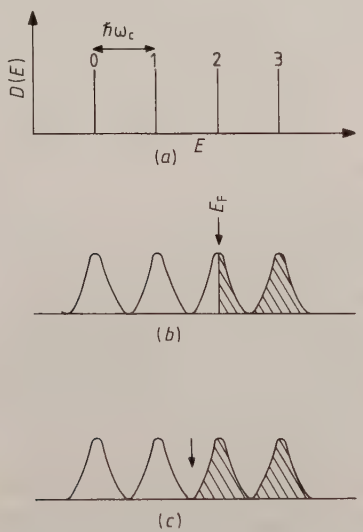

Figure 3.41 The density of states for a 2DEG in a magnetic field.

In figure 3.41(b), the Fermi energy lies within a half-filled Landau level; this is analogous to a half-filled band, and so the 2DEG behaves like a metal. In figure 3.41(c), the Fermi energy lies between a completely filled level and a completely empty one, and the 2DEG behaves like an insulator. The difference in the conductivity in these two situations can be a factor in excess of 10^9 [78]. The conductivity will thus oscillate strongly as a function of magnetic field.

Under a magnetic field, plateaux in the Hall resistance of a 2DEG (ρ_{xy}) appear, corresponding with a very high accuracy to the quantized values $\rho_{xy} = h/ie^2$, where $i = 1, 2, \ldots$, when the minimum of the magnetoresistance becomes very small. This quantum Hall effect (QHE) has been observed in modulation-doped $In_xGa_{1-x}As$–InP HJ with two populated electric sub-bands at zero magnetic field and low electron density $n_s \leqslant 5 \times 10^{11}$ cm^{-2} [79].

The $In_{0.53}Ga_{0.47}As$–InP HJ used were grown by low-pressure metall-organic chemical vapour deposition on (1 0 0) semi-insulating Fe-doped substrates. The InP layer, roughly 1000 Å thick, was n-type with $N_D - N_A \sim 3 \times 10^{15}$ cm^{-3}. The $In_xGa_{1-x}As$ layer was also n-type with $N_D - N_A \sim 2 \times 10^{15}$ cm^{-3}, its thickness being equal to 1 μm. Electrons are transferred from InP into $In_xGa_{1-x}As$ and an accumulation layer is formed at the interface [79]. The mobility of the 2DEG and the electron density at 4 K were obtained from low-field Hall measurements and are listed in table 3.5 for each sample. Standard Hall bridges were used to measure ρ_{xx} and ρ_{xy} between 1.3 and 4.2 K.

Table 3.5 Characteristics of the heterojunctions used in this work.

	Hall mobility (cm^2 V^{-1} s^{-1})			
Sample	300 K	77 K	4 K	n_s (cm^{-2}) at 4 K
S1	10 000	50 000	60 000	4.2×10^{11}
S2	11 800	55 000	70 000	5.4×10^{11}
S3	9 500	41 000	55 000	5.4×10^{11}

Figure 3.42(a) shows the B dependence of ρ_{xx} for sample S2 at low magnetic field ($B < 1$ T) applied perpendicular to the interface and at $T = 1.6$ K. Pronounced Shubnikov–de Haas oscillations are observed for $B > 0.2$ T and different oscillation periodicities appear clearly, which, we believe, originate from populated sub-bands E_0 and E_1 in the 2DEG. Figure 3.42(b) gives the reciprocal field corresponding to the oscillation maxima as a function of the Landau-level index. Two linear dependences are observed and are associated with the two periodicities in B^{-1}. From the slopes of the two linear variations, the populations $n_0 = 4.1 \times 10^{11}$ cm^{-2} and $n_1 = 1.1 \times 10^{11}$ cm^{-2} are calculated for E_0 and E_1, respectively. The total electron density $n_0 + n_1 = 5.2 \times 10^{11}$ cm^{-2} deduced from the Shubnikov–de Haas data is in good agreement with the value $n_s = 5.4 \times 10^{11}$ cm^{-2} obtained from low-magnetic-field Hall measurements at 4 K in sample S2. Using $m^* = 0.047m_0$ for the 2DEG effective mass, one finds Fermi energies

$E_{F,0} = 21$ meV and $E_{F,1} = 5.5$ meV, measured from the bottom of the two sub-bands E_0 and E_1, respectively. The sub-band separation is then approximately 15.5 meV and the higher sub-band E_1 starts to be occupied at $n_s \sim 3 \times 10^{11}$ cm^{-2}. Similar results are obtained in samples S1 ($n_0 = 3.5 \times 10^{11}$ cm^{-2}, $n_1 = 0.6 \times 10^{11}$ cm^{-2}) and S3 ($n_0 = 4.6 \times 10^{11}$ cm^{-2}, $n_1 = 0.9 \times 10^{11}$ cm^{-2}).

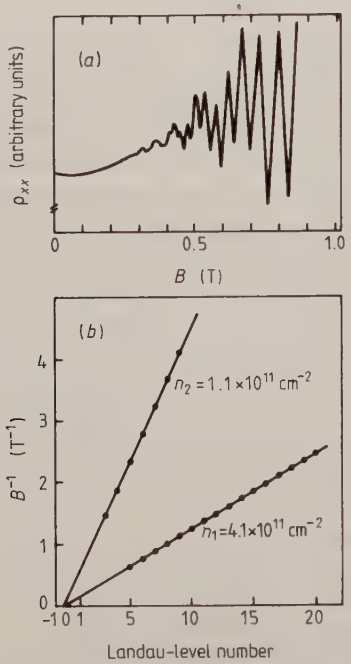

Figure 3.42 (*a*) Shubnikov–de Haas oscillations at low magnetic field ($B \leqslant 1$ T) in sample S2. $T = 1.6$ K, $\theta = 0$. (*b*) Reciprocal magnetic field at maxima of the high- and low-frequency oscillations versus the Landau index number.

The existence of two populated sub-bands gives rise to inter-sub-band scattering as calculated [80] and observed [78] in GaAs–$Al_xGa_{1-x}As$ HJ. The influence of inter-sub-band scattering can be demonstrated from magnetoresistance experiments with B parallel to the interface ($\theta = 90^\circ$). The effect of a parallel magnetic field is to increase the sub-band separation and, finally, to depopulate E_1 [81, 82]. Figure 3.43 shows the magnetoresistance ρ_{xx} as a function of B for $\theta = 90^\circ$ in sample S2, which exhibits a fall of about 60% in the resistance occurring at $B \sim 5$ T. This fall corresponds to the magnetic depopulation of the higher sub-band E_1 and to the reduction of the inter-sub-band scattering. Similar results were obtained [83] in $Al_xIn_{1-x}As$–$In_xGa_{1-x}As$ HJ and also in the resistance of GaAs–$Al_xGa_{1-x}As$ HJ as a function of the electron concentration [78].

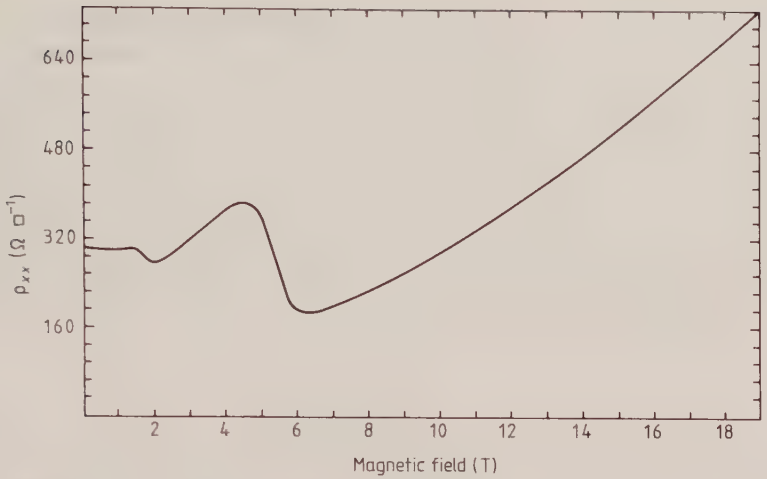

Figure 3.43 Magnetoresistance of sample S2 with B parallel to the interface. $T = 1.6$ K, $\theta = 90^{\circ}$.

Figure 3.44 shows ρ_{xx} and ρ_{xy} in sample S1 at 15 mK as a function of B applied perpendicular to the interface. Striking features are observed in ρ_{xy} compared to the usual QHE curves reported [84, 85] in similar samples with only one occupied sub-band. While the $i = 2$, 8 and 10 plateaux are well developed at $B \sim 10.3$ and 2.25 T, the $i = 4$ and $i = 6$ plateaux are nearly missing. Moreover, the width of the $i = 5$ plateau occurring at $B \sim 4.5$ T is anomalous. Indeed, in experiments previously reported on $In_xGa_{1-x}As$–InP HJ with similar values of n_s and electron mobility but with only one occupied sub-band, the $\rho_{xy} = h/5e^2$ plateau was not observed even at very low temperature, because the spin splitting of the $N = 2$ Landau level was not resolved. Remarkable features are also observed in the ρ_{xx} dependence as a function of the filling factor $\upsilon = n_s h/eB$. Figure 3.44 shows that ρ_{xx} minima occur for $\upsilon = 2, 5, 8, 10$ and 12 but only smaller structures are observed at $\upsilon = 4$ and 6. Furthermore, the best vanishing ρ_{xx} minimum occurs at $\upsilon = 2$. The anomalous behaviour of ρ_{xy} can be explained by the existence of two occupied electric sub-bands at $B = 0$. Figure 3.45 shows a schematic diagram of the Landau levels $N_{\pm}$ and $N'_{\pm}$ arising from the two occupied sub-bands E_0 and E_1, respectively. The calculations are done for $\theta = 0$ using 15 meV as the sub-band separation, $m^* \simeq 0.047 m_0$ [85] and an enhanced Landau factor [86] $g \sim 10$, independent of the Landau-level index and B. The resulting variation of the Fermi energy E_F, assuming infinitely sharp Landau levels, is also shown for a total electron concentration $n_s = 4.2 \times 10^{11}$ cm^{-2}. The middle of each ρ_{xy} plateau and the ρ_{xx} minima in figure 3.44 must correspond to vertical jumps of E_F from one level to the next one occurring for integral values of υ. Figure 3.45 shows that the two Landau levels $0'_+$ and 1_- overlap in the vicinity of $\upsilon = 4$, yielding no

significant jump of E_F. This is consistent with the absence of the $i = 4$ plateau in ρ_{xy} and the observation of a small dip instead of a real minimum in ρ_{xx} at $v \sim 4$ (figure 3.44). Similarly, the crossover of the 1_+ and $0'_+$ levels in the vicinity of $v = 3$ strongly perturbs the ρ_{xy} plateau whose value is significantly larger than $h/3e^2$. The well developed $i = 5$ plateau appears when the $0_\pm$, $1_\pm$ and $0'_+$ Landau levels are completely filled and corresponds to the jump of E_F from $0'_+$ to $0'_-$. Note that in previous experiments [84, 85] in $In_xGa_{1-x}As$–InP HJ with only one occupied sub-band, the $i = 5$ plateau would have corresponded to the jump of E_F between the two $N = 2$ spin components which are not experimentally [84, 85] resolved in samples with an electron mobility less than 70 000 $cm^2 V^{-1} s^{-1}$.

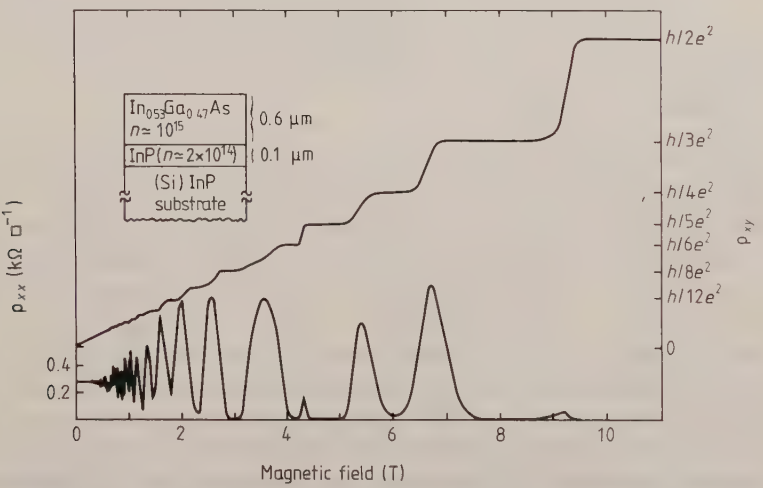

Figure 3.44 Shubnikov–de Haas and quantum Hall effects as a function of magnetic field normal to the 2D plane measured at $T = 0.045$ K.

Figure 3.45 shows that, in the case of S1, the $i = 6$ plateau would correspond to the spin splitting of $N = 2$ which, again, is weakly resolved. This is consistent with the weakness of the $i = 6$ plateau in ρ_{xy} and the ρ_{xx} minimum at $v = 6$ (figure 3.44). Finally, the $i = 8$ and $i = 10$ plateaux correspond to the usual situation when pairs of spin-split Landau levels are completely filled ($0_\pm$, $0'_\pm$, $1_\pm$, $2_\pm$ for $i = 8$ and $0_\pm$, $0'_\pm$, $1_\pm$, $2_\pm$, $3_\pm$ for $i = 10$). Note that, above 9 T, the sub-band E_1 is totally depopulated by the magnetic field (figure 3.45). The $i = 2$ plateau and the $v = 2$ minimum of ρ_{xx} in figure 3.44 correspond to the usual situation where only one sub-band is occupied. A complete redistribution of the energy levels is obtained in tilted magnetic fields ($\theta \neq 0$) since the Landau-level separation is determined only

by the B component perpendicular to the interface while the spin splitting comes from the total magnetic field. Figure 3.46 shows ρ_{xy} in sample S1 for $\theta = 45^\circ$. The $i = 4, 5, 6, 10$ and 12 plateaux are observed, but the $i = 8$ plateau is now missing. Again the result could be qualitatively interpreted with a schematic diagram of the Landau level arising from the sub-bands E_0 and E_1 at $\theta = 45^\circ$. For a more precise analysis of the results, it would be necessary to take into account the broadening of the Landau levels, the exact dependence of the effective g factor on B and N and, for $\theta \neq 0$, the shift of the E_0 and E_1 positions due to the introduction of a B component parallel to the interface.

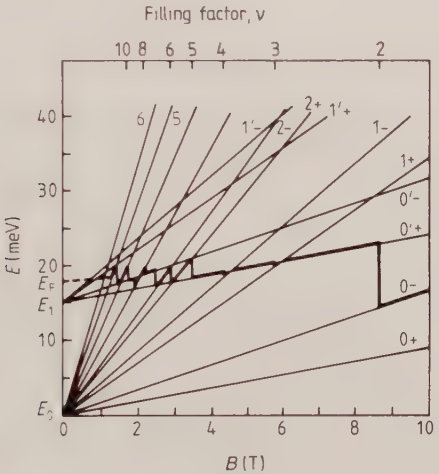

Figure 3.45 Schematic diagram of the Landau levels $N_\pm$ and $N'_\pm$ arising from the two ground sub-bands E_0 and E_1. (The subscripts + and − refer to spin up and down, respectively.) For the sake of simplicity, the spin splitting of the levels is not presented for $N \geqslant 3$. The variation of the Fermi energy E_F assuming infinitely sharp Landau levels and a constant electron concentration $n_s = 4.2 \times 10^{11}$ cm^{-2} is also shown (broken line).

3.5.2 Observation of a two-dimensional hole gas in a $Ga_{0.47}In_{0.53}As/InP$ heterojunction grown by MOCVD

The interest in two-dimensional (2D) hole systems has been spurred on by the considerable mobility enhancement attainable in modulation-doped GaAs/AlGaAs heterostructures. The first magnetotransport measurements demonstrating the two-dimensionality of the hole gas of a GaAs/AlGaAs interface were reported by Störmer and Tsang [87]. The integral and fractional quantum Hall effects were also observed [88–90], demonstrating

that these quantum phenomena are not limited to 2D electron systems and are independent of the host band structure.

One of the most outstanding features common to all 2D hole systems is the lifting of spin degeneracy due to the lack of inversion symmetry. This feature was predicted theoretically for holes in Si inversion layers [91, 92], and was also demonstrated by calculations for GaAs/AlGaAs interfaces [93, 94].

Magnetotransport studies have also been performed on a hole gas in a GaInAs–InP heterojunction [95].

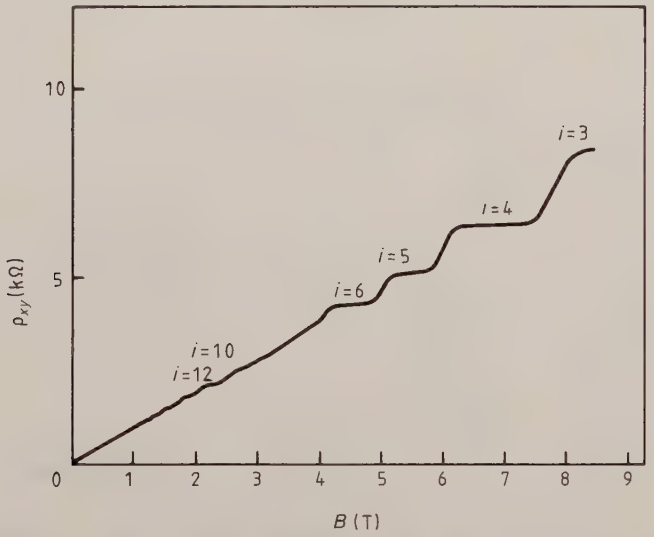

Figure 3.46 Hall resistance ρ_{xy} as a function of B for $\theta = 45^\circ$ at $T = 1.6$ K.

$Ga_{0.47}In_{0.53}As$/i-InP/p^+–InP heterojunctions were grown in an i-$Ga_{0.47}In_{0.53}As$/i-InP/p^+–InP configuration on an Fe-doped semi-insulating (1 0 0) 2° off InP substrate as shown in figure 3.47. The wide-gap InP layer was deliberately doped with Zn to a level $N_A - N_D \simeq 10^{17}$ cm^{-3} while the narrow-gap $Ga_{0.47}In_{0.53}As$ layer was not intentionally doped. The thickness of the InP (Zn-doped) layer was 1000 Å and the GaInAs layer was 0.5 μm thick. There was a 100 Å thick undoped InP layer as a spacer between doped InP and GaInAs layers (figure 3.47). Growth conditions were usual.

Figure 3.48 shows Shubnikov–de Haas (SdH) oscillations for various angles θ between the field direction and the normal to the interface. The ρ_{xx} extrema appear at constant values of the perpendicular component of the magnetic field $B_\perp = B\cos\theta$ (figure 3.49), demonstrating the two-dimensionality of the holes at the interface.

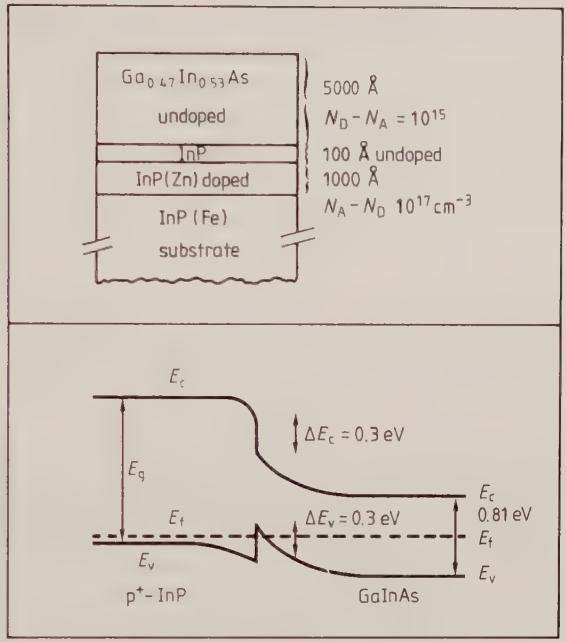

Figure 3.47 Schematic configuration of the heterojunction i-$Ga_{0.47}In_{0.53}As$/i-InP/p^+–InP.

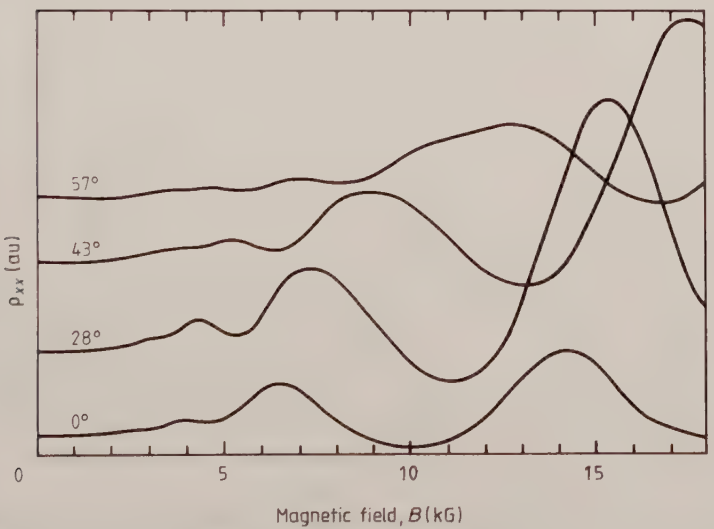

Figure 3.48 Longitudinal magnetoresistance ρ_{xx} of LP-MOCVD GaInAs–InP versus magnetic field for various angles at 4.2 K.

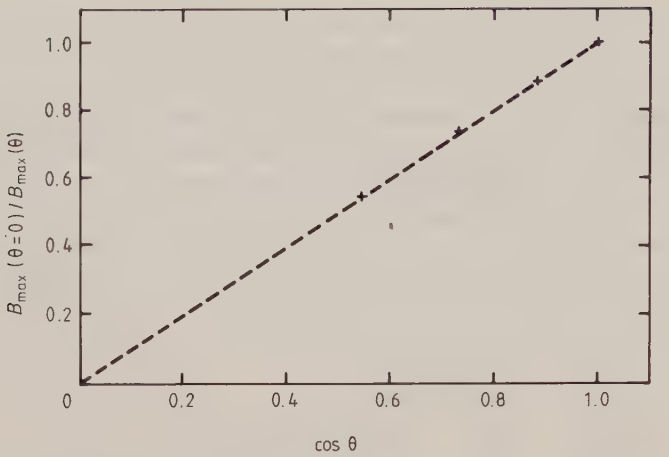

Figure 3.49 Angular dependence of the magneto-oscillations for the maximum $B_{max}(0) = 6.5$ T. $V_{max}(\theta)$ is the total field applied as the angle increases. Broken line corresponds to the theoretical prediction for 2D behaviour. LP-MOCVD GaInAs–InP, $T = 4.2$ K.

Figure 3.50 shows the diagonal resistivity ρ_{xx} and the Hall resistivity ρ_{xy} as functions of magnetic field at 4.2 K. One can distinguish the steps typical for QHE analyses which also confirm the two-dimensionality of the system under study. It is worth pointing out the relatively large width of the step $\rho_{xy} = h/3e^2$ corresponding to three entirely occupied single Landau levels. In the case of an electron system, plateaux with odd indices occur at lower temperatures and develop into narrower structures than those having even indices [96, 97]. This effect is attributed to a spin splitting of each Landau level. In contrast, the Hall plateaux observed in the hole system do not show this odd–even discrepancy [88]. This unique feature results from the lifting of the Kramers degeneracy of the 2D holes at the heterojunction interface and thus the splitting of each hole sub-band into two 'spin sub-bands' even without the presence of a magnetic field.

The standard plot of the index of maxima and minima in ρ_{xx} versus inverse field positions is shown in figure 3.51. The slope $S = 8.96$ T gives (assuming the lifting of the Kramers degeneracy) a carrier concentration $p = (e/h)S = 2.16 \times 10^{11}$ cm^{-2}. For $B > 10$ T $(1/B < 0.1\ \text{T}^{-1})$ the slope starts to change, but unfortunately the accessible magnetic field ranging up to 18 T is not sufficient to observe the minima corresponding to two partially filled and one entirely filled Landau levels and to determine the high-field SdH periodicity.

One can try to estimate the total density of the carriers from the QHE plateau $\rho_{xy} = h/3e^2$ and take the corresponding SdH minimum as a value of the magnetic field B_3 necessary for complete filling of the three single

Landau levels. Taking $p_{tot} = (e/h)NB_N$ and $NB_N = 3B_3 = 31.35$ T, we obtain $p_{tot} = 7.58 \times 10^{11}$ cm^{-2}. The carrier concentration deduced from low-field SdH oscillations is significantly smaller than that determined from either classical or quantum Hall measurements. This observation has been reported previously for a 2D hole gas in GaAs/AlGaAs [88, 89] and has been attributed to the existence of two hole 'spin sub-bands', degenerate at the Brillouin-zone centre, with different effective masses generating independent sets of Landau levels. At low fields, only the lighter mass is resolved. At sufficiently high fields all Landau levels are resolved and, independent of their energies, carry a degeneracy eB/h. If we follow the interpretation that the hole density measured at low magnetic fields represents only a fraction of the total density populating the spin-down sub-band [88, 98] then the hole concentration of the spin-up sub-band with heavier effective mass is $p_{hh\cdot} = 5.42 \times 10^{11}$ cm^{-2} and the population ratio $p_{hh\cdot}/p_{hh} = 2.5$. In a rough approximation this ratio can be treated as the ratio of the effective masses $m^*_{hh\cdot}/m^*_{hh}$. Our value $p_{hh\cdot}/p_{hh} = 2.5$ for $p_{tot} = 7.58 \times 10^{11}$ cm^{-2} is similar to those obtained for a 2D hole gas in GaAs–AlGaAs, which range between 1.8 and 3.3 for hole densities between 2.0×10^{11} and 1.15×10^{12} cm^{-2} [87, 89, 90]. This ratio has been found to increase with increasing carrier concentration, in agreement with recent calculations.

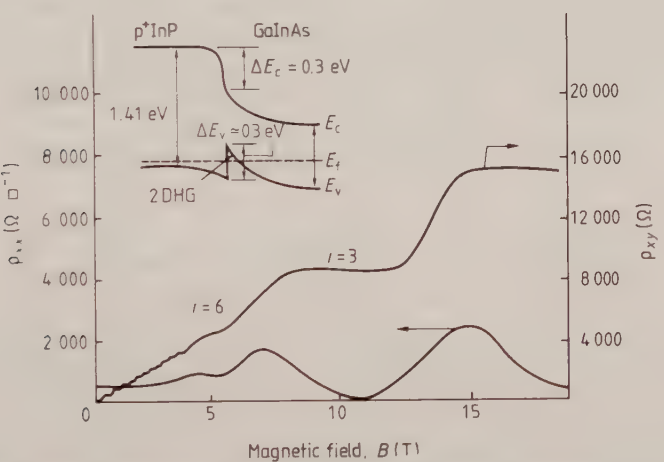

Figure 3.50 Shubnikov–de Haas $\rho_{xx}(\Omega\,\square^{-1})$ and Hall effect $\rho_{xy}(\Omega)$ measurements as functions of magnetic field recorded at 4.2 K.

In contrast to the case of a 2D hole gas in GaAs/AlGaAs heterojunctions [89, 99], a significant variation of the 2D hole concentration was found after illuminating the sample at low temperature (persistent photoconductivity effect) [100]. Figure 3.52 shows the SdH oscillations before and after

illuminating the sample. The index extrema in SdH patterns versus $1/B$ are presented in figure 3.51. An increase of the 2D hole density after illumination is evident. The densities of the holes in both spin sub-bands before and after illuminating the sample are represented in table 3.6.

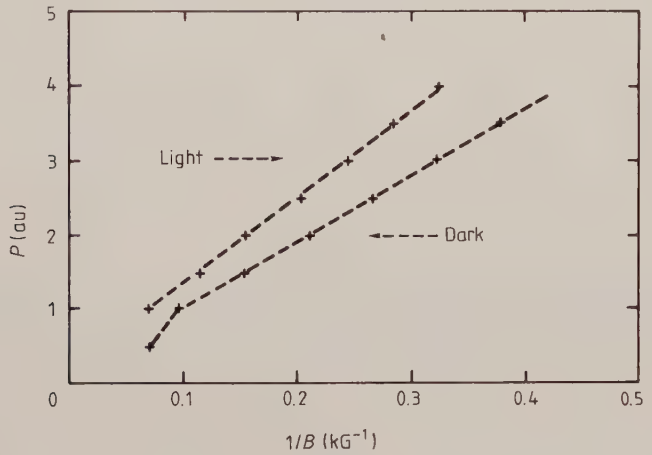

Figure 3.51 Standard plots of indices of extrema in ρ_{xx} of LP-MOCVD GaInAs–InP versus $1/B$ before and after illumination. The change in slope corresponds to a change in carrier concentration displaying persistent photoconductivity. Integral indices correspond to minima in ρ_{xx}, half-integral to maxima. Broken lines are just guides for the eye.

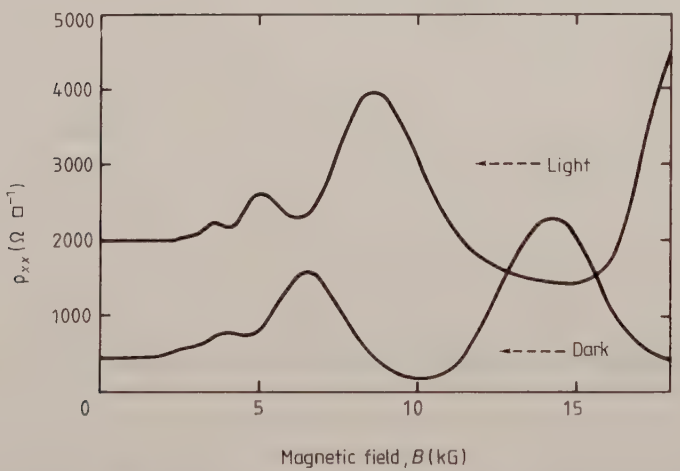

Figure 3.52 Shubnikov–de Haas $\rho_{xx}(\Omega\,\square^{-1})$ measurements of LP-MOCVD GaInAs–InP at 4.2 K in the dark and after illumination with a red light-emitting diode.

Table 3.6 Densities of the holes in both spin sub-bands before and after illuminating the sample.

	Before illuminating	After illuminating
p_H (cm^{-2})	6.31×10^{11}	8.67×10^{11}
p_{tot} (cm^{-2})	7.58×10^{11}	10.84×10^{11}
p_{hh^+} (cm^{-2})	5.42×10^{11}	8.00×10^{11}
p_{hh^-} (cm^{-2})	2.16×10^{11}	2.84×10^{11}
μ_H ($cm^2 V^{-1} s^{-1}$)	10450	7320
μ_{hh^+} ($cm^2 V^{-1} s^{-1}$)	6240	4100
μ_{hh^-} ($cm^2 V^{-1} s^{-1}$)	14850	10770
p_{hh^+}/p_{hh^-}	2.5	2.8
μ_{hh^-}/μ_{hh^+}	2.4	2.6

Considering the total hole concentration $p_{tot} = p_{hh^+} + p_{hh^-}$ and the value p_H obtained from low-field Hall measurements, one can see that p_H always underestimates the total hole concentration p_{tot}. Solving the equations which describe Hall density p_H and Hall mobility μ_H of a system consisting of two types of carriers with different mobilities, we can determine the relative mobilities μ_{hh^+} and μ_{hh^-}. Taking into account that for 2D hole spin sub-bands $p_{hh^+} > p_{hh^-}$ and $\mu_{hh^+} < \mu_{hh^-}$ we obtain

$$\mu_{hh^+} = \frac{\mu_H p_H}{p_{hh^+} + p_{hh^-}} \left\{ 1 - \left[\frac{p_{hh^-}}{p_{hh^+}} \left(\frac{p_{hh^+} + p_{hh^-}}{p_H} - 1 \right) \right]^{1/2} \right\} \tag{3.17}$$

and

$$\mu_{hh^-} = \frac{\mu_H p_H}{p_{hh^+} + p_{hh^-}} \left\{ 1 + \left[\frac{p_{hh^+}}{p_{hh^-}} \left(\frac{p_{hh^+} + p_{hh^-}}{p_H} - 1 \right) \right]^{1/2} \right\}. \tag{3.18}$$

The values of μ_{hh^+} and μ_{hh^-} calculated for two different total hole densities (before and after illuminating the sample) are presented in table 3.6.

It is worth noting that the mobility of the holes decreases with increasing density. This is in contrast to the behaviour of the impurity-scattering mobility of 2D electrons in a single sub-band.

Finally, the feasibility of confining a 2D hole gas in a GaInAs/InP interface and the expectation that the valence-band discontinuity $\Delta E_C \simeq \Delta E_V \simeq 0.3$ eV offer the possibility of generating alternating layers of 2D electron gas and 2D hole gas. Such 2D electron-gas and hole-gas structures could yield new physical phenomena as well as interesting device possibilities.

3.5.3 Precise quantized Hall resistance measurements in $In_xGa_{1-x}As$/InP heterostructures

The discovery of the quantum Hall effect offered metrologists a very remarkable means for establishing a resistance standard depending only on fundamental constants [101]: the Hall resistivity or resistance, ρ_{xy}, of a two-dimensional electron gas (2DEG) can take, in a high magnetic field and at low temperature, quantized values

$$R_H(i) = h/ie^2 \tag{3.19}$$

where h is the Planck constant, e the elementary charge and $i = 1, 2, \ldots$ the number of filled Landau levels of the 2DEG.

Several precise measurements [102–106] in metal-oxide semiconductor field-effect transistors (MOSFET) and/or $GaAs/Al_xGa_{1-x}As$ heterostructures have already demonstrated the excellent reproducibility, for a given laboratory and for a given experimental equipment, of the quantized Hall resistance $R_H(i)$. In [102], an agreement of $3 \times 10^{-8} \pm 3 \times 10^{-8}$ is reported for measurements of $R_H(i)$ made in the two kinds of devices.

However, the reproducibility from one laboratory to another, checked through the intercomparison of 1 Ω standards organized by the Bureau International des Poids et Mésures (BIPM, Sèvres), is not at present better than a few parts in 10^7. The observed differences are probably due mainly to random and systematic errors in the measurement of $R_H(i)$ in terms of the 1 Ω standards and, to a lesser extent, to the uncertainty of the 1 Ω intercomparison.

In this section, we present measurements of the quantized Hall resistance, made at LCIE over a 10-month time period, on an $In_xGa_{1-x}As$/InP heterostructure grown by LP-MOCVD with a double aim:

(1) to give further experimental confirmation of the universality of the quantum Hall effect by testing InP-based heterostructures;

(2) to measure $R_H(i = 2) \simeq 12\,906.4\ \Omega$ and $R_H(i = 4) \simeq 6453.2\ \Omega$, in terms of the four 1 Ω standard resistors which comprise Ω_{LCIE}, with a low uncertainty (2.2×10^{-8}) thanks to a specially designed resistance-ratio measurement bridge using a cryogenic current comparator (CCC) [107].

The sample consists of a 1000 Å thick InP buffer layer with carrier concentration of $N_D - N_A \simeq 3 \times 10^{15}\ cm^{-3}$ and a 1 μm $In_{0.53}Ga_{0.47}As$ layer with $N_D - N_A \simeq 2 \times 10^{15}\ cm^{-3}$. The Hall mobility of this sample was $11\,000\ cm^2\,V^{-1}\,s^{-1}$ at 300 K, $50\,000\ cm^2\,V^{-1}\,s^{-1}$ at 77 K and $60\,000\ cm^2\,V^{-1}\,s^{-1}$ at 4 K.

Figure 3.53 shows resistivity data ρ_{xx} and ρ_{xy} as a function of B, at 1.3 K, for this sample ($\mu = 60\,000\ cm^2\,V^{-1}\,s^{-1}$, $n \simeq 4.3 \times 10^{11}\ cm^{-2}$). In this sample the second electric sub-band (E_1) is populated for $B \leqslant 7.5$ T. This explains the unusual well marked plateau at about $h/5e^2$; four Landau levels of the first sub-band E_0 and one of the second (E_1, 0↑) are entirely filled.

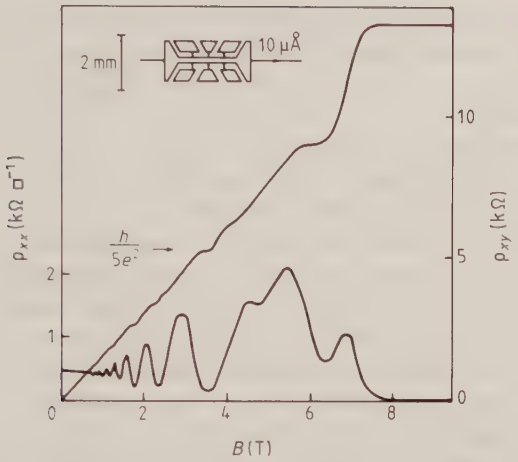

Figure 3.53 Resistivity data ρ_{xx} and ρ_{xy} at 1.3 K for an $In_{0.53}Ga_{0.47}As/InP$ heterostructure (MOCVD) growth technique ($n = 4.3 \times 10^{11}$ cm^{-2}, $\mu = 60\,000$ cm^2 V^{-1}s^{-1}).

We note here that, for $B \geqslant 7.5$ T, sub-band E_1 is entirely depleted and the $h/2e^2$ plateau is observed. Measurements of R_H on this plateau ($B \simeq 9$ T) are used for the precision measurement.

The experimental set-up (a specially designed resistance-ratio measurement bridge using a cryogenic current comparator) is described by Delahaye *et al* [107] and allows experiments with a 2.2×10^{-8} uncertainty. The $i = 2$ plateau, which is associated with the smallest minimum of ρ_{xx} ($\rho_{xx}^{min} \sim 10^{-3}$ Ω □$^{-1}$ at 1.3 K), was investigated between 2 and 1.3 K. The plateau is flat to better than $\pm 5 \times 10^{-8}$ over a 0.4 T range. The Hall resistance as a function of ρ_{xx}^{min} shows the linear variation

$$\rho_{xy}(\rho_{xx}^{min}) = \rho_{xy}(0) + 0.07\rho_{xx}^{min}. \tag{3.20}$$

A similar linear law was previously observed in GaAs–$Al_xGa_{1-x}As$ HJ and may be due, at least partly, to the misalignment of the Hall probes. The most interesting result is that the extrapolated value $\rho_{xy}(0)$ in non-dissipative conditions, i.e. at $\rho_{xx}^{min} = 0$, is the same, within experimental uncertainty, as the value obtained on GaAs–$Al_xGa_{1-x}As$ HJ. The value of $\rho_{xy}(0)$ is expected to be equal to the theoretical value $h/2e^2$. At 1.3 K, the correction $\Delta\rho_{xy}/\rho_{xy}(0)$ due to the finite value of ρ_{xx}^{min} is less than 10^{-8}.

3.5.4 Persistent photoconductivity and the quantized Hall effect in $In_{0.53}Ga_{0.47}As/InP$ heterostructures grown by MOCVD

The low-field transport of the 2DEG shows a persistent photoconductivity (PPC) for $T < 200$ K, similar to that observed in the GaAs–$Al_xGa_{1-x}As$

heterostructure [108, 109]. The persistent photoconductivity effect, in this case, is a consequence of increases in free electrons, due to photogeneration of electron–hole pairs in the heterostructure and trapping of the holes in the $In_{0.53}Ga_{0.47}As$ layer.

The heterostructure investigated by Tsui *et al* [110] consists of a 1500 Å thick n-type InP layer and a 1 μm thick undoped $In_{0.53}Ga_{0.47}As$ layer, sequentially grown on a semi-insulating InP substrate.

Figure 3.54 shows the temperature dependence of the electron density, obtained from the Hall coefficient using the one-carrier model, and the Hall mobility, obtained from the product of the conductivity and the Hall coefficient. The squares are from the dark; the crosses are from the data taken after the sample was exposed at 4.2 K to the light from a red light-emitting diode (LED). In the dark, the density is about 3.5×10^{11} cm^{-2} at 4.2 K and remains constant to better than $\pm 2\%$ for $T < 140$ K. Above 140 K, an exponential increase is observed, consistent with thermal activation of donor impurities in the InP, with an activation energy of approximately 7 meV. The mobility was $\mu = 3.5 \times 10^4$ cm^2 V^{-1} s^{-1} at 4.2 K and shows a slight increase with increasing T up to $T \simeq 60$ K, as expected from scattering of the 2DEG by screened impurity ions close to the interface. It begins to decrease above 60 K and follows an exponential decrease, consistent with scattering dominated by LO phonons [111].

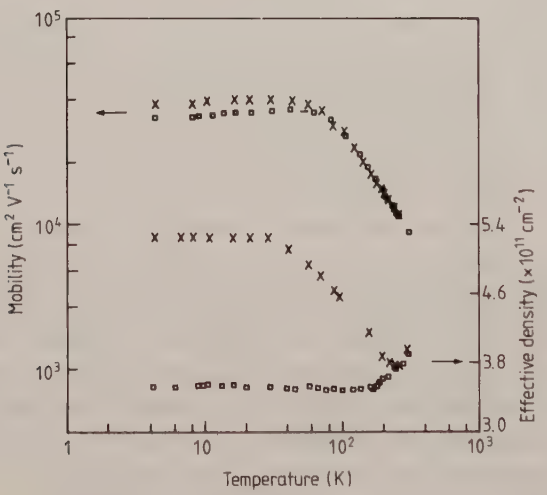

Figure 3.54 Temperature dependence of the electron mobility, from the product of the conductivity and the Hall coefficient, and the electron density, from the low-field Hall measurements, using the one-electron model. Squares (□) are data taken in the dark. Crosses (X) are taken after exposure to light from a $GaAs_{0.6}P_{0.4}$ LED at 4.2 K.

At 4.2 K, illumination with light from the red LED causes an increase of about 50% in the sample conductivity and this photoconductivity persists after the LED is turned off. As shown in figure 3.54, the electron density, after illumination, is increased to about 5.0×10^{11} cm^{-2} and it remains constant up to $T \simeq 40$ K. It starts to decrease at higher T and returns to its dark value for $T > 250$ K. The density decrease is due to the temperature dependence of the electron–hole recombination process. The mobility, on the other hand, shows a slight increase from its dark value for $T < 60$ K and no observable change at higher T. Thus, it is apparent that the observed persistent photoconductivity is due to an increase of free electrons in the heterostructure and the slight increase in mobility, below 60 K, is a result of the decrease in scattering of the 2DEG by screened impurity ions with increasing 2DEG density.

Similar persistent photoconductivity was previously observed in the transport of 2DEG in GaAs–$Al_xGa_{1-x}As$ heterostructures and the effect was attributed to photogeneration of DX centres in the $Al_xGa_{1-x}As$. More recently, the importance of electron–hole pair generation in the GaAs and their subsequent separation by the junction electric field was recognized [112]. Kastalsky and Hwang [113] concluded that the latter mechanism is in fact the dominant mechanism for the persistent photoconductivity observed in their samples.

However, InP is not known to have DX centres and the effect is interpreted as photogeneration of electron–hole pairs in the heterostructure and subsequent trapping of holes in the $In_{0.53}Ga_{0.47}As$. In figure 3.55, we show the data on the quantized Hall effect [114] at 4.2 K, under the influence of the infrared radiation from an $In_{0.53}Ga_{0.47}As$ LED which can create electron–hole pairs in the $In_{0.53}Ga_{0.47}As$ but not in the InP. In the dark, the $i = 4$ quantum Hall plateau (i.e. $\rho_{xy} = h/4e^2$) and its concomitant minimum in the diagonal resistivity ρ_{xx} are observed at $B \sim 3.5$ T. The 2DEG density obtained from the quantum oscillations is $n_{2DEG} = 3.5 \times 10^{11}$ cm^{-2}, in good agreement with that from the low-field Hall data. After illumination, two changes are apparent in the data shown in the lower two panels. First, the persistent photoconductivity is seen as decreases in the resistivity at $B = 0$. Secondly, an increase in the 2DEG density is seen as decreases in the period of the quantum oscillations and as corresponding shifts in the B field position of the quantum Hall plateaux. With excitation currents, $i_{LED} = 13$ and 29 μA, applied to the LED the $i = 4$ plateau is shifted to $B \sim 4$ and 4.8 T, indicating increases in the 2DEG density to $n_{2DEG} = 3.9 \times 10^{11}$ cm^{-2} and 4.8×10^{11} cm^{-2}, respectively. This increase in n_{2DEG} results from the photogeneration of electron–hole pairs in the $In_{0.53}Ga_{0.47}As$ and their subsequent separation by the heterojunction electric field (see inset of figure 3.56). While the electrons are added to the 2DEG, the holes are trapped, prohibiting them to recombine. It should be emphasized that there is no observable change in either the flatness of the

quantum plateau or the depth of the ρ_{xx} minima. This result is direct evidence that the illumination does not lead to any parallel conducting channels and there are no photo-induced free carriers in the InP. It differs from the 2DEG system in the $GaAs/Al_xGa_{1-x}As$ heterostructure, where illumination by infrared radiation of lower energy than both energy gaps is known to give rise to a parallel conduction channel in the $Al_xGa_{1-x}As$.

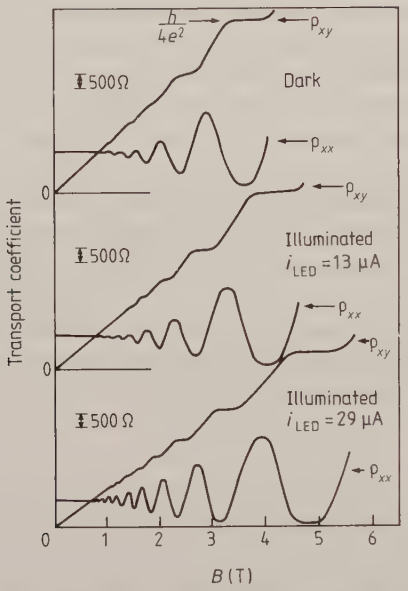

Figure 3.55 Quantum Hall effect measured in the dark (top), after exposure to a $Ga_{0.47}In_{0.53}As$ LED with current $i_{LED} = 13\ \mu A$ (middle) and with $i_{LED} = 29\ \mu A$ (bottom).

The increase of n_{2DEG} with increasing excitation current applied to the LED saturates when n_{2DEG} reaches about $5 \times 10^{11}\ cm^{-2}$. When the sample is under illumination with $i_{LED} \geqslant 1$ mA, the quantum oscillations begin to show an additional period, indicative of population of the higher sub-band, and the quantum Hall plateau begins to have extra structures. After the LED is turned off, these extra structures disappear and the 2DEG density, calculated from the quantum oscillations, remains $n_{2DEG} \sim 5 \times 10^{11}\ cm^{-2}$, independent of i_{LED}. This phenomenon is due to the fact that at saturation all the hole traps are filled and the additional electron–hole pairs generated at higher radiation intensities can contribute to charge transport only under the steady-state condition maintained by the illumination. The total number of traps in unit area obtained from the photo-induced n_{2DEG} is $1.5 \times 10^{11}\ cm^{-2}$. If we assume a uniform distribution in the $In_{0.53}Ga_{0.47}As$, we obtain a density of hole traps $n_t \sim 1.5 \times 10^{15}\ cm^{-3}$.

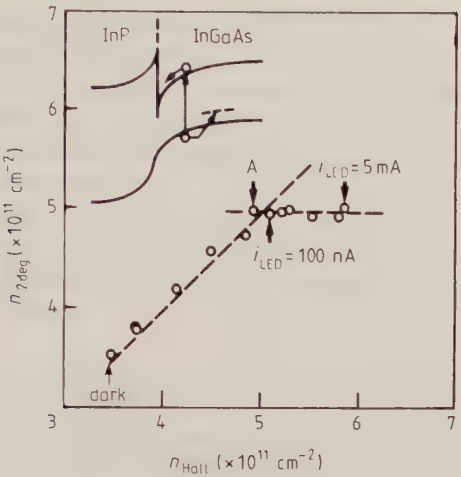

Figure 3.56 Electron density, from quantum oscillations, versus the density, from low-field Hall measurements, with different excitation currents applied to the LED. The inset illustrates the mechanism for the persistent photoconductivity. $In_{0.53}Ga_{0.47}As$–InP, $GaAs_{0.6}P$ LED, $T = 4.2$ K.

Finally, similar results are obtained with radiation from a red LED that can generate electron–hole pairs in both the InP and the $In_{0.53}Ga_{0.47}As$. When the excitation current $i_{LED} < 100$ nA, only shifts in the B field position of the quantum effects are observed. At higher excitation current, ρ_{xx} shows an increasing background with increasing B and extra structures appear in the quantized Hall plateau. Again, these extra structures disappear after the LED is turned off. Since the penetration depth of the light is comparable to the thickness of the $In_{0.53}Ga_{0.47}As$, penetration into the InP at high intensities can create electron–hole pairs in InP. However, due to the lack of available hole traps, they cannot contribute to the persistent photoconductivity. In figure 3.56, we show the results on n_{2DEG}, obtained from quantum oscillations, as a function of the density, obtained from the low-field Hall data. Each point is obtained using a different excitation current to the red LED. All the points to the right of A, obtained under illumination, return to point A after the LED is turned off. Again a saturation is observed at $n_{2DEG} \sim 5 \times 10^{11}$ cm^{-2}.

3.5.5 The effect of hydrostatic pressure on a $Ga_{0.47}In_{0.53}As$/InP heterojunction with three electric sub-bands

The GaInAs–InP heterojunction has been studied under hydrostatic pressures up to 15 kbar [115]. In the range of pressure available, Shubnikov–de Haas (SdH) as well as low-field Hall and quantum Hall effects

(QHE) (figures 3.57 and 3.58) at 4.2 K have been measured. The total electron concentration is deduced from high-field SdH measurements and from the position of the $n = 2$ plateau of the quantum Hall effect. The values are very close to those obtained by low-field Hall effect measurements, pointing out the fact that no parallel conduction is introduced (figure 3.59). For more accurate details the reader can refer to table 3.7, which summarizes the principal experimental results. The magnitude of the observed decrease of the total electron population agrees well with the pressure change of the conduction-band discontinuity ΔE_c if one assumes a constant conduction-band offset of 65%, i.e. $\Delta E_c = 0.65[E_{g2}(p) - E_{g1}(p)]$, and the triangular-well approximation.

N_0 and N_1, the populations of the ground and first excited sub-bands, are deduced from the two sets of low-field SdH oscillations. Figure 3.60 shows the dependence of N_S, N_0, N_1 and N_2 upon pressure.

A decrease of 0.95×10^{11} cm^{-2} in total population leads to a decrease of 0.64×10^{11} cm^{-2} for the ground sub-band and 0.31×10^{11} cm^{-2} for the first excited sub-band, the third sub-band keeping roughly the same population.

In order to confirm the population of the third sub-band even at high pressure we have applied a parallel magnetic field ($\theta = 90°$) (figure 3.61). Still at 15 kbar, we see a fall in resistance at about 1.5 T due to the suppression of inter-sub-band scattering, indicating that the E_2 sub-band is not entirely empty at zero magnetic field. Taking the experimental results (figure 3.61) we have extrapolated to $B = 0$ with a quadratic fit the part of the curve where only one sub-band is populated. This can give us an order of magnitude for the importance of inter-sub-band scattering in this sample

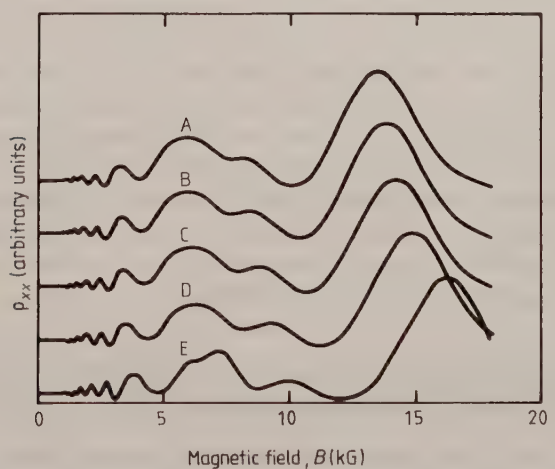

Figure 3.57 Shubnikov–de Haas recordings for five different pressures (kbar): A, 15; B, 12.1; C, 8.8; D, 4; E, 0.

(for detailed results refer to table 3.8). As can be seen, the contribution of inter-sub-band scattering decreases with increasing pressure.

The low-field Hall mobility of the 2DEG (figure 3.62) shows a decrease of about 30% for pressure up to 15 kbar. A fall in mobility of the same order of magnitude (28%) was observed earlier for pressures up to 8.8 kbar [116],

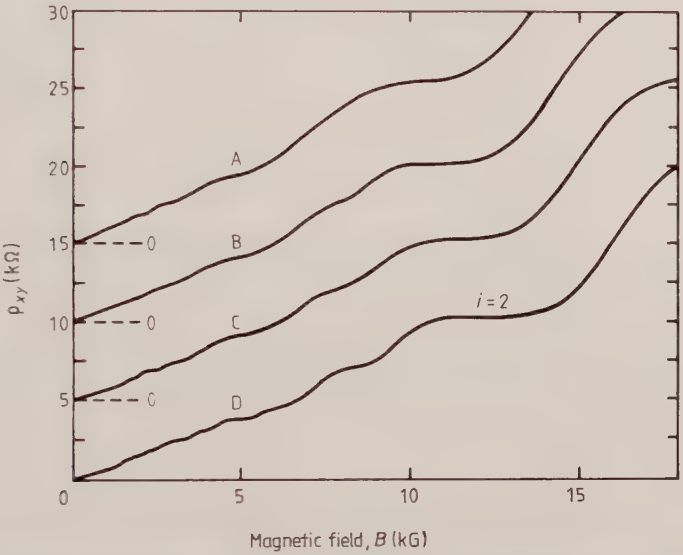

Figure 3.58 Quantum Hall effect for four different pressures (kbar): A, 15; B, 8.85; C, 4.2; D, 0. $T = 4.2$ K.

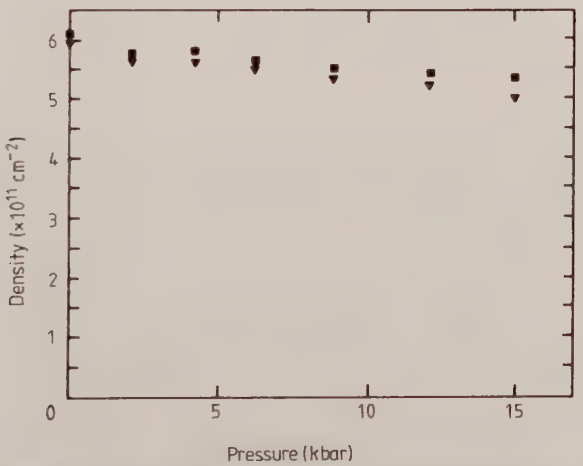

Figure 3.59 Comparison between total carrier densities obtained by Shubnikov–de Haas (■) and low-field Hall effect (▼) measurements.

Table 3.7 Effect of pressure on a GaInAs/InP heterojunction.

P (kbar)	N_H (10^{11} cm^{-2})	N_S (10^{11} cm^{-2})	N_0 (10^{11} cm^{-2})	N_1 (10^{11} cm^{-2})	N_2 (10^{11} cm^{-2})	$E_F - E_0$ (meV)	$E_F - E_1$ (meV)	$E_1 - E_0$ (meV)	$E_2 - E_1$ (meV)	$B_2^{\uparrow a}$ (T)	$B_1^{\uparrow b}$ (T)
0	6.06	6.04	4.39	1.27	0.38	21.6	6.3	15.3	4.9	1.7	5.55
2.2	5.75	5.73	4.29	1.22	0.22	20.7	5.9	14.8	4.5	1.625	4.85
4.2	5.82	5.67	4.22	1.18	0.27	20.0	5.6	14.4	4.3	1.575	4.55
6.2	5.65	5.62	4.11	1.15	0.28	19.1	5.4	13.7	4.1	1.5	4.425
8.85	5.57	5.39	4.10	1.11	0.18	18.6	5.0	13.6	3.8		
10.1										1.475	4.275
12.1	5.49	5.31	3.96	1.04	0.31	17.4	4.6	12.8	3.4	1.425	4.1
15.4	5.43	5.09	3.75	0.96	0.38	16.0	4.1	11.9	2.9	1.4	4.0

[a] $B_2^{\uparrow}$ is the parallel magnetic field at which E_2 is depopulated.
[b] $B_1^{\uparrow}$ is the parallel magnetic field at which E_1 is depopulated.

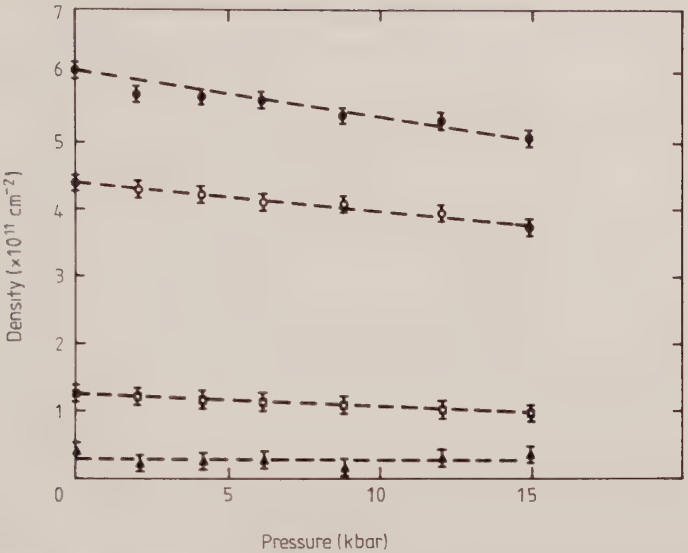

Figure 3.60 Evolution of the population of the different sub-bands as well as total electron concentration versus pressure.

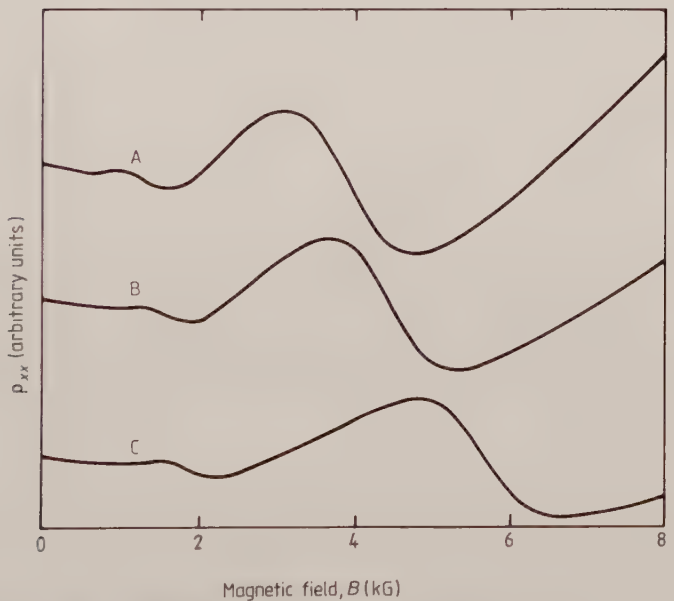

Figure 3.61 Resistivity as a function of parallel magnetic field for different pressures (kbar): A, 15; B, 6; C, 0.

Table 3.8

P (kbar)	$R(\Omega\,\square^{-1})$ $B=0$	$R'(\Omega\,\square^{-1})$ (extrapolated) $B=0$	$(R-R')/R$
0	298.4	127	0.574
2.2	357	153	0.571
4.2	393	172	0.562
6.2	432.8	193	0.554
10.1	482.4	245	0.492
12.1	535	275	0.486
15.4	587.8	310	0.471

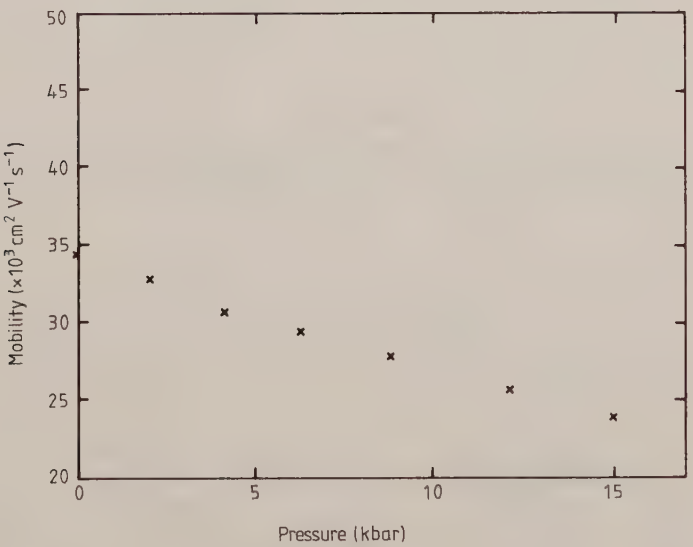

Figure 3.62 Hall mobility versus pressure at 4.2 K up to 15 kbar.

but in a sample displaying strong parallel conduction. The value of resistivity extrapolated to $B=0$ for the case when only one sub-band is populated (taken from parallel magnetic field measurements) gives a decrease of 50%.

3.5.6 Cyclotron resonance

Cyclotron resonance is the resonant absorption of light which occurs when the incident photon energy is equal to the separation between adjacent Landau levels. The resonance condition

$$\hbar\omega = \hbar\omega_c = \hbar eB/m^* \tag{3.21}$$

where ω is the frequency of the incident radiation, allows the effective mass of the electrons to be deduced.

Cyclotron resonance transitions are limited by the selection rule $\Delta n_L = \pm 1$, and so only one resonance should be seen. However, in two-dimensional systems short-range scattering can mix the Landau levels and cause additional resonances to appear [117].

Cyclotron resonance experiments described in these heterojunctions are performed by observing the transmission by the sample of fixed-frequency far-infrared (FIR) radiation as a function of magnetic field [124]. The FIR sources were the H_2O (118 μm, 78.5 μm), D_2O (171.6 μm), HCN (336.6 μm, 310.9 μm) and DCN (194.8 μm, 190 μm) molecular lasers and carcinotrons ($\lambda = 1.2$ mm, 760 μm). The detectors are semiconductors which exhibit photoconductivity in the far-infrared at 4.2 K due to excitations within the impurity bands.

The far-infrared transmission is studied at fixed photon wavelength by varying the magnetic field applied tilted or normal to the surface of the sample. The finite width of the resonance peak can be explained by the fact that the transitions induced by the incident light occur between broadened Landau levels. Ando and Uemura [118] showed that the presence of short-range scatterers in the system causes, even at $T = 0$ K, a broadening in energy Γ of the states, which can be related to the mobility μ of the electron gas, and to the magnetic field, by the relation

$$\Gamma = \frac{eh}{m^*} \left(\frac{2}{\pi} \frac{B}{\mu} \right)^{1/2}. \tag{3.22}$$

In that case, we expect the cyclotron resonance halfwidth $\Delta B_{1/2}$ to depend on the resonant magnetic field inducing the Landau-level quantization according to a law of the form

$$\Delta B_{1/2} = \alpha \, (B/\mu)^{1/2} \tag{3.23}$$

where α is a constant exhibiting the proportionality between $\Delta B_{1/2}$ and Γ. It has been found, in two-dimensional systems with mobilities similar to those of our samples, such as MOS silicium [119] and a GaAs/GaAlAs heterojunction [120], that the relation (3.23) was remarkably verified, especially at low magnetic fields, when the assumption of short-range scatterers is fairly good. These different authors agreed in finding $\alpha = 0.63 \pm 0.02$.

Furthermore, with a detailed study of the cyclotron line for two-dimensional systems, Ando has predicted quantum oscillations in the main resonance peak [121], which were experimentally reported [119, 120] in the two previous systems. These beats are a consequence of the modulation of the resonance amplitude, as the Landau levels cross the Fermi level. They are clearly resolved at low magnetic fields, when many of the Ando oscillations occur along the cyclotron absorption line.

It is clear that they appear only within the region of the cyclotron

resonance, because they arise from a variation in the resonance amplitude. Like Shubnikov–de Haas oscillations of the longitudinal component ρ_{xx} of the resistivity tensor, they are periodic in $1/B$ with a periodicity $\Delta(1/B)$, and still allow us to deduce the electronic density, namely

$$n = 2eh^{-1}[\Delta(1/B)]^{-1}. \tag{3.24}$$

In a normal configuration (magnetic field orthogonal to the surface of the sample), a cyclotron resonance experiment performed on a system exhibiting multi-sub-band transport cannot show hybrid transitions between Landau levels of different sub-bands.

The presence of a parallel magnetic field $B_\parallel$ introduces non-null terms in the overlapping matrix element, so that such hybrid transitions appear possible [117]. All spectra have been realized at $T = 1.6$ K, by varying the magnetic field in the range 0–8 T.

Figure 3.63 shows a typical cyclotron line at $\lambda = 756\ \mu$m with magnetic field applied normal to the sample for a $Ga_{0.47}In_{0.53}As/InP$ heterojunction exhibiting two occupied electric sub-bands (see following section), with respective populations $n_0 \simeq 4.2 \times 10^{11}\ cm^{-2}$ and $n_1 \sim 1.2 \times 10^{11}\ cm^{-2}$ deduced from Shubnikov–de Haas oscillations of the longitudinal resistivity ρ_{xx}. The effective mass, deduced from the plot of the resonance magnetic field, as a function of the pulsation of the incident wave, is constant. One finds $m^* = (0.047 \pm 0.001)m_0$, where m_0 is the electron mass, in good agreement with work on the same type of heterojunction [122, 123].

Quantum oscillations are clearly evidenced in the region of the cyclotron resonance (CR). They are periodic in $1/B$, with a period of about $\Delta(1/B) = 0.129\ T^{-1}$. The electronic density, deduced from equation (3.24), is $n \simeq 4 \times 10^{11}\ cm^{-2}$. It corresponds quite well to the population of the ground sub-band.

We have shown as an inset the plot of the halfwidth at half-minimum $\Delta B_{1/2}$ of the resonance cyclotron line, as a function of the square root of the resonance field, namely $B_r^{1/2}$. The evolution appears almost linear, in good agreement with equation (3.23). Hall measurements gave a (relatively high) mobility, at 4 K, of about $\mu \simeq 40\,000\ cm^2\ V^{-1}\ s^{-1}$. Putting this value into equation (3.23) we find a proportionality constant $\alpha \simeq 0.60$, by fitting the linear relation. It is worth noting that the same factor is found in all the two-dimensional systems experienced: Si MOS, GaAs/GaAlAs and $Ga_{0.47}In_{0.53}As/InP$. It further confirms the validity of the theoretical prediction of the broadening of Landau levels with magnetic field.

Figure 3.64(*a*) exhibits the CR line in a tilted configuration at a wavelength of 164 μm. There is an angle of $\theta = 45^\circ$ between the applied magnetic field and the surface of the sample.

A first resonance is resolved at $B_r \simeq 4.7$ T. It is deduced from normal cyclotron resonance, with a component of magnetic field normal to the surface of the sample: $B_\perp = B_r \cos\theta$. This further evidences the two-

dimensionality of the system under study. At about $B = 5.9$ T there appears a second absorption peak attributed to a hybrid transition between the $n = 1$ Landau level of the ground electric sub-band and the $n = 0'$ Landau level of the first excited one. In order to explain this peak, the evolution of the Landau levels of the two sub-bands, as a function of magnetic field, for $\theta = 45°$, has been plotted in figure 3.64(b). The energy level E_0 of the ground sub-band has been taken as a reference. The energy difference $(E_1 - E_0) \simeq 15$ meV between the two sub-bands at zero magnetic field has been derived from their respective populations n_0 and n_1.

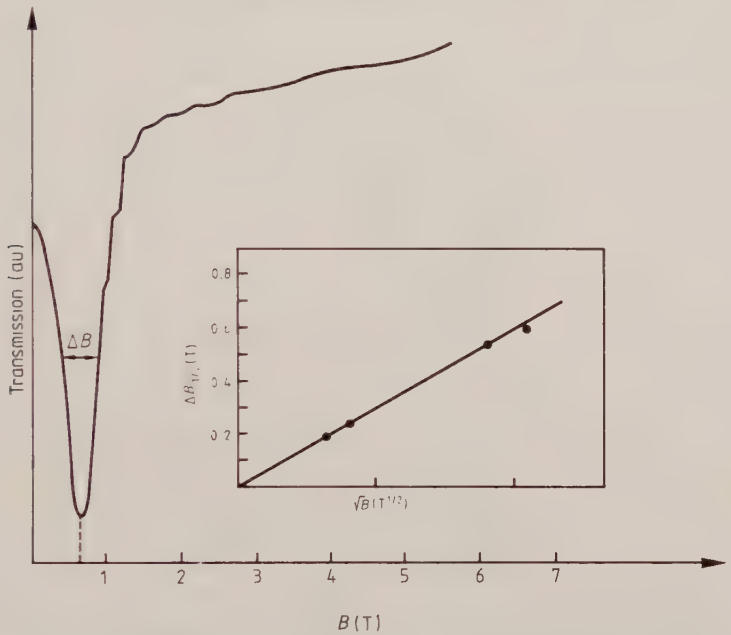

Figure 3.63 Cyclotron resonance spectrum of an LP-MOCVD $Ga_{0.47}In_{0.53}As/InP$ heterojunction at $T = 1.6$ K, for $\lambda = 756$ μm. Inset: CR linewidth $\Delta B_{1/2}$ versus square root of the resonance magnetic field.

The effect of a parallel component of the magnetic field $B_\parallel = B_T \sin\theta$ is to increase this energy gap. It has been shown [124] that this diamagnetic shift follows the equation

$$\Delta(E_1 - E_0) = \frac{e^2 B_\parallel^2}{2m}[(\Delta z_1)^2 - (\Delta z_0)^2] = \eta B_\parallel^2 \tag{3.25}$$

where $(\Delta z_i)^2 = \langle z^2 \rangle_i - \langle z \rangle_i^2$ is the spread of the wavefunction, perpendicular to the interface, for the ith sub-band. The coefficient η has been determined experimentally, by observing the depopulation of the level of energy E_1 under the effect of a parallel magnetic field [117, 125]. Depopul-

ation of the first excited sub-band manifests itself by a fall in resistance due to the elimination of inter-sub-band scattering.

This has been retained in figure 3.64(*a*) to determine the evolution of the $n = 0'$ and $n = 1'$ Landau levels relative to the ground sub-band. The arrows represent the FIR transition experimentally observed for $\lambda = 118$, 164 and 255 μm. The evolution of the Fermi level is also shown as a darker line. The $B = 5.9$ T peak, exposed in figure 3.64 for $\lambda = 164$ μm, can be well explained by an $n = 0 \rightarrow n = 1'$ transition. Such a hybrid absorption has been observed, as well, for $\lambda = 118$ μm at $B_r = 3.33$ T, and can be attributed to an $n = 2 \rightarrow n = 1'$ transition, as shown in figure 3.64(*a*).

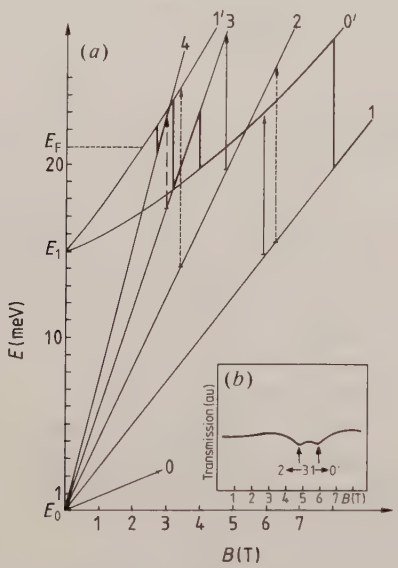

Figure 3.64 (*a*) Evolution of the energy of the Landau levels, for a $Ga_{0.47}In_{0.53}As/InP$ heterojunction, with two occupied electric sub-bands, assuming an angle $\theta = 45^\circ$ between the magnetic field and the normal to the surface of the sample. $\lambda = 118$ μm (———), 164 μm (_____) and 255 μm (— · —). (*b*) Cyclotron resonance spectrum in this configuration for $\lambda = 164$ μm.

Cyclotron resonance experiments have been performed [126] using a number of different infrared laser wavelengths from 337 to 78.6 μm, over the temperature range 15 to 150 K. Direct transmission was measured as a function of magnetic field in the Faraday geometry, and some typical experimental recordings are shown in figure 3.65.

The magnetic field positions of the resonances were then used to calculate the effective mass of the electrons. Figure 3.66 shows plots of the

temperature dependence of the effective mass for a number of different laser frequencies. The mass is found to increase with both increasing temperature and laser frequency. The data were then extrapolated to give the effective mass at 0 K for each different laser frequency. This procedure ensures that a value is obtained for m^* when only the lowest Landau level is populated. The variation of the 0 K effective mass as a function of laser energy is shown in figure 3.67. The effective mass obtained varies linearly with magnetic field. The data may again be extrapolated to zero energy to give the band-edge mass. The slope of the mass variation as a function of energy and temperature may then be used to provide a measurement of the band non-parabolicity. This is discussed in detail below, and is compared with three-band $k \cdot p$ theory [127]. The best value of the band-edge effective masses for n-$Ga_{0.47}In_{0.53}As$ are found to be in agreement with the earlier values given by Portal *et al* [128] and Nicholas *et al* [129].

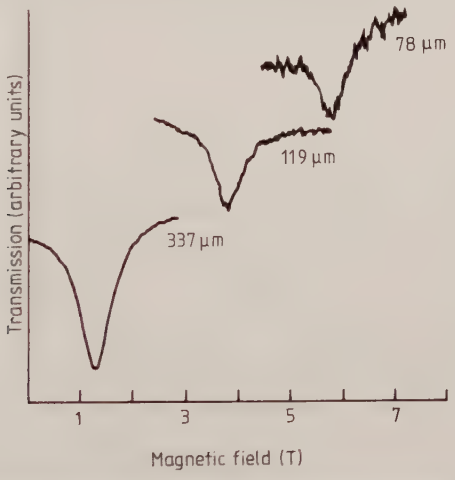

Figure 3.65 Experimental recordings of the transmission of 337, 119 and 78 μm radiation by $Ga_{0.47}In_{0.53}As$ as a function of magnetic field, for sample 85.

The same sample of $Ga_{0.47}In_{0.53}As$ was used in the magnetophonon as in the cyclotron resonance experiment. Typical experimental recordings are shown in figure 3.68. It is clear that oscillatory structure observed in sample 85 is not quite as simple as that observed in the components InAs and GaAs [130]. In these materials a single series of oscillations is observed at magnetic fields satisfying the magnetophonon resonance condition

$$N\hbar\omega_0 = \hbar\omega_{LO} \tag{3.26}$$

where ω_{LO} is the LO-phonon frequency.

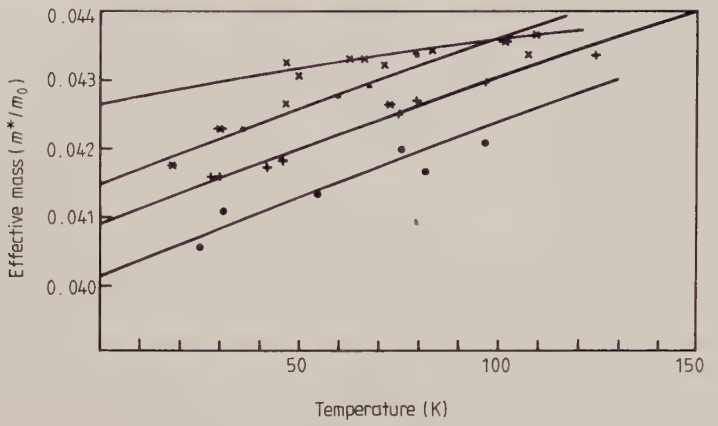

Figure 3.66 Plots of the temperature variation of the effective mass for different laser frequencies for sample 85: (X) 79 μm; (*) 119 μm; (•) 337 μm.

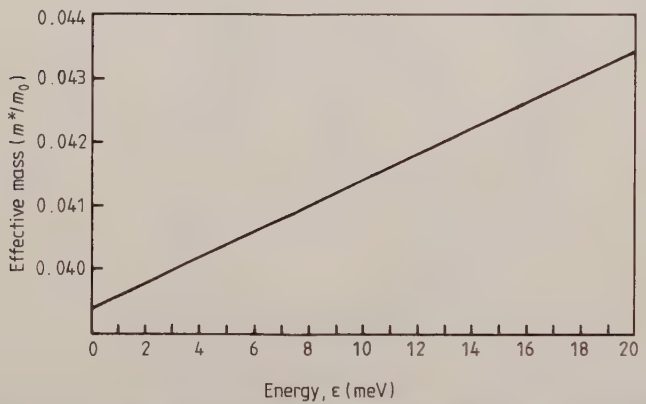

Figure 3.67 The dependence of the effective mass for sample 85 upon laser energies, as determined from the values extrapolated to zero temperature, given in figure 3.66.

The oscillatory structure in sample 85 may be interpreted as due to the presence of two close series of oscillations each determined by equation (3.26) with fundamental fields differing by only 10%. Two series of magnetophonon oscillations in GaInAs originate from two phonon modes in the alloy system. These are 'GaAs'-like and 'InAs'-like modes. This is a clear contradiction of the suggestion by Pearsall *et al* [131] that only one LO-phonon mode exists in this alloy. It was not possible to resolve the 'InAs' mode in the MBE samples, which have only one series of magnetophonon oscillations originating from the GaAs-like mode.

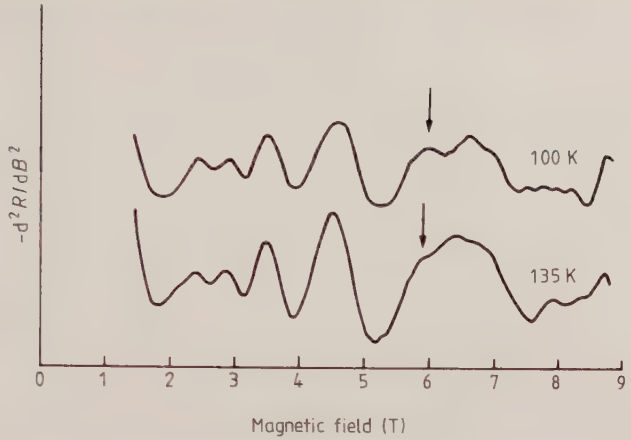

Figure 3.68 Experimental recordings of the magnetophonon oscillations in the second derivative of the magnetoresistance in sample 85. The splitting of the higher-field peak into two LO-phonon peaks is shown by the arrow.

The magnetophonon oscillations observed in $Ga_{0.47}In_{0.53}As$ obey equation (3.26) where $\hbar\omega_c$ is given by a suitably defined effective mass. Thus one may use this relation to calculate either the effective mass or the phonon frequencies by the assumption of the other. Results for the magnetophonon oscillations in the sample are given in table 3.9 using the phonon frequencies measured by Brodsky and Lucovsky [132].

The variation of the cyclotron effective mass as a function of laser energy is a consequence of the non-parabolicity of the conduction band. When the electrons are further into the conduction band, the effective mass is found to increase, as shown in figure 3.68, as a result of the non-linear variation of the Landau levels with applied magnetic field.

The general variation in the effective mass can be written as [127]

$$\frac{1}{m^*(E)} = \frac{1}{m_0^*}\left[1 + \frac{2K_2}{E_g}\left(\tfrac{1}{2}kT + \hbar\omega_c + \frac{\hbar\omega_c}{\exp(\hbar\omega_c/kT) - 1}\right)\right] \tag{3.27}$$

where the constant K_2 is given by

$$K_2 = -\left[(1 + \tfrac{1}{2}x^2)/(1 + \tfrac{1}{2}x)\right](1 - y)^2 \tag{3.28}$$

with

$$x = [1 + (\Delta/E_g)]^{-1} \qquad \text{and} \qquad y = m^*/m_0 \tag{3.29}$$

where E_g is the band gap and Δ is the spin–orbit splitting. In addition to the band non-parabolicity, the resonant polaron contribution to the effective mass increases as the laser frequency increases towards the LO-phonon frequency (ω_{LO}), as has been calculated by Larsen [133]. This can be

Table 3.9 The magnetophonon series fundamental fields and effective masses.

Sample	Temperature (K)	InAs phonon			GaAs phonon		
		NB_N^* (T)	$\hbar\omega_{LO}$ (cm^{-1})	$m^*_{mpr}(BE)$	NB_N^* (T)	$\hbar\omega_{LO}$ (cm^{-1})	$m^*_{mpr}(BE)$
85	97	11.25	235	0.041	12.61	271	0.040

NB_N^* is the fundamental field measured for the series.
$m^*_{mpr}(BE)$ is the experimental magnetophonon mass after the non-parabolic, the polaron and the second-derivative technique corrections.

accounted for in equation (3.27) by replacing K_2 by K_2' where

$$|K_2'| = |K_2| + 3\alpha E_g/40\hbar\omega_{LO} \tag{3.30}$$

where α is the Fröhlich coupling constant. However, one can simplify equation (3.27) for the low- and high-temperature limits respectively. For high temperatures, one can approximate (3.27) to

$$\frac{1}{m^*(E)} = \frac{1}{m_0^*}\left\{+\frac{2K_2}{E_g}\left[\hbar\omega_c + \tfrac{1}{2}kT + \hbar\omega_c \exp\left(\frac{-\hbar\omega_c}{kT}\right)\right]\right\} \tag{3.31}$$

and for the low-temperature regime equation (3.27) has the form

$$\frac{1}{m^*(E)} = \frac{1}{m_0^*}\left(1 + \frac{2K_2}{E_g}\left(\tfrac{1}{2}\hbar\omega_c + \tfrac{3}{2}\right)\right). \tag{3.32}$$

By considering the frequency dependence of the low-temperature effective mass, an experimental value of K_2' can be derived from the slope of the plot shown in figure 3.67. The experimental value for K_2' is $K_2' = -2.05$ for sample 85. The theoretical value for K_2' defined in Palik *et al* [127] is $K_2' = -0.9494$, including the contribution of the resonant polaron [133].

The cyclotron mass is expected to be temperature-dependent and is found to be increasing with temperature. The effective band-edge mass will be decreasing with increasing temperature owing to the decreasing energy gap as, according to $k \cdot p$ theory,

$$m_0/m_2^* \simeq 1 + 2P^2/E_g. \tag{3.33}$$

While the band-edge mass is thus decreasing with increasing temperature, the cyclotron effective mass is found to be increasing, as the carriers are excited further into the band. This temperature dependence may be used to deduce a lower limit for K_2', using equation (3.31) in the high-temperature limit.

The experimental value K_2' obtained from the slope of the straight-line fit for the effective-mass variations with temperature, given in figures 3.66 and 3.67, is $K_2' = -1.47$, at fixed laser frequency. The gradient was found to become less steep for short-wavelength measurements, as these did not reach the high-temperature limit in the temperature range studied, as suggested by equation (3.27). The values deduced from the temperature dependence will be a lower limit on K_2' owing to the compensating effect of the decrease in band gap, as described earlier.

In conclusion, the variations of the effective mass with temperature and magnetic field yield a very important result. This is that the effect of non-parabolicity in the alloy system of $Ga_xIn_{1-x}As$ is very large, larger than would be expected from conventional three-band $k \cdot p$ theory. The $k \cdot p$ theory was originally proposed by Kane [134].

Herman and Weisbuch [135] found that a linear interpolation of the momentum matrix elements for the two constituent compounds could give a

good description of the electronic g-factor in ternary alloys. However Nicholas *et al* [126, 129] and Portal *et al* [128] have shown that the variation of the effective mass as a function of alloy composition provides clear evidence for a reduction in matrix element, probably due to band mixing by disorder.

3.5.7 Shallow-donor spectroscopy and polaron coupling in $Ga_{0.47}In_{0.53}As$–InP grown by MOCVD

The energy levels associated with shallow hydrogenic impurities have been one of the most intensively studied areas in semiconductor physics. Extrinsic photoconductivity is most commonly used in these studies, frequently with the application of high magnetic fields [136, 137]. This method has been developed to provide a spectroscopic tool to identify residual contamination due to impurities in high-purity materials [136, 138].

Nicholas *et al* [139] have studied the shallow-donor energy levels in high magnetic fields, in the alloy $Ga_xIn_{1-x}As$ ($x = 0.47$), grown lattice-matched to InP. Transitions between 1s and 2p levels of the shallow hydrogenic donors have been observed in photoconductivity using Fourier-transform spectroscopy at fixed magnetic fields and also using fixed-wavelength infrared lasers in varying magnetic fields.

Epitaxial samples of high-purity n-$Ga_{0.47}In_{0.53}As$ were studied, which had been grown lattice-matched to InP. The sample characteristics are 6 μm thick GaInAs on InP substrate, with $\mu(300\ \mathrm{K}) = 12\,000\ \mathrm{cm^2\,V^{-1}\,s^{-1}}$ and $\mu(77\ \mathrm{K}) = 48\,000\ \mathrm{cm^2\,V^{-1}\,s^{-1}}$.

Some typical experimental recordings are shown in figure 3.69 for two wavelengths, and for comparison a recording of the sample transmission is also shown. The two transitions observed correspond to free-electron cyclotron resonance, at higher field, and 1s to $2p^+$ shallow-donor transitions at lower field. Both transitions are observed, due to the partial carrier freeze-out which occurs at 4.2 K in these samples. As the magnetic field increased, the sample resistivities rose rapidly due to a very pronounced magnetic freeze-out, and the $1s–2p^+$ transition became dominant at high fields. As the frequencies approached those of the optic phonons, the strength of the photoconductive signal decreased markedly, and the transitions began to broaden significantly. The optic phonon properties of $Ga_{0.47}In_{0.53}As$ are rather complex, due to its two-optic-phonon-mode behaviour [132], which leads to the definition of two separate polaron coupling constants, α_{GaAs} and α_{InAs}. Such a two-mode polaron system has been considered by Nicholas *et al* [126] and Swierkowski *et al* [140], who showed that, when the two modes are relatively close to each other in frequency, the coupling constants are modified and become

$$\alpha_1 = \left(\frac{e^2}{h\varepsilon(\infty)}\right)\left(\frac{m^*}{2h\omega_{L1}}\right)^{1/2}\left(1-\frac{\omega_{T1}^2}{\omega_{L1}^2}\right)\left(\frac{\omega_{T2}^2-\omega_{L1}^2}{\omega_{L2}^2-\omega_{L1}^2}\right) \tag{3.34}$$

$$\alpha_2 = \left(\frac{e^2}{h\varepsilon(\infty)}\right)\left(\frac{m^*}{2h\omega_{L2}}\right)^{1/2}\left(1 - \frac{\omega_{T2}^2}{\omega_{L2}^2}\right)\left(\frac{\omega_{L2}^2 - \omega_{T1}^2}{\omega_{L2}^2 - \omega_{L1}^2}\right) \tag{3.35}$$

where $\omega_{L1,2}$ and $\omega_{T1,2}$ represent the longitudinal and transverse optic-phonon frequencies, and $\varepsilon(\infty)$ is the high-frequency dielectric constant. For $Ga_{0.47}In_{0.53}As$ this gives $\alpha_{GaAs} = 0.05$ and $\alpha_{InAs} = 0.01$, indicating that the GaAs optic-phonon mode should dominate the coupling. The results shown in figure 3.70 are consistent with this conclusion, since no large discontinuity in the effectives mass is observed on passing the 'InAs'-mode LO phonon at 29 meV, although there are not sufficient measurements to make a more quantitative statement.

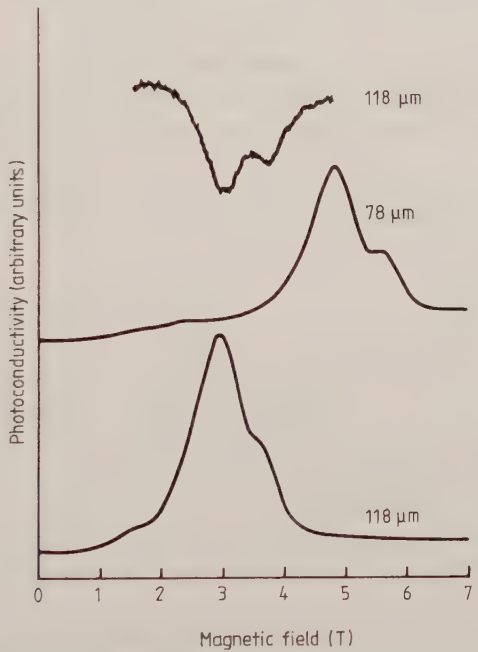

Figure 3.69 Experimental recordings of the photoconductive response of the MOCVD sample 85, at two different wavelengths at 4.2 K. The upper trace shows a recording of direct transmission.

The shallow-donor ionization energy can now be calculated from the hydrogenic-impurity approximation. The effective mass is taken from the cyclotron resonance measurements, and the low-frequency dielectric constant is taken from a linear extrapolation of the values of 12.6 for GaAs and 14.4 for InAs [141]. Variational calculations of the shallow-donor energy levels in a magnetic field [142–144], scaled with the effective Rydberg, are shown in figure 3.71 together with the experimental points. It may be seen that there is good agreement at low fields, but that as the transition energy

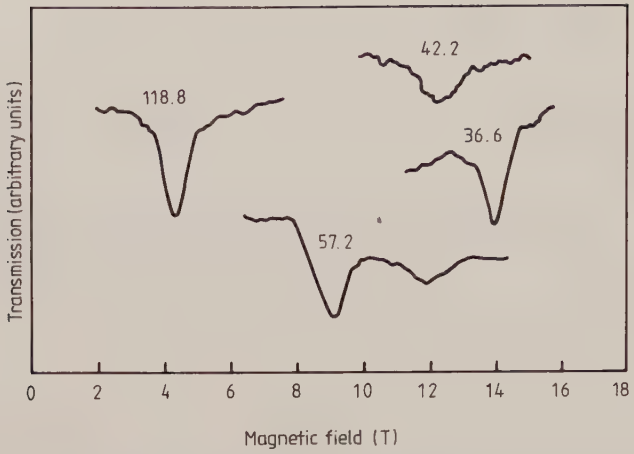

Figure 3.70 Typical experimental recordings of the cyclotron resonance at 4.2 K in the two systems studied. The wavelengths (μm) are shown.

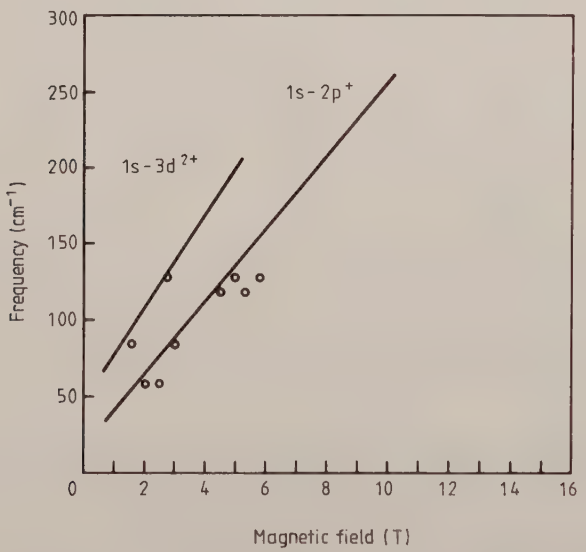

Figure 3.71 The transition frequencies as a function of magnetic field, for the three samples studied. The full lines show the calculated values of the 1s–2p$^+$ and the possible 1s–3d^{2+} transitions. (○) MOCVD.

approaches the optic phonons, bound-polaron coupling is observed [145] to cause strong shifts in the levels. The data in this case are clearer than for the unbound polaron, and it is possible to distinguish separate coupling to the two different LO-phonon modes at 233 cm^{-1} (InAs) and 273 cm^{-1} (GaAs).

Although it was not possible to detect the upper branch of the GaAs phonon, the much greater shifts in the resonance make it clear that this phonon dominates the coupling, as would be expected from the relative values of α_{GaAs} and α_{InAs} given above. It is interesting to note that very strongly broadened resonances were observed even at, or very close to, the LO-phonon frequencies for the InAs mode. These resonances fall at approximately the mean of the upper and lower polaron branches, and are visible as the almost vertical section of the experimental curve around 233 cm^{-1}. There is also an indication of a very weak peak in the photoconductivity, at energies corresponding to the transition 1s to $3d^{2+}$, for sample 85 with 78 and 118 μm wavelengths. This extra peak does not appear at longer wavelengths owing to the low magnetic field position for this transition. The observation of the extra peak 1s to $3d^{2+}$ is unexpected due to the selection rule forbidding even-parity transitions. A mechanism responsible for the symmetry breaking could be disorder, either due to the relatively high doping level or to alloy fluctuations.

3.6 APPLICATIONS OF GaInAs–InP SYSTEMS GROWN BY MOCVD

3.6.1 PIN photodetector

The use of the ternary material InGaAs lattice-matched to InP for long-wavelength detectors is now well established [146, 147]. Among the known structures, the simple and reliable PIN has become one of the more attractive, enabling the fabrication of high-sensitivity PINFET optical receivers [148] as well as that of broad-area general-purpose photodiodes [149]. Usually, the detectors reported in this field were either grown by LPE and hydride or chloride VPE; here we describe InGaAs PIN photodiodes prepared by MOCVD.

The structure consists of three nominally undoped layers deposited on an n-type InP substrate as follows: (i) an InP buffer layer 1.6 μm thick; (ii) the InGaAs absorption layer 3 μm thick; and (iii) an InP 'window' layer, whose standard thickness of 1.6 μm has been decreased in some experiments to 0.5 μm in order to enhance the response in the near-infrared spectrum beyond 0.9 μm. The background impurity concentration deduced from capacitance–voltage measurements is routinely found in the 10^{15} cm^{-3} range (n-type), and is therefore suitable to achieve the low capacitance required for PINFET implementation. The p–n junction is next formed by Zn diffusion using the semiclosed box technique [150] and is located in the InGaAs layer typically 0.5–1 μm away from the upper hetero-interface. The ohmic contacts are made by sputtered Au–Zn alloyed at 425°C for 30 s on the p side, and by sputtered Au on the n side. Mesas are finally defined by a

chemical etch in a $Br_2/HBr/H_2O$ solution, the final device structure being schematically shown in figure 3.72. At this point, it should be noted that the junction is not placed at its optimum depth in order to achieve very high speeds of response. In fact, in the top illumination scheme used, the photoelectrons created near the InP window in the p-type part of the InGaAs layer have to diffuse down to the junction since this small region of the ternary material remains undepleted under reverse bias. Nevertheless, the increase in the response time due to this effect can be expected to be small enough for current light-wave applications [151].

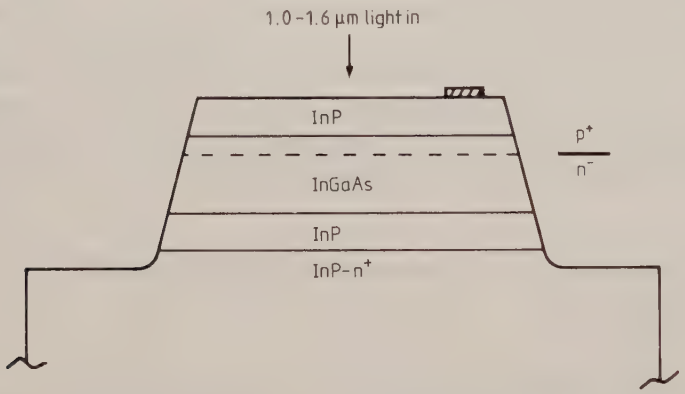

Figure 3.72 Cross-sectional view of InGaAsP/InP mesa-type PIN photodiodes.

Three kinds of detectors have been made in the previously described wafers, differing mainly by the optically active area: (i) signal PIN with an 80 μm optical diameter ($S \sim 7 \times 10^{-5}$ cm^2) to be used in front of 50 μm core fibres for the implementation of PINFET-type receivers; (ii) medium-sized feedback photodiodes ($S \sim 1.2 \times 10^{-3}$ cm^2, 300 μm optical diameter) for the monitoring of long-wavelength laser diodes; and finally (iii) large-diameter (1 mm) detectors for general-purpose both long- and short-wavelength applications.

The typical bias point found for our devices is 10 V, at which the capacitance is less than 0.3 pF, the quantum efficiency about 70% (1.3 μm wavelength), the impulse fall and rise time less than 400 ps. Figure 3.73 gives a histogram of the dark current for one of the best wafers. The mean value is 2.3 nA and the standard deviation is 2 nA. Only the units with I_D less than 10 nA have been taken into account, which represents 237 diodes for a total number of units equal to nearly 400, including wafer-edge devices. Nearly 300 units had a dark current less than 25 nA, which represents almost all the diodes if one excludes wafer-edge ones. The performances here are in very close agreement with those measured on

similar photodiodes also made in our laboratory but from LPE material. After cleaving and packaging, the performances are again checked. The quantum efficiency measured as a function of the wavelength using lock-in techniques oscillates between 60 and 70% in the 1.0–1.6 μm range, which corresponds to a nearly 100% internal efficiency for devices without an antireflection coating. The bandwidth has also been accurately determined with units mounted in a microwave package. The 3 dB cut-off frequency at the bias point is 3 GHz.

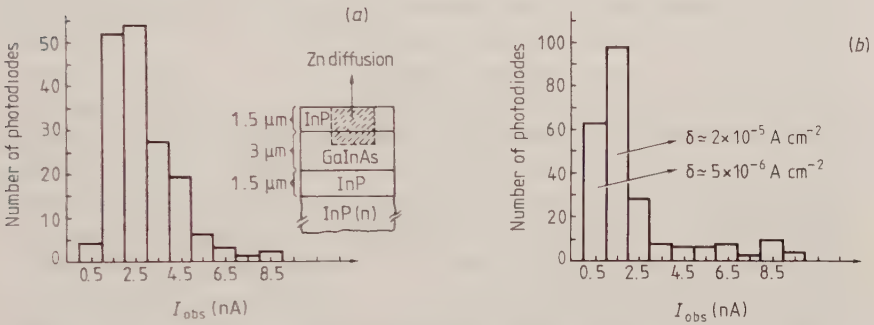

Figure 3.73 Histogram of room-temperature dark current at -10 V bias for small-area (7×10^{-5} cm^2) photodiodes: (*a*) LPE, $I_{obs} = 2.8$ nA; (*b*) MOCVD, $I = 2.3$ nA.

Concerning feedback-type and general-purpose detectors, the bias point is defined as 5 V, a voltage commonly found in electronic equipment. For the feedback type ($S \sim 1.2 \times 10^{-3}$ cm^2), the mean dark current is 24 nA with a standard deviation of 16 nA. In this statistic, only the diodes for which I_D is less than 100 nA are taken into account, which represents 215 units out of 250 including wafer-edge ones. Concerning broad-area general-purpose detectors, a poor yield of good devices was obtained since only 19 diodes out of a total number of 130 had a dark current less than 1 μA at 5 V. For these few units, the mean value is 240 nA and the standard deviation 190 nA.

3.6.2 Field-effect transistor

$In_{0.53}Ga_{0.47}As$ lattice-matched to InP has a favourable band structure configuration for the development of millimetre-wave field-effect transistors. A high electron velocity [152] can be achieved even at high doping levels, which will give high transconductance and high cut-off frequency. Furthermore such a transistor could be integrated on the same chip as optoelectronic devices used for long-wavelength applications fabricated on InP substrates. This would result in an improvement of the overall

performance of the circuit. Since InGaAs has too small a band gap to form a sufficiently high and leakage-free Schottky barrier, different solutions have been proposed to make the gate. A Si_3N_4 insulator [153] or a high-band-gap material such as InAlAs or InP [154] can be grown on top of the channel layer; one can also use a p–n junction obtained either by diffusion [155, 156], by ion implantation [157, 158] or by etching a p-type epitaxial layer [159]. In this last case, the main difficulty is to reach a submicrometre length for the gate.

The fabrication of a junction field-effect transistor (JFET) in which the junction is formed at the interface of the n-type GaInAs channel and a p-type InP top layer has been described [160].

On an InP semi-insulating substrate, an InP buffer (0.5 μm, $N_D < 1 \times 10^{14}$ cm^{-3}), an n-type GaInAs channel (0.2 μm, $N_D = 1.3–1.4 \times 10^{17}$ cm^{-3}), a p-type InP layer (0.5 μm, $N_A = 1 \times 10^{18}$ cm^{-3}) and a p-type InGaAs layer (0.5 μm, $N_A > 5 \times 10^{18}$ cm^{-3}) were successively deposited. Silicon was used as the donor and zinc as the acceptor for doping. The gate metallization was evaporated first and used as a mask for the etching of the gate. This was performed using selective acid solutions in two steps: etching of the p-GaInAs top layer first and then the p-InP layer. It was found that obtaining a submicrometre gate length was much easier when the GaInAs top layer was present. Moreover, it was difficult to obtain a good ohmic contact on p-type InP whereas it was easy on GaInAs. A low value of gate resistance is required to achieve a low-noise microwave performance. Source and drain contacts (Au–Ge, Ti, Pt, Au) were then deposited self-aligned with respect to the gate metal. The fabrication then terminates by the etching of the isolation mesa. A cross-sectional view of the structure is shown in figure 3.74. A gate length of half a micrometre in a 1.5 μm source–drain spacing can be obtained by this process. The transistor width is 150 μm.

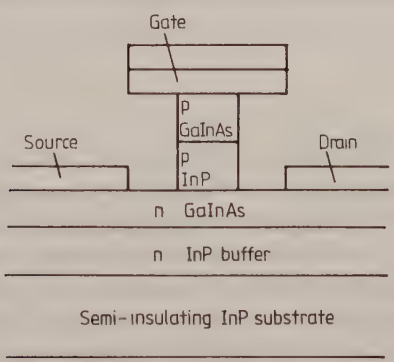

Figure 3.74 Cross-sectional view of the JFET structure.

The DC characteristics of the junction field-effect transistor are shown in figure 3.75. One can observe (i) a good saturation behaviour with high saturation currents, (ii) a good pinch-off, and (iii) a very high transconductance ($g_m = 235$ mS mm^{-1}). The barrier height of the junction measured on its $I-V$ characteristic is 0.35 V, which is lower than the expected value. The calculated value of the access resistance deduced from the slope of the characteristics at low drain voltage is 2.5 Ω for a 150 μm wide device (i.e. 0.4 Ω mm). In consequence, the intrinsic transconductance is 260 mS mm^{-1}, which is the highest value reported for a GaInAs field-effect transistor. Since the intrinsic transconductance can be approximated by the equation

$$g_m = Z\varepsilon v/\omega \tag{3.36}$$

where ω is the depletion-layer thickness, one can deduce an average electron velocity of 3.6×10^7 cm s^{-1}. Such a high value has not yet been observed in any field-effect transistor and can be attributed to an overshoot phenomenon induced by the shortness of the gate.

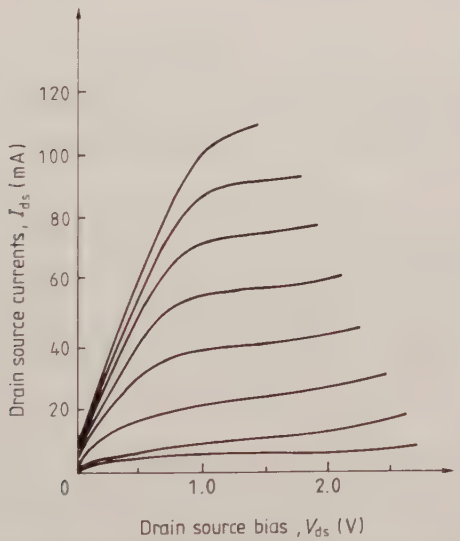

Figure 3.75 DC characteristics of the JFET. The gate is 0.5 μm long and 150 μm wide. The transconductance is 235 mS mm^{-1}. (Gate bias step is −0.5 V starting at 0 V.)

3.6.3 GaInAs–InP optical waveguides

The development of the MOCVD method introduces possibilities for the investigation of passive and active structures at 10.6 μm wavelength.

Integrated optics geometry is particularly interesting [161] as it permits

low-drive-voltage electro-optic devices, which is an important consideration at this wavelength. The large-substrate-area processing capability of MOCVD could lead to very efficient devices, especially if the propagation losses are low.

Here we describe experimental results concerning low-loss planar optical waveguides in the GaInAs–InP system obtained with the low-pressure MOCVD technique [162].

The waveguides are fabricated on heavily doped InP substrates ($2 \times 10^{18}\,cm^{-3}$) and consist of a 5 μm thick undoped InP (n^-: $2 \times 10^{14}\,cm^{-3}$) buffer layer and a 5 μm thick undoped GaInAs (n^-: $6 \times 10^{14}\,cm^{-3}$) guide layer (figure 3.76). The dimensions of the substrates are typically $10 \times 30\,mm^2$, and the losses are measured using the two-prism technique, which is very convenient at 10.6 μm.

The measurement on the GaInAs/InP waveguide is shown in figure 3.77, where losses as low as $0.7\,dB\,cm^{-1}$ are estimated for the TE_0 mode, compared with $0.3\,dB\,cm^{-1}$ theoretically expected. The small number of experimental points in figure 3.77 is related to the very low losses of the waveguide, which lead to a difficulty in obtaining sufficient points for the measurements.

It must be noted that, even if this waveguide was not purely single-mode (four modes can propagate in theory), the higher-order modes present higher losses (TE_1: $4\,dB\,cm^{-1}$; TE_2: $78\,dB\,cm^{-1}$; TE_3: $370\,dB\,cm^{-1}$), and as a consequence only the fundamental one can effectively be used for wave-guiding.

A very-low-loss quasi-single-mode waveguide was demonstrated using GaInAs/InP undoped epilayers on a heavily doped InP substrate. Losses as low as $0.7\,dB\,cm^{-1}$ have been measured, which demonstrates the usefulness of the MOCVD technique for this type of waveguide. These results are very encouraging for future implementation of more sophisticated devices around the 10.6 μm wavelength.

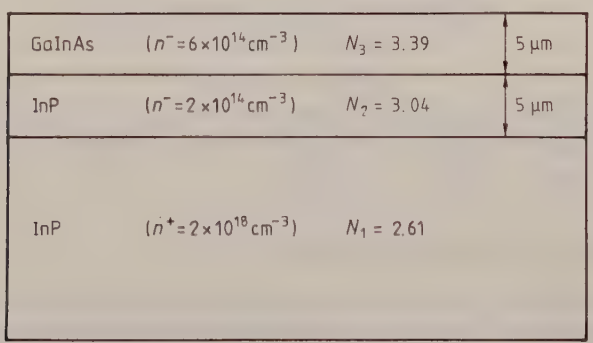

Figure 3.76 Schematic diagram of low-loss structure.

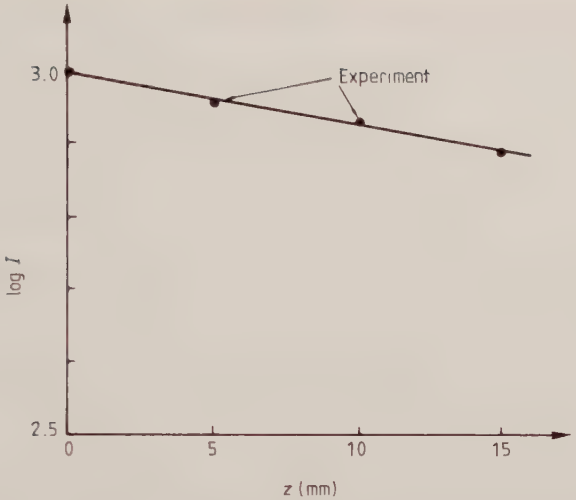

Figure 3.77 Power coupled out against prism spacing for low-loss structure.

REFERENCES

[1] Störmer H L, Dingle R, Gossard A C, Wiegmann W and Stauge M D 1979 *Solid State Commun.* **29** 705
[2] Hilsum C and Rees H D 1970 *Electron. Lett.* **6** 277
[3] Linh N T 1983 *Adv. Solid State Phys.* 227
[4] Bisaro R, Merenda P and Pearsall J P 1979 *Appl. Phys. Lett.* **34** 100–2
[5] Razeghi M and Duchemin J P 1983 *J. Cryst. Growth* **69** 76–82
[6] Goetz K H, Bimberg D and Razeghi M 1984 Unpublished observations
[7] Voisin P, Guldner Y, Vieren J P, Voos M, Delescluse P and Linh N T 1981 *Appl. Phys. Lett.* **39** 982
[8] Chen Y S and Kim O K 1981 *J. Appl. Phys.* **52** 7892
[9] Marzin J Y, Benchimol J L, Sermarge B, Etienne B and Voos M 1984 *Solid State Commun.*
[10] Oliver J and Eastman L 1980 *J. Electron. Mater.* **9** 693
[11] Goetz K H, Bimberg D, Jurgensen H, Selders J, Solomonov A V, Glenskii G F and Razeghi M 1983 *J. Appl. Phys.* **54** 4543
[12] Beneking H, Grote N and Selders J 1981 *J. Cryst. Growth* **54** 59
[13] Kordos P, Schumbera P, Heyen M and Balk P 1982 *Gallium Arsenide and Related Compounds, 1981* (Inst. Phys. Conf. Ser. 63) p 131
[14] Razeghi M, Poisson M A, Guldner Y, Vieren J P, Voisin M and Voos M 1982 *Appl. Phys. Lett.* **40** 877
[15] Ishida K, Matsui J, Kamejima T and Sakuma I 1975 *Phys. Status Solidi* a **31** 255
[16] Bartels W J and Nijman W 1978 *J. Cryst. Growth* **44** 518
[17] Nagi H 1974 *J. Appl. Phys.* **45** 3789
[18] Kawamura Y and Okamoto H 1979 *J. Appl. Phys.* **50** 4457

[19] Nahory R E, Pollack M A, Johnston W D Jr and Barns R L 1978 *Appl. Phys. Lett.* **33** 659
[20] Alavi K, Aggarwal R L and Groves S H 1980 *Phys. Rev.* B **21** 1311
[21] Pikhtin A N 1977 *Sov. Phys.–Semicond.* **11** 245
[22] Bimberg D, Sondergeld M, Schairer W and Yep T O 1970 *J. Lumin.* **3** 175
[23] Bimberg D, Sondergeld M and Grobe E 1971 *Phys. Rev.* B **4** 3451
[24] Elliott R J 1957 *Phys. Rev.* **108** 1384
[25] Shah A J, Leheny R F, Nahory R E and Pollack M A 1980 *Appl. Phys. Lett.* **37** 475
[26] Pinczuk A, Worlock J M, Nahory R E and Pollack M A 1978 *Appl. Phys. Lett.* **33** 461
[27] Brodsky M H and Lucovsky G 1968 *Phys. Rev. Lett.* **21** 990
[28] Landolt-Börnstein 1982 *Numerical Data and Functional Relationships in Science and Technology* New Ser. III/17a, ed O Madelung (Berlin: Springer)
[29] Towe E 1982 *J Appl. Phys.* **53** 5136
[30] Lorentz M R, Morgan T N and Pettit G D 1968 *Proc. Int. Conf. on the Physics of Semiconductors Moscow, 1968* ed S Ryvkin (Leningrad: Nauka) p 495
[31] Chen Y S and Kim O K 1981 *J. Appl. Phys.* **52** 7392
[32] Forrest S R and Kim O K 1982 *J. Appl. Phys.* **53** 5738
[33] Yagi T, Fujiwara Y, Nishino T and Hamakawa Y 1983 *Japan. J. Appl. Phys.* **22** L467
[34] Rao M V and Bhattacharya P K 1983 *Electron. Lett.* **19** 196
[35] Trommer R and Albrecht H 1983 *Japan. J. Appl. Phys.* **22** L364
[36] Goetz K H, Bimberg D, Brauchler K A, Jurgensen H, Selders J, Razeghi M and Kuphal E 1985 *Appl. Phys. Lett.* **46** 277
[37] Vescan L, Selders J, Krautle H, Kutt W and Neneking H 1982 *Electron. Lett.* **18** 533–4
[38] Vescan L, Selder J, Maier M, Krautle H and Beneking H 1984 *J. Cryst. Growth* **67** 353–7
[39] Tell B, Leheny R F, Liao A S H, Bridges T J, Burkhardt E G, Chang T Y and Beebe E D 1984 *Appl. Phys. Lett.* **44** 438–40
[40] L'Hanidon H, Favenrec P, Salvi M and Razeghi M 1985 *Electron. Lett.* **21** 122
[41] Ito M, Kaneda T, Nakajima K, Toyama Y and Ando H 1981 *Solid State Electron.* **24** 421–4
[42] Esaki L and Tsu R 1970 *IBM J. Res. Dev.* **14** 61
[43] Verma A R 1953 *Crystal Growth and Dislocation* (London: Butterworths)
[44] Dingle R, Wiegmann W and Henry C H 1974 *Phys. Rev. Lett.* **33** 827
[45] Chang L L, Sakaki H, Chang C A and Esaki L 1977 *Phys. Rev. Lett.* **38** 1489
[46] Störmer H L, Dingle R, Gossard A, Wiegmann W and Stauge M D 1979 *Solid State Commun.* **29** 705
[47] Chemla D S, Millers D A B, Smith P W, Gossard A C and Wiegmann W 1984 *Appl. Phys. Lett.* **44** 16
[48] Wood T H, Burrus C A, Miller D A B, Chemla D S, Gossard A C and Wiegmann W 1984 *Appl. Phys. Lett.* **44** 16

[49] Rezek E A, Chin R Jr, Holonyak N, Kirchoefer S W and Kollbas R M 1980 *J. Electron. Mater.* **9** 1
[50] Blakeslee A E and Alliota C F 1970 *IBM J. Res. Dev.* **14** 686
[51] Alferov Zh I 1967 *Sov. Phys.–Semicond.* **1** 358
[52] Gossard A C 1983 *Thin Solid Films* **104** 279
[53] Cho A Y 1979 *J. Vac. Sci. Technol.* **16** 275
[54] Chang L L, Esaki L, Howard W E, Ludeke R and Schul G 1973 *J. Vac. Sci. Technol.* **10** 655
[55] Tsang W T and Cho A Y 1977 *Appl. Phys. Lett.* **30** 293
[56] Massies J, Rochelle J, Delescluse P, Etienne P E, Chevrier J and Linh J J 1980 *J. Electron. Lett.* **16** 275
[57] Fauri J P and Million A 1982 *Thin Solid Films* **90** 107
[58] Razeghi M, Hirtz J P, Ziemelis V O, Delalande C, Etienne B and Voos M 1983 *Appl. Phys. Lett.* **43** 586
[59] Razeghi M and Duchemin J P 1983 *J. Cryst. Growth* **64** 76
[60] Razeghi M, Maurel Ph and Omnes F 1987 *NATO Workshop on Impurity Levels in Superlattices* Invited paper
[61] Razeghi M, Defour M, Omnes F, Maurel Ph, Bigan E, Acher O, Nagle J and Brillouet F 1988 *Proc. 4th MOCVD Conf.*
[62] Razeghi M, Hirtz J P, Ziemelis V O, Delalande C, Etienne B and Voos M 1983 *Appl. Phys. Lett.* **43** 585
[63] Welch D F, Wicks G W and Eastmann L F 1983 *Appl. Phys. Lett.* **43** 762
[64] Razeghi M, Nagle J and Weisbuch C 1984 *Gallium Arsenide and Related Compounds, 1984* (Inst. Phys. Conf. Ser. 74) p 379
[65] Weisbuch C, Dingle R, Gossard A C and Wiegmann W 1981 *Solid State Commun.* **38** 709
[66] Maan J C, Belle G, Fasolino A, Altarelli M and Ploog K 1984 *Phys. Rev.* B **30** 2253
[67] Weisbuch C, Miller R C, Dingle R, Gossard A C and Wiegmann W 1981 *Solid State Commun.* **37** 219
[68] Singh J and Madhukar A 1983 *J. Vac. Sci. Technol.* B **1** 305
[69] Sooryakumar R, Chemla D S, Pinczuk A, Gossard A, Weigmann W and Sham L J 1984 *J. Vac. Sci. Technol.* B **2** 349
[70] Miller R C, Kleinman D A and Gossard A C 1984 *Phys. Rev.* B **29** 7085
[71] Wood T H, Burrus C A, Weiner J S, Chemla D S, Miller D A B, Damen T C, Sivco D L and Cho A Y 1984 *Gallium Arsenide and Related Compounds, 1984* (Inst. Phys. Conf. Ser. 74) p 687
[72] Razeghi M, Maurel Ph, Nagle J, Omnes F and Pochelle J P 1986 *Appl. Phys. Lett.* **49** 1110
[73] Goetz K H, Bimberg D, Solomonov A V, Glinski G F and Razeghi M 1983 *J. Appl. Phys.* **54** 4543
[74] Davies R A 1988 *GEC J. Res.* submitted
[75] Guldner Y, Vieren J P, Voisin P, Voos M, Razeghi M and Poisson M A 1982 *Appl. Phys. Lett.* **40** 877–9
[76] Boothroyd C B and Stobbs W M 1986 Private communication
[77] Ando T, Fowler A B and Stern F 1982 *Rev. Mod. Phys.* **54** 2
[78] Störmer H L, Gossard A C and Wiegmann W 1982 *Solid State Commun.* **41** 707

[79] Razeghi M, Duchemin J P, Portal J C, Dmowski L, Remeni G, Niedas R J and Briggs A 1986 *Appl. Phys. Lett.* **48** 712
[80] Mori S and Ando T 1980 *Surf. Sci.* **98** 101
[81] Ando T 1975 *J. Phys. Soc. Japan* **39** 411
[82] Beinvogl W, Kamgar A and Koch J F 1976 *Phys. Rev.* B **14** 4274
[83] Portal J C, Nicholas R J, Brummel M A, Cho A Y, Cheng K Y and Pearsall T P 1982 *Solid State Commun.* **43** 907
[84] Briggs A, Guldner Y, Vieren J P, Voos M, Hirtz J P and Razeghi M 1983 *Phys. Rev.* B **27** 6549
[85] Guldner Y, Vieren J P, Voisin P, Voos M, Razeghi M and Poisson M A 1982 *Appl. Phys. Lett.* **40** 877
[86] Guldner Y, Hirtz J P, Vieren J P, Voisin P, Voos M and Razeghi M 1982 *J. Physique Lett.* **43** L613
[87] Störmer H L and Tsang W T 1980 *Appl. Phys. Lett.* **36** 685
[88] Störmer H L, Chang A, Tsui D C, Hwang J C M, Gossard A C and Wiegmann W 1983 *Phys. Rev. Lett.* **50** 1953
[89] Mendez E E, Wang W I, Chang L L and Esaki L 1984 *Phys. Rev.* B **30** 1087
[90] Chang L L, Mendez E E, Wang W I, Esaki L and Tedrow P M 1984 *Proc. 17th Int. Conf on the Physics of Semiconductors* ed J D Chadi (Berlin: Springer) p 299
[91] Ohkawa F J and Uemura Y 1975 *Prog. Theor. Phys. Suppl.* **57** 164
[92] Ekenberg U and Altarelli M 1984 *Phys. Rev.* B **30** 3569; 1985 *Phys. Rev.* B **32** 3712
[93] Bangert E and Landwehr G 1985 *Proc. Int. Conf. on Superlattices, Microstructures and Microdevices, Urbana-Champaign, Illinois* (New York: Academic) vol 1, p 363
[94] Ando T 1985 *J. Phys. Soc. Japan* **54** 1528
[95] Razeghi M, Maurel Ph, Tardella A, Dimovsky L, Gauthier D and Portal J C 1986 *Appl. Phys. Lett.* **60** 2453
[96] Von Klitzing K, Dorda G and Pepper M 1980 *Phys. Rev. Lett.* **45** 494
[97] Tsui D C and Gossard A C 1981 *Appl. Phys. Lett.* **37** 550
[98] Takikawa M, Komeno J and Ozeki M 1983 *Appl. Phys. Lett.* **43** 280
[99] Störmer H L, Gossard A C, Wiegmann W, Blondel R and Baldwin K 1984 *Appl. Phys. Lett.* **44** 139
[100] Kastalsky A and Hwang J C M 1984 *Solid State Commun.* **51** 317
[101] Von Klitzing K and Ebert G 1985 *Metrologia* **21** 11–18
[102] Bliek L, Braun E, Melchert F, Warnecke P, Schlapp W, Weimann G, Ploog K, Ebert G and Dorda G 1985 *IEEE Trans. Instrum. Meas.* **IM-34** 304–5
[103] Cage M E, Dziuba R F and Field B F 1985 *IEEE Trans. Instrum. Meas.* **IM-34** 301–3
[104] Wada T, Shida K, Nishinaka H and Igarashi T 1985 *IEEE Trans. Instrum. Meas.* **IM-34** 306–9
[105] Endo T, Murayama Y, Koyanagi M, Kinoshita J, Inagaki K, Yamanouchi C and Yoshihiro K 1985 *IEEE Trans. Instrum. Meas.* **IM-34** 323–7
[106] Hartland A, Davies G J and Wood D R 1985 *IEEE Trans. Instrum. Meas.* **IM-34** 309–14
[107] Delahaye F and Reymann D 1985 *IEEE Trans. Instrum. Meas.* **IM-34** 316–19

[108] Drummond T J, Kopp W, Fischer R, Morkoç H, Thorne R E and Cho A Y 1982 *J. Appl. Phys.* **53** 1238
[109] Störmer H L, Gossard A C, Wiegmann W and Baldwin K 1981 *Appl. Phys. Lett.* **39** 912
[110] Wei H P, Tsui D C and Razeghi M 1984 *Appl. Phys. Lett.* **45** 666
[111] Lin B J F, Tsui D C, Paalanen M A and Gossard A C 1984 *Appl. Phys. Lett.* **45** 695
[112] Nathan M I, Jackson T N, Kirchner P D, Mendez E E, Pettit W D and Woodall J M 1983 *J. Electron. Mater.* **12** 719
[113] Kastalsky A and Hwang J C M 1983 Unpublished
[114] Tsui D C and Gossard A C 1981 *Appl. Phys. Lett.* **38** 550
[115] Gauthier D, Dmowski L, Ben Amor S, Blondel R, Portal J C, Razeghi M, Maurel Ph, Omnes F and Laviron M 1986 *Semicond. Sci. Technol.* **1** 105
[116] Sotomayor Torres C M, Claxton P A, Roberts J S, Stradling R A and Wasilewski Z 1985 *Proc. VIth Conf. EP2DS* Kyoto, p 558
[117] Ando T, Fowler A B and Stern F 1982 *Rev. Mod. Phys.* **54** 2
[118] Ando T and Uemura 1974
[119] Abstreiter G, Kotthaus J P, Koch J F and Dorda G 1976 *Phys. Rev.* B **14** 6
[120] Voisin P, Guldner Y, Vieren J P, Voos M, Delescluse P and Linh N T 1981 *Appl. Phys. Lett.* **39** (12) 000
[121] Ando T 1975 *J. Phys. Soc. Japan* **38** (4) 000
[122] Nicholas R J, Brunel L C, Huant S, Kawai K, Portal J C, Brummel M A, Razeghi M, Cheng K Y and Cho A Y 1985 *Appl. Phys. Lett.* **55** 883
[123] Guldner Y, Vieren J P, Voisin P, Voos M, Razeghi M and Poisson M A 1982 *Appl. Phys. Lett.* **40** 877
[124] Maurel Ph, Razeghi M, Guldner Y and Vieren J P 1987 *Semicond. Sci. Technol.* **2** 695
[125] Razeghi M, Duchemin J P, Portal J C, Dmowski L, Remeni G, Nicholas R J and Briggs A 1986 *Appl. Phys. Lett.* **48** 712
[126] Nicholas R J, Stradling R A, Portal J C and Askenazy S 1979 *J. Phys. C: Solid State Phys.* **12** 1653
[127] Palik E D, Picus G S, Teitler S and Wallis R F 1961 *Phys. Rev.* **122** 475
[128] Portal J C, Perrier P, Renucci M A, Askenazy S, Nicholas R J and Pearsall T 1978 *Physics of Semiconductors, 1978* (Inst. Phys. Conf. Ser. 43) p 829
[129] Nicholas R J, Sessions S J and Portal J C 1980 *J. Appl. Phys.* **37** 178
[130] Stradling R A and Wood R A 1968 *J. Phys. C: Solid State Phys.* **1** 1711
[131] Pearsall T P, Carles R and Portal J C 1983 *Appl. Phys. Lett.* **42** 436
[132] Brodsky M H and Lucovsky G 1968 *Phys. Rev. Lett.* **21** 990
[133] Larsen D M 1964 *Phys. Rev.* **144** 679
[134] Kane E O 1957 *J. Phys. Chem. Solids* **1** 249
[135] Herman X and Weisbuch Y 1977 *Phys. Rev.* B **15** 816
[136] Stillman G E, Wolfe C M and Korn D M 1976 *Proc. 13th Int. Conf. on Physics of Semiconductors* Rome, p 623
[137] Yafet Y, Keys R W and Adams E N 1956 *J. Phys. Chem. Solids* **1** 137
[138] Cooke R A, Hoult R A, Kirkman R F and Stradling R A 1978 *J. Phys. D: Appl. Phys.* **11** 945
[139] Nicholas R J, Brummell M A and Portal J C 1984 *J. Cryst. Growth* **68** 356

[140] Swierkowski L, Zawadski W, Guldner Y and Rigaux C 1978 *Solid State Commun.* **27** 1245
[141] Landolt-Börnstein 1982 *Physics of Group IV Elements and III–V Compounds* vol 17a, ed O Madelung, M Schultz and H Weiss (Berlin: Springer)
[142] Lee T P, Bunns C A, Dentai A G and Ogawa K 1973 *Electron. Lett.* **16** 155
[143] Praddaude H C 1972 *Phys. Rev.* A **6** 1321
[144] Cabib D, Fabri E and Fioro 1972 *Nuovo Cim.* **108** 185
[145] Cohn D R, Larsen D M and Lax B 1972 *Phys. Rev.* B **6** 1367
[146] Stillman G E, Cook L W, Bulman G E, Tabatabaie N, Chin R and Dapkus P D 1982 *IEEE Trans. Electron. Devices* **ED-29** 1355–71
[147] Forrest S R 1982 *Laser Focus* **18** 81–90
[148] Brain M C, Smyth P P, Smith D R, White B R and Chidgey P J 1984 *Electron. Lett.* **20** 894–6
[149] Burrus C A, Dental A G and Lee T P 1981 *Opt. Commun.* **38** 124–6
[150] Kazmierski K, Huber A M, Morillot G and De Cremoux R 1984 *Japan. J. Appl. Phys.* **23** 628–33
[151] Poulain P and de Cremoux B 1980 *Japan. J. Appl. Phys.* **19** L189–92
[152] Windhorn T H, Cook L W and Stillman G E 1982 *IEEE Electron. Device Lett.* **EDL-3** 18
[153] O'Conner P, Pearsall T P, Chang K K, Cho A Y, Hwang J C M and Alavi K 1982 *IEEE Electron. Device Lett.* **EDL-3** 64
[154] Cheng C L, Liao A S H, Chang T Y, Leheny R F, Coldren L A and Lalevic B 1984 *IEEE Electron. Device Lett.* **EDL-5** 169
[155] Onho H, Barnard J, Wood C E C and Eastman L F 1980 *IEEE Electron. Device Lett.* **EDL-1** 154
[156] Bandy S, Nishimoto C, Hyder S and Hooper C 1981 *Appl. Phys. Lett.* **38** 817
[157] Chai Y G, Yuen C and Zdasiuk G A 1985 *IEEE Trans. Electron. Devices* **ED-32** 972
[158] Vescan L, Selders J, Kräute H, Kütt W and Beneking H 1982 *Electron. Device Lett.* **18** 533
[159] Chai Y G and Yeats R 1983 *IEEE Electron. Device Lett.* **EDL-4** 252
[160] Raulin J Y, Vassilakis-Thorngren E, Poisson M A, Razeghi M and Idomer G 1987 *Appl. Phys. Lett.* **50** 535
[161] Falco C, Botineau J, Azema A, Demicheli M and Ostrowky D B 1983 *Appl. Phys.* A **30** 23–6
[162] Delacourt D, Papuchon M, Poisson M A and Razeghi M 1987 *Electron. Lett.* **23** 451
[163] Razeghi M 1985 *Semiconductors and Semimetals* vol 22, Part A ed W T Tsang (New York: Academic)
[164] Razeghi M, Poisson M A, Guldner Y, Vieren J P, Voisin P and Voos M 1982 *Appl. Phys. Lett.* **40** 877
[165] Razeghi M, Hirtz P, Blandeau R, de Cremoux B and Duchemin J P 1983 *Electron. Lett.* **19** 181
[166] Razeghi M, Tardella A, Davies R A, Long A P, Kelly M K, Brittan E, Boothroyd C and Stobbs W M 1987 *Electron. Lett.* **23** 116

Chapter 4 GaInAsP–InP System: MOCVD Growth, Characterization and Application

As long-wavelength 1–1.65 μm GaInAsP electro-optical devices have become more widely used, motivated by low fibre absorption and dispersion, high transmission through water and smoke and greatly enhanced eye safety at wavelengths greater than 1.4 μm, the low-pressure metallorganic chemical vapour deposition (MOCVD) growth technique has been used to grow $Ga_xIn_{1-x}As_yP_{1-y}$ ($0 < x < 0.47$ and $0 < y < 1$) lattice-matched to InP for the complete compositional range between InP ($\lambda = 0.91$ μm, $E_g = 1.35$ eV) and the ternary compound $Ga_{0.47}In_{0.53}As$ ($\lambda = 1.67$ μm, $E_g = 0.75$ eV). Growth takes place in an RF induction-heated horizontal cold-wall reactor using triethylindium (TEIn) and triethylgallium (TEGa) for In and Ga sources, and AsH_3 and PH_3 for As and P sources.

4.1 GROWTH CONDITIONS

Growth apparatus and processes have been described in chapter 1. $Ga_xIn_{1-x}As_yP_{1-y}$ layers lattice-matched to an InP substrate can be grown at 76 Torr and at a substrate temperature between 630 and 650°C using TEIn, TEGa, AsH_3 and PH_3 in an $H_2 + N_2$ carrier gas. The growth rate depends linearly upon the sum of the partial pressures of TEIn and TEGa, and is independent of the arsenic and phosphorus partial pressures (see figure 4.1). The epitaxial-layer quality is sensitive to the pretreatment of the substrate and the alloy composition. The optimum growth conditions for $Ga_{0.23}In_{0.77}As_{0.51}P_{0.49}$ ($\lambda = 1.3$ μm) lattice-matched to InP are listed in table 4.1.

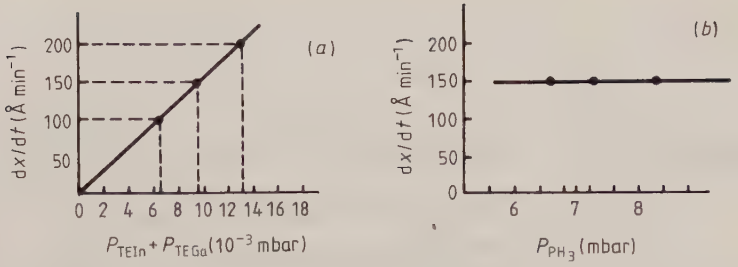

Figure 4.1 Variation of growth rate of GaInAsP on InP ($\lambda = 1.3\ \mu m$) with (*a*) TEIn + TEGa flow-rate and (*b*) PH_3 flow-rate at $T_G = 650^\circ C$ and $P_{AsH_3} = 0.3$ mbar. In (*a*) $P_{PH_3} = 6.6$ mbar; in (*b*) $P_{TEGa} = 2.5 \times 10^{-3}$ mbar, $P_{TEIn} = 7 \times 10^{-3}$ mbar.

Table 4.1 Optimum growth conditions for GaInAsP ($\lambda = 1.3\ \mu m$) lattice-matched to the InP substrate; the growth temperature is 650°C and the growth pressure is 76 Torr; the total flow-rate ($H_2 + N_2$) is $7\ l\,min^{-1}$.

Sources	Partial pressure (mbar)	Temperature (°C)
TEIn	8.5×10^{-3}	31
TEGa	3×10^{-3}	0
AsH_3	0.31	25
PH_3	7	25

Figure 4.2 shows the variation of lattice mismatch $\Delta a/a = (a_{InP} - a_{GaInAsP})/a_{InP}$ for a GaInAsP epilayer with TEIn flow-rate, keeping all of the remaining growth parameters constant. By changing the TEIn flow-rate one can obtain GaInAsP layers with $\lambda = 1.3\ \mu m$ lattice-matched to the InP substrate with $\Delta a/a \leqslant 4 \times 10^{-4}$ (which is the limit of precision of single-crystal x-ray diffraction measurements).

Figure 4.3 shows the evolution of the x-ray spectrum as a function of TEIn flow-rate. The full width at half-maximum (FWHM) of $K\alpha_1$ and $K\alpha_2$ reflection of the x-ray spectra of the GaInAsP epilayer is the same as the substrate, which indicates that the GaInAsP layer is homogeneous.

Figure 4.4 shows (*a*) the ratio $R_5 = PH_3/(PH_3 + AsH_3)$ versus band-gap wavelength λ_g, betweeen InP and $Ga_{0.47}In_{0.53}As$, (*b*) the ratio $R_3 = TEGa/(TEGa + TEIn)$ versus λ_g and (*c*) the ratio R_5/R_3 versus λ_g for $Ga_xIn_{1-x}As_yP_{1-y}$ ($0 < x < 0.47$ and $0 < y < 1$) lattice-matched to InP between InP ($\lambda = 0.9\ \mu m$) and $Ga_{0.47}In_{0.53}As$ ($\lambda = 1.67\ \mu m$) for a growth temperature of 650°C, growth pressure of 76 Torr and total flow-rate of $7\ l\,min^{-1}$.

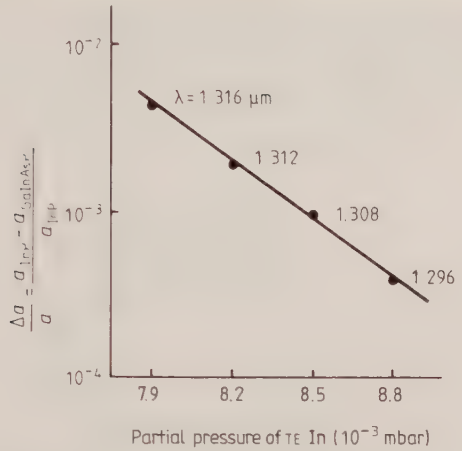

Figure 4.2 Variation of lattice mismatch for a GaInAsP epilayer with TEIn flow-rate, keeping all of the remaining growth parameters constant, i.e. $T_G = 650^\circ C$, $P_{Ga} = 30$ mbar, $P_{AsH_3} = 0.31$ mbar and $P_{PH_3} = 7$ mbar.

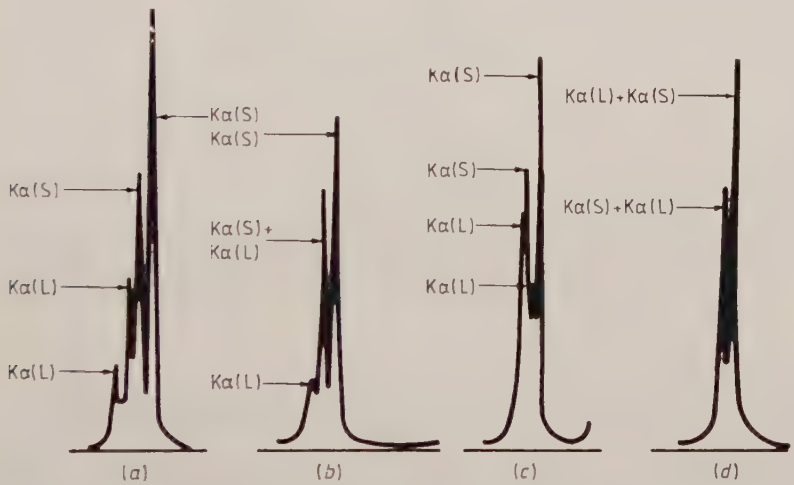

Figure 4.3 Evolution of x-ray spectrum as a function of TEIn flow-rate. $\Delta a/a = 4.5 \times 10^{-3}$ (*a*), 2×10^{-3} (*b*), 10^{-3} (*c*), $\leqslant 4 \times 10^{-4}$ (*d*).

Figure 4.4 shows that the incorporation behaviour of group V elements is different, because both arsenic and phosphorus are volatile and a significant proportion of these elements can be lost to the gas phase. The probability of incorporation for arsenic is much higher than for phosphorus, since phosphorus has a lower sticking coefficient than arsenic. For GaInAsP

($\lambda = 1.3\ \mu$m), one obtains the partial pressure ratios

$$\begin{aligned} P_{PH_3}/P_{AsH_3} &= (1-y)/y = 20 \\ P_{TEIn}/P_{TEGa} &= (1-x)/x = 3 \\ P_{(AsH_3+PH_3)}/P_{(TEIn+TEGa)} &= 600. \end{aligned} \tag{4.1}$$

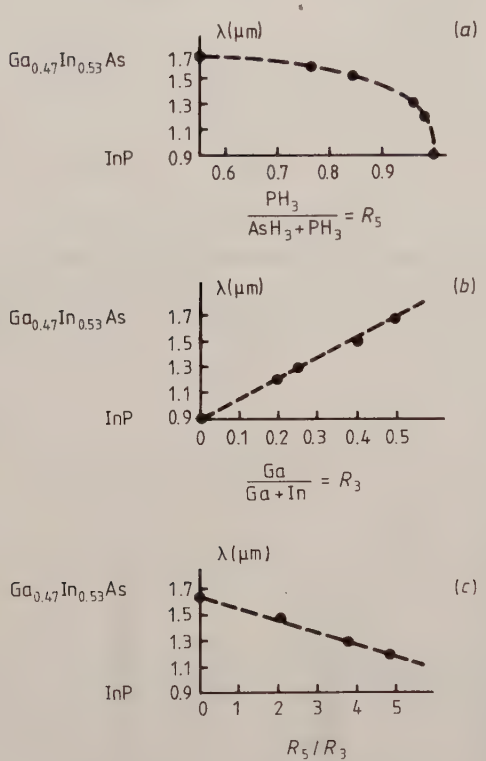

Figure 4.4 The ratios (*a*) $R_5 = PH_3/(PH_3 + AsH_3)$, (*b*) $R_3 =$ TEGa/(TEGa + TEIn) and (*c*) R_5/R_3. (See text for details.)

Using these results and the data indicated in figure 4.3 for a growth temperature of 650°C and total flow-rate of 7 l min^{-1}, it is easy to obtain $Ga_xIn_{1-x}As_yP_{1-y}$ epitaxial layers with different compositions between InP ($x = 0$, $y = 0$) and $Ga_{0.47}In_{0.53}As$ ($x = 0.47$, $y = 1$).

The MOCVD technique is attractive for its ability to grow uniform layers over a large area of substrate [1]. Figure 4.5 shows the variation of x-ray spectra (lattice mismatch measured by single-crystal x-ray diffractometry, using (4 0 0) Cu K_α reflection), photoluminescence band-edge wavelength λ_g and growth rate dx/dt of $Ga_{0.28}In_{0.72}As_{0.46}P_{0.54}$–InP over an area of

10 cm^2, having a thickness of 3 μm. The layer exhibits uniform composition over a large area, the variation of lattice mismatch $\Delta a/a$ and of photoluminescence wavelength λ_g being less than 2% and the variation of thickness less than 10%.

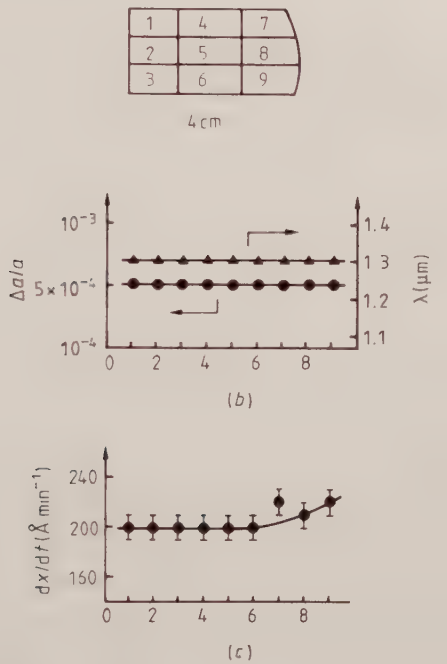

Figure 4.5 Variation of photoluminescence wavelength λ_g, lattice mismatch $\Delta a/a$ and growth rate dx/dt of a GaInAsP epitaxial layer over an area of 10 cm^2 of InP substrate; the thickness of the layer is 3 μm.

4.1.1 Orientation effects

Growth of GaInAsP layers has been carried out on (1 0 0) substrates misoriented 2° off towards (1 1 0). Razeghi *et al* [1] have performed a study of MOCVD growth on (1 0 0), (1 1 1) and (1 1 5) surfaces at 650°C in one run upon six adjacent InP substrates.

Table 4.2 lists the relative PL intensity I, PL halfwidth $\Delta h\nu$ and lattice mismatch $\Delta a/a$ of MOCVD $Ga_{0.28}In_{0.72}As_{0.46}P_{0.54}$ grown on InP substrates of various orientations at 650°C (1 μm thickness).

The relative PL intensity (a measure of the radiative recombination efficiency within the material) is higher for (1 1 5) than for (1 0 0) orientation. Also I is higher for (1 0 0) 2° off than for (1 0 0) exact [1]. The PL

halfwidth (a measure of crystalline quality and impurity incorporation) is higher for (1 1 5) than for (1 0 0) orientation. SIMS analysis shows that the concentration of Si impurity in (1 1 5) samples is higher than in (1 0 0) 2° off, so it is possible that higher PL intensity is due to the higher donor impurity in this layer.

Table 4.2 Relative PL intensity I, PL halfwidth $\Delta h\nu$ and lattice mismatch of GaInAsP ($\lambda = 1.3\ \mu m$) grown on InP substrates by MOCVD.

Orientation	I (au)	$\Delta h\nu$ at 300 K	$\Delta a/a$
InP(Sn)(1 0 0) 2° (1 1 0)	0.1	65	$+1 \times 10^{-3}$
InP(S)(1 0 0) 2° (1 1 0)	0.05	70	$+1 \times 10^{-3}$
InP(Fe)(1 0 0) 2° (1 1 0)	0.05	60	$+1 \times 10^{-3}$
InP(Sn)(1 0 0) exact	0.01	65	$+1 \times 10^{-3}$
InP(S)(1 1 1) 2°	0.8	70	$+1 \times 10^{-3}$
InP(S)(1 1 5) 2°	1	90	$+1 \times 10^{-3}$

4.1.2 Carrier-gas effects

Razeghi [2] has studied the growth of $Ga_xIn_{1-x}As_yP_{1-y}$ layers using 100% H_2 and mixtures of $H_2 + N_2$ as carrier gas, the best morphology and highest photoluminescence intensity being obtained using 50% H_2 + 50% N_2.

Razeghi [2] has also studied the growth of $Ga_xIn_{1-x}As_yP_{1-y}$ layers as a function of total flow-rate ($H_2 + N_2$). The best morphology and highest photoluminescence intensity were obtained for a total flow-rate between 6 and 7 l min^{-1}.

4.1.3 Pyrolysis-oven effects

Razeghi [2] has performed a study of MOCVD growth of GaInAsP layers at a growth temperature of 650°C as a function of temperature of the pyrolysis oven for cracking the PH_3.

Under the growth conditions mentioned above, the PL intensity decreases when the temperature of the pyrolysis oven becomes higher than 750°C. When the parasitic reaction in the gas phase increases, the quality of the epilayer is degraded. The PL intensity and surface quality become independent of the pyrolysis-oven temperature for temperatures lower than 750°C. This implies that, for a growth temperature of 650°C, the pyrolysis oven for cracking of PH_3 is not necessary.

Duchemin *et al* [3] reported that it was very difficult to grow an InP layer at temperatures of 500°C under hydrogen or nitrogen atmospheres containing a flow of PH_3 even up to 1 l min^{-1} without damaging its surface

because of preferential loss of phosphorus. The interpretation was that there was a parasitic reaction between PH_3 and $In(C_2H_5)_3$ with the formation of a complex addition compound which appeared in the form of black fumes or 'aerosol'. They circumvented these difficulties by introducing PH_3 into the reactor through the pyrolysis oven (whose internal temperature was 760°C).

Razeghi [4] previously showed that the purity of starting material such as the alkyl (triethylindium and triethylgallium) or the hydride (arsine and phosphine) sources is responsible for the quality (carrier concentration and mobility) of the epitaxial layers grown by MOCVD (see also chapter 2).

Razeghi [2] showed that, by elimination of the pyrolysis oven for PH_3, considerably better material has been obtained. Without the pyrolysis oven $Ga_xIn_{1-x}As_yP_{1-y}$–InP heterojunctions had a higher mobility, a lower carrier concentration and a higher photoluminescence (PL) intensity with sharper PL halfwidth.

In fact, the temperature of 760°C is not enough to crack PH_3, and the optimal flow-rate of PH_3 for the growth of InP and related compounds with and without the pyrolysis oven is the same. When the temperature of the pyrolysis oven is higher than 760°C, the epitaxial layers become compensated with the impurities coming from the hot quartz tube. Shubnikov–de Haas measurements of these samples also demonstrate the improvement of the quality of epitaxial layers after the elimination of the PH_3 pyrolysis oven.

With the pyrolysis oven present, there is a parasitic reaction between the gas compound inside the reactor near the pyrolysis oven, which induces the deposition of parasitic compounds on the reactor wall. During growth these parasitic particles fall on the epitaxial layer and create the dark spot defects in the layer, degrading its optical and electrical properties.

4.1.4 Photoluminescence spectra

The highly efficient photoluminescence of GaInAsP–InP quantum wells grown by MOCVD has been studied at various temperatures [5]. The high quantum efficiency of the material and careful optimization of the experiment for maximum sensitivity allow the detection of luminescence signals with excitation powers well below the microwatt range.

Figure 4.6 shows a typical photoluminescence spectrum for a four-well structure of $Ga_{0.22}In_{0.78}As_{0.45}P_{0.55}$–InP. The remarkable feature is the sharpness of the lines, even for QW with a 10 Å nominal thickness (10 meV FWHM) at 5 K. Extremely large energy shifts of the luminescence due to the quantum confinement effect of QW are observed up to 1.285 eV for a nominally 10 Å thick QW. As a preliminary test of these multilayer structures, Auger scans were carried out. Samples were prepared by chemically etching a linear bevel through all layers and interfaces.

Figure 4.7 indicates the nature of the bevel and also shows the Auger line scan of the bevel. The four GaInAsP layers are clearly visible, and the interfaces are abrupt.

Growing several QW with different layer thicknesses on the same substrate makes it possible to compare different QW grown under similar conditions. Especially in the case of alloy QW, it is then possible to ascertain the spatial homogeneity of composition and thickness across the wafer:

$$E = h\nu = E_g + E^e_{conf} + E^h_{conf} \tag{4.2}$$

$$E^{e,h}_{conf} \simeq \frac{h^2}{2m^*}\left(\frac{n\pi}{L_z}\right)^2 \qquad n = 1, 2, 3, \ldots$$

where E_g is the alloy band gap, E^e_{conf} and E^h_{conf} are the confining energies for the electron and hole ground states, respectively, L_z is the thickness of the QW and m^* is the effective mass.

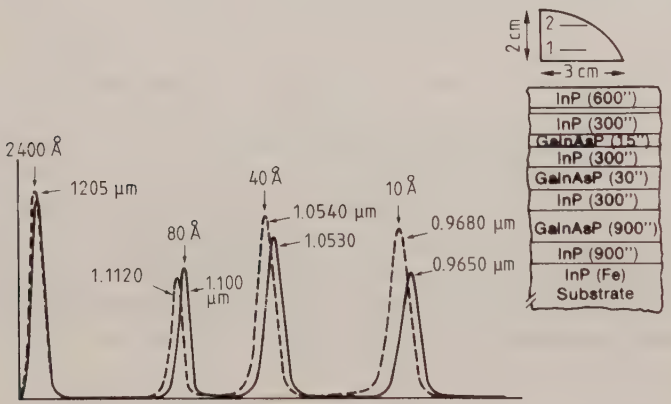

Figure 4.6 Photoluminescence spectrum for a four-well structure of $Ga_{0.22}In_{0.78}As_{0.45}P_{0.55}$, at 7 K.

If the alloy composition varies across a multi-well sample, it gives rise to a constant shift of the ground-state energy (E_g) of the well, *independent* of the well thickness.

On the other hand, if R_1 and R_2 are the two growth rates at two points 1 and 2 (see figure 4.7) of the sample, in the infinitely-deep-well limit we find

$$E^{e,h}_{conf} \simeq L_z^{-2}$$
$$\Delta E \simeq L_z^{-3}\Delta L \simeq L_z^{-2}(R_2 - R_1)/R_2. \tag{4.3}$$

In this case the energy shift between two points on the sample *depends* on the well thickness.

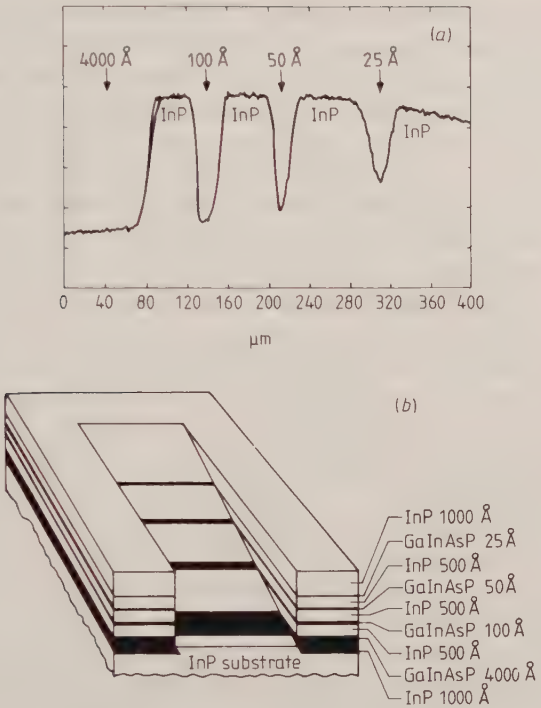

Figure 4.7 (*a*) Auger spectrum of a chemically etched bevel that cuts all four GaInAsP layers. The abscissa indicates the distance along the bevel in micrometres. (*b*) Layer assignments. MOCVD $Ga_{0.25}In_{0.75}As_{0.5}P_{0.5}$–InP.

Figure 4.6 shows that the energy shifts are due to a small variation in well thickness rather than in alloy composition.

4.2 CHARACTERIZATION

4.2.1 Calorimetric absorption and photoluminescence studies of interface disorder in InGaAsP/InP quantum wells

Classical semiconductor devices consist of collections of semiconductor regions separated by interfaces. The devices of the future consist of a collection of interfaces with the minimum of semiconductor between them. The characterization and control of structural, chemical and electronic properties of interfaces therefore is presently at the centre of interest of semiconductor physics. A quantum well (QW) is the simplest possible model system to study the influence of structural interface disorder and variations

of the chemical composition on electronic and optical properties of vertical semiconductor microstructures or heterostructure devices in general. Such disorder results from imperfect growth conditions and has a direct impact on novel devices like graded-index separate-confinement heterostructure single-quantum-well (GRINSCH-SQW) lasers or ballistic transistors. Following Bimberg *et al* [6], we show the results of an investigation of the interface disorder of $In_{0.75}Ga_{0.25}As_{0.5}P_{0.5}$/InP quantum wells grown by MOCVD. We will concentrate here on wells having a width $L_z = 10$ nm.

Calorimetric absorption spectroscopy (CAS) and photoluminescence (PL) are powerful complementary methods for characterizing the interface roughness of such materials. Luminescence spectra of quantum wells are dominated by (radiative) excitonic recombination processes. In contrast, the CAS signal is caused by single-particle interband absorption processes, since only non-radiative recombination is observed. A simple low-temperature thermometer as phonon detector is used to detect the calorimetric absorption signal.

Figure 4.8 shows a photoluminescence spectrum of an $In_{0.75}Ga_{0.25}As_{0.5}P_{0.5}$/InP double quantum well with $L_z = 10$ nm (nominal width, derived from growth parameters). A deconvolution of the luminescence lineshape shows that it represents a superposition of two electron–heavy hole X(e,hh) [7, 8] and one electron–light hole $X(\text{e,lh})_1$ exciton $n = 1$ sub-band transitions. Apparently the two wells of the sample are different, since the energetic position of the excitonic transitions are displaced with respect to each other by 18 meV. Thus the chemical composition of both wells (As/P ratio) cannot be the same, since during the MOCVD growth process the average thicknesses L_z of the two wells can be precisely controlled. The energetic positions of the different components of the luminescence can be used to calculate the compositional variation of the wells. One finds a deviation of the As/P ratio of 3% between the two wells. The energy difference between the X(e,hh) and X(e,lh) transitions—corrected for the different exciton binding energies for heavy and light holes—yields a real thickness of 10.1 nm, in very good agreement with 10 nm, derived from growth parameters. The band-gap discontinuities fitting these results best are $E_c/E_g = E_v/E_g = 0.5$. The lineshape analysis further shows that all lines have a pronounced Gaussian shape. The halfwidth of the two dominant Gaussians is roughly the same (19 meV). Such Gaussian profiles can be taken as indicative of interface disorder [9].

Unfortunately, however, thermalization of the charge carriers into the states of lowest total energy induces a low-energy shift of the luminescence and a reduction of halfwidth, as proved by temperature- and excitation-dependent experiments. The minimum of total energy of the electron–hole pairs corresponds to the region with the largest local thickness L_z. Figure 4.9 visualizes in a qualitative way the difference of band structure between QW with ideal and real interfaces. Thus low-temperature luminescence does not display the true thickness distribution and can underestimate

the interface disorder of the quantum well, as will now be shown. In view of the fact that a detailed statistical interpretation of the halfwidth of the Gaussians has still to be developed, a quantitative determination of the interface roughness ΔL_z is usually based on the formula

$$\Delta L_z = \tfrac{1}{2}\,\Delta(\hbar\omega) L_z / \Delta E_g \tag{4.4}$$

where $\Delta(\hbar\omega)$ is the full width at half-maximum of the X(e,hh) luminescence line and ΔE_g the energy-gap difference between the QW and the

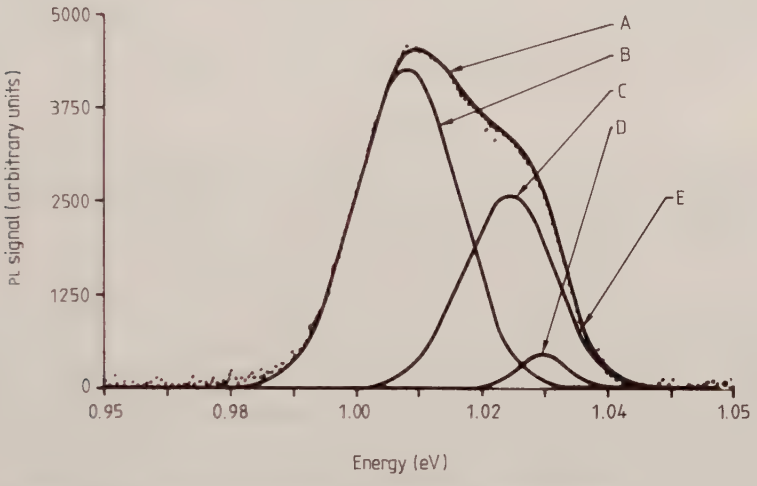

Figure 4.8 Photoluminescence of an $In_{0.75}Ga_{0.25}As_{0.5}P_{0.5}$/InP double quantum well with $L_z = 10$ nm nominal at 1.4 K. A, experimental curve; B, Gaussian fit X (e, hh), well 1; C, Gaussian fit X (e, hh), well 2; D, Gaussian fit X (e, lh), well 1; E, superposition of all three Gaussian lines.

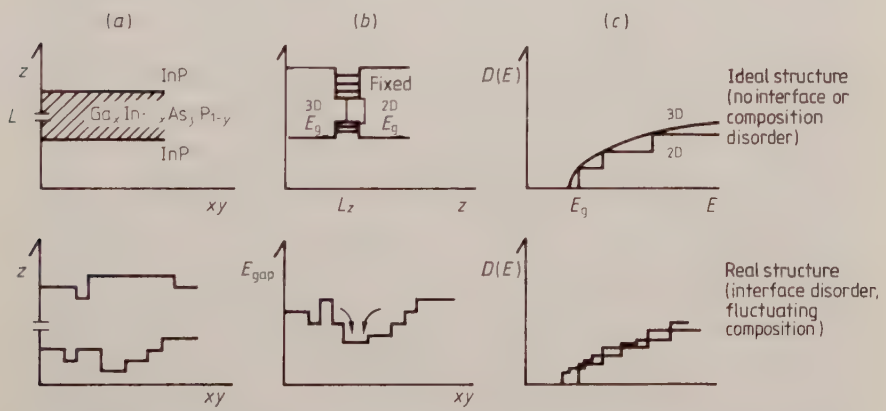

Figure 4.9 Comparison of the ideal and real structures of quantum-well interfaces. (*a*) Sample structure; (*b*) 2D energy gap; (*c*) density of states.

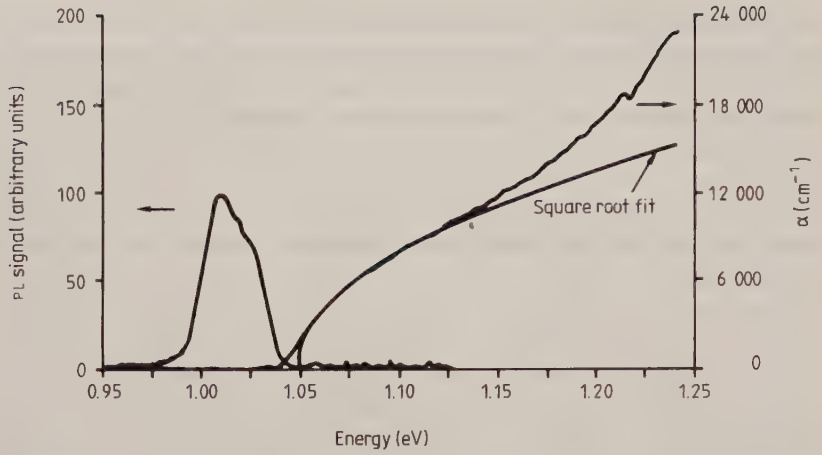

Figure 4.10 Calorimetric absorption spectrum (right scale) and photoluminescence spectrum (left scale) of an $In_{0.75}Ga_{0.25}As_{0.5}P_{0.5}$/InP double quantum well with $L_z = 10$ nm nominal at 1.3 K.

three-dimensional material. In the present case, one can derive from $\Delta(\hbar\omega) \simeq 19$ meV an interface roughness $\Delta L_z = 1$ nm.

Figure 4.10 shows the calorimetric absorption spectrum and additionally the luminescence for comparison. The luminescence is shifted to lower energy by about 35 meV compared to the onset of absorption. Surprisingly the shape of the absorption curve is well described by a $1/E(E - E_g)^{1/2}$ dependence known from textbook theory of electron–hole interband absorption in three-dimensional semiconductors.

No influence of excitonic enhancement effects can be seen. This is due to the extremely high radiative efficiency of the excitonic recombination in quantum wells [8]. CAS in contrast reveals only non-radiative recombination processes. Structural disorder of the interface causes not only the Gaussian luminescence lineshape but also the square-root dependence of the absorption coefficient (see figure 4.10). For a quantum well with ideally abrupt interfaces one would expect a step-function density of states and absorption coefficient. If we take into account interface disorder or fluctuations of the chemical composition, then the two-dimensional energy gap (E_g) fluctuates in the plane parallel to the interface. Thus the ideal step-function-like density of states is smeared out and the square-root dependence is re-established. Therefore the absorption curve is a superposition of all different absorption processes according to the statistical weight of a given thickness and displays the thermal equilibrium situation. The onset of the square-root fit to the absorption gives the mean quantum-well width. The energy difference of the onset of the CAS spectrum and the onset of the dominant luminescence band (X(e,hh)) is 48 meV. This value has to be corrected by the binding energy of the 2D exciton ($\simeq 10$ meV) and its

localization energy ($\simeq 5$ meV) [9]. The resulting difference can be used to estimate the interface roughness. Again using $\Delta L_z = \frac{1}{2}\Delta(\hbar\omega)L_z/\Delta E_g$, but now $\Delta(\hbar\omega) = 33$ meV, one can find $\Delta L_z = 1.8$ nm. This value is by almost a factor 2 larger than that derived from the full width at half-maximum of the dominant luminescence line in figure 4.9.

Both the surprising square-root dependence of the CAS spectrum and the Gaussian shape of the photoluminescence (PL) prove consistently the dominant influence of interface disorder on optical and electronic properties of quantum wells. Luminescence alone, however, strongly underestimates the magnitude of the disorder. In contrast to PL, CAS displays the true interface structure of the quantum well, since no thermalization effects induce low-energy shifts.

4.2.2 Magnetotransport

Here we describe the growth of single-quantum-well (SQW), multiquantum-well (MQW) and superlattice (SL) samples from GaInAsP($\lambda = 1.3$ μm)/InP heterostructures by low-pressure metallorganic chemical vapour deposition [10]. Evidence of two-dimensional electron gases (2DEG) in these structures is also presented.

The optimum conditions for the reduced-pressure growth of InP and $Ga_{0.25}In_{0.75}As_{0.50}P_{0.50}$ ($\lambda = 1.3$ μm) are presented in table 4.3. InP/GaInAsP interfaces can be obtained by switching both TEGa and AsH_3 flows into the reactor. GaInAsP/InP interfaces can be obtained by turning off the AsH_3 and TEGa flows. The growth rate is small (3 Å s^{-1}) and it takes less than 1 s for a gas flow to reach its new steady state.

The exact composition of the QW samples is difficult to measure directly; however, x-ray diffraction and photoluminescence measurements carried out on thick ($\simeq 1$ μm) layers of GaInAsP grown under identical conditions indicate that the GaInAsP ($\lambda = 1.3$ μm) is lattice-matched to within $\Delta a/a \simeq \pm 10^{-3}$.

Various heterojunction, SQW, MQW and SL samples were employed for this study. The SQW consisted of GaInAsP of 100 Å thickness, located

Table 4.3 Optimized growth parameters.

Parameter	InP	$Ga_{0.25}In_{0.75}As_{0.50}P_{0.50}$
Growth temperature (°C)	650	650
Total flow ($N_2 + H_2$) (l min^{-1})	7	7
N_2–TEIn bubbler flow (cm^3 min^{-1})	350	350
H_2–TEGa bubbler flow (cm^3 min^{-1})	–	60
PH_3 flow (cm^3 min^{-1})	530	530
AsH_3 flow (cm^3 min^{-1})	–	21
Growth rate (Å min^{-1})	100	150

between InP layers. The MQW samples consisted of 3–8 GaInAsP wells of $L_z = 100$–400 Å thickness with $L_B \simeq 100$–200 Å (L_z is the thickness of the GaInAsP well and L_B is the InP barrier thickness). The superlattices, consisting of 21 alternate layers of n-$Ga_{0.25}In_{0.75}As_{0.50}P_{0.50}$ of 75 Å thickness and n-InP of 50 Å thickness, were grown on a semi-insulating InP substrate.

Figure 4.11 indicates the Auger line scan along the bevel, which had an angle of 0.02°. The Auger results indicate that three distinct GaInAsP layers with abrupt interfaces exist. Shubnikov–de Haas measurements were also performed on these samples.

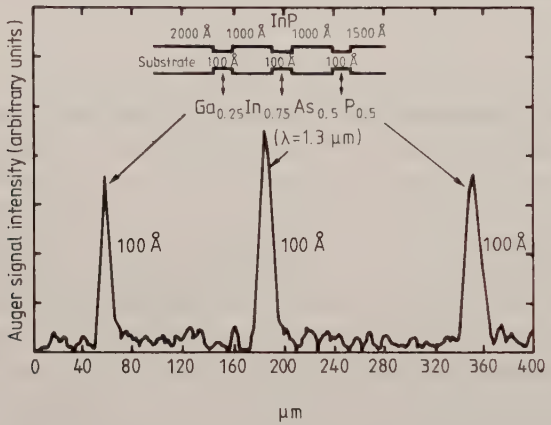

Figure 4.11 Phosphorus profile using Auger measurements on a chemically etched bevel of MQW of GaInAsP–InP, comprising three GaInAsP ($\lambda = 1.3$ μm) wells of 100 Å thickness.

The band discontinuities in lattice-matched GaInAsP–InP heterostructures have been studied by Forrest *et al* [11] using the C–V technique: they found the conduction-band discontinuity ΔE_c to be 39% of the difference in the band gaps across the whole range of alloy compositions. This gives $\Delta E_c \simeq 170$ meV in the samples considered here, with the exception of the quantum well with higher phosphorus content, for which a discontinuity of $\Delta E_c \simeq 140$ meV is deduced.

Figure 4.12(*a*) [12] shows typical Shubnikov–de Haas oscillations obseved at $T = 4.2$ K, performed on MQW of $Ga_{0.25}In_{0.75}As_{0.50}P_{0.50}$–InP with the magnetic field B perpendicular to the MQW heterojunction interfaces. These oscillations disappear when the magnetic field B is applied parallel to the interfaces. This field orientation dependence of the Shubnikov–de Haas oscillation is evidence for the formation of a 2DEG in the wells of $Ga_{0.25}In_{0.75}As_{0.5}P_{0.5}$.

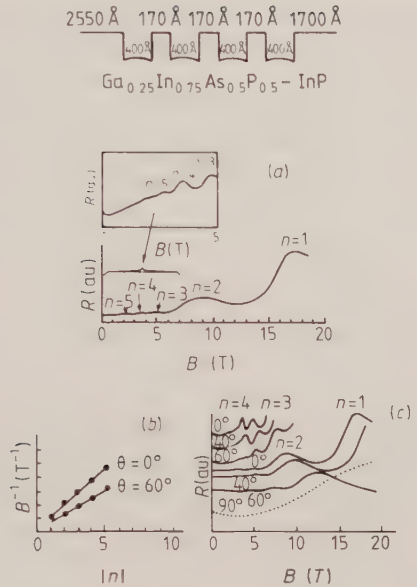

Figure 4.12 (*a*) Magnetoresistance oscillations as a function of the magnetic field B. For reasons of clarity, the oscillations in the range 0–5 T are shown at higher magnification in the inset. (*b*) Reciprocal of magnetic field at maxima of magneto-oscillations versus Landau quantum number (n) for different values of θ for a $Ga_{0.25}In_{0.75}As_{0.50}P_{0.50}$–InP MQW grown by MOCVD. (*c*) Magnetoresistance oscillations as a function of the magnetic field B for different values of θ.

Figure 4.12(*b*) shows the reciprocal magnetic field corresponding to the magneto-oscillation maxima of resistivity as a function of the Landau index for different values of θ (figure 4.12(*c*)), which is the angle between B and the normal to the interfaces. The oscillations are periodic in $1/B$, and they follow the expected $(\cos\theta)^{-1}$ dependence of a 2DEG. This is evidence for the two-dimensionality of the electron gas under consideration.

Figure 4.13 gives the reciprocal magnetic field corresponding to the magneto-oscillation maxima of the resistivity as a function of the Landau index for different values of θ for a MQW with 21 alternate layers of $Ga_{0.25}In_{0.75}As_{0.50}P_{0.50}$ ($L_z = 70$ Å) and InP ($L_B = 50$ Å). The oscillations are periodic in $1/B$, and they follow the expected $(\cos\theta)^{-1}$ dependence of a 2DEG.

Figure 4.14 gives the reciprocal magnetic field corresponding to the magneto-oscillations versus Landau quantum number for different values of θ for a $Ga_{0.25}In_{0.75}As_{0.50}$–InP single-quantum-well structure with $n_{2D} = 4.16 \times 10^{11}$ cm^{-2}.

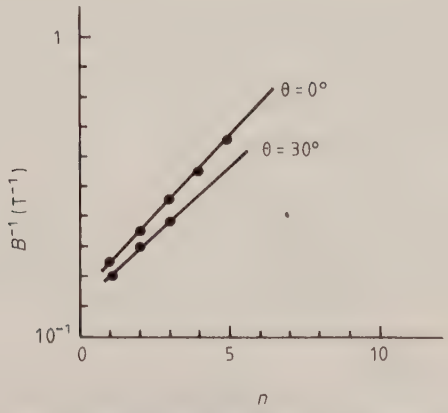

Figure 4.13 Reciprocal of magnetic field at maxima of magneto-oscillations versus Landau quantum number for different values of θ for a $Ga_{0.25}In_{0.75}As_{0.50}P_{0.50}$–InP superlattice with 21 alternate layers ($L_z = 70$ Å and $L_B = 50$ Å).

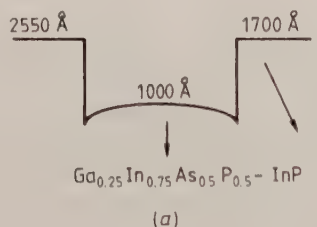

(*a*)

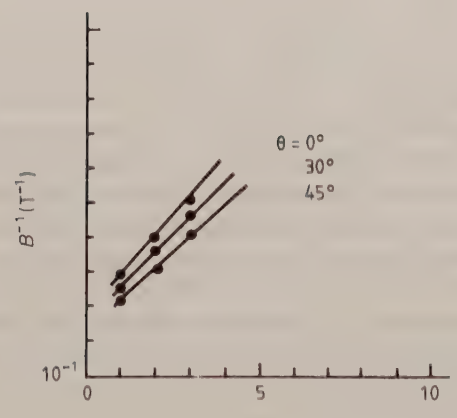

(*b*)

Figure 4.14 Reciprocal field at maxima of the magneto-oscillations versus Landau quantum number for different values of θ (*b*), for a $Ga_{0.25}In_{0.75}As_{0.50}P_{0.50}$–InP heterojunction (*a*).

Table 4.4 The sample characteristics.

Sample	Well width, L_z (Å)	Barrier width, L_B (Å)	Number of wells	λ (μm) at 300 K	Y	n_{SdH} (10^{11} cm^{-2})	m_c^*/m
A	100	–	1	1.18	0.50	5.9	0.0665
B	100	1360	3	1.32	0.69	6.7	0.0600
C	100	85	10	1.31	0.68	4.95	0.0609
D	400	200	2	1.34	0.67	5.46	0.0625
E	400	200	3	1.32	0.65	5.53	–
F	400	200	4	1.30	0.62	5.58	0.0586
G	1000	–	1	1.32	0.64	4.2	0.0616

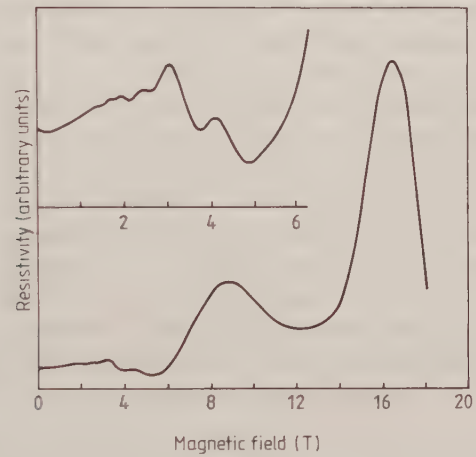

Figure 4.15 The Shubnikov–de Haas oscillations in GaInAsP–InP sample F at 1.6 K. The two series of oscillations, with fundamental fields of 5.2 and 12 T, can be clearly seen in the expanded inset.

The individual sample details and the results of Shubnikov–de Haas measurements of the two-dimensional electron concentrations are given in table 4.4. The latter range from 4×10^{11} to 8×10^{11} cm^{-2}, and were all shown to be due to two-dimensional conduction by rotation of the samples relative to the magnetic field. Perhaps the most interesting of these measurements are shown in figure 4.15 for sample F, a multiquantum-well structure consisting of four 400 Å wells. Two series of Shubnikov–de Haas oscillations are seen, corresponding to electron concentrations of 5.8×10^{11} and 2.5×10^{11} cm^{-2} in either two electric sub-bands or two different layers. Hall effect measurements on this sample give a total sheet carrier concentration of 9×10^{11} cm^{-2}, indicating that these two populations are contributing the majority of the conduction. It is a general feature of the

Shubnikov–de Haas measurements that the two-dimensional carrier concentrations deduced are consistent with conduction in a single layer, even in the multiquantum-well samples, from comparison with the doping levels. The electron concentrations are sufficiently high to require the transfer of charge from the buffer and capping layers, which may lead to the formation of what might be termed a 'depleted superlattice', as shown schematically in figure 4.16. The band structure has tipped sideways, so that the majority of the electrons have accumulated at a single interface. This sort of behaviour has also been suggested in GaInAs–InP superlattices (see chapter 3), where the use of lightly doped buffer and capping layers leads to the apparent formation of an accumulated layer at one interface only of a multiquantum-well structure, while structures without buffer and capping layers showed uniform behaviour with conduction occurring in all the quantum wells. Similar effects have also been seen in GaInAs–AlInAs superlattices [13]. The two separate populations observed in sample F might arise from the occupation of a second sub-band at the first heterojunction interface, from population of two adjacent layers, or from the formation of a 2DEG at the interfaces with both buffer and capping layers. The last of these is thought to be the most likely in view of the extent of the electron wavefunctions at a single heterojunction, of order 100 Å, compared with the well width of 400 Å, and the relatively small proportion of the total electron concentration found in the second sub-band in GaInAs–AlInAs, GaInAs–InP and GaAs–GaAlAs heterojunctions [14–16]. Shubnikov–de Haas measurements on heterojunctions where two sub-bands are occupied also show that the two series of oscillations should interact at high fields, so that neither series is periodic in $1/B$ [14]. This is not observed in the present case.

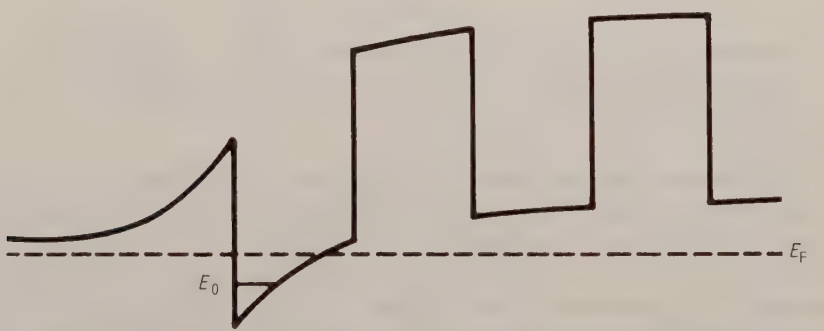

Figure 4.16 The conduction-band edge of the depleted superlattice, with a 2DEG in one well only, proposed to explain the electron concentrations measured using the Shubnikov–de Haas effect.

Cyclotron resonance measurements have been performed [17] at 4.2 K using an optically pumped far-infrared laser at wavelengths between 119 and 54 μm. The electron effective masses deduced were in the range

$m^*/m = 0.0585–0.0625$ except for the quantum well with higher phosphorus content, where a value of $m^*/m = 0.0665$ was measured. These values are 10–16% higher than the band-edge masses in GaInAsP of the appropriate composition [18] because of the non-parabolicity of the conduction band. Three-band $k \cdot p$ theory [19] gives the expression

$$m_0^*/m_{cr}^* = 1 + (2K_2/E_g)(E_F + T_z) \tag{4.5}$$

for the cyclotron mass in the limit $h\omega_c < E_F$; here m_0^* is the band-edge mass and T_z is the kinetic energy associated with motion perpendicular to the layers. The coefficient K_2 (see chapter 3) is a negative quantity, which should be related to the band structure of the material and have the value -0.8 in GaInAsP. If the 2DEG are considered to be confined in square potential wells, T_z is approximately equal to the sub-band energy E_0 and mass enhancements of 3–9% are calculated. However, the enhancements will be different if the multiquantum-well samples are assumed to form depleted superlattices containing one heterojunction-like 2DEG. For a heterojunction T_z can be estimated from the variational wavefunction proposed by Fang and Howard [20], and mass enhancements in the range 6–8% are deduced. The non-parabolicity is thus greater than predicted by equation (4.5) regardless of whether the samples form uniform or depleted superlattices. However, recent measurements on bulk $Ga_{0.47}In_{0.53}As$ (see chapter 3) and GaAs [21], and on 2DEG in the same materials [22, 23], also show higher non-parabolicities than predicted by three-band $k \cdot p$ theory and are well described by equation (4.5) if K_2 is taken to be greater than the calculated values by a factor of approximately 2. These results cannot be used to derive a value for the effective K_2 because of the uncertainty of the nature of the potential confining the electrons and possible errors in the measured effective masses due to the broad resonances seen, but they do suggest that, as in other III–V semiconductors, the non-parabolicity in GaInAsP is considerably greater than predicted by three-band $k \cdot p$ theory.

Figure 4.17 shows measurements of weak magnetophonon resonances in the second derivative of the magnetoresistance of sample F. Rotation of the sample relative to the magnetic field showed that the oscillations were due to two-dimensional conduction. The magnetophonon effect results from resonant scattering of the electrons by longitudinal optic (LO) phonons [24], and in GaInAsP the scattering has been found to be dominated by an optic-phonon frequency of about 270 cm^{-1} associated with the $Ga_{0.47}In_{0.53}As$ ternary alloy and thought to result primarily from Ga–As vibrations [25]. The resonance positions are given by

$$\omega_{LO} = NeB/m^* \tag{4.6}$$

in which the effective mass must be corrected for the effects of non-parabolicity [26, 27]. The product NB_N is constant and has a value of 17.4 T in sample F. This corresponds to a phonon frequency of 269 cm^{-1}, in

good agreement with the values measured in bulk material [25]. The oscillations observed were rather weak and showed no evidence of the long-range electron–phonon interactions and interface phonon effects seen in GaInAs–InP and GaInAs–AlInAs heterostructures [26, 27].

So, the electron effective masses are found to be enhanced over the band-edge masses in the bulk material due to non-parabolicity, and the energy of the optic phonon dominating the electron scattering is found to be similar to that in bulk GaInAsP. The uniformly doped multiquantum-well structures display a tendency to form a depleted superlattice, in which all the carriers are confined at a single interface, and this is believed to be due to the presence of thick InP buffer and capping layers.

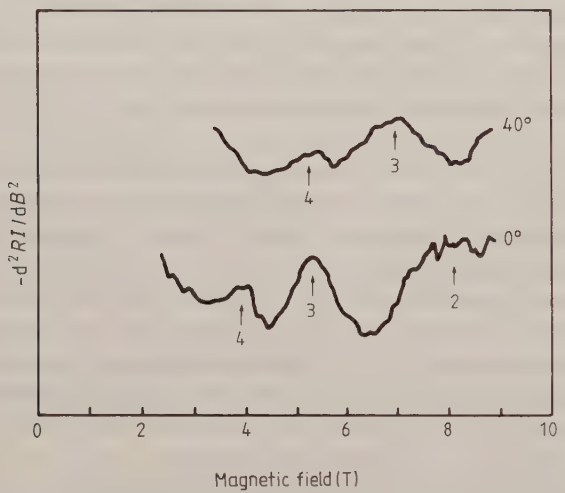

Figure 4.17 The magnetophonon resonances in the second derivative of the magnetoresistance of sample F at 80 K. Rotation of the sample normal 40° away from the magnetic field direction shows that the oscillations are due to two-dimensional conduction.

4.2.3 Observation of quantum Hall effect in a GaInAsP–InP heterostructure grown by MOCVD

Razeghi *et al* [28] have used high-quality trimethylindium (TMIn) instead of triethylindium (TEIn) for the growth of InP and GaInAsP by MOCVD.The growth conditions for InP and $Ga_{0.25}In_{0.75}As_{0.50}P_{0.50}$ (TMIn) determined during these investigations are presented in table 4.5. High-quality InP epitaxial layers have been grown, with carrier concentration as low as 3×10^{13} cm^{-3} and electron Hall mobility as high as 6300 cm^2 V^{-1}s^{-1} at 300 K and 200 000 cm^2 V^{-1}s^{-1} at 50 K (see chapter 2). GaInAsP epilayers lattice-matched to InP have been grown, with a carrier

concentration of 6×10^{14} cm^{-3} and electron Hall mobility as high as 6400 cm^2 V^{-1} s^{-1} at 300 K and 36 000 cm^2 V^{-1} s^{-1} at 77 K.

Figure 4.18 shows the evolution of the mobility as a function of temperature. The structure is described in the inset. It consists of a 1000 Å thick n-doped InP layer with an electron concentration of 10^{17} cm^{-3}, and a 150 Å thick undoped InP spacer layer, covered by 5000 Å thick undoped $Ga_{0.25}In_{0.75}As_{0.50}P_{0.50}$.

Table 4.5 Optimized growth conditions.

Parameter	InP	$Ga_{0.25}In_{0.75}As_{0.50}P_{0.50}$
Growth temperature (°C)	550	550
H_2 flow (l min^{-1})	6	6
H_2–TMIn bubbler flow (cm^3 min^{-1})	50	50
H_2–TEGa bubbler flow (cm^3 min^{-1})	–	40
PH_3 flow (cm^3 min^{-1})	270	270
AsH_3 flow (cm^3 min^{-1})	–	20
Growth rate (Å min^{-1})	200	350
Carrier concentration (cm^{-3})	3×10^{13}	6×10^{14}
Electron mobility (77 K) (cm^2 V^{-1} s^{-1})	150 000	36 000

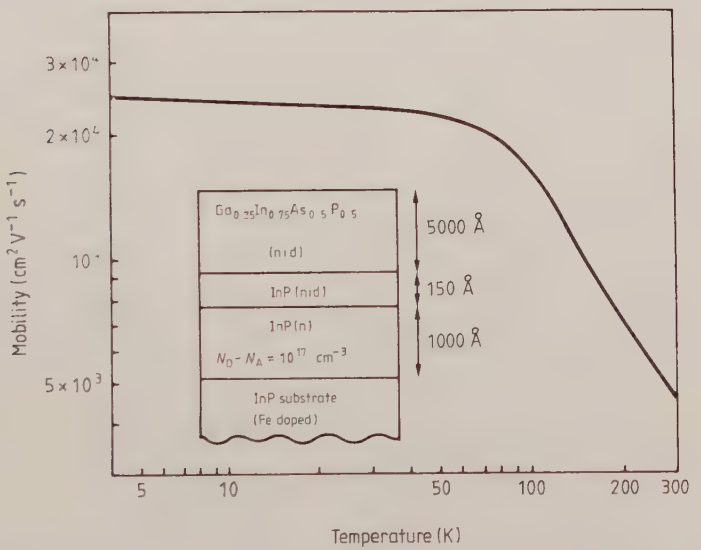

Figure 4.18 Variation of electron Hall mobility as a function of temperature for a GaInAsP–InP epilayer grown by MOCVD (nid = non-intentionally doped).

The electron Hall mobility of this modulation-doped structure was 5500 $cm^2 V^{-1} s^{-1}$ at 300 K, 20 000 $cm^2 V^{-1} s^{-1}$ at 77 K and 25 000 $cm^2 V^{-1} s^{-1}$ at 4 K, with a sheet carrier concentration of about 4.4×10^{11} cm^{-2} at low temperature. The variation of mobility as a function of temperature is clearly characteristic of a two-dimensional electron gas, with high mobility at low temperature due to the fact that carriers located in the quaternary compound near the interface are separated from the ionized donor impurities.

Figure 4.19 shows the evolution of the Shubnikov–de Haas oscillations for various angles θ between the magnetic field direction and the normal to the interface. The ρ_{xx} extrema appear at constant values of the perpendicular component of the magnetic field $B_\perp = B \cos \theta$, and the oscillations vanish completely at $\theta = 90°$, demonstrating the two-dimensionality of the system. In figure 4.20, the low-field oscillations of the longitudinal resistivity ρ_{xx} at $\theta = 0$ are detailed. A plot of the index of the extrema observed, as a function of the inverse magnetic field, is shown in the inset of figure 4.20. It is clearly periodic, with a period $\Delta(1/B) = 0.11$ T^{-1}. The electron density is derived from the expression (see chapter 3)

$$n = \frac{2e}{h\ \Delta(1/B)}. \tag{4.7}$$

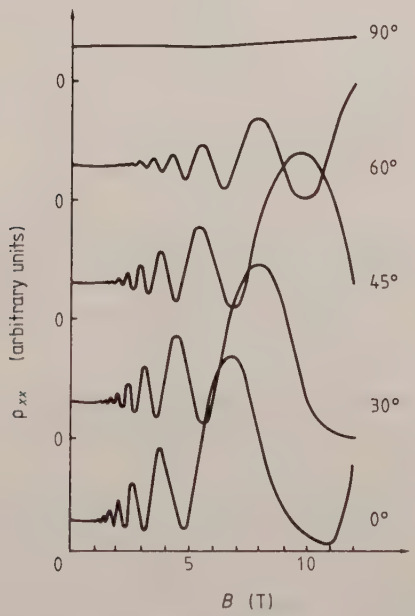

Figure 4.19 Shubnikov–de Haas oscillations as a function of magnetic field for various tilt angles measured at 1.6 K for a GaInAsP–InP epilayer grown by MOCVD.

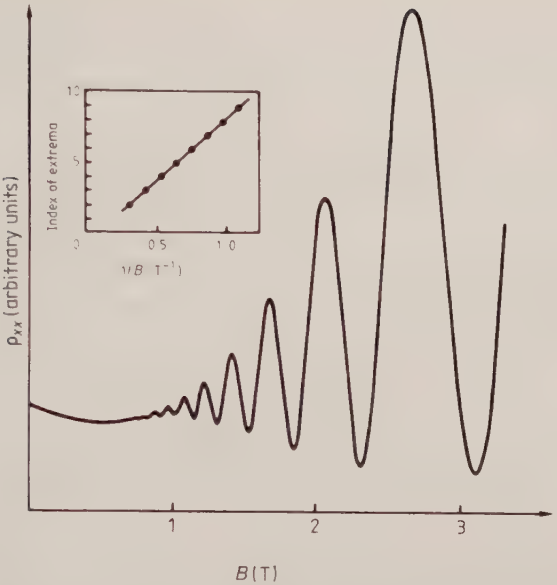

Figure 4.20 Experimental recordings of magnetoresistance at low field (inset: standard plot of the inverse of the field position of the maxima in Γ_{xx} versus their index), for a GaInAsP–InP epilayer grown by MOCVD.

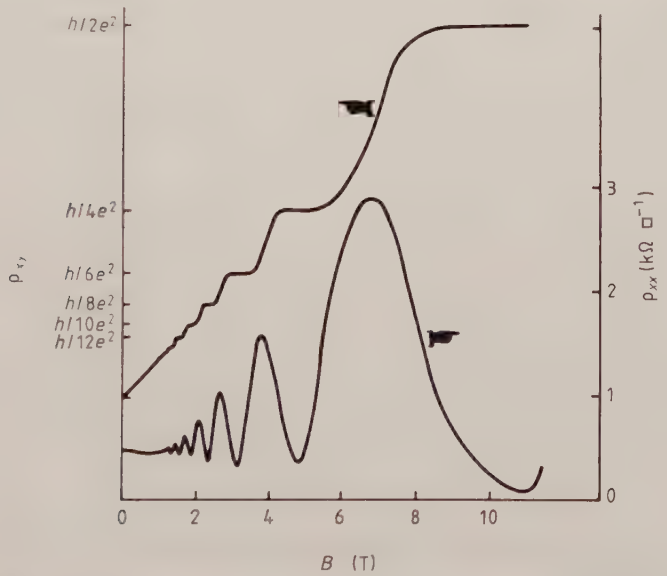

Figure 4.21 Shubnikov–de Haas and quantum Hall effect as a function of magnetic field measured at 1.6 K for a GaInAsP–InP epilayer grown by MOCVD. The field is normal to the heterojunction plane.

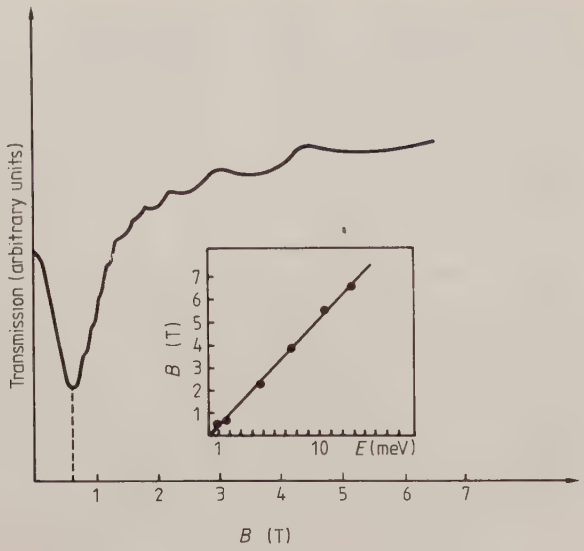

Figure 4.22 Cyclotron resonance spectrum of a $Ga_{0.25}In_{0.75}As_{0.6}P_{0.4}$–InP heterojunction at $T = 1.6$ K, for $\lambda = 1205$ μm. Inset: plot of the resonance magnetic field versus excitation pulsation.

One can deduce in this case $n = 4.4 \times 10^{11}$ cm^{-2}, in perfect agreement with the value of population n_H obtained from the classical Hall effect measurement.

Figure 4.21 shows the diagonal resistivity ρ_{xx} and the Hall resistivity ρ_{xy} as functions of magnetic field at 4 K, for $\theta = 0$. Hall plateaux h/ie^2 with even values of i are resolved up to $h/20e^2$. The field at which only one Landau level is occupied is determined to be $B = 18.9$ T.

Figure 4.22 shows a typical cyclotron resonance spectrum obtained at a wavelength of 1205 μm, for $\theta = 0°$ [29]. Ando oscillations are clearly resolved. Their period in $1/B$ is about $\Delta(1/B) \equiv 0.1085$ T^{-1}, so that the electronic density derived at the heterojunction is $n \equiv 4.4 \times 10^{11}$ cm^{-2}. It remains in quite good agreement with low-field Hall measurements. The plot of the resonance field as a function of the energy of the excitation source is shown in the inset of figure 4.22. The dependence is clearly linear, as expected, and allowed the deduction of an electronic effective mass of $m^* = (0.059 \pm 0.001)m_0$ in the quaternary compound.

4.2.4 Disorder of a $Ga_xIn_{1-x}As_yP_{1-y}$–InP quantum well by Zn diffusion

Optical integrated circuits (IC) require that optical and electrical components can be fabricated on a single chip: for instance, monolithic optical IC

with a combination of lasers and waveguides; lasers and field-effect transistors (FET); or PIN detectors and FET; etc. In this case, semi-insulating Fe-doped InP substrates should be used, and p–n junctions can be achieved by Zn diffusion.

However, the diffusion of Zn into an $Al_xGa_{1-x}As$–GaAs superlattice and a $Ga_xIn_{1-x}As$–GaAs superlattice has been shown to enhance intermixing of these SL layers greatly [30].

Razeghi *et al* [31] have shown that Zn-enhanced intermixing is not just peculiar to the $Al_xGa_{1-x}As$–GaAs lattice-matched system or the $Ga_xIn_{1-x}As$–GaAs lattice-mismatched system. It is also effective in $In_xGa_{1-x}As_yP_{1-y}$–InP (lattice-matched) single-quantum-well and multi-quantum-well structures.

For that study, various SQW and MQW were employed. The SQW consisted of a $Ga_{0.25}In_{0.75}As_{0.5}P_{0.5}$ QW of 100 Å thickness located between two 1000 Å thick InP layers. The MQW consisted of 10 $Ga_{0.25}In_{0.75}As_{0.5}P_{0.5}$ wells of $L_z = 100$ Å thickness with $L_B = 100$ Å (L_B is the InP barrier), also between two 1000 Å thick InP layers. Zn diffusion was accomplished via a semi-closed quartz box using Zn_3P_2 as the Zn source [32].

Figure 4.23 shows the variation of photoluminescence wavelength λ(PL) of the SQW of GaInAsP as a function of diffusion temperature T_d, for a diffusion time of 120 min. The λ(PL) increases when T_d increases, up to 650°C, and then λ(PL) decreases for $T_d > 650$°C.

Figure 4.24 represents the variation of λ(PL) of this SQW as a function of diffusion time t_d for $T_d = 550$°C. The λ(PL) increases when t_d increases.

Figure 4.25 shows the variation of λ(PL) of a 10-period GaInAsP–InP superlattice with $L_z = 100$ Å and $L_B = 100$ Å.

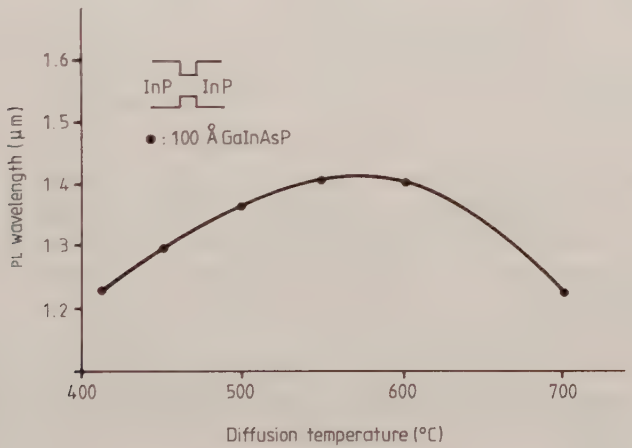

Figure 4.23 The variation of photoluminescence wavelength of a single quantum well of GaInAsP–InP with 100 Å thickness as a function of Zn diffusion temperature for a diffusion time of 120 min.

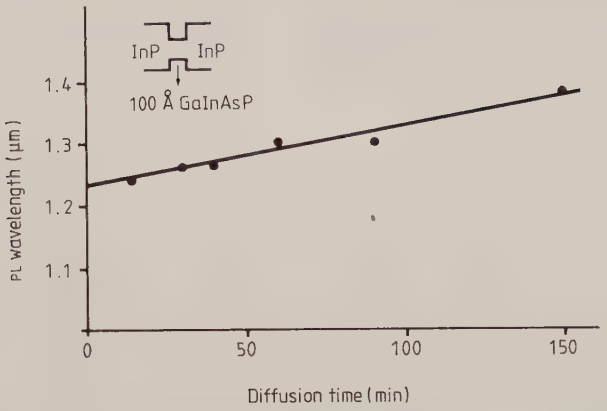

Figure 4.24 The variation of photoluminescence wavelength of a quantum well of GaInAsP, 100 Å thick, as a function of Zn diffusion time for a diffusion temperature of 550°C.

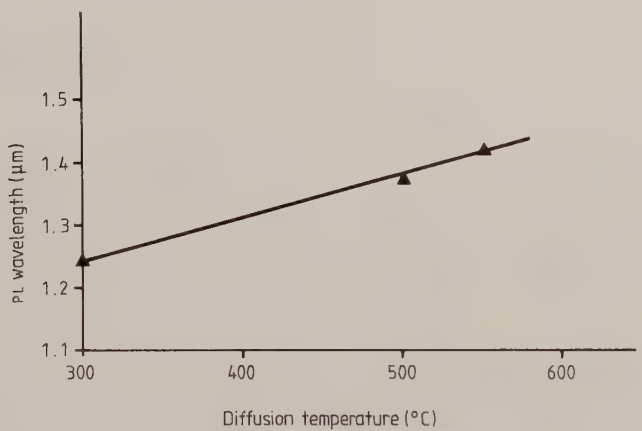

Figure 4.25 The variation of photoluminescence wavelength of a 10-period GaInAsP–InP superlattice with $L_z = 100$ Å and $L_B = 100$ Å (L_z is thickness of GaInAsP quantum well, and L_B is thickness of InP barrier) as a function of Zn diffusion temperature for a diffusion time of 120 min.

The morphology of SQW and MQW after Zn diffusion did not change. The intensity of the PL spectra decreases and the FWHM of the PL peak increases with diffusion time.

Thermal annealing without Zn diffusion of an SQW at 650°C did not result in any wavelength change.

In situ Zn-doped GaInAsP–InP SQW and MQW layers did not show any variation of λ(PL) after 4 h annealing at $T = 650^{\circ}C$ (under PH_3 and H_2). This shows that the variation of PL wavelength is due to Zn diffusion.

Discussion

Van Vechten [33], Burnham *et al* [34] and Laidig *et al* [35] have demonstrated that the diffusion of Zn into GaAs–GaAlAs superlattice structures promotes the intermixing of Al and Ga dramatically. They have suggested that this effect might be caused by an association between the interstitially diffusing Zn ions (Zn_i^+) and vacancies on the cation sublattice V_a (cation atoms are Ga or Al). A similar interpretation can be used for GaInAsP–InP QW layers diffused with Zn.

The increase of the photoluminescence wavelength must be attributed to the interdiffusion of In and Ga at the interfaces of the InP–GaInAsP–InP layers; interdiffusion of As and P would provide a *lower* λ(PL), which is contrary to the experimental results, at least up to a diffusion temperature of $T_d = 650^{\circ}C$.

It is suggested that a closely associated Zn–vacancy pair formed by substitutional Zn moving into a neighbouring interstitial site forms an intermediate link between purely interstitial and substitutional Zn according to the reactions [30]

$$Zn_i^+ + V_a^0 \rightleftarrows (Zn_i, V)^+ \rightleftarrows Zn_s^- + 2h^+. \tag{4.8}$$

V_a^0 indicates a neutral cation vacancy and h a hole. Neighbouring Ga or In atoms could move into the vacancy of the (Zn_i, V) pair, but the Zn_i would remain attached. In this way, interdiffusion of Ga and In would be promoted as well as provide an additional mechanism for Zn diffusion; however, the interdiffusion of As and P can be neglected.

The interdiffusion of In from the InP barriers into the $Ga_xIn_{1-x}As_yP_{1-y}$ quantum well and the opposite, Ga from the quantum well into the InP barriers, can be approximated as

$$X(Z, t) = \frac{1}{2} X_0 \left[\operatorname{erf}\left(\frac{L_z/2 - Z}{2(Dt)^{1/2}} \right) + \operatorname{erf}\left(\frac{L_z/2 + Z}{2(Dt)^{1/2}} \right) \right] \tag{4.9}$$

with $X(Z, t)$ the molar fraction of Ga at time t and position Z, OZ the diffusion axis (the reference $Z = 0$ is the centre of the quantum well), L_z the quantum-well thickness, t the diffusion time, X_0 the initial molar fraction of Ga in the QW and D the In–Ga interdiffusion coefficient.

The variation of the Ga molar fraction $X_d(t)$ in the QW after Zn diffusion time t is then

$$X_d(t) = X_0 - (1/L_z) \int_{-L_z/2}^{+L_z/2} X(Z, t)\, dZ. \tag{4.10}$$

Integration gives

$$X_d(t) = X_0\left\{1 - \operatorname{erf}\left(\frac{L_z}{2(Dt)^{1/2}}\right) + \frac{2(Dt)^{1/2}}{L_z\pi^{1/2}}\left[1 - \exp\left(\frac{L_z^2}{4Dt}\right)\right]\right\}. \quad (4.11)$$

$X_d(t)$ can be experimentally deduced from photoluminescence measurements. The recombination energy in an alloy QW can be approximated by

$$E = h\nu = hc/\lambda = E_g(t) + E^e_{conf} + E^h_{conf} \quad (4.12)$$
$$\lambda(\mu m) = 1.24/E(eV).$$

E^e_{conf} and E^h_{conf} are the confining energies for the electron and hole ground states respectively, λ is the photoluminescence wavelength, h is Planck's constant and c is the speed of light in a vacuum.

As we neglect the interdiffusion of As and P, y (in $Ga_xIn_{1-x}As_yP_{1-y}$) is considered constant, and the band-gap energy of a QW layer after Zn diffusion may be approximated by the formula [36]

$$\begin{aligned} E_g(t) = {} & 1.35 + 0.668(X_w(t)) - 1.17\,Y + 0.758(X_w(t))^2 + 0.18\,Y^2 \\ & + 0.069\,Y(X_w(t))^2 - 0.069\,Y(X_w(t)) \\ & - 0.322(X_w(t))\,Y^2 + 0.03(X_w(t))^3 \end{aligned} \quad (4.13)$$

with $X_w(t)$ the concentration of Ga at time t in the QW,

$$E_g(t) = 1.24/\lambda(t) \quad (4.14)$$

$$\Delta\lambda = \frac{1.24}{E(X_w(t))} - \frac{1.24}{E(X_0)}. \quad (4.15)$$

Figure 4.26 shows the experimental and calculated data of X_d as a function of diffusion time. Experimental data for a diffusion temperature of 500°C can be reasonably well fitted assuming $D = 2.5 \times 10^{-16}\ cm^2\,s^{-1}$ in equation (4.11).

This intermixing presents a problem for applications. For example, the transverse-junction stripe (TJS) laser is a laser structure in which the current is injected laterally into the active layer at the p–n junction. The p-type region is obtained by Zn diffusion into part of an n-type grown double heterostructure. The current flows laterally across the junction from the p-type region to the n-type region. In the case of a GaAs–GaAlAs system, GaAlAs has a wider band gap than GaAs, and carriers are injected predominantly across the GaAs p–n junction into the active layer. Disorder of a GaAs–GaAlAs quantum well by Zn diffusion increases the GaAs (active layer) energy gap so that injection into the non-diffused active layer is enhanced.

In the GaInAsP–InP system, Razeghi *et al* [31] have shown that intermixing due to Zn diffusion reduces the gap, so that injection into the

non-diffused part is greatly reduced. This means that the GaInAsP system is not well suited for TJS lasers.

Moreover, the compositional change after Zn diffuses in GaInAsP wells causes a change in the lattice parameter. The deterioration of material quality when lattice mismatch is over 5×10^{-4} is well known in the case of the GaInAsP/InP double-heterostructure laser, where it increases the threshold current density with rapid degradation.

According to the Razeghi *et al* model the composition of the well after Zn diffusion is near to $InAs_yP_{1-y}$, and the lattice mismatch exceeds 1%. Such an important mismatch creates dislocations and defects at the interface, which drastically increase the probability of non-radiative recombination.

The GaAlAs–GaAs system does not have this problem, since the lattice parameter hardly depends on composition. This is another difference that makes GaInAsP/InP TJS and QW lasers work less well than GaAlAs/GaAs ones.

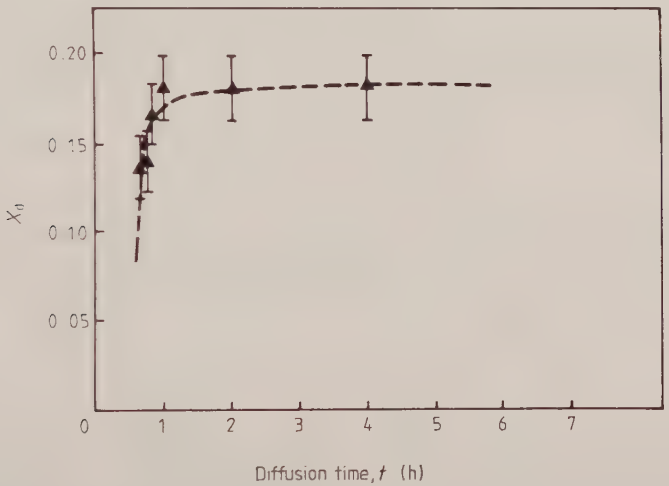

Figure 4.26 The experimental (▲) and calculated (— — — — —) values of X_d for a GaInAsP single QW of 100 Å thickness as a function of diffusion time, for a diffusion temperature of 500°C.

4.2.5 Interface study of $Ga_xIn_{1-x}As_yP_{1-y}$/InP heterojunctions grown by MOCVD by spectroscopic ellipsometry

Knowledge of MOCVD material structure, on an atomic scale, in the interface region between various layers is important for understanding the electronic properties of heterojunctions and superlattices. High sensitivity makes spectroscopic ellipsometry (SE) a useful tool for addressing this problem.

Here we present a study [37] of $In_{0.53}Ga_{0.47}As/InP$ and $Ga_{0.25}In_{0.75}As_{0.5}P_{0.5}/InP$ heterostructures by SE. The steepness of the heterojunctions will be compared for two types of structures: those produced by the growth of InGaAs (or InGaAsP) on InP and those obtained by the reverse growth sequence.

(a) Experimental details

Two types of heterojunctions were considered for this study: $In_{0.53}Ga_{0.47}As/InP$ and $Ga_{0.25}In_{0.75}As_{0.5}P_{0.5}/InP$. Growth conditions are as summarized earlier in table 4.3. The heterostructures are obtained by depositing a 70 Å thick epilayer on top of the corresponding substrate. This thickness was chosen in order to enable SE measurements to be sensitive to the interface region. Before exposure to air, in order to prevent As and/or P effusion, the heterostructures were cooled in the deposition reactor under a gaseous atmosphere which depended on the nature of the top layer of the sample. The following gases were used: PH_3 (InP as top layer), AsH_3 (InGaAs as top layer) and an $AsH_3 + PH_3$ mixture (InGaAsP as top layer).

The spectroscopic ellipsometer is a polarization-modulation type described in detail elsewhere [37]. Let us recall that SE measures, as a function of the energy, the complex reflectance ratio

$$\rho = R_p R_s^{-1} = (\tan \varphi) \exp(i\Delta) \tag{4.16}$$

between the reflection coefficients R_p and R_s for linearly polarized light with its polarization parallel and perpendicular, respectively, to the plane of incidence. In the case of a bulk material with a sharp surface, ρ is directly related to the dielectric function $\varepsilon(E)$ of the material through the relationship

$$\varepsilon(E) = \varepsilon_1 - i\varepsilon_2 = (\sin^2 \theta)\left[(\tan^2 \theta)\left(\frac{1-\rho}{1+\rho}\right)^2 + 1\right] \tag{4.17}$$

where θ is the angle of incidence of the light on the sample. Chemical treatments of the samples, prior to SE measurements, were performed by flowing solutions over the vertical surface of an optically pre-aligned substrate, then maintaining the sample in a dry N_2 flow while taking SE data in order to prevent a native oxide growth.

(b) Reference dielectric functions

As already mentioned, the SE study of heterojunctions requires knowledge of the dielectric functions of the bulk InP, $In_{0.53}Ga_{0.47}As$ and $In_{0.75}Ga_{0.25}As_{0.5}P_{0.5}$ materials. But, the corresponding $\varepsilon(E)$ functions cannot be deduced directly from SE measurements using equation (4.17) because of the presence of a native oxide surface layer. Different chemical etching and cleaning procedures were compared by x-ray photoelectron spectroscopy (XPS) and SE measurements. The SE measurements were

performed, in a dry N_2 flow, immediately after XPS. XPS measurements revealed that this procedure prevents native oxide growth. The best results were obtained by using a 1:10 solution of HF:deionized H_2O. However, it has been shown, in the case of (1 0 0) GaAs surfaces, that acid solutions can produce deep micro-roughness [38]. These effects are illustrated below by comparing SE and XPS measurements.

The XPS measurements are shown in figures 4.27 to 4.31. Core-level and Auger lines P(2p), In($3d_{5/2}$), As(Auger LMM) and Ga(Auger LMM) have been recorded. In order to observe oxide removal from InP, GaInAs and GaInAsP surfaces, it is important to know the binding energies of the core levels and the kinetic energies of the Auger lines corresponding to the elements In, As, Ga and P in their oxidized forms in the III–V compounds. GaAs and InP, because they have been extensively studied, have been chosen as reference samples. The spectra shown in figures 4.27–4.30 (curves A) and 4.31(*a*) correspond to air-oxidized InP and GaAs samples that have been chemically etched prior to air exposure. Concerning P(2p), Ga and As(Auger), oxide components are clearly visible in all XPS spectra. This is less clear for In(3d) because of the small chemical shifts existing between In in InP (binding energy BE = 444.4 eV) and In in In_2O_3 (BE = 444.7 eV) or $In(OH)_3$ (BE = 4445.3 eV). As a matter of fact, the In core level has been

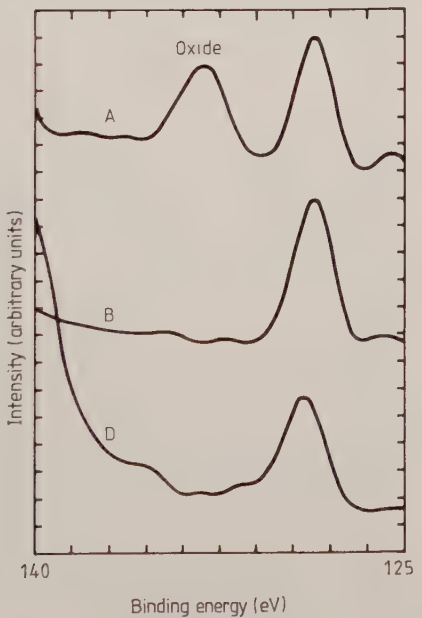

Figure 4.27 P(2p) core-level peak recorded for (A) InP air-oxidized; and for HF:H_2O (1:10) etched samples of (B) InP and (D) InGaAsP.

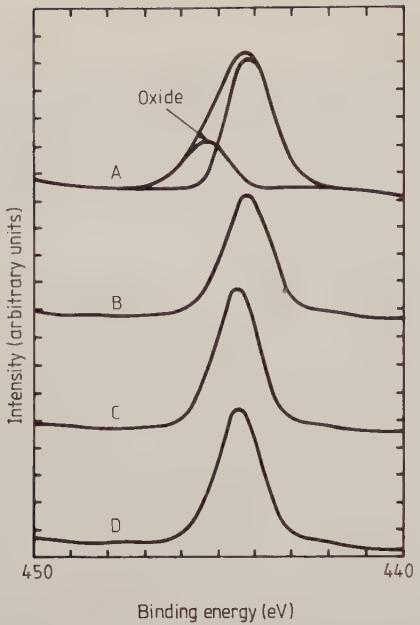

Figure 4.28 In(3d) core-level peak recorded for (A) InP air-oxidized; and for HF:H_2O (1:10) etched samples of (B) InP, (C) InGaAs and (D) InGaAsP.

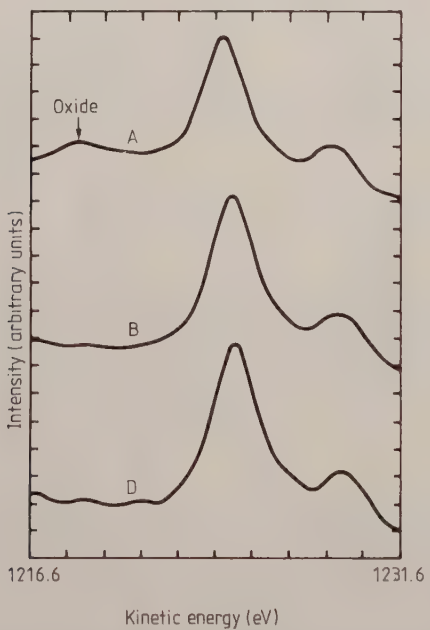

Figure 4.29 As(LMM) Auger lines recorded for (A) GaAs air-oxidized; and for HF:H_2O (1:10) etched samples of (B) InP and (D) InGaAsP.

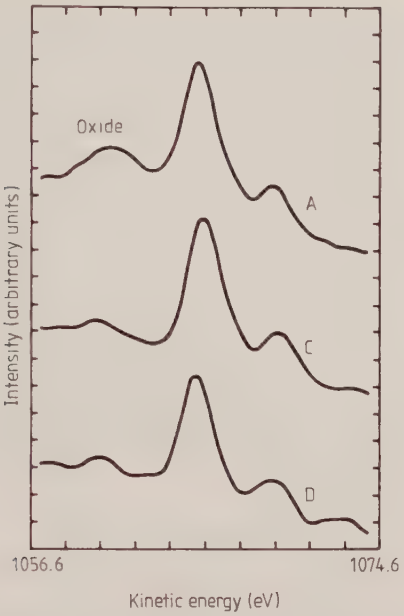

Figure 4.30 Ga(LMM) Auger lines recorded for (A) GaAs air-oxidized; and for HF:H_2O (1:10) etched samples of (C) InGaAs and (D) InGaAsP.

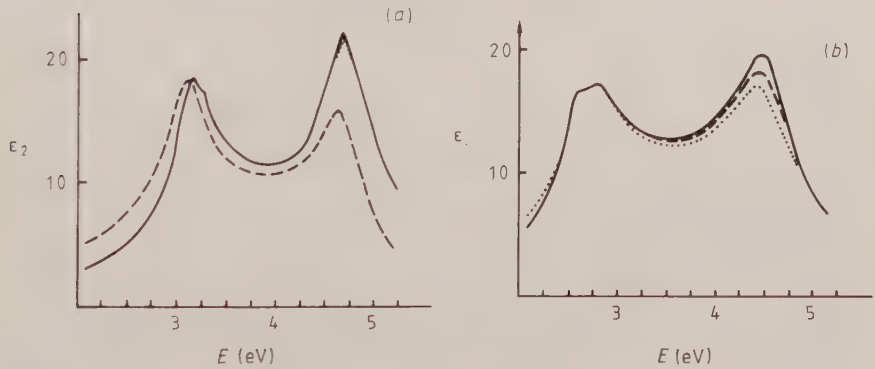

Figure 4.31 Influence of (1:10) HF:H_2O solution etching on the pseudo-dielectric function of InP (*a*) and $In_{0.53}Ga_{0.47}As$ (*b*): broken curves, as-deposited samples; full curves, 1 s treatment; dotted curves, 3 s treatment.

fitted with Gaussians in order to show the oxide component (see figure 4.28 (curve A)). XPS data were then taken after performing the HF:H_2O (1:10) etching treatment on three different air-oxidized substrates: InP, GaInAs and GaInAsP (figures 4.27–4.31). We note that the component characteristic of overlayer oxide has disappeared from all XPS spectra, inferring oxide

removal due to the etching treatment. All these results are in agreement with previous analyses, which have also shown the efficiency of HF etching solution in performing oxide removal [39]. Immersion times from 1 s to 1 min in the etching solution did not produce any modification in the XPS spectra.

The SE measurements corresponding to the extreme values of y (InP and $In_{0.53}Ga_{0.47}As$) are presented in figure 4.32. In order to interpret the data, let us recall that the presence of an oxide layer and/or a surface microroughness both induce a decrease of the ε_2 spectra (together with a shift to lower energies), these effects being more sensitive in the 4.5 eV region (E_2 peak) [40, 41]. The first chemical treatment (full curves) performed by flowing the solution for 1 s over the surface results in an increase of the E_2 peak which corresponds to oxide removal, as evidenced by the XPS measurements. However, an extension of this chemical treatment for more than 1 s produces a decrease of the E_2 peak, revealed by SE measurements (figure

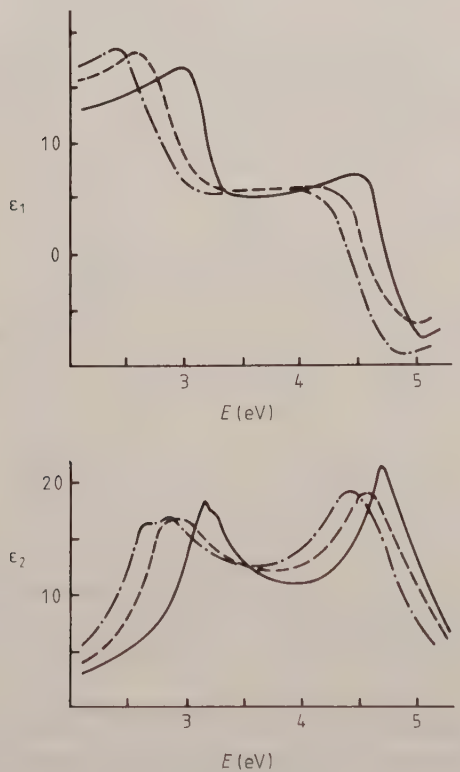

Figure 4.32 Real part ε_1 and imaginary part ε_2 of the dielectric function spectra of InP, $In_{0.53}Ga_{0.47}As$ and $In_{0.75}Ga_{0.25}As_{0.5}P_{0.5}$ (see text for details).

4.32, broken curves), which can be correlated to the presence of surface micro-roughness.

The real and imaginary parts $\varepsilon_1(E)$ and $\varepsilon_2(E)$ of the complex dielectric functions of the three reference materials are shown in figure 4.33 [37]. The two major features of the spectra are the E_1 and E_2 structures at 3.0 and 4.5 eV respectively. More precisely, all of the ε_2 spectra displayed in figure 4.33 have two features in the E_1 structure corresponding to the E_1 and $E_1 + \Delta_1$ transitions between the spin–orbit split upper valence band and

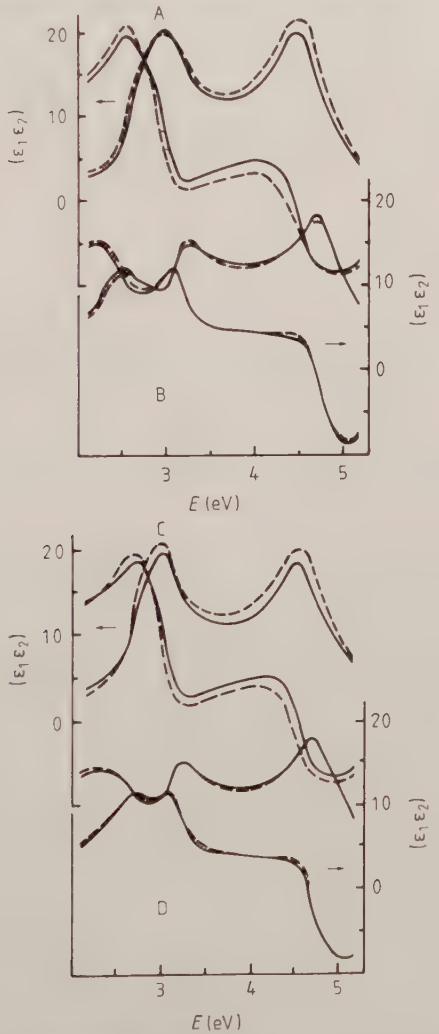

Figure 4.33 Experiment (full curves) and best fit to the data using the physical interface model (broken curves) of the $In_{1-x}Ga_xAs_yP_{1-y}/InP$ heterostructures.

the lowest conduction band along the [1 1 1] direction in the Brillouin zone. The three ε_1 (or ε_2) spectra are clearly distinguishable; the E_1 and E_2 structures move to lower energies with increasing y from $y = 0$ (InP) to $y = 1$ ($In_{0.53}Ga_{0.47}As$). The data displayed in figure 4.32 can be compared to previous measurements obtained on InGaAsP samples grown by liquid-phase epitaxy using a rotating analyser ellipsometer (RAE). The overall agreement is rather good. However the dominant E_2 peaks in $\varepsilon_2(E)$ are 2–5% higher in the measurements by Kelso *et al* [42], but are 10% lower in the E_1 region ($\simeq 3.0$ eV). The weak discrepancy in the E_2 region can possibly be attributed to differences in sample growth and surface preparation. As a matter of fact it was checked that a 5 Å thick In_2O_3 overlayer, or a very small surface micro-roughness (5 Å thick overlayer with 50% density deficiency), can account for the observed discrepancy in InP near 4.5 eV. But more generally, differences in $\varepsilon_2(E)$ data can reflect differences in the measurement procedures.

(c) Experimental results and discussion

Four samples of heterostructures have been examined:

(*a*) a 70 Å $In_{0.53}Ga_{0.47}As$ epilayer on an InP substrate;

(*b*) a 70 Å epilayer on an $In_{0.53}Ga_{0.47}As$ thick layer (2000 Å) on an InP substrate;

(*c*) a 70 Å $In_{0.75}Ga_{0.25}As_{0.5}P_{0.5}$ epilayer on an InP substrate; and

(*d*) a 70 Å epilayer on an $In_{0.75}Ga_{0.25}As_{0.5}P_{0.5}$ thick layer (2000 Å) on an InP substrate.

In each case, the cleaning procedure described above was applied before SE measurements. The $\varepsilon(E)$ functions of the heterostructures, given in figure 4.33, clearly differ from the data of figure 4.32, which correspond to the bulk materials. Because of the thinness of the epilayer (70 Å), the optical responses of the substrates clearly influence the SE measurements displayed in figure 4.33, this effect being more sensitive in the E_1 region ($\simeq 3.0$ eV). In order to detect the presence of an interface region between the substrate and the epilayer, the experimental $\varepsilon_2(E)$ measurements have been compared in figure 4.34 to a calculation using the reference dielectric functions shown in figure 4.32 and assuming a sharp interface between the substrate and a 60 Å (broken curves) or 80 Å (dotted curves) overlayer. The experimental ε_2 curves are only between both calculations in figure 4.34(*d*) (InP/InGaAsP). In contrast in figures 4.34(*a*), (*b*) and (*c*) the experimental curves clearly depart from the calculation in the E_2 region, showing the influence of a transition region in those cases.

This interface region may be tentatively described by assuming that the substrate and the epilayer are mixed inside a very thin layer without changing their chemical nature [43]. Such a physical mixture simulates a rough interface at the atomic scale between the substrate and the epilayer.

The dielectric function of the interface layer is computed using the standard effective-medium approximation. A least-squares fit of the data displayed in figure 4.33 is then performed, the free parameters of the fit being f_s, the volume fraction of the substrate inside the interface layer, and d_o and d_{int}, the thicknesses of the overlayer and the interface layer, respectively.

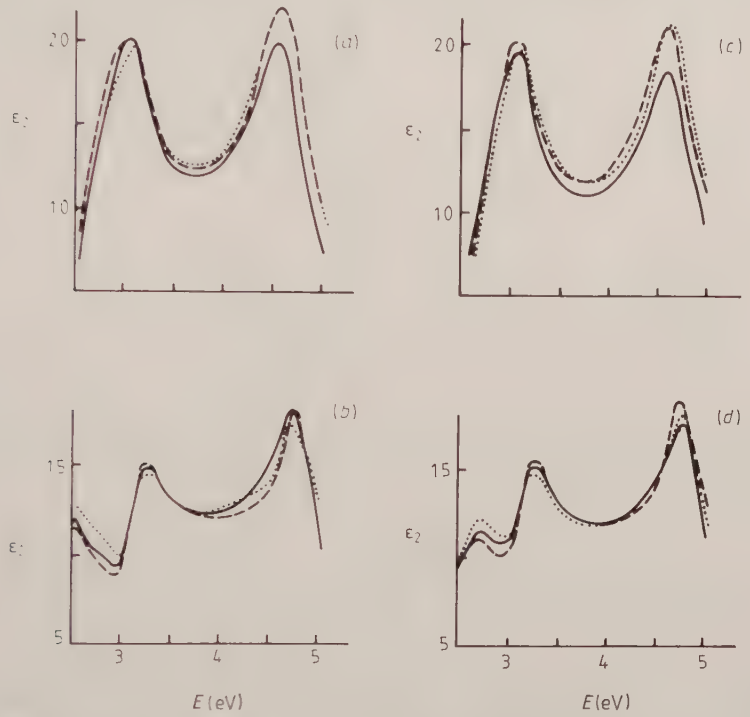

Figure 4.34 Experiment (full curves) and modelling (broken and dotted curves) assuming a sharp interface of the $In_{1-x}Ga_xAs_yP_{1-y}$/InP heterostructures (see text for details).

The results of the fits are compared to the experimental $\varepsilon(E)$ curves in figure 4.33 (broken curves). The best matches between calculated and experimental curves are obtained for samples (*b*) and (*d*) (InP epilayer). When using the reverse growth sequence (InP substrate), however, the physical interface model fails to reproduce the $\varepsilon_2(E)$ data in the E_2 region (see figures 4.33(*a*) and (*c*)).

Let us discuss first the cases corresponding to InP epilayer (samples (*b*) and (*d*)). The values of the fitted parameters obtained with these samples are displayed in figure 4.35. It can be seen that the overall thickness value ($d_{int} + d_o$) obtained using the physical interface model is in very good agreement with the expected overlayer thickness (70 Å). The precision on

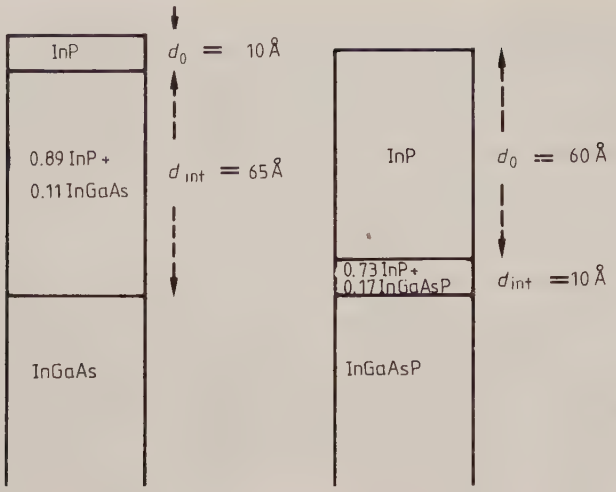

Figure 4.35 Structures of heterojunctions (InP overlayer) as determined by using the physical interface model.

the fitted parameter values can be estimated by varying the spectral range of the dielectric function used in the fit. The following typical values were obtained: ± 0.01 on f_s and ± 10 Å on d_{int} and d_o. In each case a small interface layer is obtained whose physical composition is close to InP ($f_s \simeq 0.80$). However, the sharpest interface is obtained by depositing InP on InGaAsP (sample (*d*)); in this case the existence of an interface layer is not apparent ($d_{int} = 10 \pm 10$ Å). The dielectric functions of both interface layers can be estimated by using the fitted values of f_s. The corresponding imaginary parts of the dielectric functions are compared to those of InP in figure 4.36. As expected, the optical repsonses of the interface layers of samples (*b*) and (*d*) are found to be very close to those of InP. This leads to two possible interpretations. First, a rough interface is produced in sample (*b*), but the difference between samples (*b*) and (*d*) revealed by the physical interface model (see figure 4.35) remains unclear. Secondly, there is an interdiffusion between the substrate and the overlayer (InP), leading to the formation of a thin layer of quaternary alloy with chemical nature different from the substrate. In this frame, the results displayed in figure 4.36 can be understood as an estimation of the optical response of the interface layer. An inspection of figure 4.36 shows that the composition of this quaternary alloy $In_{1-x}Ga_xAs_yP_{1-y}$ is probably close to InP ($y = 0$). Moreover, with this latter chemical interface model, a sharper interface is expected in sample (*d*) in which the underlayer is already a quaternary alloy ($In_{0.75}Ga_{0.25}As_{0.5}P_{0.5}$) than in sample (*b*) (substrate InGaAs). Indeed, the difference between samples (*b*) and (*d*), revealed by the physical interface model, can be correlated with the growth conditions. In both cases, before

the growth of the InP layer, the introduction of $Ga(C_2H_5)_3$ and AsH_3 is interrupted but phosphine remains present in the reactor only in the case of the deposition of InP on InGaAsP (sample (*d*)). Then, the difference between both interfaces can reflect the diffusion time of the phosphorus towards the neighbourhood of the growth surface in the case of InP/InGaAs (sample (*b*)). This interpretation has recently been confirmed by Auger analysis along a chemically bevelled InP/InGaAs/InP quantum well [44].

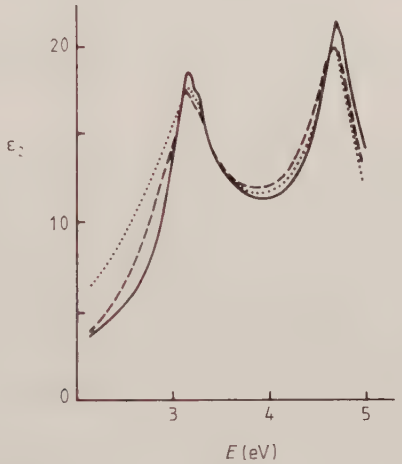

Figure 4.36 Determination of the imaginary part of the dielectric function of the interface layers (InP overlayer) using the physical interface mode, compared to InP. ———, InP; – – –, InP–InGaAs; ····, InP–InGaAsP.

Let us now consider the opposite cases in which InP is the substrate (samples (*a*) and (*c*)). In both cases very bad agreement with the physical interface model is obtained. This may be attributed to the presence of a large chemical interface. But results from Auger spectra of a chemically etched bevel through $Ga_{0.47}In_{0.53}As$–InP quantum wells do not seem to support this hypothesis. However, it has to be noted that the quantum-well structures are produced using a different growth procedure. In this latter case, the ternary layer is located between InP epitaxial layers. So, we favour another interpretation. Obviously, the optical responses of the thin 70 Å epilayers (InGaAs and InGaAsP) are incompatible with the corresponding bulk dielectric functions obtained by using 2000 Å thick InGaAs and InGaAsP grown on InP, as shown in figure 4.32. These differences may possibly reflect differences in sample preparation. In particular, let us recall that, during the cooling procedure in the deposition reactor before SE measurements, the introduction of group III alkyls is interrupted in both cases, group V hydrides still being resident in the reaction tube. Then, the

composition of the gaseous boundary layer is expected to vary in the early stage of the cooling procedure, before complete evacuation of the group III alkyls. However, the epitaxial growth is controlled by the mass transport of group III species (see chapter 1). This can result in a modification of the composition of the InGaAsP epilayer near the surface. Furthermore, as the gaseous composition inside the deposition reactor is fixed, the chemical nature of the $In_{1-x}Ga_xAs_yP_{1-y}$ alloys is known to vary as a function of substrate temperature. The influence of these effects on the optical response of the sample is expected to be relatively stronger for a thin overlayer (70 Å) than for the bulk InGaAs or InGaAsP. Because of the lower substrate temperature dependence of the InP layer, the discrepancy between the dielectric functions of a thin layer and bulk material is not observed in samples (*b*) and (*d*) (InP epilayer).

Obviously, *in situ* ellipsometric measurements have to be performed in real time to check this hypothesis. First, spectroscopic ellipsometry appears to be a valuable tool to measure *in situ* the variation in chemical nature of $In_{1-x}Ga_xAs_yP_{1-y}$ alloys during the cooling procedure in the deposition chamber. Secondly, real-time measurements at a fixed wavelength, by kinetic ellipsometry, are known to be very sensitive to the early stage of growth on an atomic scale. This technique appears to be well adapted to perform *in situ* high-precision studies of the interface region in the MOCVD growth reactor.

4.3 APPLICATIONS OF GaInAsP–InP SYSTEMS GROWN BY MOCVD

There is strong pressure for the development of optoelectronic components necessary for trunk telecommunications, local area networks, cable TV distribution and avionic communications. The optoelectronic devices that are being incorporated into communications systems are quite sophisticated but further advanced components are required for future systems which make strong demands on cost, complexity and performance.

These advanced optoelectronic components exploit particular material parameters and the optimization of these parameters has led to the need for several new group III–V materials, new materials structures and alloy combinations, and novel preparation techniques.

System optimization here is heavily influenced by the need to keep the optoelectronic component and interconnection costs to a minimum and hence the drive is to employ the principles of integrated circuits as soon as possible.

Telecommunications systems have a hierarchy on the number of telephone lines multiplexed. Data rates of 8, 34, 140 and 565 Mbit s^{-1} have emerged as the standards so far. The 8, 34 and 140 Mbit s^{-1} systems have

been implemented with LED and PINFET receivers and multimode fibres, but the emphasis has been to optimize the LED parameters for high switching speed, launch power and spectral purity, and the receiver for sensitivity so that repeater spacings up to 15 km can be achieved.

Longer repeater spacing and high levels of multiplexing requirements have led to 140 and 565 Mbit s^{-1} laser-sourced monomode fibre systems. These systems require light control of laser and detector parameters and the early introduction of sophisticated fabrication techniques.

4.3.1 Broad-area 1.2–1.6 μm $Ga_xIn_{1-x}As_yP_{1-y}$–InP DH lasers grown by MOCVD

After optimization of growth conditions for InP and GaInAsP layers, MOCVD has been successfully used for the growth of GaInAsP–InP double heterojunctions (DH) for laser applications emitting at 1.3 and 1.5 μm. The various interfaces are produced by controlling the flow of the relevant component, as in the case of GaInAs mentioned previously.

The growth rate for these quaternary materials is small ($\simeq 3$ Å s^{-1}), and the gas flow is stabilized to its new steady-state value in less than 1 s after switching.

Figures 4.37 and 4.38 show the Auger and SIMS profiles of a GaInAsP–InP DH emitting at 1.3 μm. The structure consists of four layers:

(1) S-doped InP ($n \simeq 10^{18}$ cm^{-3}), confinement layer;
(2) GaInAsP ($\lambda \simeq 1.3$ μm), no intentional doping, active layer;
(3) Zn-doped InP ($p \simeq 10^{17}$ cm^{-3}), confinement layer; and
(4) Zn-doped GaInAsP ($\lambda \simeq 1.3$ μm), cap layer.

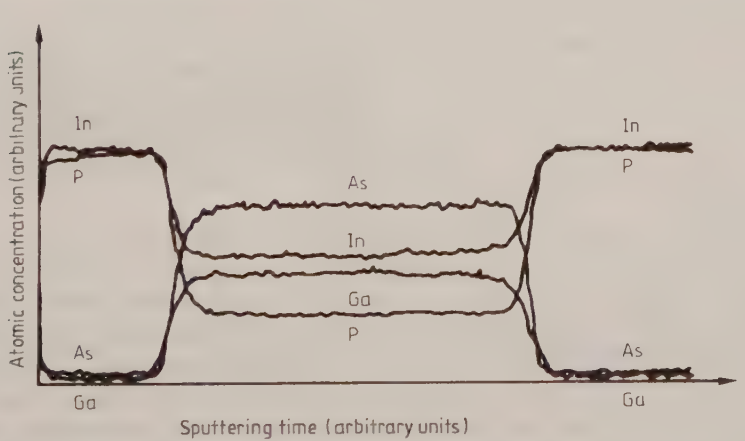

Figure 4.37 Auger profile for GaInAsP/InP DH for laser applications (the sputter timescale is not linear in the central region).

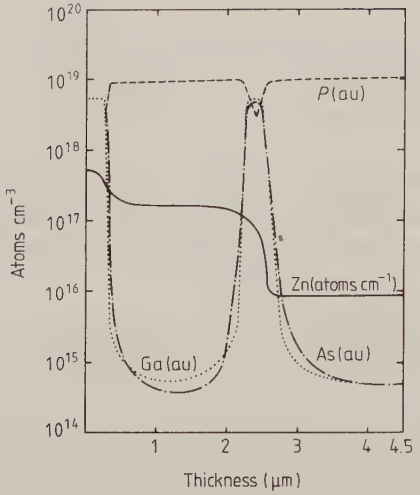

Figure 4.38 SIMS profile of GaInAsP/InP DH for laser applications, at $\lambda = 1.3$ μm.

The Zn profile shows that it is possible to control the p-type doping level, to avoid the diffusion of Zn into the n-type confinement InP layer, and to keep the p–n junction in the quaternary active layer.

Figure 4.39 shows the transition region after chemical etching (see chapter 3) of a GaInAsP–InP DH laser. The etch-pit density (EPD) is the same in the substrate as in the confinement InP layers, and the interfaces are defect-free.

(a) Laser fabrication and characteristics

Broad-area and stripe-geometry lasers have been fabricated from MOCVD grown materials. A typical example of a broad-area laser is shown schematically in figure 4.40. The DH structure of these laser diodes is described in table 4.6. These layers are grown successively on (1 0 0) Sn-doped ($n \simeq 2 \times 10^{18}$ cm^{-3}) InP substrates, 2° off (1 0 0) towards (1 1 0). The growth temperature of the epilayers is 650°C, and the working pressure is 100 mbar.

The lattice mismatch of the $Ga_xIn_{1-x}As_yP_{1-y}$ epitaxial layer is less than or equal to 5×10^{-4} at room temperature. The grown wafers are then lapped to a thickness of 100 μm and Au–12%Ge and Au–8%Zn contact metallizations are deposited on the n and p sides, respectively. The contacts are then annealed at 400°C for 5 min in an argon atmosphere. The devices are cleaved and sawn, producing chips of width 150 μm with cavity lengths in the range 300–1000 μm. The laser chips are tested unmounted under pulsed conditions at a pulse repetition rate of 10^4 Hz with a pulse length of 100 ns. For chips cleaved from the same bar, the standard deviation in the

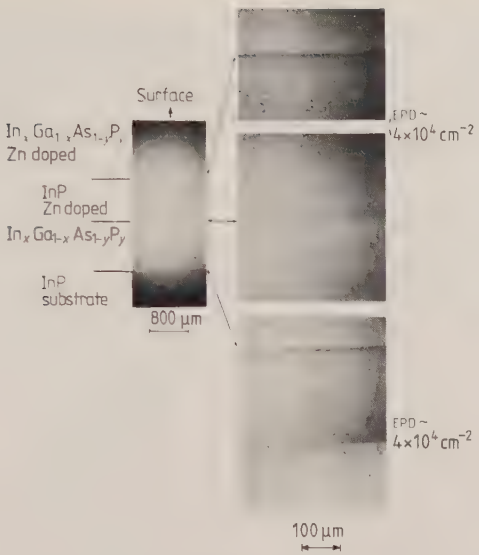

Figure 4.39 The depth of a chemical bevel, realized on a GaInAsP/InP DH grown by LP-MOCVD, for laser applications, in a bromine solution. It is not possible to reveal the interfaces between the InP n-type confinement layer and the substrate. $In_xGa_{1-x}As_{1-y}P_y$/InP/$In_xGa_{1-x}As_{1-y}P_y$/InP substrate n^+; $x = 0.75$, $y = 0.44$; bevel angle $\alpha = 0.065°$; etchant H, 2 min.

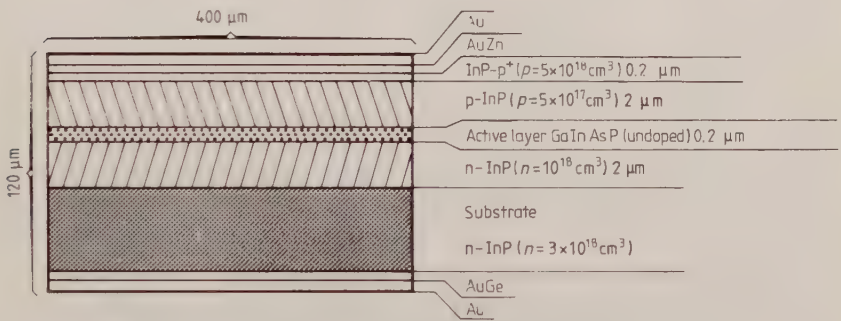

Figure 4.40 Typical broad-area GaInAsP/InP laser diode.

lasing threshold current density is only ±5%. For a large slice area (10 cm^2), the standard deviation in lasing threshold is typically less than 20%. The emitting wavelengths can be controlled with an accuracy of 0.02 μm in the range 1.2–1.6 μm.

The dependence of threshold current density J_{th} on thickness d of the active layer of a laser diode grown by MOCVD is shown in figure 4.41. The threshold current density of broad-area lasers with 300 μm cavity length and

200 μm cavity width decreases linearly with decreasing thickness of the active layer down to $d = 2000$ Å and is about 500 A cm^{-2} for $d = 0.2$ μm. The threshold current density increases when the thickness is less than 1500 Å. These results are in satisfactory agreement with those obtained with LPE-grown materials [45].

Table 4.6 DH structure of laser diodes.

Layer	Composition	Type	Thickness(μm)
Substrate	InP(Sn)	n^+, 2×10^{18} cm^{-3}	100
Buffer	InP	n^+, 10^{18} cm^{-3}	1
Active	$Ga_xIn_{1-x}As_yP_{1-y}$	Undoped	$\simeq 0.2$
Confinement	InP	p, 2×10^{18} cm^{-3}	2
Contact	$Ga_xIn_{1-x}As_yP_{1-y}$	p^+, 5×10^{18} cm^{-3}	0.5

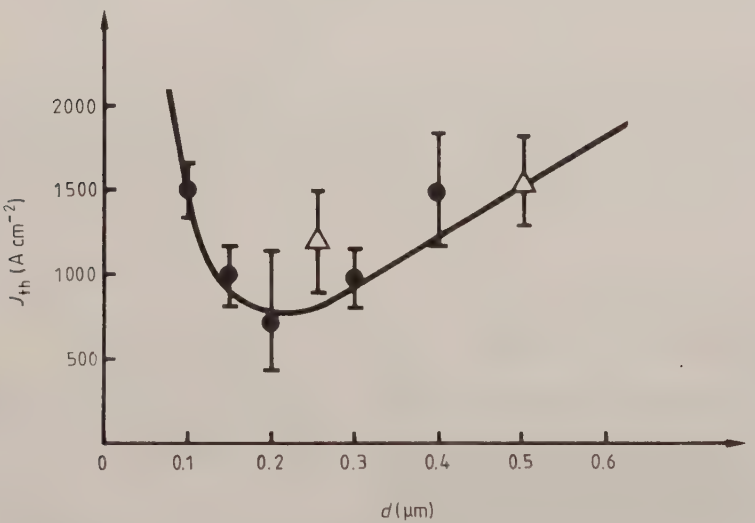

Figure 4.41 Experimental threshold current density as a function of the thickness of the active layer for GaInAsP/InP MOCVD laser diodes emitting at wavelengths of 1.3 (•) and 1.5 (▵) μm.

(b) Lasers emitting at 1.5 μm

Here, we describe the continuous-wave (CW) 1.5 μm room-temperature operation of $In_{1-x}Ga_xAs_yP_{1-y}$/InP double-heterostructure (DH) diode lasers grown by the low-pressure metallorganic chemical vapour deposition technique. The DH structure is given in table 4.7.

The composition of the $Ga_{1-x}In_xAs_yP_{1-y}$ epitaxial layer was determined by x-ray diffraction and photoluminescence. Rather thick active layers were grown (0.4–0.6 μm) in order to allow us to measure the mismatch of the

active layer, which, for the data mentioned here, is $\Delta a/a < 3 \times 10^{-4}$. The compositional uniformity of the active layer was characterized by measurement of the photoluminescence wavelength at various points on an epitaxial layer of 8 cm^2 area. The wavelength varied by less than 2 nm over 95% of the area, the photoluminescence efficiency changed by less than 2%, and the thickness unformity was better than 0.48 ± 0.01 μm over the same area.

The contacting technology and fabrication of broad-area lasers are as described in the previous section. Broad-area laser chips are made by standard cleaving and sawing procedures producing Fabry–Perot cavities 400 μm in length. Figure 4.42 shows a typical spectrum under CW operation at room temperature of a MOCVD GaInAsP/InP laser emitting at 1.5 μm.

Table 4.7 DH structure of laser diode.

Layer	Composition	Type	Thickness(μm)
Substrate	InP(Sn)	n^+, 2×10^{18} cm^{-3}	100
Buffer	InP	n^+, 10^{18} cm^{-3}	1
Active	$Ga_{0.37}In_{0.63}As_{0.8}P_{0.2}$	Undoped	0.5
Confinement	InP	p, 5×10^{17} cm^{-3}	2
Contact	InP	p^+, 5×10^{18} cm^{-3}	0.5

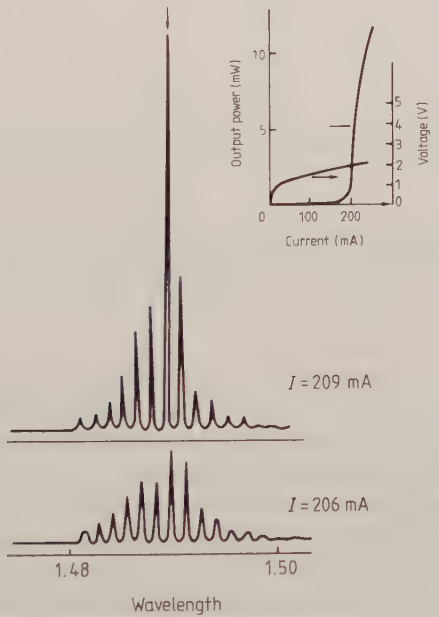

Figure 4.42 Lasing spectrum and light–current and voltage–current characteristics of a single-transverse-mode GaInAsP/InP DH CW laser diode emitting at 1.5 μm at room temperature.

All the chips from the same cleaved bar showed the same results. The minimum threshold current is 1.0 kA cm^{-2}. Figure 4.43 shows the threshold current for a 1.5 μm laser for several temperatures ranging from 10 to 70°C. As with GaInAsP/InP lasers grown by LPE, the lasing threshold varies exponentially with temperature, and the T_0 value (see equation (4.19)) for a 1.5 μm laser tested in pulsed operations is about 62 K in the room-temperature range.

This section gives the life test of a laser diode emitting at $\lambda = 1.5$ μm grown by MOCVD, which operated at room temperature for more than 10^4 h without significant degradation. The DH structure of this diode is described in table 4.7.

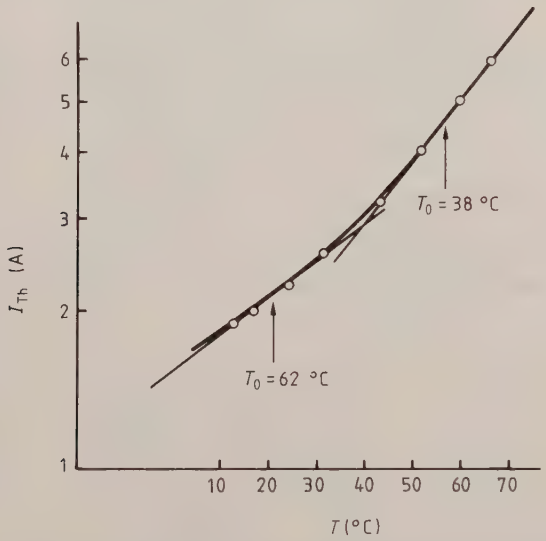

Figure 4.43 Typical CW light–current characteristics at different temperatures for a GaInAsP/InP buried-ridge-structure (BRS) laser emitting at 1.5 μm.

These lasers have a stripe width of 9 μm and a cavity length of 300 μm. The localization of the current flow was obtained by shallow-proton implantation. After cleaving and sawing, individual diodes were mounted p-side down on gold-plated copper heat-sinks.

Figure 4.42 shows the continuous-wave (CW) light–current characteristic of one of these diodes with its emission spectrum before life testing. A threshold current of 200 mA and a P–I curve with fundamental transverse-mode operation up to 10 mW were obtained.

The characteristics of a laser diode were life tested under the following conditions. The diode was placed under dry nitrogen and aged in the lasing mode. The injected current was periodically adjusted to keep a constant

output power of 1 mW/facet. The diode was aged at 20°C owing to its high threshold current.

Figure 4.44 shows threshold current against time for a laser soldered with indium to a gold-plated copper mount and operating at 1 mW output power at room temperature. The degradation rate is approximately

$$\Delta I_{th}/I_{th}\,\Delta t \simeq 10^{-5}\ h^{-1}$$

with no detectable change in external quantum efficiency over 12 000 h.

The external quantum efficiencies of the diode after 12 000 h CW operation are illustrated in table 4.8 in comparison with the values before life testing. Table 4.8 shows that η_{ext} after 12 000 h CW operation is comparable to the value before life testing.

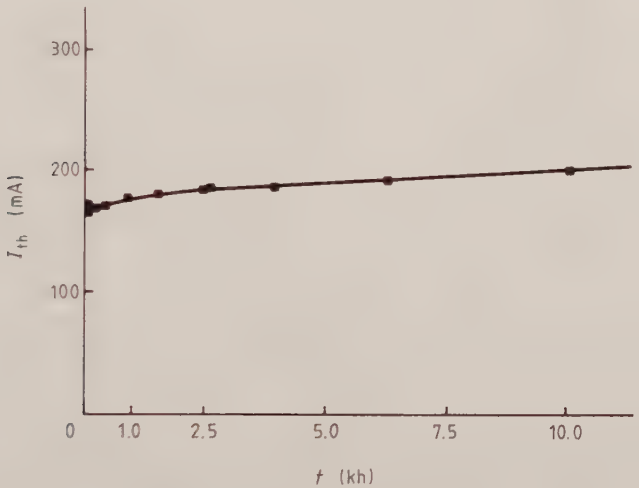

Figure 4.44 Variation of threshold current density I_{th} for InP–GaInAsP DH lasers emitting at 1.5 μm by LP-MOCVD with time ($T = 20°C$, $P = 1$ mW).

The far-field patterns of this laser diode are shown in figure 4.45. These patterns were measured under CW operation ($I_{th} = 254$ mA) after 12 000 h. The laser operated stably in the fundamental lateral mode without significant distortion of the field patterns. Far-field full angles at half power, both parallel and perpendicular to the junction plane, are 12° and 38°, respectively.

These preliminary results on non-optimized structures are most encouraging and demonstrate that the MOCVD-grown GaInAsP/InP DH lasers have comparable degradation rates to those of LPE lasers, suggesting that the MOCVD technique is promising for large-scale production of laser diodes.

Table 4.8 External quantum efficiencies of diode before and after life testing.

	η_{ext} (W A^{-1}) for one facet	
	Before life testing	After 12 000 h
Pulsed operation	0.40	0.39
CW operation	0.23	0.20

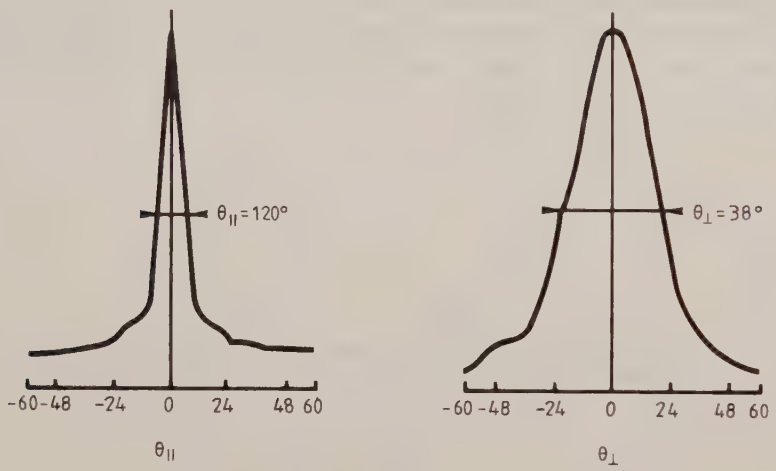

Figure 4.45 Far-field patterns parallel and perpendicular to the junction plane for an MOCVD laser with 9 μm stripe width; $\lambda = 1.5$ μm, $T = 20^{\circ}$C, $I_{th} = 254$ mA, $P = 3.5$ mW.

(c) $Ga_{0.25}In_{0.75}As_{0.5}P_{0.5}$–InP DH lasers emitting at 1.3 μm

A good layer uniformity was demonstrated by the experimental result that the threshold current density continued to fall with lasing cavity length for cavity lengths up to 950 μm. The variation of lasing threshold current density J_{th} with cavity length L is shown in figure 4.46. The value of the absorption coefficient α was 16 cm^{-1} and was obtained by fitting, to the data in figure 4.46, the standard exression

$$J_{th} = \frac{1}{\beta}\left[\alpha + \frac{1}{2L}\ln\left(\frac{1}{R_1 R_2}\right)\right] \tag{4.18}$$

where R_1 and R_2 are the facet reflectivities ($R_1 = R_2 = 0.32$) and β is a constant equal to 0.058 cm A^{-1}. In a series of 10 laser slices the average emission wavelength was 1.284 μm with a standard deviation of only $\pm 1\%$ for a broad-area laser of cavity length 300 μm (width 150 μm). The average threshold current density is 800 A cm^{-2}. The latter decreases to 500 A cm^{-2} for a cavity length of 950 μm, the lowest threshold being 430 A cm^{-2} for a cavity length of 950 μm.

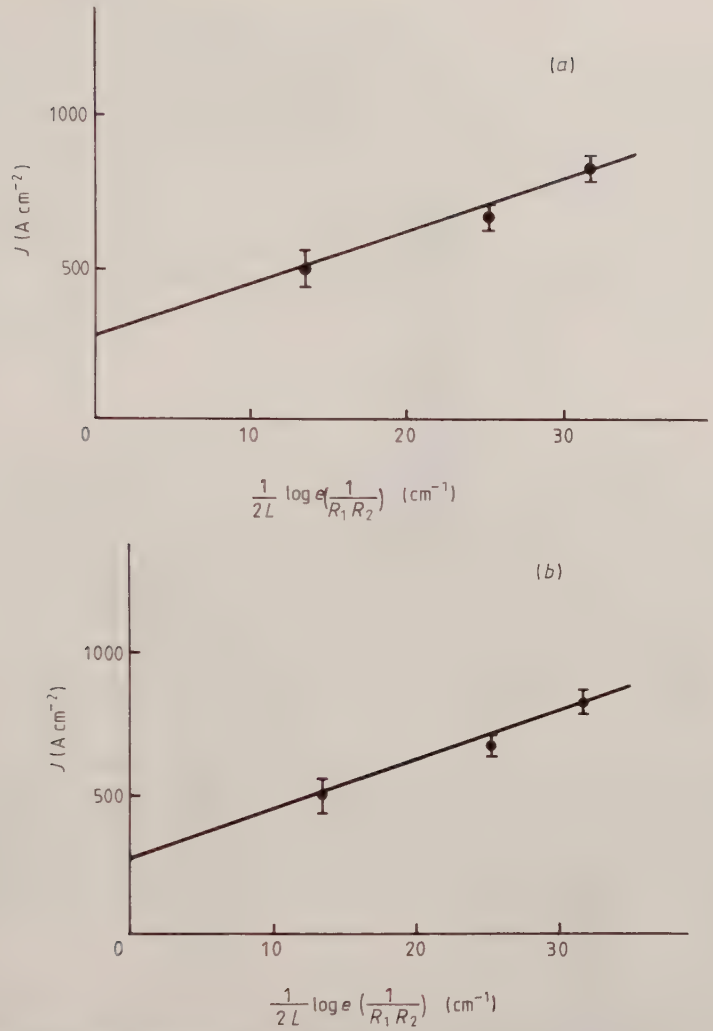

Figure 4.46 Variation of threshold current density J_{th} with reciprocal of cavity length: (*a*) 1.3 μm lasers; (*b*) 1.5 μm lasers. In equation (4.18), $\alpha = 16\ \text{cm}^{-1}$, $\beta = 5.8 \times 10^{-2}\ \text{cm A}^{-1}$ and $R_1 = R_2 = 0.32$.

A 1.3 μm laser diode can be operated CW at room temperature at a typical current of 80–120 mA. The characteristic was kink-free up to 10 mW/facet with fundamental transverse-mode operation up to 10 mW.

Figure 4.47 shows a typical lasing spectrum, light–current and voltage–current characteristics of an MOCVD GaInAsP–InP DH CW laser diode emitting at 1.26 μm. The far-field patterns of this laser diode are represented in figure 4.48. The full widths at half-maximum (FWHM) are 15°

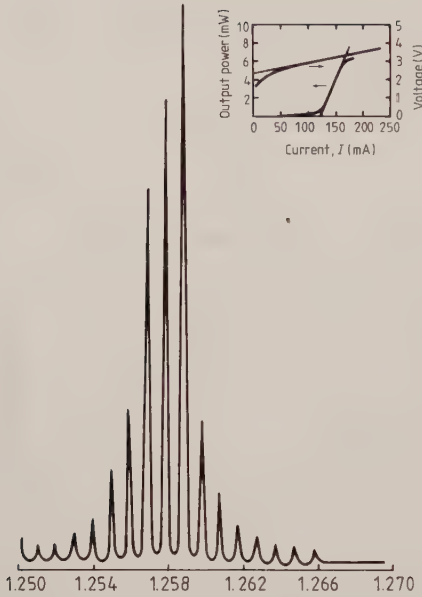

Figure 4.47 Lasing spectrum, light–current and voltage–current characteristics of a single-transverse-mode GaInAsP/InP DH CW laser diode emitting at 1.26 μm at room temperature ($T = 20^{\circ}$C); output power 3.01 mW, current 143.5 mA, refractive index 3.29, laser RAZ 558 6A.

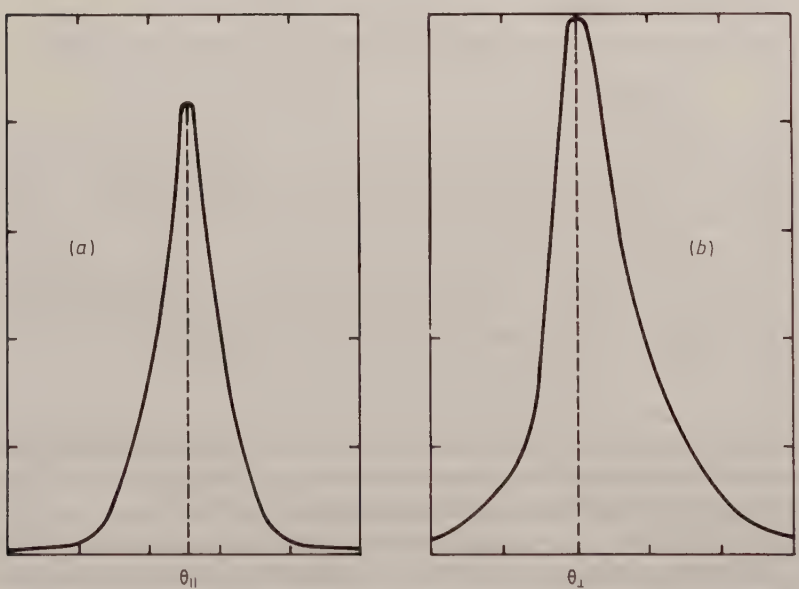

Figure 4.48 Far-field patterns (*a*) parallel and (*b*) perpendicular to the junction plane of an LP-MOCVD GaInAsP/InP laser diode emitting at 1.26 μm; $T = 20^{\circ}$C, $P = 3$ mW, $I = 143$ mA, laser RAZ 558 6A.

and 22°, parallel and perpendicular to the junction plane, respectively, up to 4 mW output power, measured by scanning a Ge avalanche photodiode perpendicular to the junction. These patterns were measured under CW operation for a stripe width of 12 μm. For the same laser structure grown by LPE, $\theta_{\perp}$ varies between 25° and 40°. In the field of optical-fibre communication, the fabrication of laser diodes with low beam divergence is essential for coupling the emission into an optical fibre.

Figure 4.49 shows the light power versus pulsed threshold current of this diode for various temperatures; the 20°C average threshold current is 70 mA. The threshold current density of DH lasers depends empirically on temperature as

$$J_{th}(T) = J_{th}(T_0) \exp(T/T_0) \tag{4.19}$$

where T_0 is a characteristic temperature. The average T_0 value is 67°C. A few diodes were aged with a constant power of 5 mW/facet at room temperature. The results are illustrated in figure 4.50, which shows that GaInAsP/InP lasers emitting in the wavelength region of 1.3 μm made by MOCVD can be operated at room temperature for more than 6000 h without significant degradation.

4.3.2 Buried-ridge-structure lasers grown by MOCVD

In order to decrease the injection current a buried-ridge structure (BRS) can be chosen. Figures 4.51 and 4.52 show SEM micrograph and schematic diagrams of the cross section of a BRS laser grown by two-step MOCVD. This laser was fabricated as follows. First the following layers were grown successively on an InP(Sn) substrate with orientation (1 0 0) exact or (1 0 0)

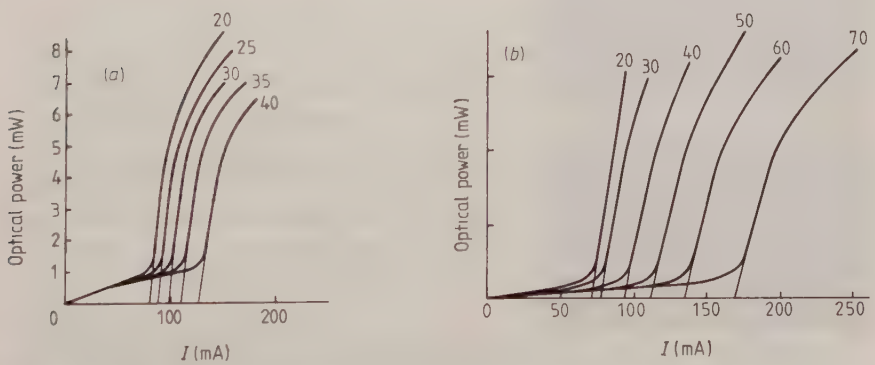

Figure 4.49 Light output versus pulsed current at several heat-sink temperatures of 1.3 μm GaInAsP/InP laser grown by LP-MOCVD: (*a*) under CW operation (sample 558); (*b*) under pulse operation ($T_0 = 67$°C).

2° off:

(1) 1 μm InP, sulphur-doped, for confinement layer;
(2) 0.2 μm GaInAsP ($\lambda = 1.3$ or 1.55 μm), undoped, active layer; and
(3) 0.2 μm InP, Zn-doped, confinement layer.

Next, a ridge of about 1 μm width and 0.5 μm depth was etched in the InP and GaInAsP layers through a photolithographic resist mask, using a selective etch composed of H_2SO_4, H_2O_2 and H_2O (1:8:40).

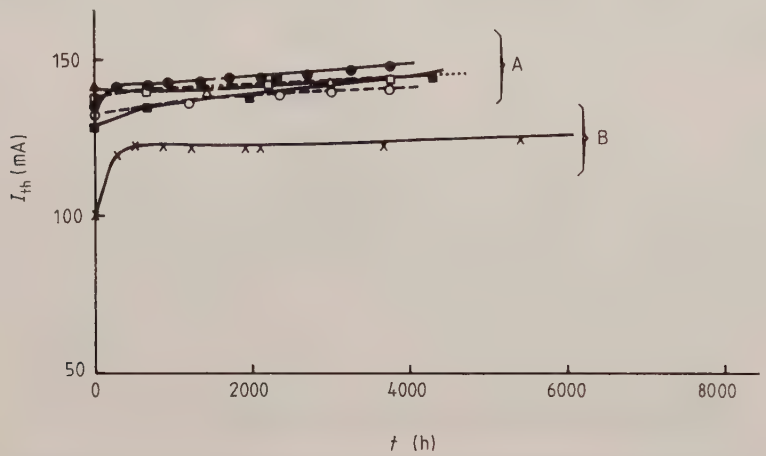

Figure 4.50 Current versus time aging characteristics (at room temperature) of GaInAsP–InP laser diodes made from LP-MOCVD material: (A) $P_1 = 5$ mW, $\lambda = 1.26$ μm; (B) $P_1 = 2$ mW, $\lambda = 1.29$ μm; $T =$ RT.

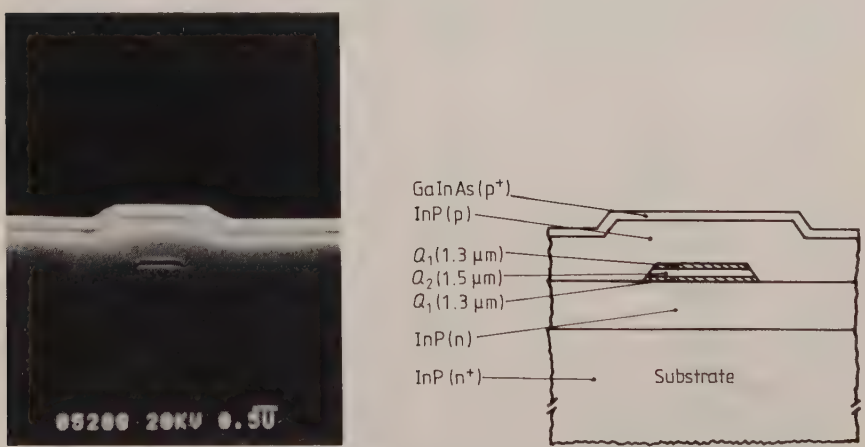

Figure 4.51 Scanning electron micrograph and schematic diagram of the cross section of a buried-ridge structure (BRS) of a 1.3 μm laser grown by two-step LP-MOCVD.

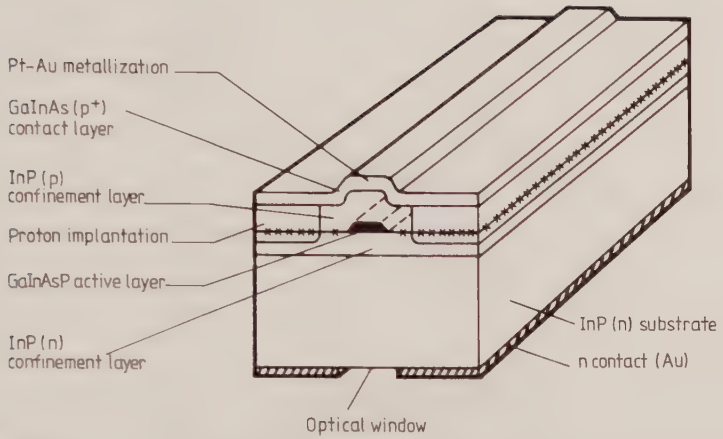

Figure 4.52 Schematic diagram of the cross section of a BRS 1.3 μm laser grown by two-step LP-MOCVD, with proton implantation.

After removing the resist mask, the ridge was then covered by a 1 μm thick Zn-doped InP confinement layer and 0.5 μm Zn-doped GaInAsP contact layer with $N_A - N_D = 1 \times 10^{19}$ cm^{-3} (using again the MOCVD growth technique). Figure 4.53 shows an electrochemical profile (polaron) of this structure before and after regrowth. In order to localize the injection in only the buried-ridge active region, a deep-proton implantation was realized through a 5 μm wide photoresist mask after metallization of the contacts. The n contact is realized by the deposition of Au. The p contact is made by the deposition of Pt–Au and annealing at 450°C for 30 s. After cleaving and scribing into chips of 300 μm length and 350 μm width, the lasers were mounted, epilayer-side down, onto nickel-plated copper heat-sinks using indium bonding.

(a) BRS lasers emitting at 1.3 μm

Typical light–current, voltage–current and lasing characteristics under CW operation at 20°C are shown in figures 4.54 and 4.55; CW linear output powers up to 10 mW have been measured. An external quantum efficiency $\eta_q \simeq 60\%$ has been obtained.

Typical far-field patterns parallel and perpendicular to the junction plane are shown in figure 4.56. These patterns were measured under CW operation for different optical output powers. A single transverse mode without significant distortion was observed at least up to 10 mW. The far-field full widths at half-maximum (FWHM) power, parallel and perpendicular to the junction plane, were about 26° and 36°, respectively.

Figure 4.57 shows the variation of threshold current as a function of stripe width. The threshold current increases linearly with buried-ridge width.

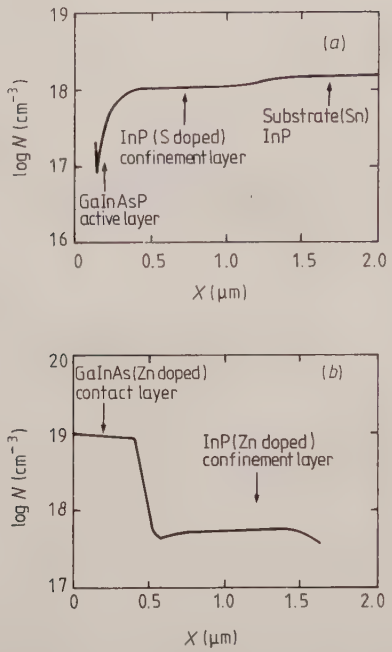

Figure 4.53 Polaron profile of a GaInAsP–InP BRS 1.5 μm laser: (*a*) first step growth; (*b*) second step growth.

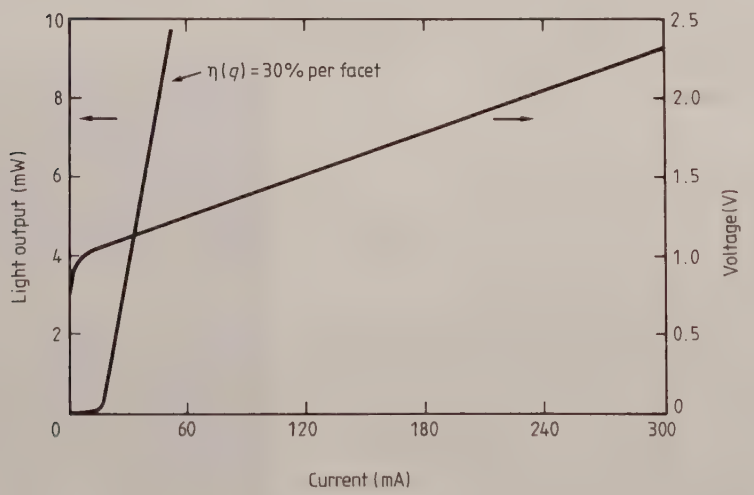

Figure 4.54 Light–current (*P–I*) and voltage–current (*V–I*) characteristics of LP-MOCVD BRS laser under CW operation at 20°C.

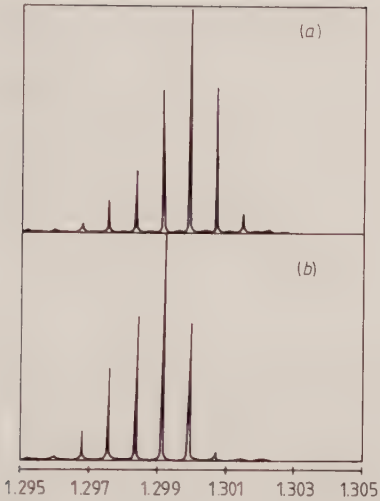

Figure 4.55 Lasing spectra of a BRS laser of a single traverse mode under CW operation at 20°C: (*a*) $P = 8$ mW, $I = 40$ mA, $\lambda = 1.2998$ μm; (*b*) $P = 4$ mW, $I = 30$ mA, $\lambda = 1.299$ μm.

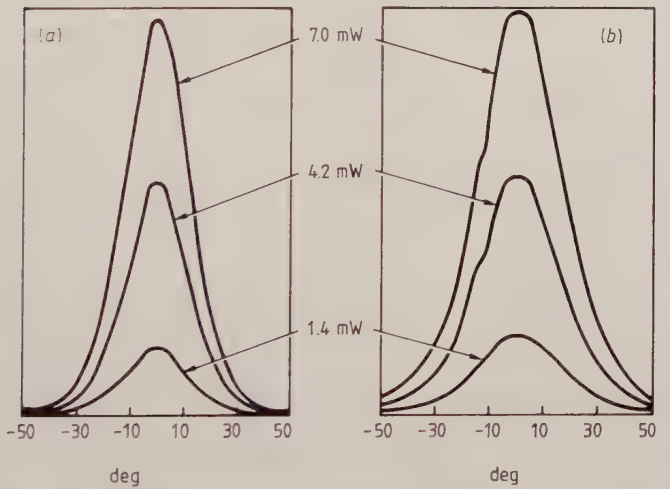

Figure 4.56 Far-field patterns (*a*) parallel and (*b*) perpendicular to the junction of a BRS laser for different output powers under CW operation.

Excellent reproducibility, homogeneity and uniformity have been obtained over 10 cm^2. Table 4.9 shows the threshold current, quantum efficiency η_q and wavelength of nine wafers of 8 cm^2. The standard deviation of threshold current density over 8 cm^2 becomes less than 5%. Table 4.9 also presents the threshold current density of diodes over 8 cm^2 using two different technologies.

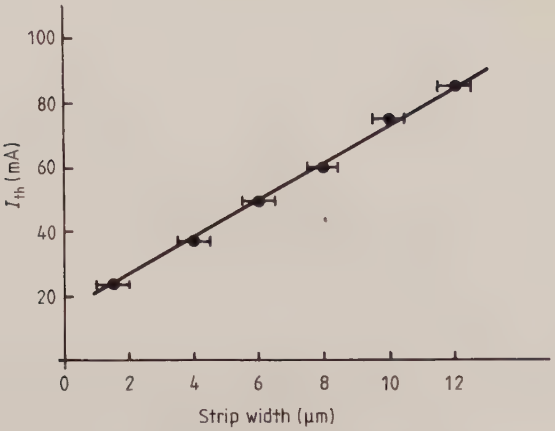

Figure 4.57 Variation of threshold current (I_{th}) as a function of stripe width; LP-MOCVD BRS laser, $\lambda = 1.3$ μm, $\eta_q \simeq 60\%$.

Table 4.9 Threshold current I_{th}, number of diodes tested, measurement temperature T_{meas}, lasing wavelength λ and external quantum efficiency η_q of nine wafers.

Wafer number	I_{th} (mA)	Number of diodes tested	T_{meas} (°C)	λ (μm)	η_q (%)
1262–83	24.2 ± 1.9	25	27	1.32	≃60
1264–91	17.9 ± 2.0	20	24	1.29	≃60
1266–88	26.3 ± 5.6	25	29	1.32	≃60
1267–89	37.4 ± 2.9	20	24	1.23	≃60
1268–88	36.0 ± 3.1	20	27	1.3	≃60
1204–06	45.7 ± 5.0	60	23	1.32	≃60
1205–06	50.0 ± 2.5	60	26	1.3	≃60
1218–27	36.6 ± 3.3	19	25	1.3	≃60
1223–30	26.7 ± 5.4	20	28	1.3	≃60

Figure 4.58 shows the variation of threshold current (I_{th}) and external quantum efficiency (η) of a $Ga_{0.28}In_{0.72}As_{0.46}P_{0.54}$–InP BRS laser, under CW operation at room temperature, from four bars randomly selected from one wafer of 10 cm^2. Threshold currents as low as 6 mA, with an external quantum efficiency as high as 30% for a cavity length of 300 μm, have been measured.

(b) GaInAsP–InP BRS lasers emitting at 1.5 μm

Figure 4.59 shows the variation of threshold current (I_{th}), external quantum efficiency (η) and emitting wavelengths of a GaInAsP–InP buried-ridge-

structure laser emitting at 1.5 μm, fabricated on material grown by two-step MOCVD over 4 cm^2 of InP substrate. The measurements are done at room temperature. The fabrication process is similar to the 1.3 μm BRS laser mentioned before. Bars are taken from different parts of a wafer in order to have a typical sample representative of the wafer. The average threshold current is 14.53 mA with a standard deviation of 1.82 mA. For 79 tested lasers the average external differential efficiency is 0.17 $W A^{-1}$ per facet with a standard deviation of 0.01 $W A^{-1}$.

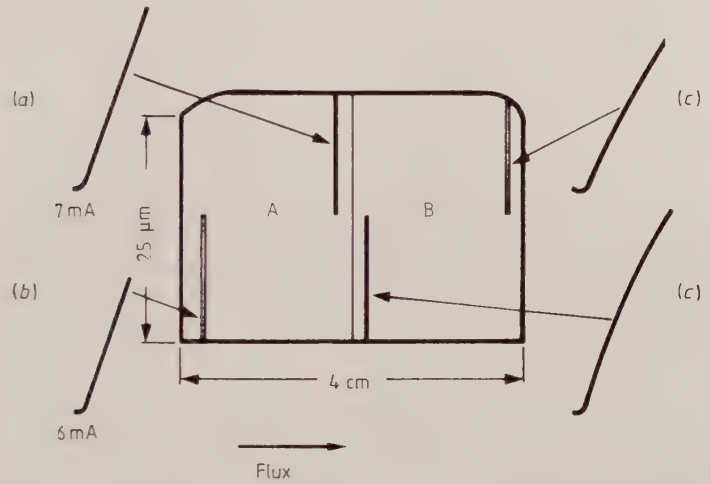

Figure 4.58 The variation of threshold current (I_{th}) and external quantum efficiency (η) of a GaInAsP–InP BRS laser over 10 cm^2 of InP substrate; $\lambda = 1.30$ μm, 48 tested lasers.

Figure 4.60 shows light–current characteristics of 12 diodes randomly selected from another wafer emitting at 1.55 μm. External quantum efficiency as high as 20% per facet and threshold current as low as 8 mA at room temperature have been measured under pulse operation. The typical far-field full widths at half-maximum parallel and perpendicular to the junction for the lasers are 28° and 35° respectively, with excellent uniformity. The T_0, measured under pulsed operation between 20 and 70°C, is 65 K. The maximum operating temperature is around 110°C.

(c) Validation of MOCVD GaInAsP–InP lasers by photoluminescence imaging method

Photoluminescence imaging is done with simple equipment represented in figure 4.61, which consists of an argon laser and infrared PbS camera–monitor system. The laser spot is focused on the sample, the luminescence image of which is then magnified and detected by the vidicon of the camera.

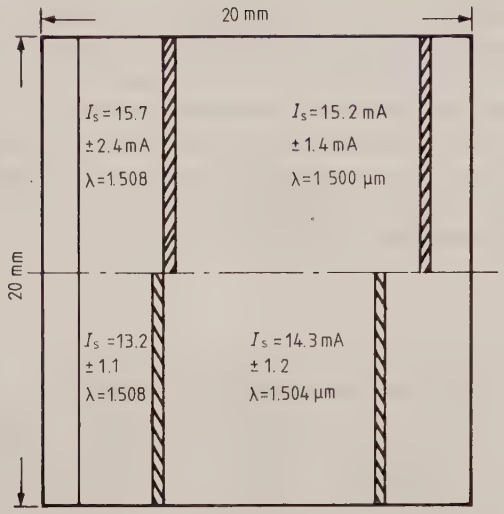

Figure 4.59 Variation of threshold current (I_{th}), external quantum efficiency (η) and emitting wavelengths of a GaInAsP–InP BRS laser over 4 cm^2 of InP substrate; laser RAZ 112.120/n H$^+$; 79 tested lasers; good lasers 74–94%; $\lambda = 1.5$ μm, $\bar{I}_{th} = 14.53 \pm 1.02$ mA, $\bar{\eta} = 0.17 \pm 0.01$ W A^{-1}.

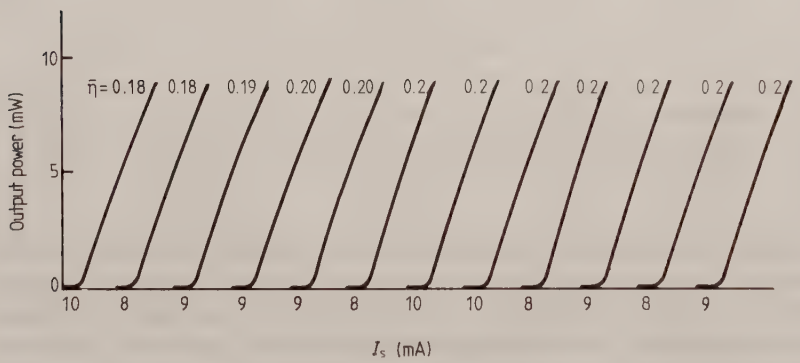

Figure 4.60 Light–current characteristics of 12 MOCVD BRS laser diodes emitting at 1.55 μm, at $T = 28°C$.

For practical reasons, the observed surface is 2×10^{-3} cm^2. So, x–y mechanical movements have been added in order to observe the wafers over a typical surface area of about 8 cm^2.

The image observed on the monitor screen is magnified 600 times so that the luminescence microstructure of layers is observed rather than accidental growth defects. Under these observation conditions, the image spatial resolution is limited by generation and recombination mechanisms and not by the detection method.

Three validations of epitaxy and lithography steps are provided by PL imaging, two of which are in wafer processing. Figure 4.62 represents the localization of the PL tests between the technology steps showing simultaneously, in a schematic manner, the observed structure. It is seen that the observed layers are double heterostructures consisting of an active quaternary layer (small gap) on InP buffer covered by a thin InP layer (large gap). In this structure a strong luminescence from the active layer can be observed because of the carrier confinement in the small-gap material and of the relatively smaller absorption of laser light in the surface layer. Moreover, the luminescence from different materials can be separated and identified using appropriate selective optical filters.

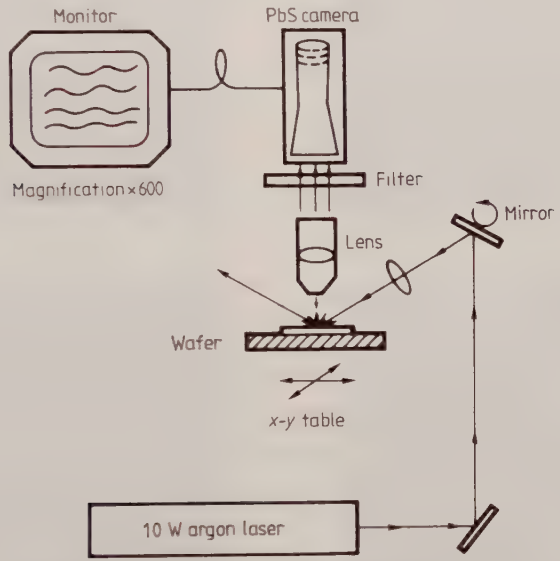

Figure 4.61 Photoluminescence imaging system.

In addition to the tests in wafer processing, a standard electroluminescence imaging of the stripe active area in mounted lasers is provided using the same camera–monitor system.

Dark line defects (DLD) and dark spot defects (DSD) have been typically detected by PL imaging of the active layer. The DLD, attributed to deviations from lattice matching, can be eliminated by readjustments in gas composition during MOCVD growth. A correlation between DSD and chemically revealed defects has shown that some of the dark spots can correspond to dislocations, but the origin of the DSD is still not well understood.

Two examples of layers with DSD density below $10^3\ \text{cm}^{-2}$ and above $3 \times 10^4\ \text{cm}^{-2}$ will now be considered in the light of luminescence image tests. Figures 4.63 and 4.64 present the luminescence images of both the

examples. It can be seen that a good PL image test after the first epitaxy, where the DSD were not detected ($< 10^3$ cm^{-2}), leads to good tests of stripe PL image after lithography and the second epitaxy. On the other hand, the DSD present in the first epitaxy layer image (3×10^4 cm^{-2}) could also be found in the buried stripe after lithography and the second epitaxy. Systematic tests on tenths of wafers have confirmed that the DSD are principally localized in the layers of the first epitaxy. Also, it was seen that the second epitaxy did not perturb the good PL quality of the buried stripe.

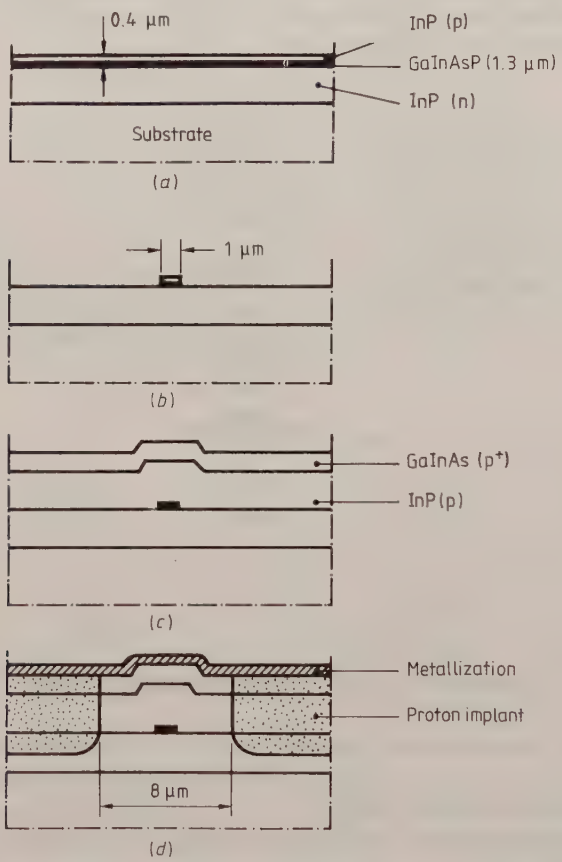

Figure 4.62 Technology and image test steps of BRS laser fabrication. (*a*) First epitaxy; (*b*) photolithography; (*c*) second epitaxy; (*d*) completed structure.

The PL and electroluminescence (EL) images have been systematically correlated with an accelerated aging test. The aging of lasers was carried out at 70°C maintaining 5 mW of optical power. The characteristics of threshold current under aging are presented in figure 4.65. Good ageing

behaviour was observed only in the absence of DSD in buried stripes. On the other hand, an important dispersion of aging characteristics has been noted if DSD over 10^4 cm^{-2} were present in the active layer.

Validations of the wafers are done after the first epitaxy, after strip lithography and after the second epitaxy by a photoluminescence imaging method. The electroluminescence of the active area of lasers mounted p-side down can be observed by a window in the n contact.

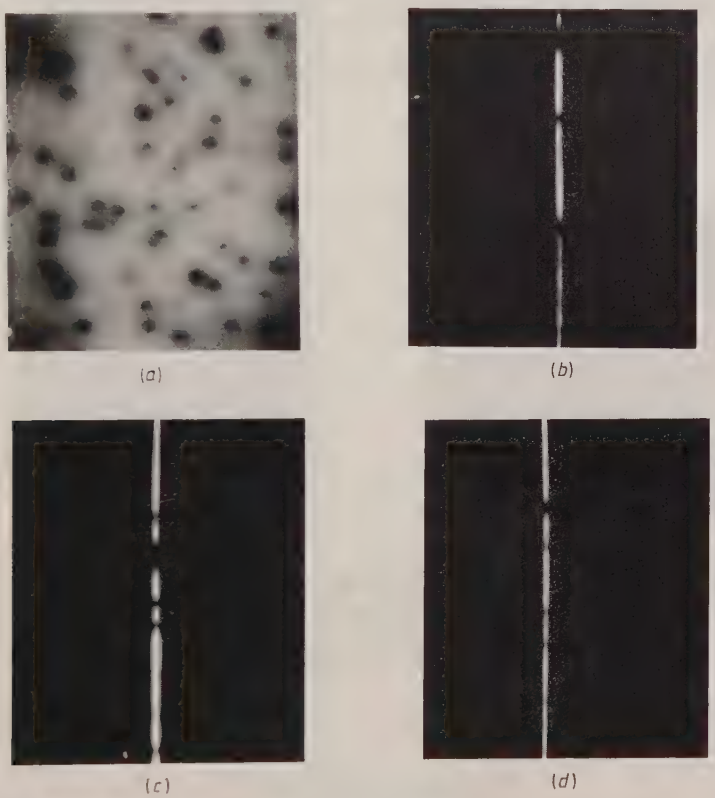

Figure 4.63 Luminescence test images, wafer 1383/1393, DSD < 10^3 cm^{-2}. (*a*) After first epitaxy (wafer process); (*b*) after lithography (wafer process); (*c*) after second epitaxy (separated bar); (*d*) electroluminescence test (mounted laser).

In order to localize the injection current in the active region, two processes have been used:

(1) realization of a Schottky mesa of 6 μm width and 0.7 μm depth through the GaInAs cap layer (figure 4.66), and

(2) realization of a deep-proton implantation of 6 μm width through the InP homojunction (figure 4.67).

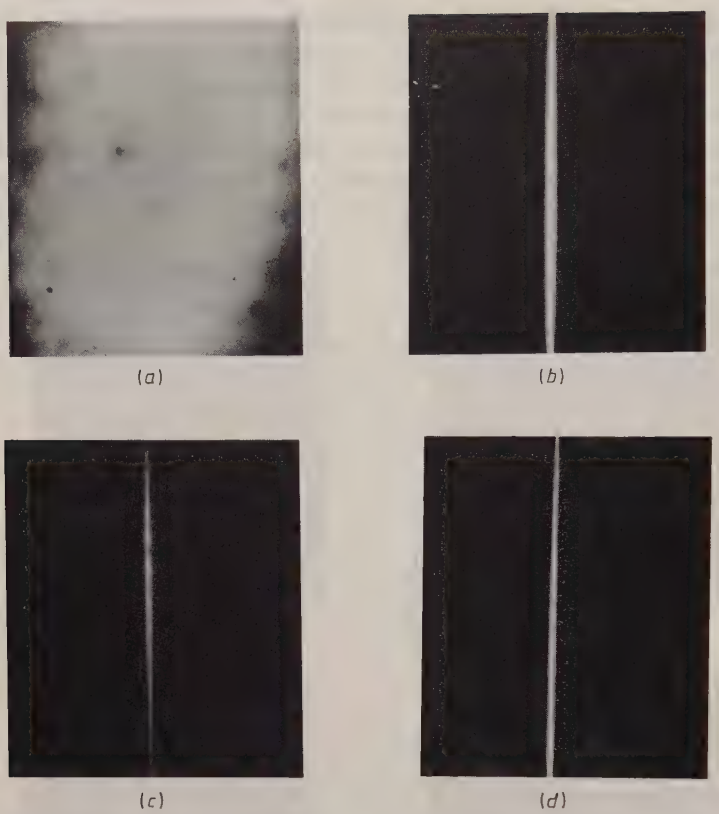

Figure 4.64 Luminescence test images, wafer 1262/1263, DSD $\simeq 3 \times 10^4$ cm^{-2}. (*a*)–(*d*) as in figure 4.63.

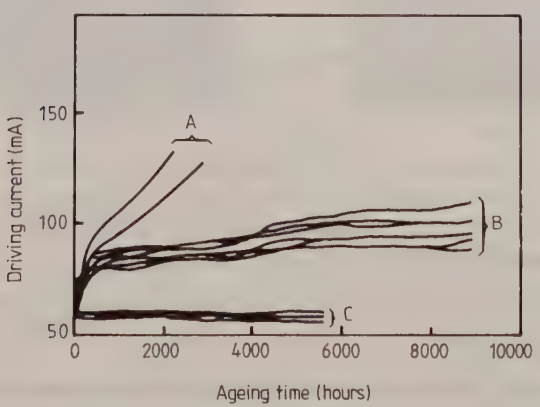

Figure 4.65 Ageing characteristics of BRS 1.3 μm lasers with and without DLD and DSD under accelerated test conditions (5 mW, 7°C): A, with DSD and DLD; B, with DSD only; C, without DSD and DLD.

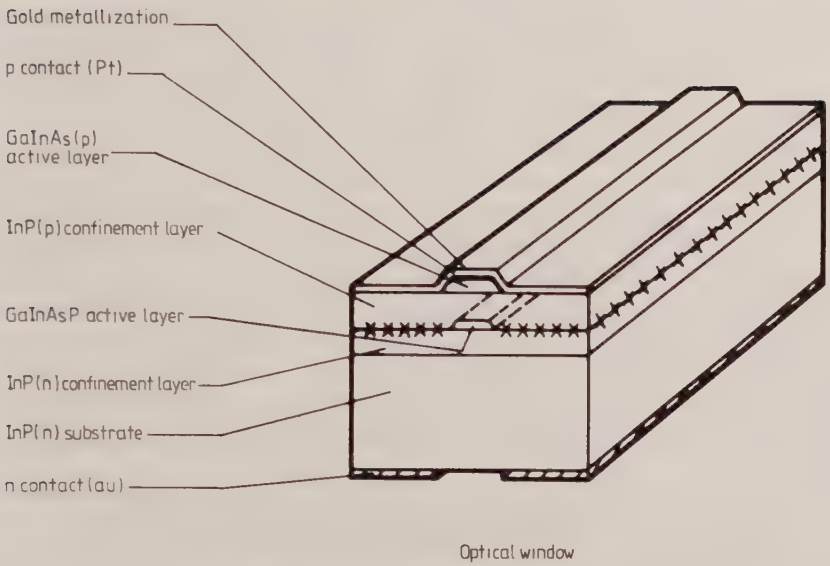

Figure 4.66 Diagram of a BRS laser with Schottky mesa.

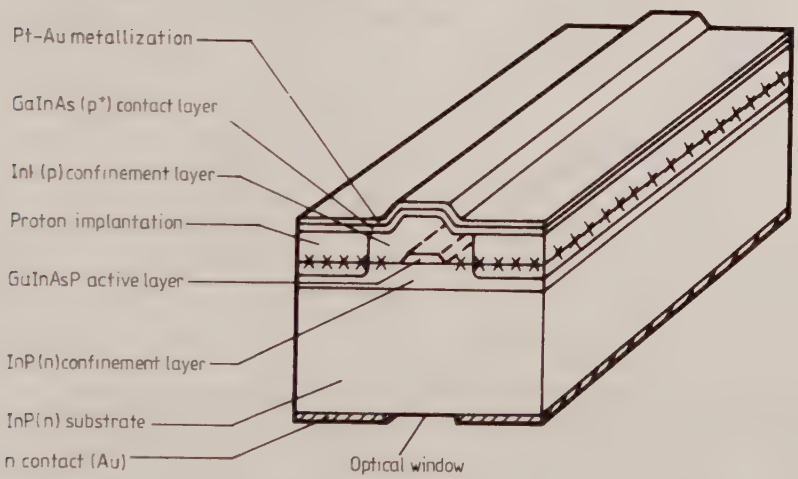

Figure 4.67 Diagram of a BRS laser with proton implantation.

Figure 4.68 shows the histogram of threshold current under pulsed operation at room temperature for 864 chips, from the two processes, randomly selected from one wafer. The average current is 19.0 mA with a standard deviation of 2.2 mA.

Figure 4.69 shows the histogram of CW threshold current at 20°C for a total of 72 lasers mounted down or up, from the two processes. The average threshold current is 19.9 mA with a standard deviation of only 1.4 mA.

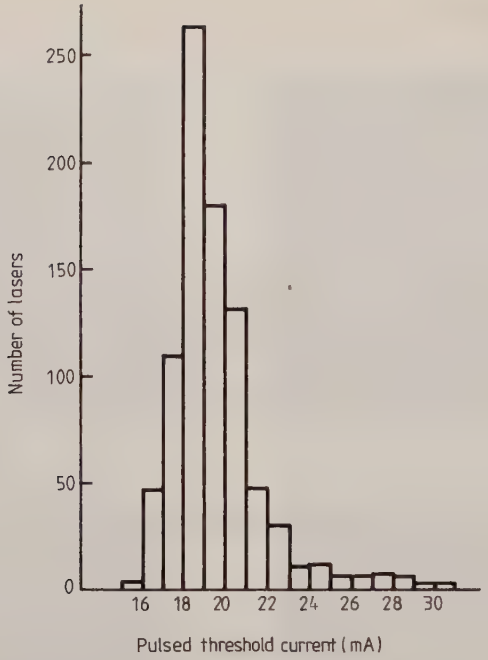

Figure 4.68 Histogram of threshold current under pulsed operation at room temperature for 864 chips randomly selected from one wafer: $\bar{I}_{th} = 19.0 \pm 2.2$ mA, $\lambda = 1.3$ μm.

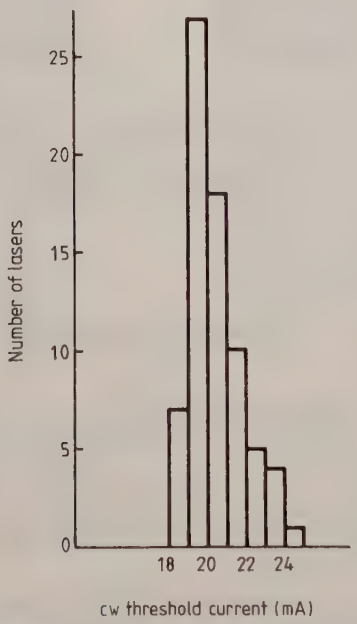

Figure 4.69 Histogram of CW threshold current at 20°C for 72 mounted lasers from one wafer: $\bar{I}_{th} = 19.9 \pm 1.4$ mA.

(These parameters are respectively 45.8 and 3.5 mA at 70°C for 58 lasers mounted down.) For the 72 lasers the average external differential efficiency is 0.22 W A^{-1} per facet with a standard deviation of 0.01 W A^{-1}.

Figure 4.70 shows typical CW light–current characteristics at different temperatures. The maximum operating temperature is around 130°C. A stable fundamental transverse mode was observed at least up to 7 mW. Typical far-field patterns parallel and perpendicular to the junction plane measured at 1.4, 4.2 and 7 mW are shown in figure 4.71. The far-field full widths at half-maximum parallel and perpendicular to the junction are, respectively, 27° and 35° with a good uniformity. The T_0, measured under pulsed operation between 20 and 70°C, is 70 K. The low serial resistance of 2.5 Ω is favourable for CW operation at high temperature and also at high modulation frequency. For 50 lasers randomly selected on the wafer, the average wavelength is 1.3012 μm with a standard deviation of 68 Å.

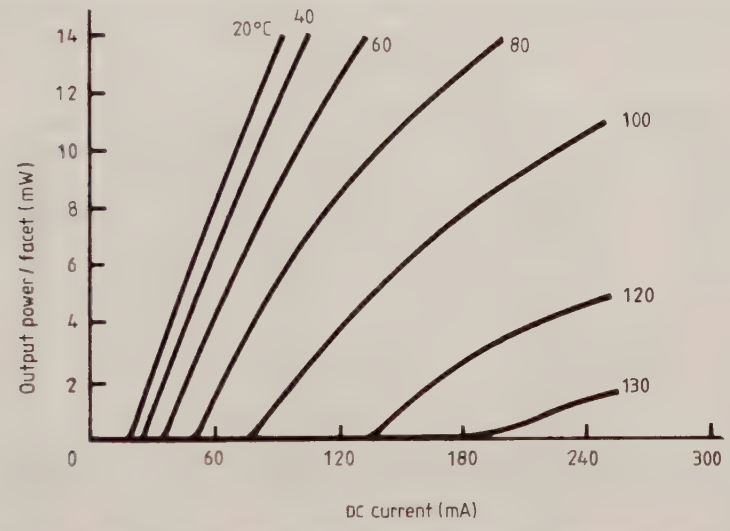

Figure 4.70 Light output versus pulsed current at several heat-sink temperatures of 1.3 μm GaInAsP–InP BRS laser grown by two-step LP-MOCVD.

Table 4.10 presents statistical results on the threshold currents of 2117 chips taken randomly from the 20 wafers processed into lasers. The measurements are done at room temperature under pulsed operation. Bars are taken from different parts of the wafer (except the sides) in order to have a typical sample representative of the wafer.

The yield, which is defined as the number of good chips that work with a threshold current less than three times the standard deviation above the average divided by the total number of tested chips, gives an indication of

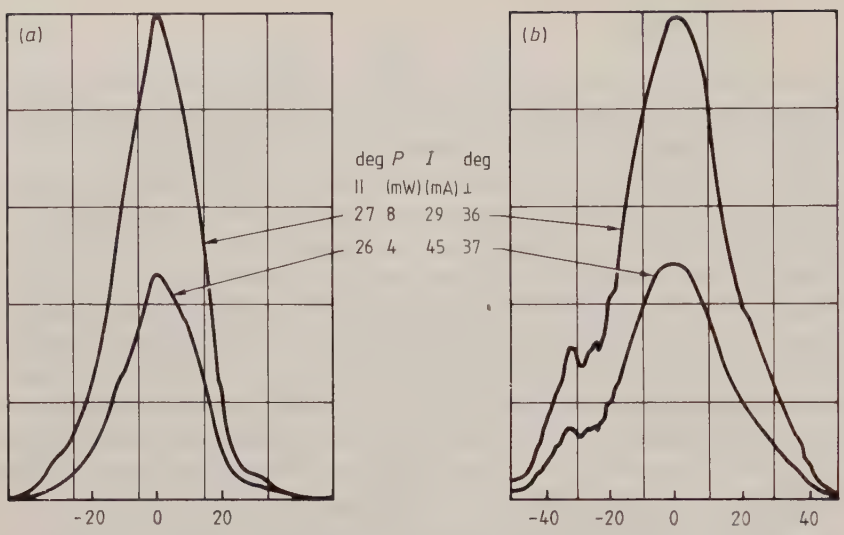

Figure 4.71 Far-field patterns (*a*) parallel and (*b*) perpendicular to the junction of a BRS $\lambda = 1.3\ \mu$m laser for different output powers under CW operation at 20°C; FWHM are indicated, along with P and I, for each curve.

Table 4.10 Statistical results concerning the currents of 2117 chips.

Wafer number	Number of tested chips	Average threshold current (mA)	Standard deviation (mA)
1380	87	26.0	6.5
1383	864	19.0	2.2
1386	75	17.0	3.0
1424	62	18.4	2.3
1426	181	36.2	3.3
1427	136	45.1	8.2
1428	109	38.8	2.8
203	31	16.3	1.3
204	28	17.3	2.4
215	46	20.2	7.4
234	16	7.6	1.4
302	98	12.4	2.9
303	48	9.5	1.3
304	61	13.4	3.3
305	50	10.5	1.9
308	53	9.8	3.1
445	61	21.1	4.6
447	43	24.2	5.5
448	31	22.9	3.0
449	37	27.2	2.9
Average		20.6	3.5
Standard deviation		10.1	2.0

the quality of the epitaxy, of the process and of the cleaving. The average yield obtained on these 20 wafers has the high value of 95% with a standard deviation of 4%.

The amplitude response of a laser diode is characterized with a sweep oscillator, which covers the frequency range 10 MHz–8.4 GHz, with a network analyser, which provides magnitude and phase measurement capability from 100 MHz to 40 GHz, and with a photodiode having a bandwidth of 8 GHz.

Figure 4.72 shows a typical modulation characteristic of a proton-implanted laser biased at 27 mA ($2I_{th}$) with a modulation current of 18 mA peak-to-peak at 20°C.

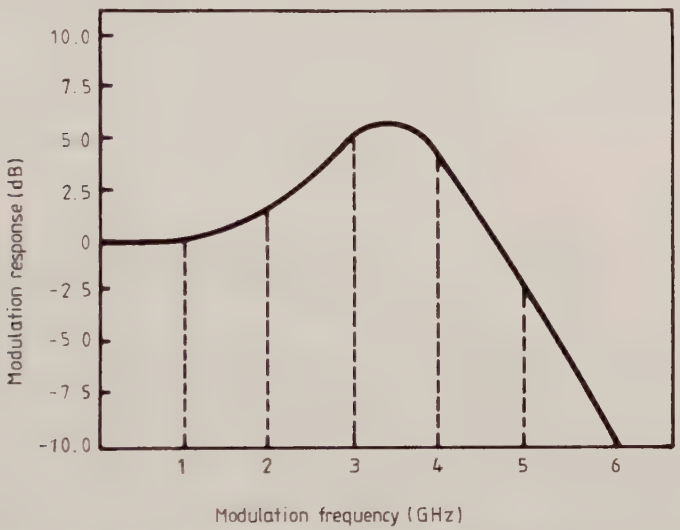

Figure 4.72 Typical modulation characteristic of a 300 μm long BH laser with proton implantation at 20°C (2.9 mW/facet).

Eleven proton lasers, 300 μm long, from five wafers have been characterized. The average bandwidths f at -3 dB and the standard deviations are the following:

at 1 mW/facet:	$f = 3.0$ GHz	$\sigma = 0.6$ GHz
at 2 mW/facet:	$f = 3.9$ GHz	$\sigma = 0.5$ GHz
at 4 mW/facet:	$f = 4.5$ GHz	$\sigma = 0.4$ GHz.

Modulation characteristics are nearly flat from 2000 MHz to 1 GHz (no roll-off limits the bandwidth). The overshoot is less than 10 dB and has a typical value of 5 dB. Results show a good reproducibility of modulation characteristics from wafer to wafer. These proton laser diodes can be used in optical transmission systems in the S band (2–4 GHz).

On the contrary in the Schottky mesa laser diodes some roll-off limits the bandwidth at around 1 GHz. Since the two kinds of laser diodes come from the same wafers, have the same stripe structure and the same serial resistance, the difference in the modulation characteristics is attributed to a lower parasitic capacitance in the proton laser diodes (the deep-proton implantation through the InP p–n junction reduces the surface parastic capacitance).

Accelerated ageing tests are performed at 70°C and at an output power of 5 mW/facet without any preliminary screening test. Twenty-two lasers, mounted down, from the two processes and from two wafers have been ageing for a total of 209 630 h and have not yet shown any significant degradation. Figures 4.73(*a*) and (*b*) show the driving current as a function of the ageing time for, respectively, six and nine lasers with Schottky mesa from the two wafers. Figure 4.74 shows ageing characteristics of seven lasers with proton implantation from the two wafers. Degradation satur-

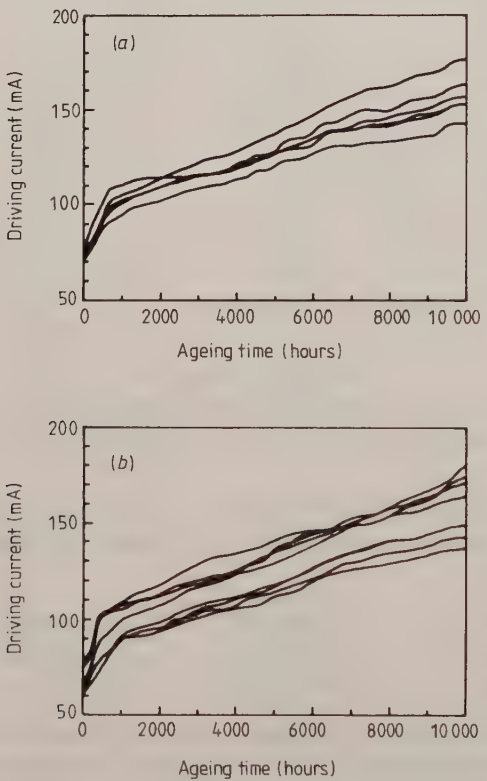

Figure 4.73 Ageing characteristics of (*a*) six BRS lasers with Schottky mesa from one wafer and (*b*) nine BRS lasers with Schottky mesa from another wafer (70°C, 5 mW).

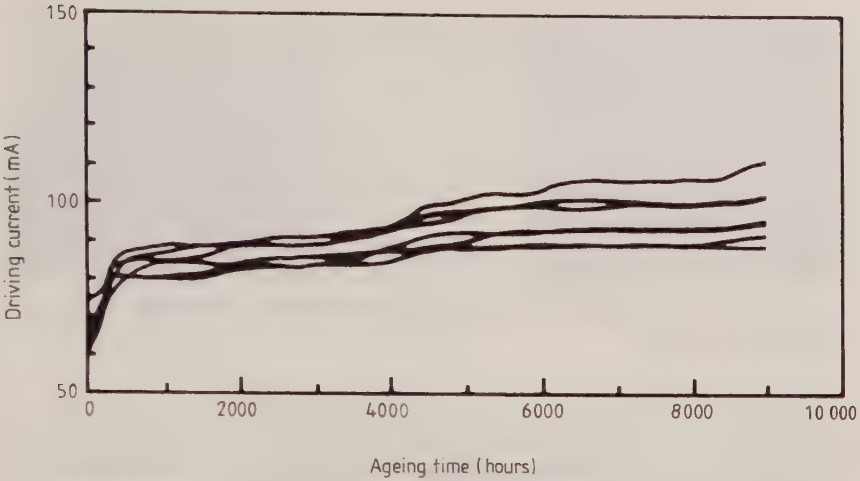

Figure 4.74 Ageing characteristics of seven BRS lasers with proton implantation from two wafers (70°C, 5 mW).

ation appears between 500 and 1000 h. The time for stabilization is shorter for the proton lasers than for the mesa lasers. The long-term degradation rates are calculated using the values of the driving currents at 100 h and at the maximum aging time.

The better reliability of the proton-bombarded lasers could be attributed to their smaller InP homojunction width (about 5 μm) compared to the 350 μm homojunction width of the Schottky lasers. But this hypothesis has not been confirmed since the different possible causes of degradation (homojunction, active layer, thermal impedance) have not yet been correlated with the observed aging.

The two wafers show identical and homogeneous degradation. With a 50% increase in driving current as a failure criterion, the above value of degradation rate for proton lasers corresponds to a lifetime of 23 800 h at 70°C.

4.3.3 Distributed feedback lasers fabricated on material grown completely by MOCVD

Semiconductor lasers which oscillate in single longitudinal mode (SLM) under high-speed direct modulation are expected to improve the performance of optical transmission systems. In order to obtain the SLM oscillation, a semiconductor laser should include a wavelength-selective optical feedback mechanism in the device structure. In distributed feedback (DFB) lasers, a corrugation grating near the active layer is responsible for the wavelength-selective optical feedback mechanism. In the laser cavity,

right-travelling waves and left-travelling waves couple through the grating. The strength of coupling, which governs the stability of SLM operation, is determined by the corrugation depth, the refractive indices and the thicknesses of the layer structure.

GaInAsP–InP DFB lasers have been studied using LPE [46], a hybrid of MBE and LPE [47] and a hybrid of LPE and MOCVD [48]. Many important problems exist in DFB laser fabrication. Prominent among them is the phenomenon of surface deformation, which occurs during LPE regrowth. The MOCVD growth technique can be used to overcome this problem and has produced structures after overgrowth without any deformation in corrugation depth.

(a) Device fabrication

The DFB laser structure is manufactured in the following manner. First, the following layers were successively grown by MOCVD on an Sn-doped (1 0 0) 2° off or (1 0 0) exact InP substrate:

(1) 1 μm InP confinement layer, sulphur-doped, with $N_D - N_A = 10^{18}$ cm^{-3};

(2) 0.2 μm thick undoped GaInAsP (composition $\lambda = 1.55$ μm) active layer;

(3) 0.2 μm thick Zn-doped ($N_A - N_D = 2 \times 10^{17}$ cm^{-3}) GaInAsP (composition $\lambda = 1.3$ μm) guiding layer.

Next, second-order corrugation gratings with a period of 4700 Å ($\Lambda = \gamma_L/2n_{eq}$) and a depth of 1500 Å were formed in the top of the guiding layer by holographic photolithography followed by chemical etching, orienting the gratings along the (0 1 1) direction. The gratings were then covered with 1 μm of Zn-doped InP and 0.5 μm of Zn-doped GaInAsP cap layer, regrown by MOCVD.

To avoid surface deformation, great care must be exercised during the MOCVD regrowth. The corrugated InGaAsP ($\lambda = 1.3$ μm) surface is heated from room temperature to 650°C for 3 min in an $N_2 + H_2$ carrier gas, and then the TEIn and PH_3 are switched into the reactor. Figure 4.75 shows scanning electron microscope cross sections of the corrugated structure before and after MOCVD overgrowth. It appears from these photomicrographs that no significant surface deformation has occurred and the final depth of the corrugation is similar to the pregrowth height.

The ridge-waveguide structures developed by Kaminow *et al* [49] have been fabricated (figure 4.76) from these wafers. The devices are separated by cleaving two facets and scribing the other two facets. The width of the ridge is 5 μm and the length of the cavity about 300 μm. Individual diodes are bonded with In to an Ni-plated copper heat-sink.

Figure 4.77 shows typical light–current characteristics and the lasing spectrum of a DFB laser at 20 and 60°C under CW operation. The typical

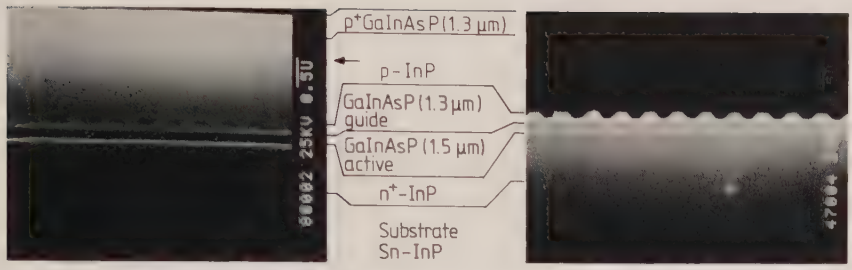

Figure 4.75 Scanning electron microscope cross sections of the corrugated structure before and after LP-MOCVD overgrowth.

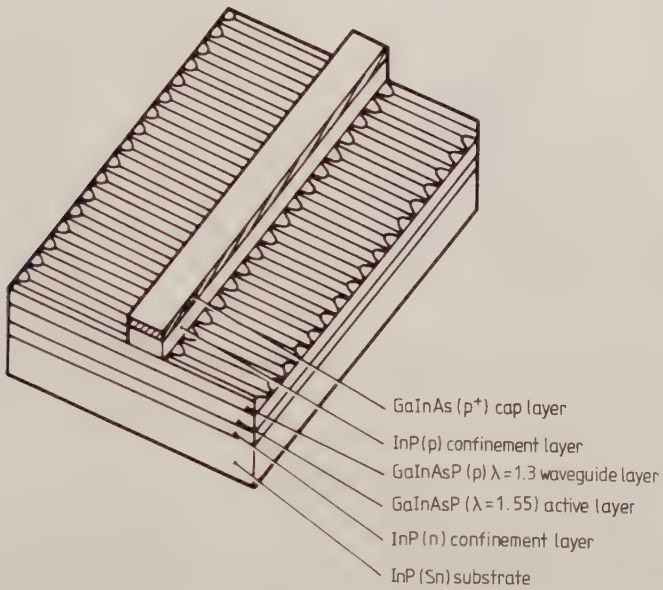
GaInAs (p⁺) cap layer
InP (p) confinement layer
GaInAsP (p) λ = 1.3 waveguide layer
GaInAsP (λ = 1.55) active layer
InP (n) confinement layer
InP (Sn) substrate

Figure 4.76 Ridge-waveguide structures of GAInAsP–InP DFB laser.

threshold current I_{th} of CW operation was 60 mA. A CW output power of 6 mW/facet was measured. These results can be improved with antireflective (AR) coating on the front facet. Quantum efficiencies of 15% per facet have then been obtained. The temperature dependences of the threshold current I_{th} and the lasing wavelength under CW operation are shown in figure 4.78. Stable SLM operation is obtained in the temperature range from 9 to 90°C, with a temperature coefficient of the lasing wavelength $d\lambda_I/dT$ of 0.9 Å °C^{-1}.

Figure 4.79 shows the far-field patterns parallel and perpendicular to the junction plane of these DFB lasers. These patterns were measured under CW operation for different optical output powers. A stable operation in the

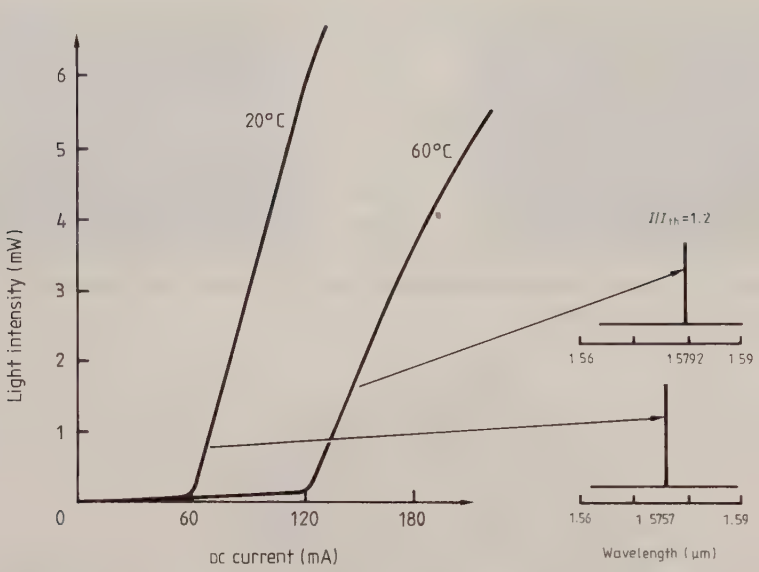

Figure 4.77 Light–current characteristics of DFB laser at 20 and 60°C under CW operation.

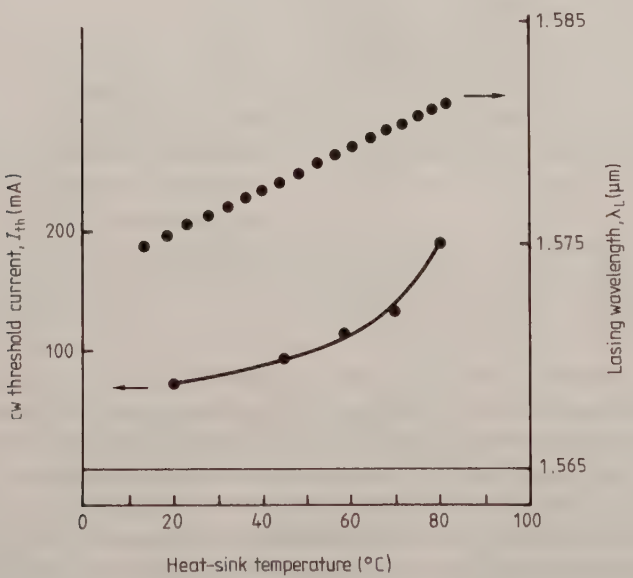

Figure 4.78 The variation of threshold current and lasing wavelength of a DFB laser as a function of heat-sink temperature under CW operation.

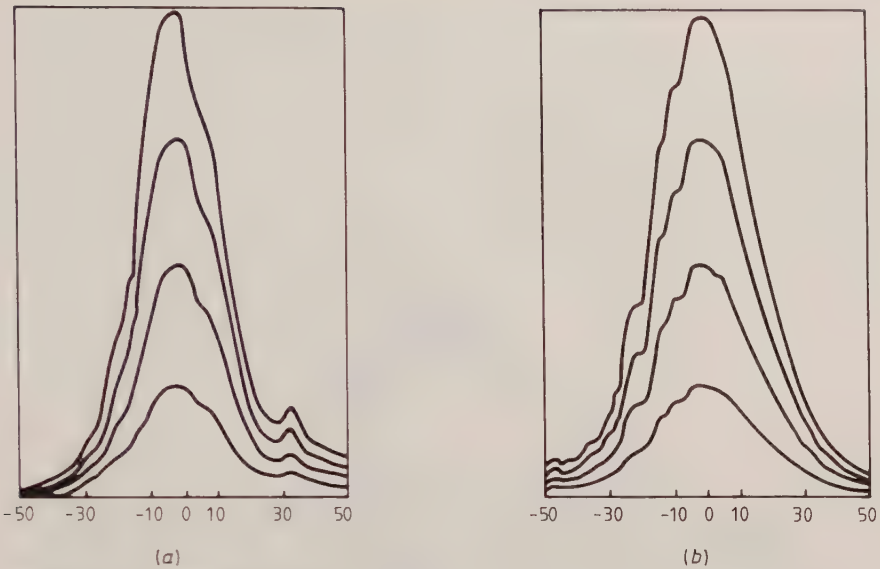

Figure 4.79 Far-field patterns (*a*) parallel and (*b*) perpendicular to the junction of a DFB 1.5 μm laser for different output powers under CW operation, at 20°C.

fundamental transverse mode without significant distortion was observed at least up to 8 mW. The far-field full widths at half-maximum power parallel and perpendicular to the junction planes were about 28° and 35°, respectively.

The detailed spectrum of a DFB laser just below the threshold is shown in figure 4.80. The maximum of gain peak wavelength is 1.55 μm, which is the same as the photoluminescence wavelength of the active layer. The distance between two Fabry–Perot modes is 12 Å. The DFB mode wavelength is 1.57 μm. The cavity length is 300 μm, so the value of the effective refractive index can be obtained by

$$n_{\text{eff}} \simeq \lambda^2/2L \simeq 3.4. \tag{4.20}$$

Kogelnik and Shank [50] predicted that periodic structures consisting of corrugation gratings have a stopband of frequencies in which propagation is forbidden. In figure 4.81, the stopband of 25 Å, where no resonance-mode emission existed, is clearly observed between DFB modes. In the output spectrum of the DFB laser, most of the lasing power is concentrated in a mode next to the stopband. As current increases, the intensity of the lasing line abruptly increases and the highest satellite mode becomes more than 30 dB (see figure 4.82).

The coupling coefficient K, per unit length, was experimentally

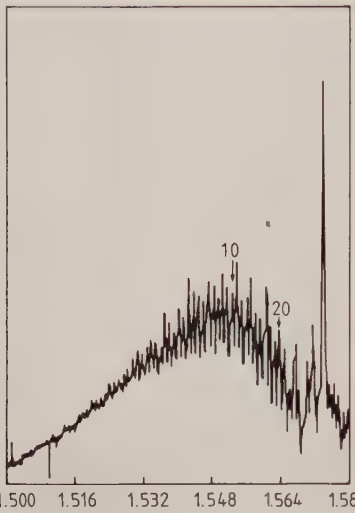

Figure 4.80 Emission spectrum of a DFB laser just below the threshold; $\Delta\lambda = 12$ Å, $L = 300\ \mu$m, $n_{\text{eff}} = \lambda/(2L\Delta\lambda) = 3.4$.

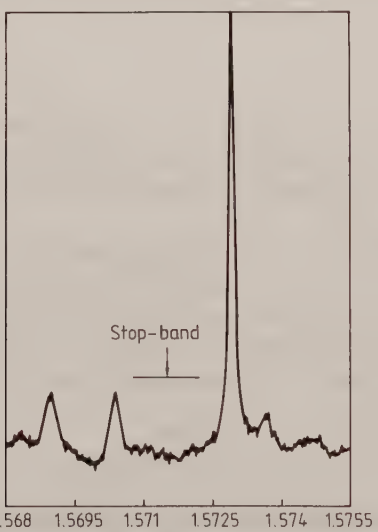

Figure 4.81 The detailed emission spectrum of a DFB laser; $I_{\text{th}} = 78$ mA, $I/I_{\text{th}} = 0.89$.

determined by using the relation [47]

$$K = n_{\text{eff}}\Delta\lambda_s/\lambda_B^2 \tag{4.21}$$

where $\Delta\lambda_s$ is the width of the 'stopband' in the subthreshold laser emission spectrum, n_{eff} is the effective refractive index and λ_B is the stopband centre

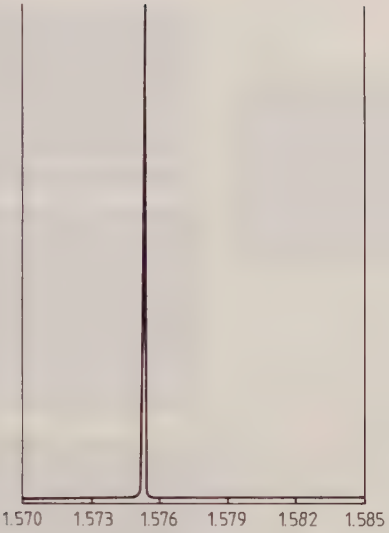

Figure 4.82 Lasing spectrum of a DFB laser under CW operation; $T = 20^{\circ}C$, $dB = 10 \log(P_0/P) \simeq 30$.

wavelength. The coupling coefficient K of DFB lasers using this equation was 108 cm^{-1} (with two cleaved facets). Single-longitudinal-mode operation under high-speed direct modulation up to 2 ns has been obtained (figure 4.83). Stable SLM was also maintained under sinusoidal modulation at 1 GHz (see figure 4.83). This should be compared to the lasing spectrum of a conventional Fabry–Perot single-mode semiconductor laser, which becomes multimode or is broadened under rapid direct modulation; the lasing mode of these lasers sometimes hops from one to another, even when operating in single mode.

The threshold current density in DFB lasers is found to depend on temperature, as in classical DH lasers (equation (4.19)):

$$J_{th}(T) = J_{th}(T_0) \exp(T/T_0)$$

where T_0 describes the characteristic temperature. The average T_0 value is $61^{\circ}C$ without break point up to $75^{\circ}C$ (see figure 4.84).

(b) Theoretical analysis of MOCVD DFB lasers by Correc et al [51]

The waveguide geometry and indices used in the calculations are shown in figure 4.85. The grating of period $\Lambda = 4650$ Å has a trapezoidal shape with $L_1 \simeq 0.27\Lambda$ and $L_2 \simeq 0.23\Lambda$. Its depth is $g \simeq 1500$ Å. Following the usual method [52], it is possible to compute the coupling coefficient for such gratings [53]. The thicknesses of the waveguide layer (T_{wg}), active layer (T_a) and buffer layer (T_b) are 0.18, 0.2 and 0.1 μm, respectively. T_{wg} has been slightly decreased from 0.2 μm (its value before the corrugation was

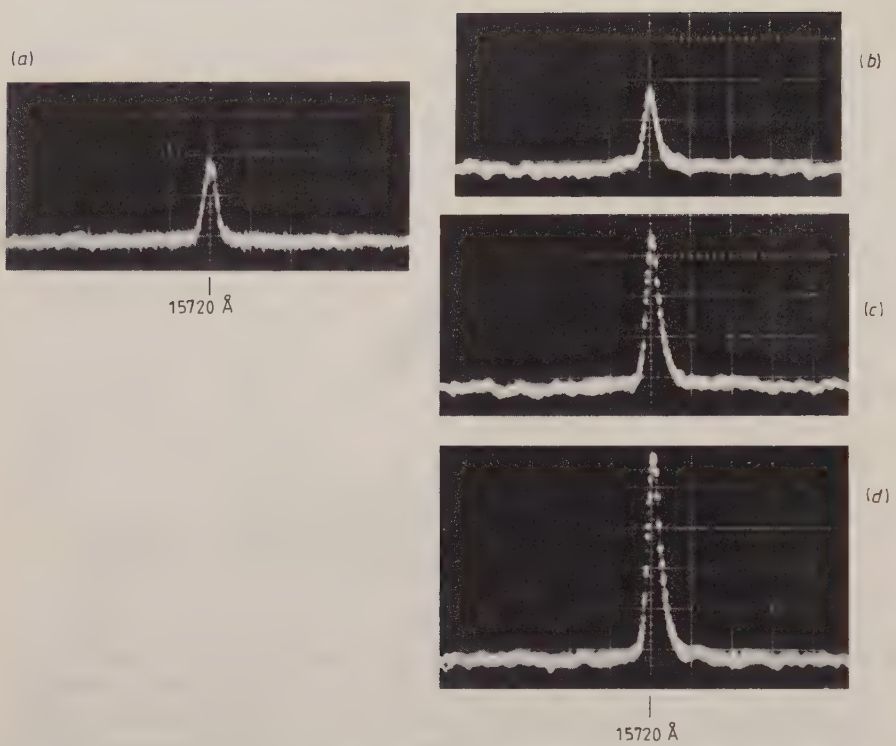

Figure 4.83 Lasing spectra under rapid direct modulation at 1 GHz; 1.57 μm ridge MOCVD DFB laser. (*a*) Sinusoidal modulation at 1 GHz; pulsed modulation time-resolved spectra at (*b*) 0.5 ns; (*c*) 1 ns; (*d*) 2 ns.

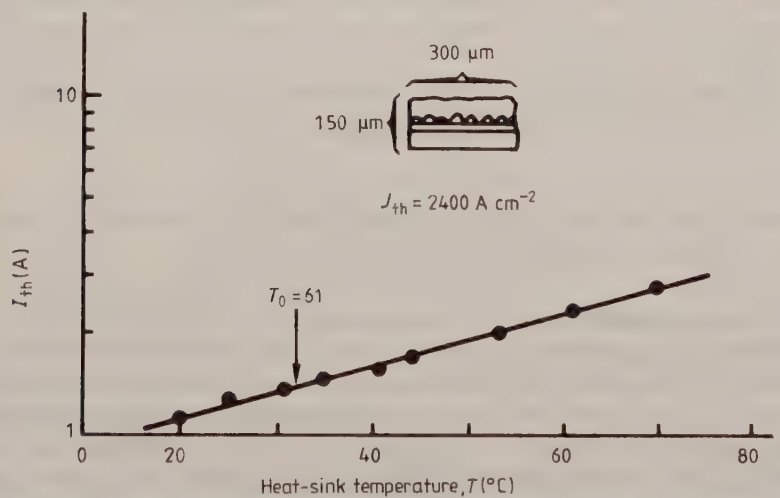

Figure 4.84 Variation of threshold current of DFB laser as a function of temperature; $J_{th} = 2400$ A cm^{-2}.

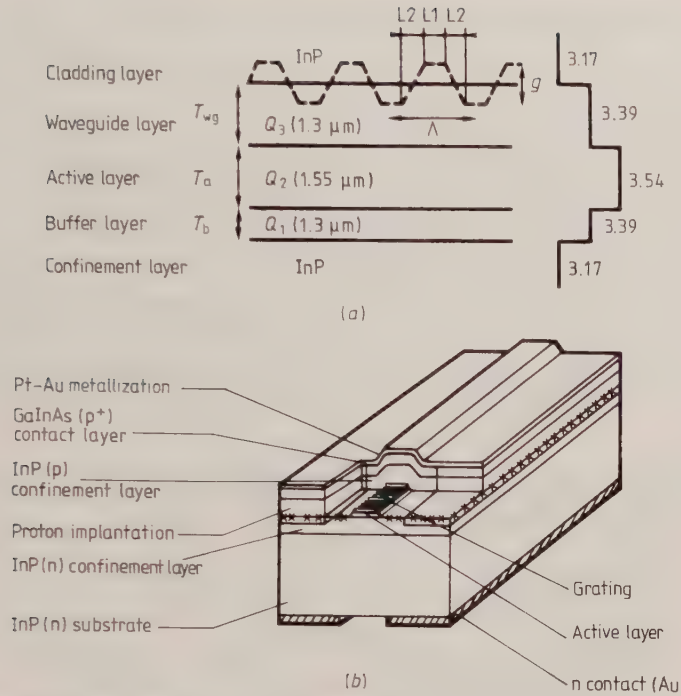

Figure 4.85 Schematic waveguide structure of the GaInAsP/InP DFB laser showing: (*a*) the layers and the grating; and (*b*) the indices at 1.55 μm.

made) to 0.18 μm to take the presence of the grating into account. Figure 4.86 shows the dependence of the coupling coefficient K on the corrugation depth g. The Bragg order is denoted by m. Since the grating profile is rather smooth and almost sinusoidal, the higher-order coefficients are much smaller than that of the first order. This stresses the importance of abrupt tooth-shape gratings for large higher-order coupling coefficients and the necessity to avoid surface deformation during regrowth.

Using K, the field threshold gain α_{th} is computed using the coupled-wave theory [50, 54]. Moreover, since in actual devices there are facets where reflections occur, one has to take them into account. The position of the uncoated facet with respect to the grating will have an important impact on the properties of the laser [55–57], especially on the discrimination between modes [58]. The field reflectivities are ρ_r and ρ_l for the right and left facets and the positions of the latter with respect to the grating are given by angles called 'facet phases' θ_r and θ_l, which are incorporated into the reflectivities in complex form. With $\rho_r = 0$ for the AR-coated facet, it is possible to compute the threshold gain as a function of the mirror phase θ_l for various KL, L being the laser length.

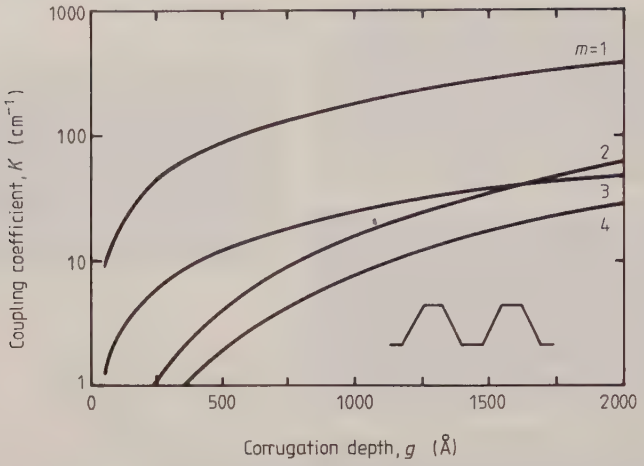

Figure 4.86 Coupling coefficient as a function of corrugation depth for trapezoidal grating. The Bragg order is denoted by m.

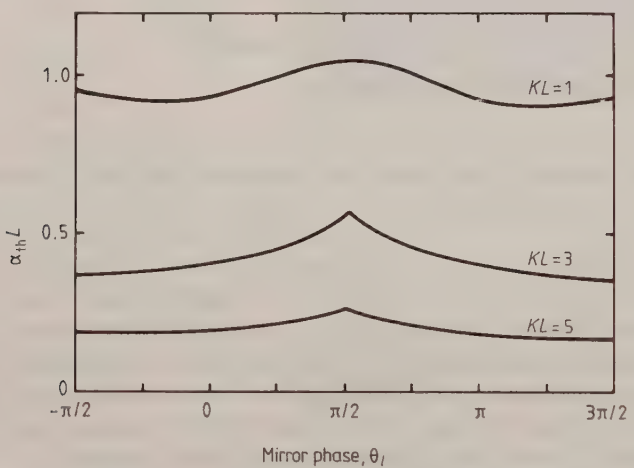

Figure 4.87 Effect of the mirror phase θ_l on the threshold gain α_{th}; $\rho_r = 0$, $\rho_l = 0.565 \exp(i\theta_l)$.

Figure 4.87 shows this dependence. From these curves, it appears that α_{th} is weakly dependent on θ_l and that a good estimation can be obtained with $\theta_l = 0$. Therefore, in the following calculations, $\theta_l = 0$ will be assumed. The uncertainty concerning θ_l will somewhat widen the curves obtained with $\theta_l = 0$. The threshold current I_{th} is calculated by

$$I_{th} = e \frac{B_{eff}}{A_0^2} dWL \left| \frac{2\alpha_{th}}{\Gamma} + (\alpha_{in} + \alpha_{ac}) + \alpha_{ex} \frac{1-\Gamma}{\Gamma} \right|^2. \qquad (4.22)$$

The notations and numerical values are those of Utaka *et al* [59]; W is the active-region width.

Figure 4.88 shows I_{th} as a function of the active-layer thickness T_a with the waveguide layer T_{wg} as a parameter. The broken curves illustrate the case where both facets are AR-coated and the full curves the case where only one facet is AR-coated. The threshold current corresponding to $T_{wg} = 0.3$ and $\rho_l = 0$ is higher than 50 mA and the corresponding curve cannot be displayed. As expected, the additional feedback provided by the facet decreases I_{th} by roughly 30%. Optimum values of T_a range from 0.1 to 0.15 μm. If T_a is too small, the optical confinement factor Γ is too small and I_{th} increases; but if T_a is too large, then K is too small, hence α_{th} is too large and I_{th} increases again. Also of interest is the fact that, for usual thicknesses ($T_a \geqslant 600$ Å), the thinner the waveguide layer the better.

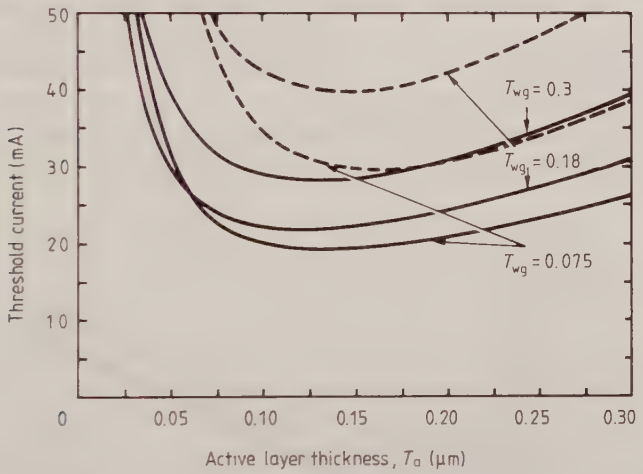

Figure 4.88 Threshold current as a function of active-layer thickness for various waveguide-layer thicknesses; $g = 1500$ Å, $L = 240$ μm, $W = 2$ μm; $\rho_r = 0$, $\rho_l = 0$ (— — — —) and $\rho_r = 0$, $\rho_l = 0.565$ (————).

Figure 4.89 shows the threshold current as a function of the cavity length L for various coupling coefficients. It appears that the optimum laser length is around 200 μm for lasers where reflection has been suppressed only on one side ($\rho_r = 0$). For shorter lasers, the coupling coefficient is too small and the threshold gain α_{th} increases rapidly for decreasing L; and for longer lasers, α_{th} decreases, but then the cavity volume is too large and I_{th} increases again. The broken line indicates the asymptote for large L.

(c) Wavelength dispersion

Some particular applications, such as heterodyne detection, demand lasers

with well controlled lasing wavelength λ_L, which requires excellent homogeneity over the entire wafer. Since lasing occurs in the vicinity of the Bragg wavelength λ_B, the first source of dispersion is due to λ_B. For second-order gratings, λ_B is simply the product of the effective refractive index of the guide n_e and the grating period Λ. If we consider that Λ is constant over the entire wafer, then λ_B variations $\Delta\lambda_B$ are solely due to n_e variations, which can arise from inhomogeneities in the layer thicknesses and/or stripe width. Here, we want to address the problem of the influence of waveguide parameter variations upon n_e and hence λ_B. For that, Correc *et al* [51] consider a rectangular waveguide composed of three layers $(\Omega_1, \Omega_2, \Omega_3)$ embedded into InP. The unperturbed geometry corresponds to $T_{wg} = 0.18\ \mu m$, $T_a = 0.2\ \mu m$, $T_b = 0.1\ \mu m$ and $W = 2\ \mu m$. Then, they vary one of the four parameters, keeping the other three constant and evaluate the change in λ_B. The range of variation is $\pm 5\%$ around the nominal value. The results are displayed in figure 4.90. It appears that the most crucial parameter is the active-layer thickness, since a variation of only $\pm 5\%$ shifts λ_B by more than 20 Å. The Bragg wavelength λ_B is less sensitive to the other parameters: $\pm 5\%$ variation results in a smaller shift of the order of 5 Å. Therefore, wavelength reproducibility demands excellent control of layer thickness, especially that of the active region.

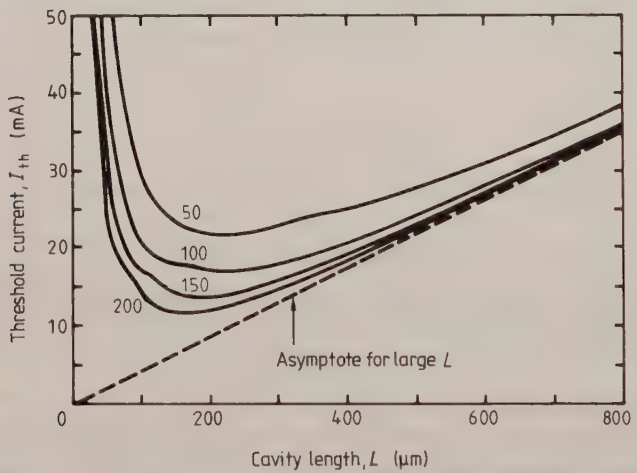

Figure 4.89 Threshold current as a function of cavity length for various coupling coefficients; $\rho_r = 0$, $\rho_l = 0.565$.

The other source of dispersion is the facet phase θ_l of the uncoated facet. So far, it has been impossible to control it by cleavage, and sophisticated methods are required to achieve phase control. It is known [46] that, for high enough coupling coefficient, lasing is prohibited at λ_B and that, depending on θ_l, the lowest-threshold DFB mode is located on one side or

the other of λ_B. This means that the allowed λ_L will be distributed into two sets located on each side of λ_B and separated by the stopband. Within each set, λ_L variations induced by θ_i variations are denoted by $\Delta\lambda_\theta$. Using the coupled-mode theory, Correc *et al* [51] have estimated $\Delta\lambda_\theta$ to be 2–3 Å.

In actual lasers, both sources of dispersion are present and one expects to see two sets of λ_L, separated by a stopband. Each set will have a width $\Delta\lambda_L$ that will be the sum of λ_B variation $\Delta\lambda_B$ and uncertainty due to θ_i, i.e.

$$\Delta\lambda_L = \Delta\lambda_B + \Delta\lambda_\theta. \tag{4.23}$$

Since we know $\Delta\lambda_\theta$, we can deduce $\Delta\lambda_B$ from $\Delta\lambda_L$ and consequently have some knowledge of the homogeneity of the wafer.

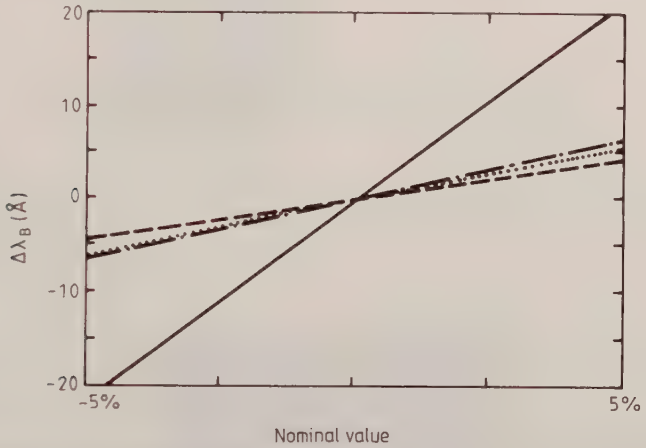

Figure 4.90 Influence of waveguide parameters on λ_B. Nominal values are indicated in parentheses: (— · — · —) waveguide layer ($T_{wg} = 0.18\ \mu$m); (————) active layer ($T_a = 0.2\ \mu$m); (— — — —) buffer layer ($T_b = 0.1\ \mu$m); (. . . . . .) waveguide width ($W = 2\ \mu$m).

(d) Experimental results

BRS-DFB lasers have been made by a two-step MOCVD growth technique. Typical threshold current was 30 mA for 240 μm long lasers with two cleaved facets and 40 mA for lasers with one AR-coated facet. Thresholds as low as 10 mA have been measured. Figure 4.91 shows light–current characteristics under CW operation of a BRS-DFB laser. A single longitudinal mode is observed for temperatures up to 70°C and output powers up to 6 mW. Beyond, power saturates. An 18–20 Å wide stopband is clearly visible in the near-threshold spectrum. From this, the coupling coefficient can be estimated at 40 cm^{-1} [48]. This value is in good agreement with that deduced from figure 4.88 for $g = 1500$ Å. The theoretical threshold current of this structure can be estimated as 25 mA from figure 4.88, whereas the

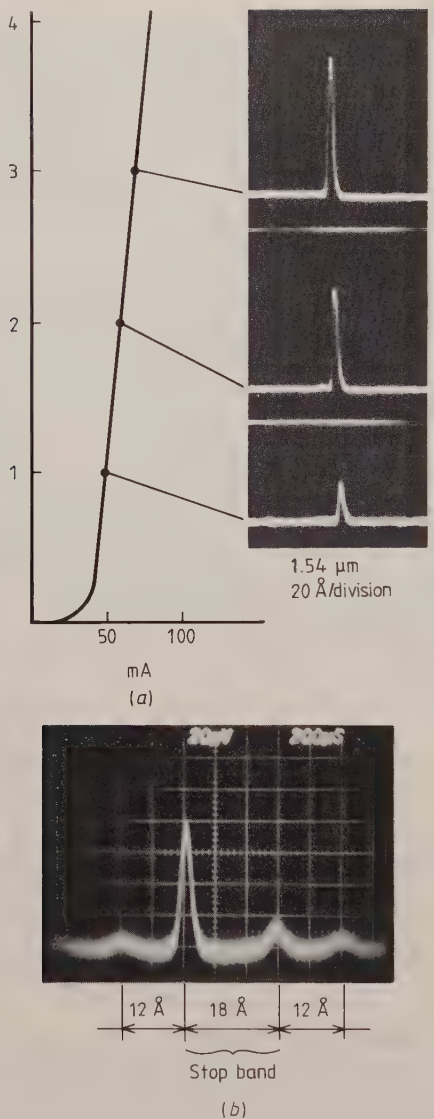

Figure 4.91 DFB laser with SiO_x AR coating: (*a*) light–current characteristics; (*b*) stopband. Coupling coefficient is 40–50 cm^{-1} and side-mode suppression 10^3. CW operation at 20°C.

experimental value of 40 mA is somewhat higher. This discrepancy can be explained by the fact that the DFB mode is not exactly located at the maximum of the gain curve and that it does not experience the maximum available gain.

Figure 4.92 shows the wavelength of 10 lasers obtained from the same

wafer. Obviously, there are two sets of lasing wavelengths, separated by a region where lasing is apparently forbidden. In each set, the wavelength dispersion is of the order of 8 Å. This wavelength distribution can be explained by the theoretical analysis given above. In this case, $\Delta\lambda_L = 8$ Å and $\Delta\lambda_\theta = 3$ Å. Using these, we infer that $\Delta\lambda_B \simeq 5$ Å, and from figure 4.90, we deduce that the control over the waveguide parameters is very good. It is better than 5% over T_{wg}, T_b and W, and better than 2% over T_a. This demonstrates the quality and homogeneity of material grown by MOCVD.

Some of these lasers have been successfully tested on an installed optical link [60]. One of them has been used in a 40 km, 560 Mbit s^{-1} link with a bit error rate of the order of 10^{-11} and another one on a 1.7 Gbit s^{-1} link with a similar error rate [61].

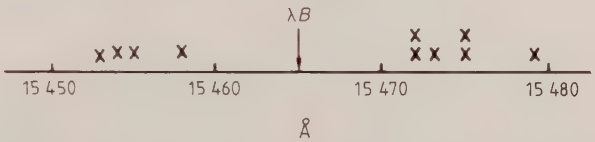

Figure 4.92 Lasing wavelength of 10 lasers from the same wafer. Wavelength dispersion is about 3 Å due to facet phase and about 5 Å due to Bragg wavelength dispersion.

4.3.4 CW phase-locked array $Ga_{0.25}In_{0.75}As_{0.5}P_{0.5}$–InP high-power semiconductor laser grown by MOCVD

Optically coupled semiconductor laser arrays are increasingly gaining importance for applications where high CW or pulsed power in a coherent radiation pattern is needed. It has been suggested [62] that individual emitters in a phase-locked diode laser array can be expected to oscillate collectively in modes characteristic of a composite waveguide formed as a result of the optical coupling between individual waveguides of the array. These collective oscillations, called 'supermodes', are determined primarily by the strength and uniformity of the optical coupling between modes of individual emitters in the array. The model characteristics of phase-locked arrays have been studied by several authors. The first direct experimental evidence confirming the existence of supermodes in an array of coupled diode lasers has been reported by Paoli *et al* [63]. An array of N lasers can be expected to possess N supermodes, each of which has an optical field whose amplitude and phase show characteristic profiles from emitter to emitter. As with any collection of identical interacting oscillators, coupling shifts the oscillating frequency of the emitters to N different values, one for each supermode.

To date, all phase-locked arrays reported in the literature have been fabricated with GaAs–GaAlAs semiconductor material. In general most of

the gain-guided or index-guided laser arrays have operated with adjacent emitters 180° out of phase, resulting in a far field with two lobes symmetrically located about the facet normal [64].

A fundamental problem in array design is the development of a structure that will operate with a single diffraction-limited beam.

Razeghi *et al* [65] have described the operation of a phase-locked GaInAsP–InP high-power semiconductor laser array emitting at 1.3 μm fabricated on materials grown completely by a two-step LP-MOCVD growth technique. This phase-locked array laser was manufactured by two-step MOCVD as follows. First, the following layers were grown successively on an InP(Sn) substrate with orientation (1 0 0) exact or (1 0 0) 2° off:

(1) 1 μm InP sulphur-doped ($n = 1 \times 10^{18}$ cm^{-3}) for confinement layer;
(2) 0.2 μm undoped GaInAsP lattice-matched to InP (1.3 μm wavelength composition) for active layer;
(3) 100 Å undoped InP as blocking layer;
(4) 100 Å $Ga_{0.25}In_{0.75}As_{0.5}P_{0.5}$ undoped waveguide layer.

Next, an array consisting of seven stripes of 2 μm width and stripe–stripe spacing of 1 μm was etched in the 100 Å GaInAsP layer (100 Å InP layer is used as a blocking layer) through a photolithographic resist mask, using a selective etch composed of H_2SO_4:H_2O_2:H_2O (1:8:200). After removing the resist mask, the array was then covered by a 1 μm thick Zn-doped InP confinement layer ($N_A - N_D \simeq 5 \times 10^{17}$ cm^{-3}) and a 0.5 μm Zn-doped $Ga_{0.47}In_{0.53}As$ contact layer with $N_A - N_D \simeq 10^{19}$ cm^{-3} (again using MOCVD).

Figure 4.93 shows a schematic diagram of the ridge-island laser array (RILA) structure before and after regrowth, with details of technology stages. In order to localize the injection only in the RILA active region, a shallow layer of protons (0.5 μm from active region) was implanted through a 20 μm wide photoresist mask after metallization of the contacts. The n contact was realized by the deposition of Au. The p contact was made by the deposition of Pt–Au and annealing at 450°C for 30 s. After cleaving and scribing into chips 300 μm long and 350 μm wide, the lasers were mounted, epilayer-side down, onto nickel-plated copper heat-sinks using indium.

Figure 4.94 shows a scanning electron microscope cross section of the RILA before and after regrowth. Typical pulsed and CW light–current characteristics of this RILA are displayed in figure 4.95. The pulsed and CW threshold was 200 mA; external quantum efficiencies were 0.19 W A^{-1} (pulsed operation) and 0.13 W A^{-1} (CW operation) at 20°C. Output powers of more than 300 mW at a pulse-modulated current of 2 A (limited by the pulse generator) and 120 mW at 1.3 A (CW) were measured at 20°C. These results were obtained without optical surface treatment, which indicates that the radiated power can be increased by a factor of 1.5–2.

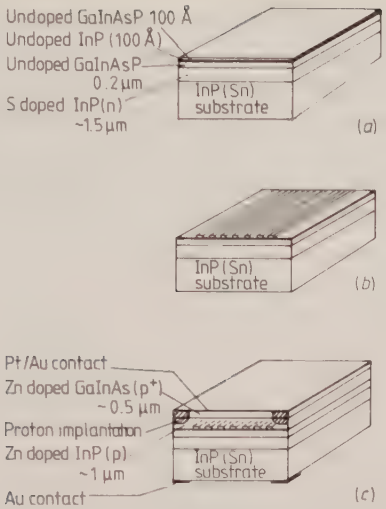

Figure 4.93 Schematic diagram of ridge-island laser array (RILA) structure: (*a*) first epitaxy; (*b*) selective chemical etching of seven stripes; (*c*) after regrowth, metallization and proton implantation.

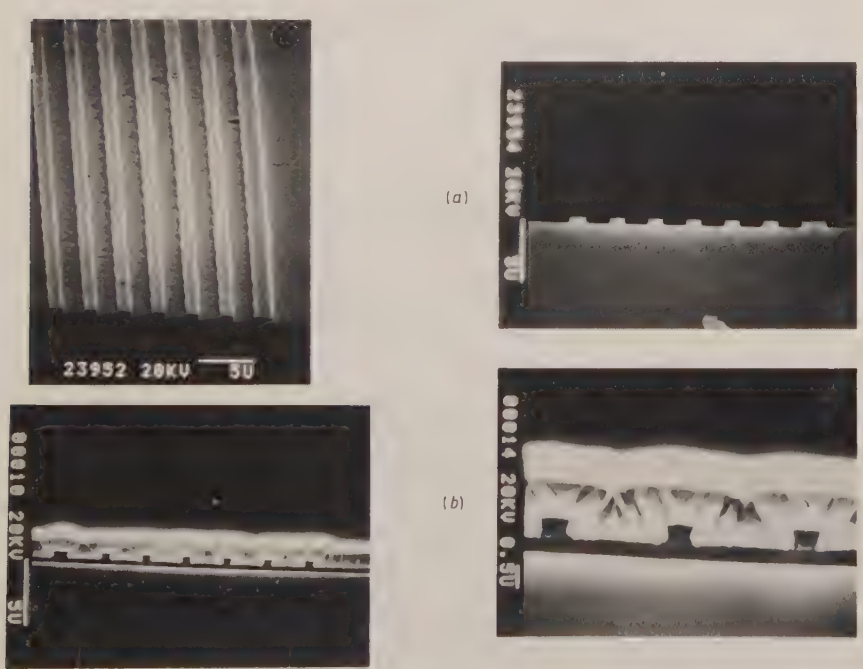

Figure 4.94 Scanning electron micrographs of cross sections of a phase-locked high-power GaInAsP–InP laser array with seven stripes of 2 μm width (*a*) before and (*b*) after LP-MOCVD overgrowth.

Figure 4.96 shows the far-field patterns parallel and perpendicular to the junction plane of these RILA. These patterns were measured under CW operation for 10 and 90 mW output powers. The far-field full widths at half-maximum power parallel and perpendicular to the junction plane were 3° and 45°, respectively, at 10 mW, which shows the phase-locked behaviour of these RILA. At higher output power the far-field lobe broadens and at 90 mW it becomes about 16° parallel to the junction plane (see figure 4.96(*c*)).

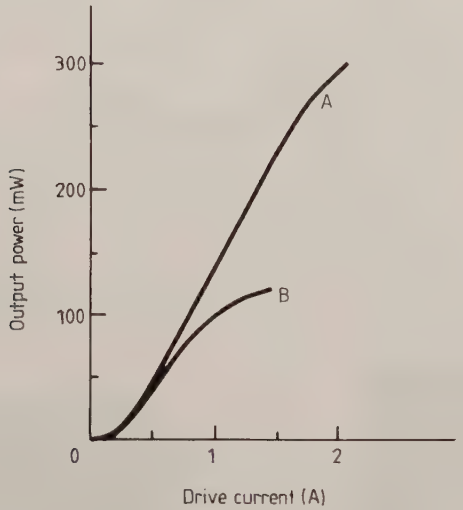

Figure 4.95 Typical light–current characteristics of phase-locked high-power GaInAsP–InP 1.3 μm laser arrays at 20°C, under (*a*) pulsed and (*b*) CW operations. Under pulsed operation, $I_{th} = 220$ mA and $\eta = 0.19\ W\,A^{-1}$; under CW operation, $I_{th} = 225$ mA and $\eta = 0.13\ W\,A^{-1}$.

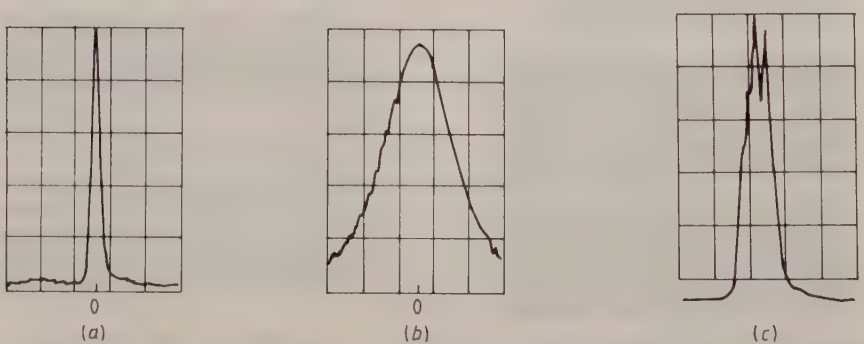

Figure 4.96 Far-field patterns of a CW phase-locked GaInAsP–InP high-power laser array (*a*), (*c*) parallel and (*b*) perpendicular to the junction plane, at 20°C.

Figure 4.97 shows the appearance of two sets of longitudinal modes at 10 mW, indicating the onset of lasing on higher-order supermodes, which is consistent with the broadening of the far-field pattern.

The devices should be useful in applications requiring high CW output power in single-longitudinal-mode communications systems. Because these devices are phase-locked, it is possible to achieve even higher output power levels by adding more diodes to the array and using facet coatings.

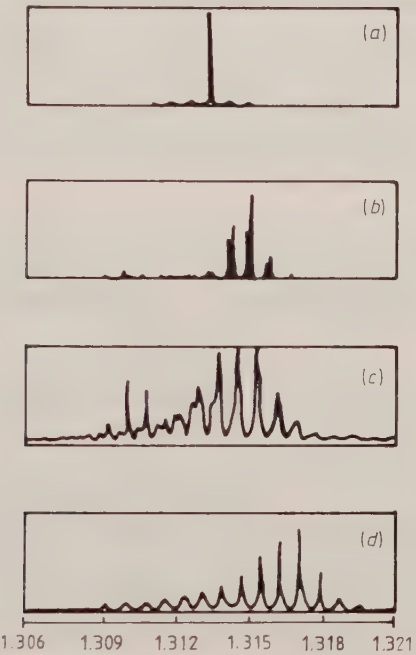

Figure 4.97 CW longitudinal-mode spectra of a phase-locked GaInAsP–InP laser array, at $T = 20^{\circ}$C. (*a*) $P = 2$ mW; (*b*) 10 mW; (*c*) 20 mW; (*d*) 30 mW.

4.3.5 GaInAsP–InP quantum-well lasers

The superiority of the quantum-well laser (QWL) over the double-heterostructure (DH) laser as regards threshold current properties has been established for the GaAs–GaAlAs system [66, 67]. Comparing the DH and QWL structures it is necessary to consider three key parameters: the optical confinement factor, the cavity absorption losses and the gain properties.

The confinement factor Γ of the optical wave is the part of the light intensity that is in the active layer. It is poorer for the quantum well due to the reduced thickness of the active layer. The situation can be improved if a separate optical cavity is placed around the active layer (separate-confinement heterostructure (SCH) or graded-index separate-confinement

heterostructure (GRINSCH) lasers). Typical values of Γ calculated using a five-layer model [68] are given in table 4.11. It is interesting to note that although Γ is lower for GaInAsP/InP lasers than for GaAs/GaAlAs lasers, the ratio of the Γ values for the DH and QWL structures is similar for each material system. Values of Γ for the SCH and GRINSCH QWL structures are similar when the width of the optical confinement cavity is carefully chosen [69, 70].

Absorption losses α (free-carrier losses, scattering at interface defects, etc) affect the propagation of the optical wave in the optical cavity. Nagle *et al* [71] have measured the quantity α by extrapolating the curve of threshold current density as a function of the inverse of chip length, as described by Hersee *et al* [72]. Many DH and QWL structures were measured and it was found that the value of α was typically below 20 cm^{-1} and independent of the type of structure.

Table 4.11 Values of the optical confinement factor.

	L(Å)				
Structure	50	100	200	1000	1500
GaAs/GaAlAs DH, $x_C = 40\%$	–	0.004	0.018	0.312	0.508
GaAs/GaAlAs SCH, $x_B = 20\%$, $x_C = 40\%$	0.013	0.027	0.057	0.347	0.517
GaAs/GaAlAs SCH, $x_B = 20\%$, $x_C = 60\%$	0.019	0.038	0.078	0.420	0.600
GaInAs/InP DH	–	0.002	0.008	0.163	0.305
GaAs/GaAlAsP(1.3 μm)/InP SCH	0.009	0.019	0.039	0.222	0.343

L represents the width of the active layer. For GaAs/GaAlAs lasers, x_B and x_C indicate respectively the aluminium fraction in the optical cavity and in the confinement layers. The width of the optical cavity for SCH lasers is chosen for optimum confinement (2000 Å for GaAs and 3500 Å for GaInAs).

The value of the material gain at a given injection is increased for a narrow active layer (two-dimensional case) and can compensate for the deleterious effects of a small Γ in QWL structures. This can be understood if we consider the number of states that must be filled in order to achieve the population inversion that is required for lasing action. This corresponds roughly to the number of states between the band edge and kT above the edge, and at room temperature is 4.5 times higher in a DH laser (active layer = 1000 Å) than in a QWL (with GaAs effective mass $m^* = 0.067$). This ratio r is given by

$$r = \frac{2\sqrt{2}(m^*)^{1/2}(kT)^{1/2}L}{3\pi h} \tag{4.24}$$

where L is the active-layer width of the DH laser. The above arguments should also apply to GaInAsP/InP quantum-well lasers; experimentally,

however, these devices exhibit threshold currents similar to DH lasers [73]. The origin of this different behaviour is discussed below.

Razeghi *et al* [74] and Nagle *et al* [75] extensively studied a $Ga_{0.47}In_{0.53}As/Ga_{0.27}In_{0.73}As_{0.59}P_{0.41}/InP$ SCH laser with a 50 Å active layer and a 3000 Å optical cavity. Figure 4.98 shows the schematic diagram of this SCH QW structure. At ambient temperature, the diodes lased at 1.30 μm for an average current of 450 mA under pulsed operation. The spontaneous emission (shown in figure 4.99) exhibits three main characteristics as the injection current is increased:

(1) The maximum of the spontaneous emission shifts towards higher energy.

(2) The integrated spontaneous emission intensity tends to saturate.

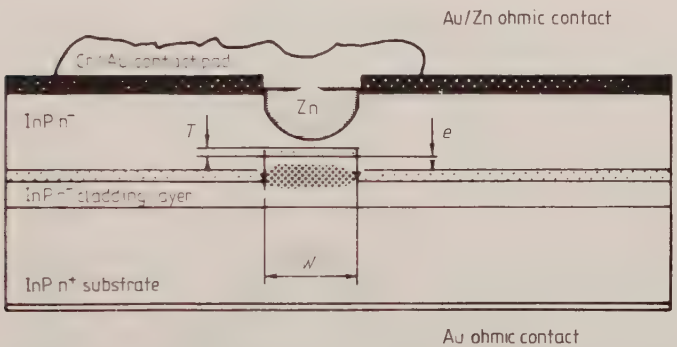

Figure 4.98 Schematic diagram of GaInAs–GaInAsP–InP SCH QW laser.

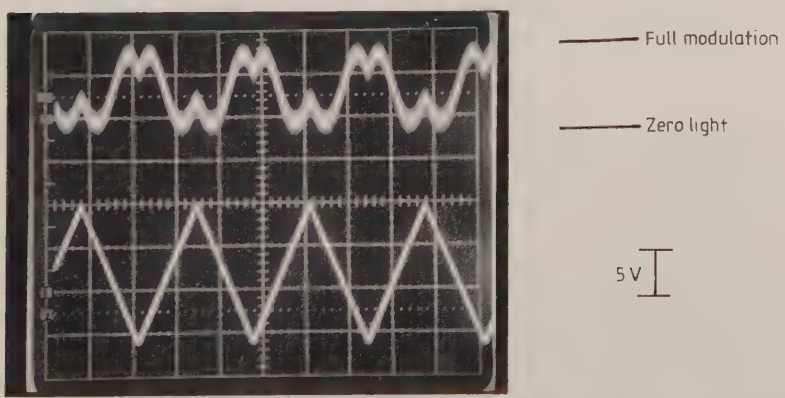

Figure 4.99 The spontaneous emission of a GaInAs SCH QW laser. Relative intensities are significant. The spikes on the curves around 0.9 eV are due to atmospheric water absorption. $T = 295$ K, $I_{th} = 450$ mA.

(3) The spectral shape broadens and the slope of the high-energy tail decreases until carriers escape from the well and recombine in the optical cavity. Eventually, at high injection, population inversion and lasing take place in the cavity and emission occurs at 1.30 μm.

It was shown by Nagle *et al* [75] that this behaviour is most probably caused by carrier heating in the quantum well. The increase of the quasi-Fermi levels with injection cannot explain the observed behaviour, since it is found that the maximum value of gain decreases with increasing injection current (figure 4.100). Equally this cannot be due to an inefficient capture of carriers by the quantum well since there was no luminescence from the cavity at low injection levels. Also studies of the photoluminescence emitted by GaInAs/InP undoped quantum wells have shown that the capture is efficient even for narrow wells [76].

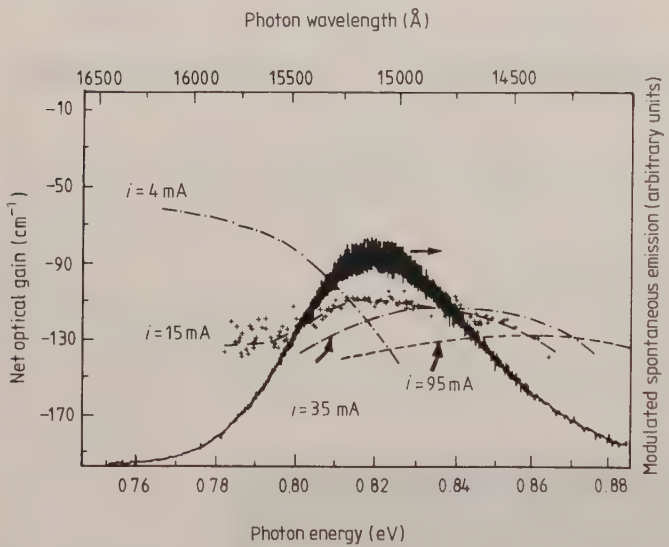

Figure 4.100 Gain spectra of a GaInAs SCH QW laser at room temperature (TE polarization). For clarity we trace the corresponding modulated spontaneous emission and calculated values (crosses) only for $i = 15$ mA).

As the temperature is lowered the maximum gain of the quantum well increases and approaches that required for lasing. At a temperature between 100 and 150 K (chip-dependent), lasing occurs in the quantum well. At 5 K, the threshold current was only 0.9 mA. Figure 4.101 shows the lasing spectrum and light–current characteristics of this SCH QWL (lasing wavelength 1.40 μm), showing that it is not the intrinsic properties of the GaInAs quantum well or the interfaces that prevent lasing at room temperature. For

the temperature range 5–120 K the T_0 value of these lasers was approximately 100 K.

This extremely strong temperature-dependent behaviour indicates that non-radiative Auger recombination is probably responsible for carrier heating. This conclusion is further supported by the observation that, as the temperature is increased, the photoluminescence efficiency of GaInAs quantum wells decreases more rapidly than the T^{-2} variation corresponding to a band-to-band recombination with a 2D density of states [76].

Whereas the superiority of SQW and MQW is not well established in the GaAs–GaAlAs system, the opposite is true in the GaInAsP–InP system. A major issue in QWL is therefore to understand this outstanding difference: up to now, all the reported MQW lasers in GaInAsP–InP systems have features that are not better than those of DH lasers [73, 77].

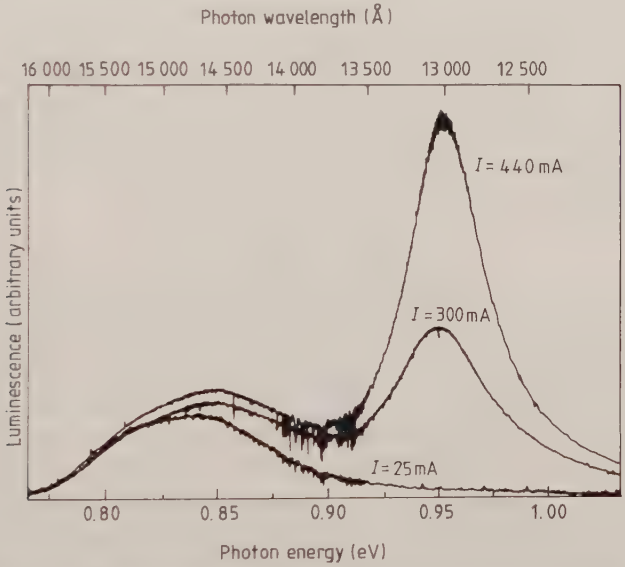
Photon wavelength (Å)
16 000 15 500 15 000 14 500 14 000 13 500 13 000 12 500
Luminescence (arbitrary units)
I = 440 mA
I = 300 mA
I = 25 mA
0.80 0.85 0.90 0.95 1.00
Photon energy (eV)

Figure 4.101 Lasing spectrum and light–current characteristics of this SCH QWL. $T = 5$ K, $I_{th} = 0.8$ mA.

The case of the GaInAsP/InP standard DH lasers has been a source of numerous studies [78]. Although state-of-the-art GaInAsP DH lasers have threshold current densities quite similar to those of GaAs DH lasers, their T_0 is much worse. The T_0 question in GaInAsP/InP lasers has long been a matter of controversy, but there seems now to be a consensus about the following points [78]:

(1) For optimum lasers ($d \simeq 0.15$ μm), the threshold current can be as low as 500 A cm^{-2} [79]. Typical values of T_0 are 60–80 K. The density of carriers at threshold is about 2×10^{18} cm^{-3}.

(2) The threshold current has a radiative component and several non-radiative components. The radiative component is roughly 60% at 300 K [78]. The main non-radiative component is due to Auger recombination, with smaller contributions due to inter-valence-band light absorption and thermal-carrier leakage from the active region. The Auger recombination process is of the CHSH type, i.e. an electron and a heavy hole recombine by exciting a heavy hole to the spin-split-off valence band.

(3) The Auger coefficient value is $C_A = 4 \times 10^{-29}\ cm^6\ s^{-1}$ and $2 \times 10^{-29}\ cm^6\ s^{-1}$ for GaInAs and 1.3 μm GaInAsP material, respectively.

A central issue is the value of the Auger coefficient in quantum wells. There is an abundant literature on the theoretical evaluation of the various possible processes in 3D [80], but there seems to be a consensus now about the dominance of the CHSH process. At some point, the Auger effect in QW has been predicted to be much weaker than in 3D but consensus is now that it should be comparable, as is also the experimental result [81].

Sugimura [82] and Asada *et al* [83] have produced detailed calculations where they can optimize I_{th} and T_0 separately for the various types of QW lasers in the GaInAsP/InP system. However, the values found for the threshold current are significantly lower than those obtained up to now in MQW InGaAsP/InP lasers.

4.3.6 Buried waveguides in InGaAsP/InP material grown by MOCVD

In the case of 2D guiding in III–V materials using a classical ridge structure, the main problem to overcome is in general the necessary lateral confinement to obtain a single-mode regime and the corresponding difficulty of controlling very precisely the different etching processes. As a matter of fact, widths of the waveguides have currently to be decreased below 3 μm at $\lambda = 1.55\ \mu$m, which makes the structure sensitive to imperfections in its optogeometrical parameters. As a result, high scattering losses may occur despite the good quality of the material. In the vertical direction, light confinement can be tailored by stacking layers of suitable composition, i.e. refractive index. Anyway, in any waveguide structure the only non-compressible cause for losses is due to interface quality.

A natural way to overcome that problem is to buy the guiding material in a cladding material whose refractive index can be adjusted to provide the desired lateral confinement. It then becomes possible to design a pair of waveguides conveniently in order to make a directional coupler switch with specified coupling strength or coupling length. A new technique relaxes the difficult control of the etching processes and permits layers whose thicknesses are well defined by the epitaxial growth. A schematic drawing of a cross section of the structure is given in figure 4.102. The steps for its fabrication are explained below. On a heavily doped ($2 \times 10^{18}\ cm^{-3}$) n-type

InP substrate are grown a low-doped $x\ \mu$m thick cladding InP layer ($<10^{15}$ cm^{-3}) and a low-doped ($<10^{15}$ cm^{-3}; $\lambda_g = 1.3\ \mu$m) $y\ \mu$m thick guiding InGaAsP layer. They bear an $e\ \mu$m thick low-doped ($<10^{15}$ cm^{-3}) InP layer and a $\tau\ \mu$m thick low-doped quaternary material. Then photolithographic and selective etching techniques can be used to reveal $W\ \mu$m wide strips in the upper quaternary material, the $e\ \mu$m thick InP upper layer acting as a barrier to the etching process. Then an epitaxial regrowth occurs during which an InP layer is deposited. The waveguide structure is more flexible to design than more conventional ones because of the extra parameters e and τ. Its obvious disadvantage is the need for an epitaxial regrowth.

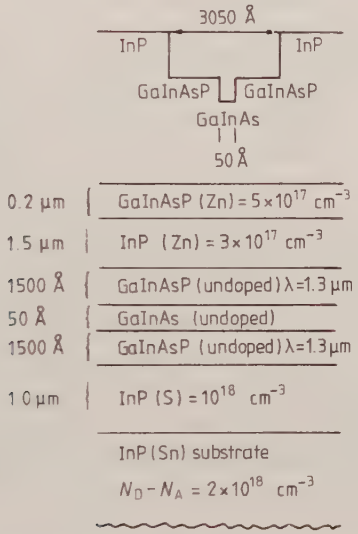

Figure 4.102 Schematic drawing of a cross section of the modulator.

Among the many techniques available for waveguide modelling, the effective-index method (EIM) can be used in order to adjust the guiding characteristics of the structure. The goal is mainly to achieve low lateral guiding, allowing a reasonable range of guide widths W for single-mode operation. In our case, InGaAsP ($\lambda_g = 1.3\ \mu$m) and InP have been chosen respectively for the guiding and cladding layers and a 100 Å thick etching barrier layer was assumed. For $x = 0.4\ \mu$m, $y = 0.55\ \mu$m and $e = \tau = 100$ Å, table 4.12 shows the calculated results for the propagation constant β in channel waveguides. It is clear that there exists a large range of W values ($0 \leqslant W \leqslant 8\ \mu$m) ensuring a single 2D mode regime with low $\partial\beta/\partial W$ values [84].

A directional coupler switch can also be designed using the effective-index

method. Once W has been chosen, the only free parameter to adjust is the inter-guide spacing d in order to reach a given value of the coupling length. With $W = 7\ \mu m$, $e = \tau = 100$ Å and $d = 5\ \mu m$ the difference between the propagation constants of the eigenmodes of the structure is about 14×10^{-5} for TE waves. With $d = 10\ \mu m$, it becomes 3×10^{-5}. This gives coupling lengths of 5.3 and 25.8 mm, respectively, constituting a realistic range of interaction lengths suitable for low drive voltages if the coupler is operated through the electro-optic effect [85].

Table 4.12 Variation of propagation constant β with respect to strip width.

	W (μm)				
	3	5	7	8	10
TE	3.29183	3.29216	3.29240	3.29948	3.29261
				3.29142	3.29162
TM	3.28516	3.28552	3.28577	3.28586	3.28599
				3.28471	3.28496

Two samples have been fabricated from the same substrate with the structure as described above ($e = \tau = 100$ Å; $x = 0.4\ \mu m$; $y = 0.55\ \mu m$). The epitaxial regrowth that occurred just after selective chemical etching consisted of 1.8 μm n^--InP (less than 10^{15} cm^{-3}). The same mask as that used to reveal the guiding regions was used for opening windows in a top SiO_2 layer in order to diffuse Zn ions in InP for making the p–n junction. Two masks have been used during the photolithographic process: one composed of straight waveguides and one composed of directional couplers.

The straight-waveguide sample consisted of a series of waveguides with different W values ranging from 3 to 11 μm. Sample length was 22 mm and light guiding was first observed at $\lambda = 1.55\ \mu m$ through it by using an IR camera. The modal regime was studied by looking at the output light pattern when coupling was laterally displaced. A second-order mode was shown to exist for widths greater than 8 μm as predicted by theory. For the monomode waveguides, loss measurements were carried out by the cut-back method. Loss values were found to be independent of W and were all around 4 dB cm^{-1} (best 2 dB cm^{-1}).

Phase modulation was then observed on 7 μm wide waveguides by applying a voltage on the contacts (figure 4.103). By polarization interferometry, one finds a modulation efficiency of about 5° V^{-1} mm^{-1}.

A capacitance measurement with respect to the applied voltage V shows that, for V ranging from 0 to -10 V, the capacitance was less than 8 pF for the 4.5 mm long electrode. It then makes it possible to have $1/\tau$ ($\tau = RC$) of

the order of 2 GHz if the load resistor is chosen equal to the conventional value of 50 Ω.

The directional coupler sample consisted of a series of couplers (using 7 μm wide guides with inter-waveguide spacing ranging from 5 to 15 μm in 0.5 μm steps). Its length was 20 mm between the two cleaved end faces and all the guides were shown monomode. Light was launched in one guide and the intensities emerging from the two guides made it possible to look at the light exchange between them. For that 20 mm long interaction, all the couplers were found to be in the parallel state for $d > 8$ μm, which is consistent with the predicted value (26 mm with $d = 10$ μm) [86].

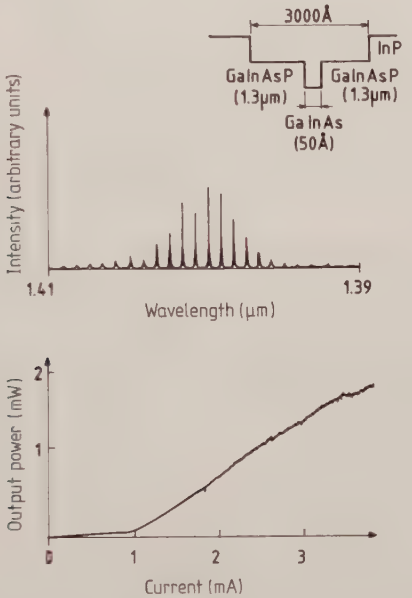

Figure 4.103 Observation of phase modulation. Interaction length is 10 mm; phase modulation at $\lambda = 1.5$ μm.

REFERENCES

[1] Razeghi M, Blondeau R, de Cremoux B and Duchemin J P 1984 *Appl. Phys. Lett.* **45** 784

[2] Razeghi M, Poisson M A, Larivain J P and Duchemin J P 1983 *J. Electron. Mater.* **12** 371

[3] Duchemin J P, Bonnet M, Beuchet G and Koelsch F 1979 *Gallium Arsenide and Related Compounds, 1978* (Inst. Phys. Conf. Ser. 45) p 10

[4] Razeghi M, Poisson M A, Guldner Y, Vieren J P, Voisin M and Voos M 1982 *Appl. Phys. Lett.* **40** 877

[5] Wei H P, Chang A M, Tsui D C and Razeghi M 1985 *Phys. Rev.* B **37** 32
[6] Bimberg D, Christen J, Steckenborn A, Weimann G and Schapp W 1985 *J. Lum.* **30** 562
[7] Bimberg D and Bubenzer A 1981 *Appl. Phys. Lett.* **38** 803
[8] Christen J, Bimberg D, Steckenborn A and Weimann G 1984 *Appl. Phys. Lett.* **44** 84
[9] Bastard G, Delalande C, Meynadier M H, Frijlink P M and Voos M 1984 *Phys. Rev.* B **29** 7042
[10] Razeghi M, Maurel P, Omnes F, Defour M, Acher O, Tsui D, Wei H P, Vieren J P and Guldner Y 1987 *Appl. Phys. Lett.* **51** 1821
[11] Forrest S R, Schmidt P H, Wilson R B and Kaplan M L 1984 *Appl. Phys. Lett.* **45** 1199
[12] Razeghi M, Duchemin J P and Portal J C 1985 *Appl. Phys. Lett.* **46** 46
[13] Portal J C, Nicholas R J, Brummell M A, Cho A Y and Sivco D L 1985 unpublished
[14] Portal J C, Nicholas R J, Brummell M A, Cho A Y, Cheng K Y and Pearsall T P 1982 *Solid State Commun.* **43** 907
[15] Razeghi M, Duchemin J P, Portal J P, Dmowski L, Remenyi G, Nicholas R J and Briggs A 1986 *Appl. Phys. Lett.* **48** 712
[16] Störmer H L, Gossard A C and Wiegmann W 1982 *Solid State Commun.* **41** 707
[17] Razeghi M, Nicholas R J, Brunel L C, Huant S, Karrai K, Portal J C, Brummell M A, Cheng K Y and Cho A Y 1985 *Phys. Rev. Lett.* **55** 883
[18] Nicholas R J, Sessions S J and Portal J C 1980 *Appl. Phys. Lett.* **37** 178
[19] Palik E D, Picus G S, Teitler S and Wallis R F 1961 *Phys. Rev.* **122** 475
[20] Fang F F and Howard W E 1966 *Phys. Rev. Lett.* **16** 797
[21] Nicholas R J, Stradling R A, Portal J C and Askenazy S 1979 *J. Phys. C: Solid State Phys.* **12** 1653
[22] Brummell M A 1985 *DPhil Thesis* University of Oxford
[23] Hopkins M A, Nicholas R J, Brummell M A, Harris J J and Foxon C T 1986 *Superlattices Microstruct.* **2** 319
[24] Nicholas R J 1985 *Prog. Quantum Electron.* **10** 1
[25] Nicholas R J, Sessions S J and Portal J C 1980 *Appl. Phys. Lett.* **37** 178
[26] Portal J C, Cisowski J, Nicholas R J, Brummell M A, Razeghi M and Poisson M A 1983 *J. Phys. C: Solid State Phys.* **16** L573
[27] Brummell M A, Nicholas R J, Portal J C, Cheng K Y and Cho A Y 1983 *J. Phys. C: Solid State Phys.* **16** L579
[28] Razeghi M, Maurel P, Omnes F, Ben Amor S, Dmowski L and Portal J C 1986 *Appl. Phys. Lett.* **48** 1267
[29] Maurel P, Razeghi M, Guldner Y and Vieren J P 1987 *Semicond. Sci. Technol.* **2** 695
[30] Laidig W D, Holonyak N, Camras M D, Hess K, Coleman J J, Dapkus P D and Barden J 1981 *Appl. Phys. Lett.* **38** 776
[31] Razeghi M, Acher O and Launay F 1987 *Semicond. Sci. Technol.* **2** 793
[32] Kazmierski K, Huber A M, Morillot G and de Cremoux B 1984 *Japan. J. Appl. Phys.* **23** 628
[33] Van Vechten J A 1982 *J. Appl. Phys.* **53** 7081

[34] Burnham R D, Holonyak N, Hirch K C, Kalishi R W, Nan D W, Thornton R L and Paoli T L 1986 *Appl. Phys. Lett.* **48** 800
[35] Laidig W D, Lee J W, Chiang P K, Simpson L W and Bedair S M 1983 *J. Appl. Phys.* **54** 6382
[36] Olsen G H 1978 *IEEE Trans. Electron. Devices* **ED-2** 217
[37] Drevillon B, Perrin J, Marbot R, Violet A and Dalby J L 1982 *Rev. Sci. Instrum.* **53** 969
[38] Hollinger G, Gergignal E, Joseph J and Robach Y 1985 *J. Vac. Sci. Technol.* A **3** 2082
[39] Krawczik S K and Hollinger G 1984 *Appl. Phys. Lett.* **45** 871
[40] Aspnes D E 1980 *J. Vac. Sci. Technol.* **17** 1057
[41] Aspnes D E and Studna A A 1985 *Appl. Phys. Lett.* **46** 1071
[42] Kelso S M, Aspnes D E, Pollack M A and Nahory R E 1982 *Phys. Rev.* B **26** 6669
[43] Erman M, Theeten J B, Vodjdani N and Demay Y 1983 *J. Vac. Sci. Technol.* B **1** 328
[44] Alnot P, Huber A and Olivier J 1985 *Surf. Interface Anal.* in press
[45] Nahory R E and Pollack M A 1978 *Electron. Lett.* **14** 727
[46] Suematsu Y, Arai S and Kishino K 1983 *J. Lightwave Technol.* **LT-1** 162–4
[47] Itaya Y, Matsuoka J, Nakano Y, Suzuki Y, Kuroiwa K and Ikegami T 1982 *Electron. Lett.* **18** 1006–8
[48] Westbrook L D, Nelson A W, Fiddyment P J and Evans J S 1984 *Electron. Lett.* **20** 225–6
[49] Kaminow I P, Stulz L W, Ko J S, Milles B, Feldman R D and Pollack M A 1983 *Electron. Lett.* **19** 877–9
[50] Kogelnik H and Shank C V 1972 *J. Appl. Phys.* **43** 2327–35
[51] Correc P, Landreau J, Bouley J C, Razeghi M, Blondeau R, Kazmierski K, Krakowski M, de Cremoux B and Duchemin J P 1985 *Optical Fiber Sources and Detectors* SPIE, p 2
[52] Streifer W, Scifres D R and Burnham R D 1982 *IEEE J. Quantum Electron.* **QE-11** 867–73
[53] Westbrook L, Henning I D, Nelson A and Fiddyment P 1984 *IEEE J. Quantum Electron.* **QE-21** 512–18
[54] Streifer W, Burnham R D and Scifres D R 1980 *IEEE J. Quantum Electron.* **QE-11** 154–61
[55] Matsuoka T, Nagai H, Noguchi Y, Suzuki Y and Kawaguchi Y 1982 *Japan. J. Appl. Phys.* **23** L138–40
[56] Matsuoka T, Nagai H, Suzuki Y, Noguchi Y and Wakita K 1984 *Japan. J. Appl. Phys.* **23** L782–4
[57] Itaya Y, Wakita K, Motosugi G and Ikegami T 1982 *IEEE J. Quantum Electron.* **QE-21** 527–33
[58] Razeghi M, Blondeau R, Krakowski M, Bouley J C, Papuchon M, de Cremoux B and Duchemin J P 1985 *IEEE J. Quantum Electron.* **QE-21** 507–11
[59] Utaka K, Akiba S, Sakai K and Matsushima Y 1982 *IEEE J. Quantum Electron.* **QE-20** 236–45
[60] Le Boutet A, Auffret R, Claveau G, Guibert M, Moalic J, Pophillat L, Sorel Y and Tromeur A 1985 *Electron. Lett.* **20** 834–6

[61] Le Boutet A and Sorel Y 1985 *IOOC-ECOC'85* Venezia, Italy
[62] Butler J K, Ackley D E and Botez D 1984 *Appl. Phys. Lett.* **44** 293
[63] Paoli T L, Streifer W and Burnham R D 1984 *9th Int. Semiconductor Laser Conf.* 7–10 August, Rio de Janeiro, Brazil
[64] Ackley D E 1983 *Appl. Phys. Lett.* **42** 152
[65] Razeghi M, Blondeau R, Kazmierski K, Krakowski M and Duchemin J P 1985 *Appl. Phys. Lett.* **46** 131
[66] Tsang W T 1982 *Appl. Phys. Lett.* **40** 217
[67] Hersee S D, Baldy M, de Cremoux B and Duchemin J P 1983 *Gallium Arsenide and Related Compounds, 1982* (Inst. Phys. Conf. Ser. 65) p 281
[68] Casey H C, Panish M B, Schlosser W O and Paoli T L 1984 *J. Appl. Phys.* **45** 1
[69] Streifer W, Burnham R D and Scifres R D 1983 *Opt. Lett.* **8** 283
[70] Chinn S R 1984 *Appl. Opt.* **23** 3508
[71] Nagle J, Hersee S, Krakowski M, Weil T and Weisbuch C 1985 *Appl. Phys. Lett.* **46** 1325
[72] Hersee S D, Baldy M, Assenat P, de Cremoux B and Duchemin J P 1982 *Electron. Lett.* **18** 870
[73] Dutta N K, Napholtz S G, Yen R, Brown R L, Shen T M, Olsson N A and Craft D C 1985 *Appl. Phys. Lett.* **46** 19
[74] Razeghi M, Duchemin J P and Portal J C 1985 *Appl. Phys. Lett.* **46** 46
[75] Nagle J, Hersee S, Razeghi M, Krakowski M, de Cremoux B and Weisbuch C 1986 *Surf. Sci.* **174** 148
[76] Razeghi M, Nagle J and Weisbuch C 1985 *Gallium Arsenide and Related Compounds, 1984* (Inst. Phys. Conf. Ser. 74) p 379
[77] Razeghi M, Blondeau R and Duchemin J P 1985 *Gallium Arsenide and Related Compounds, 1984* (Inst. Phys. Conf. Ser. 74) p 679
[78] Henry C H, Logan R A, Temkin H, Nevit F R and Luongo J P 1983 *IEEE J. Quantum Electron.* **QE-19** 941
[79] Razeghi M, Blondeau R, Krakowski M, de Cremoux B, Duchemin J P, Lozes F, Martinot M and Bensonsson M A 1987 *Appl. Phys. Lett.* **50** 230
[80] Etienne B, Shah J, Leheny R F and Nahory R E 1982 *Appl. Phys. Lett.* **41** 1018
[81] Sermage B, Chemla D S, Sivco D and Cho A Y 1986 *IEEE J. Quantum Electron.* **QE-22** 774
[82] Sugimura A 1983 *IEEE J. Quantum Electron.* **QE-19** 932
[83] Asada M, Kaweyama A and Suematsu Y 1984 *IEEE J. Quantum Electron.* **QE-20** 745
[84] Albrecht P, Bach H G, Bornholdt C, Doldissen W, Franke D, Grote N, Krauser J, Niggebrugge U, Nolting H P, Schalk M and Tiedke I 1983 *2nd ECIO* Firenze, p 72
[85] Fujiwara M, Ajisawa A, Sugimoto Y and Ohta Y 1984 *Electron. Lett.* **20** 790
[86] Mikami O and Nakagome H 1985 *Opt. Quantum Electron.* **17** 449–55

Chapter 5 MOCVD Growth, Characterization and Applications of III–V Semiconductor Strained Heterostructures

We have seen that MOCVD is well adapted for the growth of a variety of III–V semiconductor binary, ternary and quaternary heterojunctions, multiquantum wells and superlattices on lattice-matched substrates for optoelectronic or microwave device applications.

In heterostructures, it is certainly desirable to select a pair of materials closely lattice-matched in order to minimize defect formation or stress. However, heterostructures lattice-mismatched to a limited extent can be grown with essentially no misfit dislocations, if the layers are sufficiently thin, because the mismatch is accommodated by a uniform lattice strain. Without the requirement of lattice matching, the number of available pairs for device applications and integrated circuits is greatly increased.

Strained heterostructures of high-quality InP and related compounds have been grown on alternative substrates by the low-pressure metallorganic chemical vapour deposition growth technique. Photoluminescence, SIMS and Auger measurements have shown the high-quality optical and electrical properties of these layers.

5.1 GROWTH PROCEDURE AND CHARACTERIZATION

5.1.1 Growth procedure

The growth apparatus has been described in chapter 1. The optimum conditions for the low-pressure growth of these layers are presented in table

5.1. Growth was carried out at 76 Torr. Pretreatment of the substrates was found to be crucial. The pretreatment procedure for InP and InAs was given in chapter 2.

Smooth single-crystal films exhibiting mirror-like surfaces have been obtained, even in the presence of a large layer–substrate lattice-parameter mismatch. These layers tend, however, to be heavily dislocated, and their electrical and optical characteristics, especially those related to minority-carrier properties such as diffusion length and lifetime, are generally inferior to those of the typical lattice-matched system. These effects tend to be especially severe for thin layers, but it has been found that they can be partly eliminated by the use of thick buffer layers or special grading or superlattice techniques. Table 5.2 shows the range of heterostructures grown so far.

Featureless mirror-like surfaces have been grown over a wide temperature range of 500 to 650°C. The x-ray diffraction rocking curve about the (4 0 0) Kα reflection from an InP epilayer on GaAs and GaAs on InP substrate is shown in figure 5.1. The x-ray diffraction rocking curve of a heterostructure of InAs–GaAs on InP substrate is shown in figure 5.2. Razeghi *et al* [1]

Table 5.1 Optimized growth parameters.

	InP	GaAs	InAs	GaP	GaInAs	GaInP	GaInAsP
Growth temperature (°C)	550	550	550	550	550	550	630
Total flow-rate ($N_2 + H_2$) (l min^{-1})	6	6	6	6	6	6	6
N_2–TEIn bubbler flow (cm^3 min^{-1})	200	–	200	–	200	200	350
H_2–TEGa bubbler flow (cm^3 min^{-1})	–	120	–	120	120	120	120
PH_3 flow (cm^3 min^{-1})	300	–	–	300	–	300	530
AsH_3 flow (cm^3 min^{-1})	–	90	90	–	90	–	21
Growth rate (Å min^{-1})	100	100	100	100	200	200	150

Table 5.2 Strained heterostructures grown by LP-MOCVD.

Substrate	First epilayer	Second epilayer
InP	GaAs	
InP	InAs	
GaAs	InP	
GaAs	InAs	
InAs	InP	
InAs	GaAs	
InP	GaAs	InAs
InP	$Ga_{0.47}In_{0.53}As$	$Ga_{0.49}In_{0.51}P$
GaAs	$Ga_xIn_{1-x}As$	
GaAs	InP	$Ga_xIn_{1-x}As_yP_{1-y}$

have performed a study of LP-MOCVD growth of InP simultaneously on InP, GaAs and InAs substrates with orientations of (1 0 0) placed adjacent to one another within the reactor for a growth temperature of 550°C.

Figure 5.3 shows the photoluminescence spectra of these layers at 5 K. A series of luminescence transitions, which can be attributed to recombination mechanisms such as free excitons, excitons bound to shallow impurities (such as Zn) and donor–acceptor recombination, were observed on these

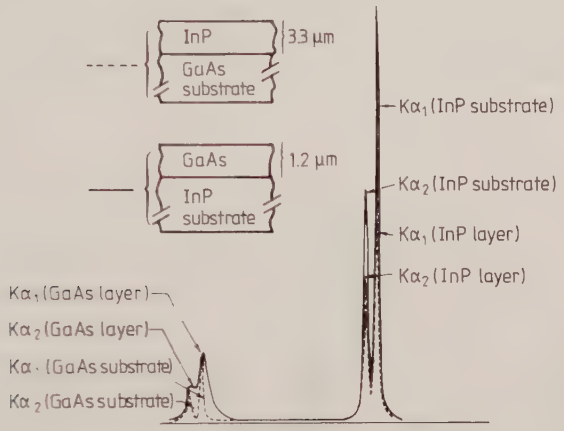

Figure 5.1 X-ray diffraction rocking curve of (4 0 0) Cu Kα reflection from an InP epilayer on a GaAs substrate and a GaAs epilayer on an InP substrate.

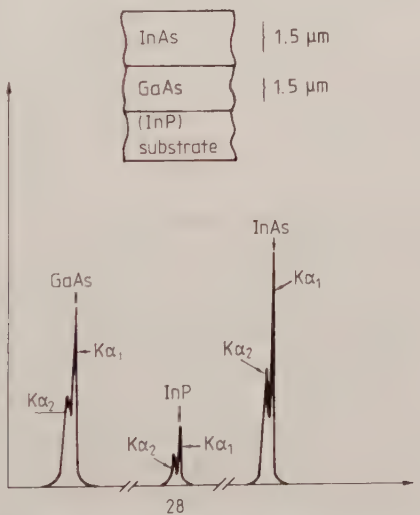

Figure 5.2 X-ray diffraction rocking curve of (4 0 0) Cu Kα reflection from an InAs–GaAs–InP heterostructure grown by LP-MOCVD.

spectra. The exciton recombination energy of InP on InP, InP on GaAs and InP on InAs substrates are 1.419, 1.423 and 1.421 eV respectively. Considering that the lattice parameters of InP, GaAs and InAs are 5.869, 5.633 and 6.057 Å respectively, one expects the InP layer on GaAs substrate to be compressed, and the InP layer on InAs substrate to be expanded. Usually these layers are pseudomorphic (i.e. the elastic straining of the deposited lattice produces a zero misfit with the substrate). The accommodation of the mismatch by elastic strains induces changes in the magnitude of the gap. Thus in the case of an InP epilayer on an InAs substrate, one expects a lower energy for exciton recombination than for an InP epilayer on an InP substrate. This is not observed and there is no interpretation for these results yet.

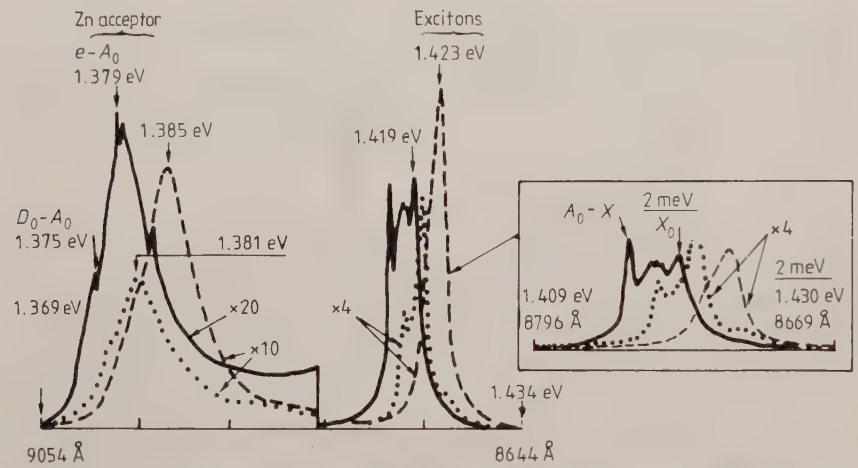

Figure 5.3 Photoluminescence spectrum of an InP epilayer on InP, GaAs and InAs substrates at 5 K using a He–Ne laser: InP on GaAs (– – –), InP on InAs (. . .), InP on InP (———).

5.1.2 Secondary-ion mass spectrometry

SIMS analyses have been performed for quantitative determination of impurities accumulated at the substrate–epilayer interfaces.

Figure 5.4 shows depth profiles of Mg, Si, Cr, Fe, Mn, As and P in InP layers grown on InP, InAs and GaAs substrates by LP-MOCVD. Each sample was analysed in two different areas about 10 mm apart. Generally, analysis of two clean areas gives reproducible and representative results for the material. We have already shown (see chapter 2) that the major source of impurities at the interfaces is the adsorption of atoms on the substrate surface during chemical etching prior to epitaxy. The pretreatments of the InP and InAs substrates are similar (described in chapter 2), so their SIMS profiles are identical. But the chemical etch of the GaAs substrate prior to

epitaxy is $H_2SO_4 + H_2O + H_2O_2$, and the concentration of impurities at the interface of InP–GaAs is lower than InP–InP or InP–InAs.

These results show that the quality of InP layers far from the interfaces is independent of substrate origin. Figure 5.5 shows an automatic electrochemical profile through an InP layer grown on a GaAs substrate, with and without light (under illumination, for n-type semiconductors, to generate holes required for the reaction). The result shows that near the interface there are some perturbations, but far from the epilayer–substrate interfaces the quality of the epilayer and the carrier concentration become similar to those for an InP epilayer grown on InP substrate under the same conditions.

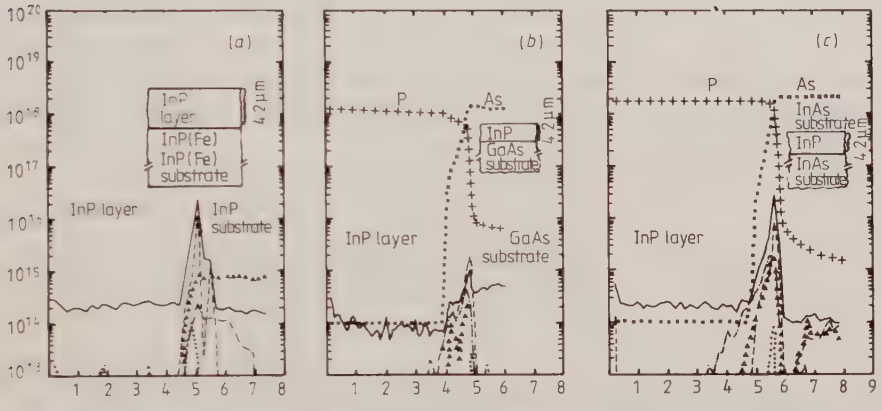

Figure 5.4 Depth profiles of Mg, Si, Cr, Fe, Mn, P and As in the MOCVD growth of: (*a*) InP on InP substrate; (*b*) InP on GaAs substrate; and (*c*) InP on InAs substrate. P(+), As(. . .), Mg(– – –), Si(———), Cr(– · –), Fe(▲).

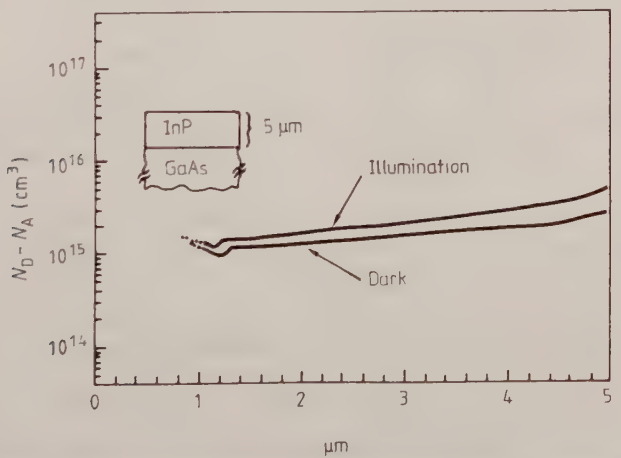

Figure 5.5 Electrochemical polaron profile of an InP epilayer on GaAs substrate.

5.1.3 Auger analysis

The constituent concentration gradients at an InP/GaAs interface have been determined by Auger analysis on a chemical bevel. The sample was chemically etched by using a methanol–bromine solution (15% Br), in order to obtain a bevel having a mean amplification coefficient (M) of 2100 (measured with a Talysurf). This means that a change of 1 μm along the surface corresponds to a change of 4.5 Å in depth (z direction). Figure 5.6 shows a schematic representation of the bevel. By scanning the incident electron beam four times along the bevel, the successive Auger profiles of the four elements P, As, In and Ga have been obtained. The four profiles are shown in figure 5.7.

Under certain simplifications, the relation between Auger intensity I^A and concentration C^A of an element A can be easily obtained by assuming that the interface region consists of n slices each of thickness a, where the slices are numbered starting from the deepest one (at the end of the homogeneous GaAs concentration, here) [2]—see figure 5.6.

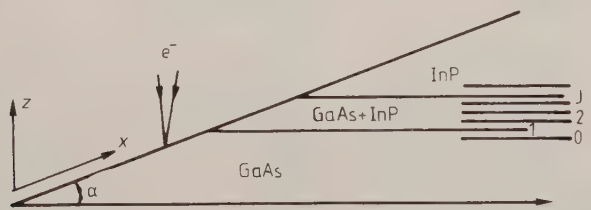

Figure 5.6 Schematic representation of the bevel of the InP/GaAs structure showing how a surface analysis along the bevel is converted into depth analysis.

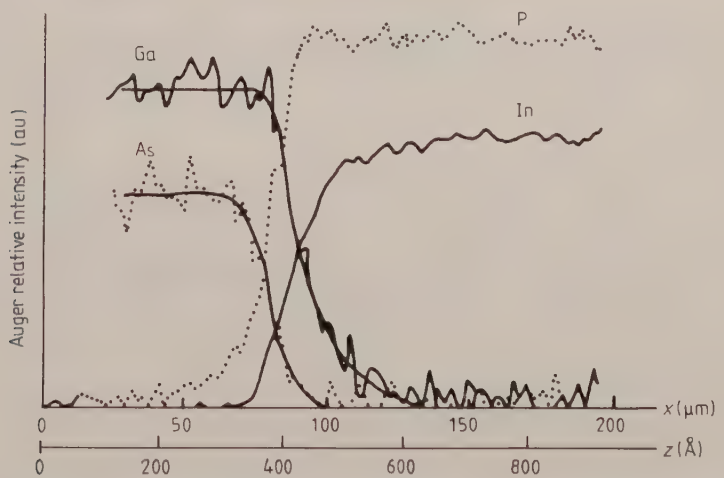

Figure 5.7 Corresponding Auger profiles relative to the four components: P, In, As and Ga.

The intensity due to the element A in the Jth slice corresponds to the intensity flowing from outside the slice, I_J^A, minus the intensity coming from all the other deeper slices, I_{J-1}^A, which is attenuated by the factor K by travelling through the Jth slice of thickness a. The interface composition (transition region) of InP–GaAs is $Ga_xIn_{1-x}As_yP_{1-y}$ where $0 \leqslant x, y \leqslant 1$.

After Auger analysis, the transition region constituting the interface can be subdivided into three parts (starting from the GaAs substrate):

(1) A region (thickness 150 Å) where In is absent. Its chemical composition is $GaAs_yP_{1-y}$ with $0.87 \leqslant y \leqslant 1$, which corresponds to the heating of the GaAs substrate under PH_3 before growth. So it is possible to have the adsorption of As and adsorption of P. This can be remedied by heating the GaAs substrate under AsH_3 pressure, before introducing PH_3 into the reactor.

(2) The mid-region (thickness 120 Å) where all four components are present. Its chemical composition is $Ga_xIn_{1-x}As_yP_{1-y}$ with $0 \leqslant y \leqslant 0.87$ and $0.24 \leqslant x \leqslant 1$.

(3) The region (thickness 115–130 Å) where As is absent. Its chemical composition is $Ga_xIn_{1-x}P$ with $x \leqslant 0.24$.

Such analyses can be developed on any hetero-epitaxial structure if a good composition of the chemical etching is found [2].

5.1.4 Etch-pit density

Figure 5.8 shows photomicrographs of the layers after forming a chemical bevel with very low angle and selective etching. The EPD of epitaxial layers and substrates are indicated in table 5.3.

The results show that the EPD in InP/GaAs and InP/InAs interfaces is independent of the EPD of the InAs or GaAs substrates [24].

5.2 GROWTH OF GaInAs–InP MULTIQUANTUM WELLS ON $Gd_3Ga_5O_{12}$ GARNET (GGG) SUBSTRATE

The composition of the garnets is given by the formula $R_3A_2B_3O_{12}$, in which the trivalent R ions are rare earths such as lutetium, yttrium, gadolinium, or other large ions and the A and B ions are smaller ions, such as Ga^{3+} or Al^{3+}. The R ions are surrounded by a decahedron (not the regular one, but a distorted cube of eight oxygen ions). The B ions are surrounded by a tetrahedron of four oxygen ions and the A ions by an octahedron of six oxygen ions. The basic structure of GGG is cubic. The lattice parameter is 12.383 Å. The GGG is an insulator and can be used as a substrate.

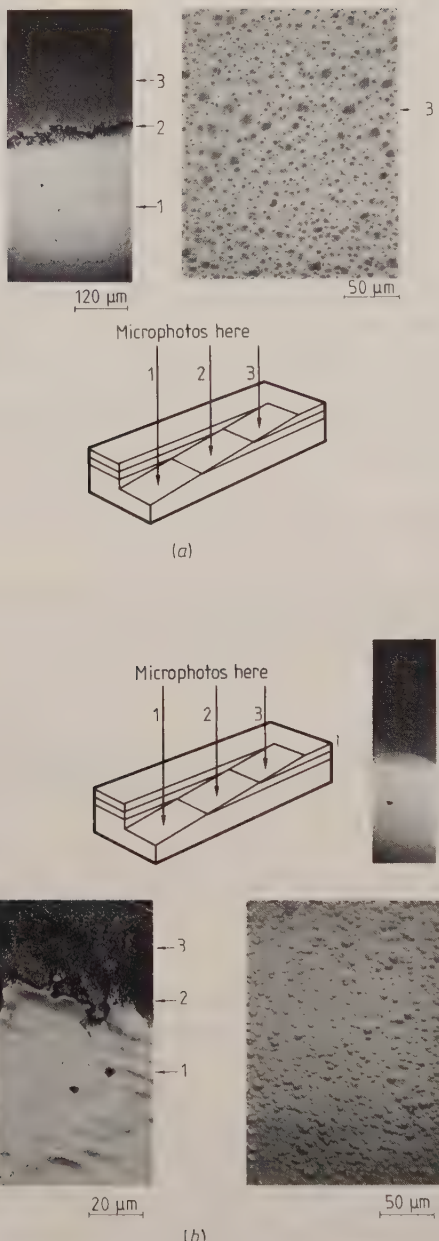

Figure 5.8 Etch-pit density photographs of (*a*) InP/InAs, (*b*) InP/GaAs and (*c*) InP/InP.

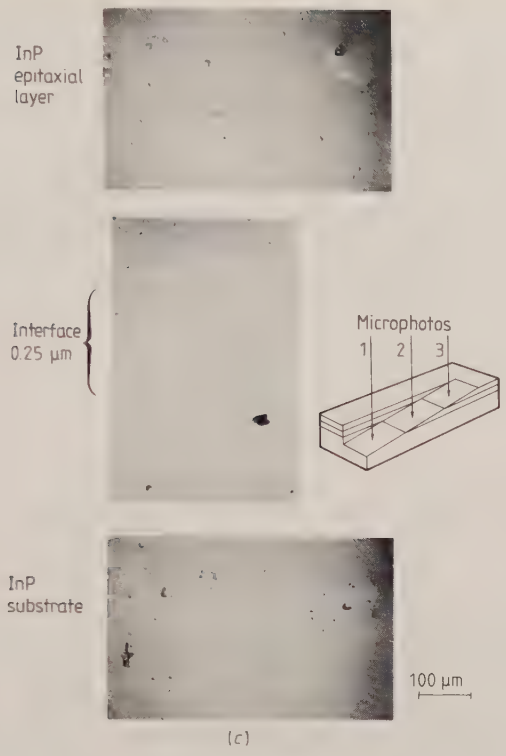

Table 5.3 EPD in epitaxial layers of InP on InP, InP on GaAs and InP on InAs substrate.

Epilayer/substrate	EPD(epilayer) (cm^{-2})	EPD(substrate) (cm^{-2})
InP/InP	8×10^3	8×10^3
InP/GaAs	6×10^5	2×10^3
InP/InAs	5×10^5	1×10^2

$Y_3Fe_5O_{12}$ (YIG) is a magnetic garnet material having the same lattice parameter as GGG, and it can be epitaxially grown on GGG. Figure 5.9 shows the elementary lattice cell of GGG. YIG is a potentially useful material for application to integrated optical devices, non-reciprocal elements such as isolators and circulators in planar integrated optics.

The growth of these III–V semiconductor compounds on GGG substrate can be used for:

(1) Optical telecommunications, such as integrated magneto-optical isolators and the integration of a laser diode with an isolator (YIG).

(2) Integrated magneto-optical circulators with possibilities for integrated emitters, detectors, isolators, circulators, non-reciprocal phase-shifters, modulators, etc.

(3) Magnetic recording with integrated magnetic read heads.

(4) Magnetometry.

The growth processes have been presented in table 5.1.

In a typical experiment to demonstrate the application of garnet substrate a GGG of (1 0 0) orientation and an InP substrate were placed on the susceptor, which was then placed inside the reactor [3]. The substrates were heated to 550°C. The growth pressure was 76 Torr. The growth conditions for InP and GaInAs are indicated in table 5.1.

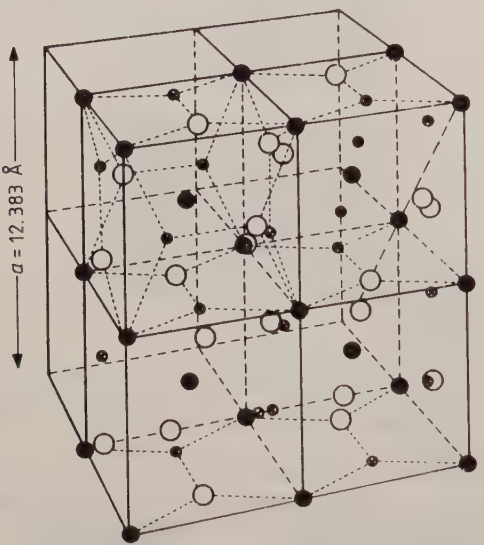

Figure 5.9 Crystal structure of GGG.

The epitaxial structure was as follows: one 1.5 μm InP buffer layer, five quantum wells of GaInAs (200 Å thick) with InP barriers (200 Å thick), and one 1.5μm InP top layer. The growth process for the GaInAs–InP multiquantum wells was the same as indicated in chapter 3.

X-ray diffraction was used to examine the quality of the deposited layers. Figure 5.10 presents the x-ray diffraction pattern of GaInAs–InP multilayers grown on GGG substrate indicated in table 5.4. These data show that the orientation of the epitaxial layer is (1 1 1) while the orientation of the substrate is (1 0 0). The lattice mismatch between the substrate and epilayer is $\Delta a/a = 0.526$. However, there are many important cases where the epitaxial layer has either a different orientation from the substrate, for

example CdTe(1 1 1) on GaAs(1 0 0) ($a_{GaAs} = 5.653$ Å and $a_{CdTe} = 6.481$ Å [4]), or a totally different crystal structure (for example, silicon on sapphire) [5].

In such cases the criterion of lattice match, namely, comparing the lattice parameters, is no longer applicable, and a new criterion should be used. Zur and McGill [6] defined the concept of lattice match for any pair of crystal lattices in any given crystal direction, allowing for a periodic reconstruction of the interface. Instead of comparing the bulk lattice parameters, they

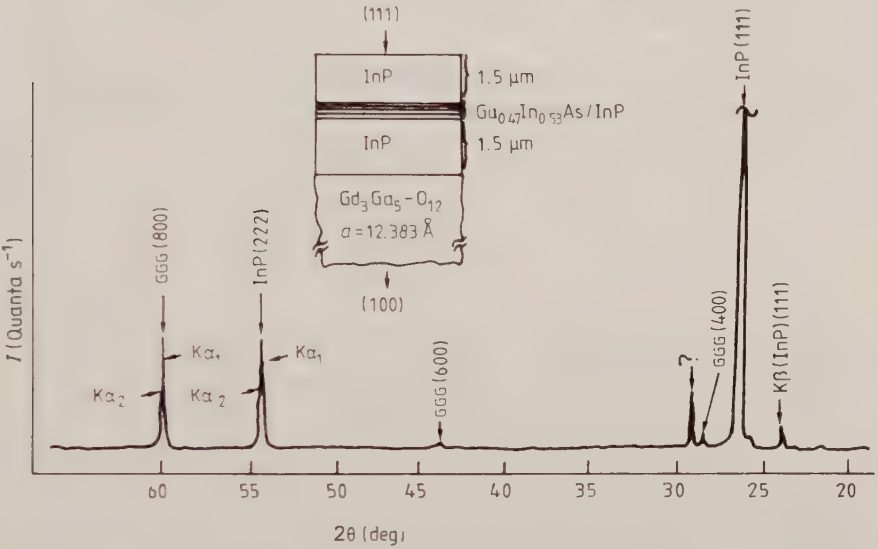

Figure 5.10 X-ray diffraction pattern of the 3 μm thick InP/GaInAs/InP epitaxial layer grown by LP-MOCVD on a GGG(1 0 0) substrate. The inset shows a schematic view of the sample configuration.

Table 5.4 Comparison between the experimental and reference value of 2θ (x-ray diffraction data) due to GaInAs–InP multilayers grown on GGG substrate.

Layers	*h k l*	$2\theta_{exp}$(deg)	$2\theta_{calc}$(deg)
InP	1 1 1	26.60	26.30
InP	2 2 2	54.30	54.10
InP	3 1 1	51.85	51.63
GGG	8 0 0	60.08	59.70
GGG	6 0 0	43.85	43.83
GGG	4 0 0	28.60	28.82

compared the interface translational symmetry with that of the bulk materials on both sides of the interface.

A cut in any crystal direction through a three-dimensional lattice results in a surface which has two-dimensional (2D) translational symmetry. Any additional reconstruction of the atoms near the interface during the interface formation may, in general, reduce the symmetry of the reconstructed surface; thus the symmetry group of the reconstructed surface will be a subgroup of the symmetry group of the unreconstructed surface. Therefore, the problem of lattice match is reduced to scanning the 2D cuts in a given pair of lattices, and then comparing the two resulting 2D lattices, looking for a common superlattice.

Figure 5.11 shows the photoluminescence (PL) spectrum of this sample at 77 K. The difference of the PLwavelengths may be due to misfit dislocations at the interface between the epilayer and the GGG substrate.

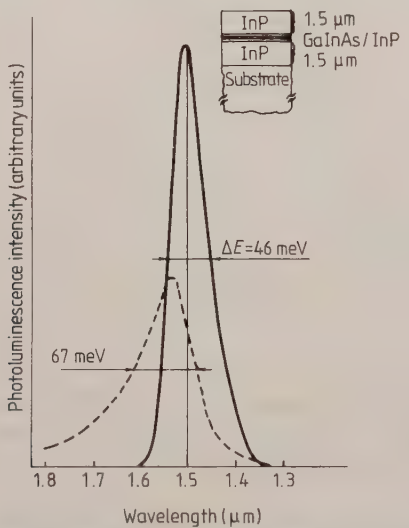

Figure 5.11 Photoluminescence spectra at 77 K of InP/GaInAs/InP epitaxial layer on a GGG(100) substrate (broken curve) and InP(100) substrate (full curve). The inset shows a schematic view of the sample configuration.

Razeghi *et al* [3] have grown thick layers (7 μm) of InAs, InP, GaAs and GaInAs on GGG substrate. In these cases, all of the epilayers were polycrystalline. After growing the MQW structure they succeeded in growing single crystals of III–V compounds on top of the MQW on the GGG substrates. These results indicate that a wide range of potentially useful new phenomena based on multilayer epitaxy on alternative substrates is becoming available and with imaginative implementation may be expected to lead to further novel device structures.

5.3 APPLICATIONS

5.3.1 Photonic devices based on strained layers

Long-distance optical links use lasers emitting at 1.3 μm fabricated by material grown on InP substrates. Unfortunately the technology of integrated circuits (IC) for signal treatment is a lot more difficult in this material than on GaAs substrates. A solution would be to combine the advantages of these two materials, which is against nature, owing to the large lattice mismatch.

Nevertheless, it is possible to do it with the MOCVD growth technique. $Ga_{0.25}In_{0.75}As_{0.5}P_{0.5}$–InP buried-ridge-structure (BRS) lasers emitting at 1.3 μm have been fabricated on GaAs substrates using the LP-MOCVD growth technique [7]. The BRS laser structure was manufactured as follows.

First the following layers were successively grown by LP-MOCVD on a Si-doped (1 0 0) 2° off GaAs substrate:

(1) 2 μm InP confinement layer, sulphur-doped with $N_D - N_A \simeq 10^{18}$ cm^{-3};

(2) 0.2 μm thick undoped GaInAsP (composition 1.3 μm) active layer;

(3) 0.2 μm thick Zn-doped ($N_A - N_D \simeq 2 \times 10^{17}$ cm^{-3}) InP layer in order to avoid the formation of defects near the active layer during etching.

The morphology of these layers was excellent, and the photoluminescence intensity and PL halfwidth were *the same* as for material grown on an InP substrate. The details of growth conditions were those given in table 5.1. Next, a ridge of about 2 μm width was etched in the InP(p) and GaInAsP active layers through a photolithographic resist mask.

After removing the resist mask, the ridges were covered with 1 μm of Zn-doped InP confinement layer and 0.5 μm Zn-doped GaInAs (with $N_A - N_D \simeq 10^{19}$ cm^{-3}) cap layer, also grown by LP-MOCVD. In order to localize the injection current only in the buried-ridge active region, a deep-proton implantation was performed through a 5 μm wide photoresist mask after metallization of the contacts. Further localization of the current in the buried ridge is achieved by the built-in potential difference between the p–n InP homojunction on each side of the active region and the n–p InP–GaInAsP heterojunction of the active region.

Figure 5.12 shows schematically the resulting GaInAsP–InP BRS laser. The devices were cleaved and sawn, producing chips of width 350 μm with cavity lengths of 300 μm.

Figure 5.13 shows the light–current characteristics of seven LP-MOCVD laser diodes obtained from the same wafer. Pulse threshold currents of 190 mA at room temperature have been measured with an output power of up to 10 mW.

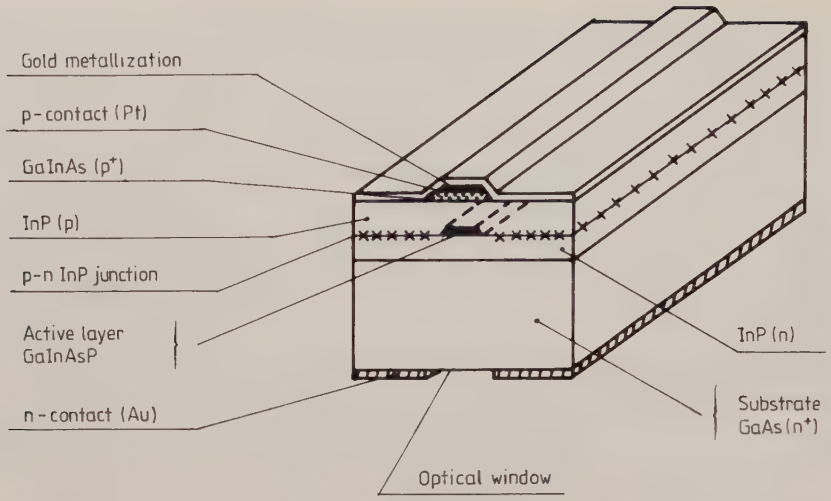

Figure 5.12 Schematic diagram of the cross section of a GaInAsP/InP BRS laser emitting at 1.3 μm grown by LP-MOCVD on a GaAs substrate.

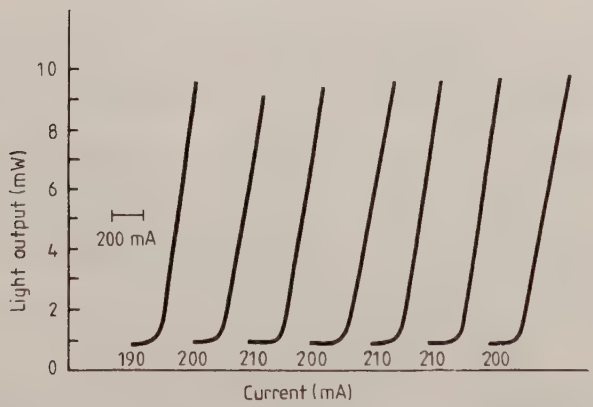

Figure 5.13 Light–current characteristics of GaInAsP–InP laser diodes emitting at 1.3 μm grown by LP-MOCVD on a GaAs substrate.

5.3.2 Electronic devices—GaInP/GaInAs/InP MESFET

$Ga_{0.47}In_{0.53}As$ lattice-matched to InP is a potentially important material for field-effect transistors (FET) with high peak electron velocity and high electron mobility for application in optoelectronic integration.

Metal–Schottky barrier heights on GaInAs are too low to be used as MESFET gates. FET in lattice-matched $Al_{0.48}In_{0.52}As$/InP which exploit the increased Schottky barrier height provided by AlInAs [8, 9] and lattice-mismatched GaAs gate/GaInAs structures have also been prepared [10].

The preparation of a $Ga_{0.49}In_{0.51}P/Ga_{0.47}In_{0.53}As/InP$ MESFET fabricated from material grown by LP-MOCVD has also been reported by Razeghi *et al* [1]. The energy gap of $Ga_{0.49}In_{0.51}P$ is 1.9 eV [11] and the lattice parameter is 5.65 Å. The growth conditions are given in table 5.1.

Figure 5.14 represents the FET device structure. The structure consists of n-type $Ga_{0.47}In_{0.53}As$ 1500 Å thick, doped to 3×10^{17} cm^{-3} with sulphur, and undoped $Ga_{0.49}In_{0.51}P$ 800 Å thick with a carrier concentration $N_D - N_A = 10^{16}$ cm^{-3} grown at 550°C onto (1 0 0) oriented Fe-doped semi-insulating InP substrates.

Large-geometry FET with 2 μm gate lengths, 150 μm gate widths and 5 μm source–drain spacing have been fabricated. Figure 5.14 shows source–drain current–voltage characteristics of a GaInP–GaInAs–InP FET; the gate bias step is 0.5 V. The transconductance of this device is $g_m \simeq 50$ mS mm^{-1}.

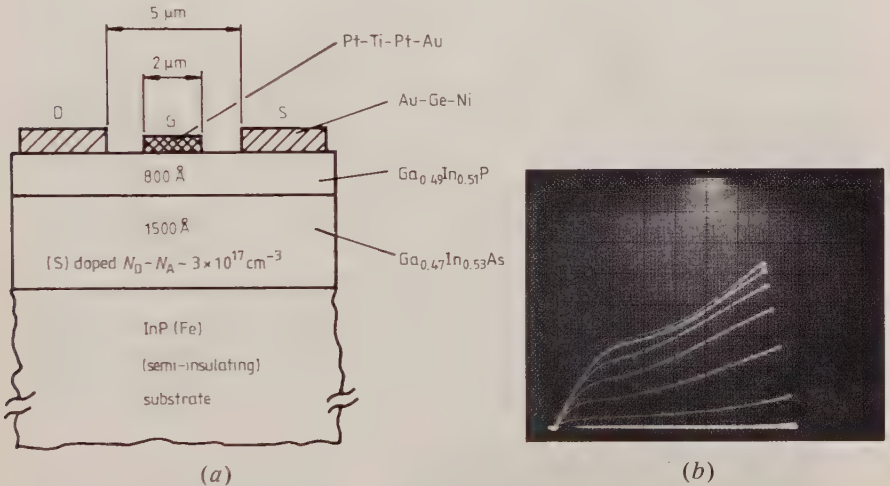

Figure 5.14 (*a*) Schematic representation of the GaInP/GaInAs/InP MESFET structure (*b*).

5.3.3 Opto-electronic integrated circuits (OEIC)

(a) Planar monolithic integrated photoreceiver for 1.3–1.55 μm wavelength applications using GaInAs–GaAs heteroepitaxies

Planar monolithic integrated photoreceivers are desirable devices for fibre-optic communication systems. In particular, the planar structure simplifies the problem of interconnecting the components and, for high-speed applications, such a technique reduces the parasitic capacitances. The feasibility of such devices has recently been demonstrated for 0.8 μm wavelength applications [12–14], and to a lesser extent for 1.3–1.55 μm

wavelength applications [15, 16, 19]. The purpose of this section is to present a planar monolithic integrated photoreceiver suitable for long-wavelength optical communications systems ($\lambda \simeq 1.3$–$1.55\ \mu m$) using $Ga_{0.47}In_{0.53}As$–GaAs strained heteroepitaxies [20, 25]. It consists of a planar $Ga_{0.47}In_{0.53}As$ photoconductive detector associated with a GaAs field-effect transistor (FET). The strained heteroepitaxy is constituted of an undoped $Ga_{0.47}In_{0.53}As$ layer grown on a classical GaAs FET epitaxy (figure 5.15).

A scanning electron micrograph of the integrated circuit and its electrical

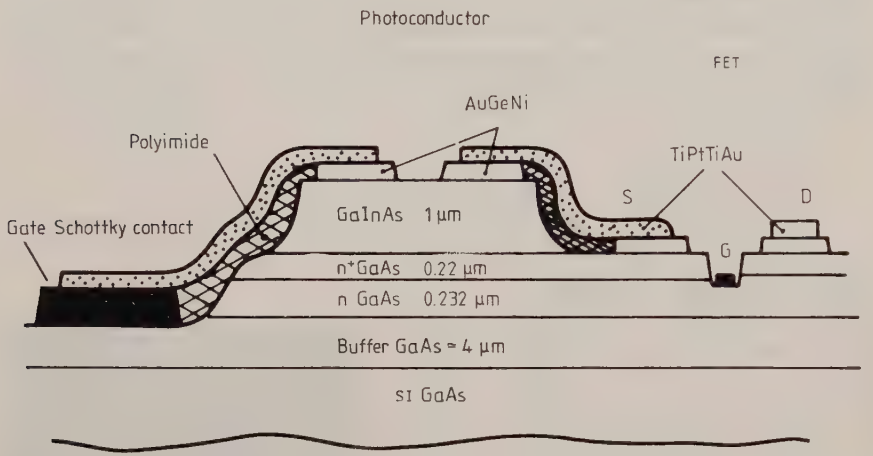

Figure 5.15 Schematic cross section of integrated photoreceiver. The gate metallization has been deposited on the n-GaAs layer to fabricate the FET and on a part of the buffer GaAs (called gate Schottky contact on the figure) to realize an insulated interconnection between the gate and the photoconductor.

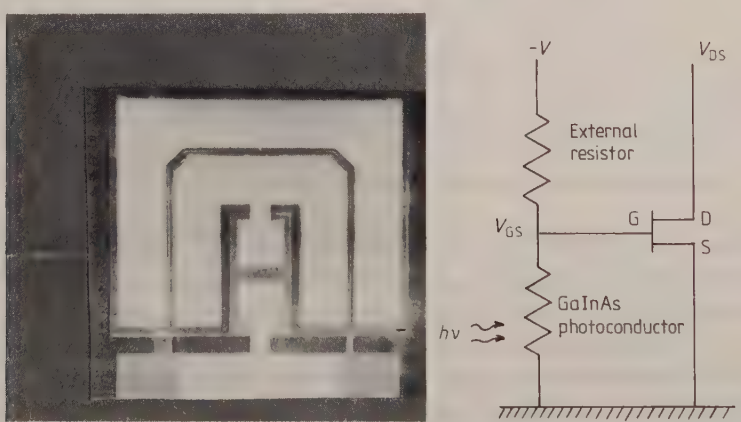

Figure 5.16 Photograph and electrical circuit of monolithic integrated photoreceiver.

circuit is shown in figure 5.16. The photoconductive detector has been formed by ion etching the $Ga_{0.47}In_{0.53}As$ up to the n^--GaAs layer, except for the area corresponding to the photoconductor. The lattice is constituted of two ohmic contacts (Au–Ge–Ni 2000 Å) separated from each other by 20 μm, leading to a 20×80 μm photosensitive area. The FET has been fabricated on the GaAs layers. The FET has a 2×900 μm gate (Ti 500 Å; Pt 300 Å; Ti 300 Å; Au 2000 Å), and, to produce a compact design integrated circuit, the FET surrounds the photoconductor. The interconnection between one of the photoconductor ohmic contacts and the FET source (Au–Ge–Ni 2000 Å) is made using a polyimide bridge. The same technique allows an interconnection to be made between the other photoconductor ohmic contact and the FET gate. It can be noticed that the n^+-GaAs layer reduces the dark resistance of the $Ga_{0.47}In_{0.53}As$ photoconductor; this effect will be discussed in the next paragraphs. A photoconductor was also processed on the same chip but without the transistor, in order to perform test experiments on the photodetector only. All experimental results presented on the photoconductor have been performed on the latter device.

Figure 5.17 shows typical steady-state gain (defined as the number of charges collected in the external circuit per incident photon) obtained for the photoconductor versus bias voltage. We observe that the gain value increases when the bias voltage increases; this result is due to the reduction of the transit time τ_t when the electron drift velocity increases corresponding to the expression for the gain $G = \tau_v/\tau_t$ [17, 18], where τ_v is the electron–hole pair lifetime. The low value of the gain is explained by a short lifetime τ_v, as can be observed on the picosecond response (figure 5.18). Typical dynamic gains $G(\omega)$ are given in figure 5.19. The experimental

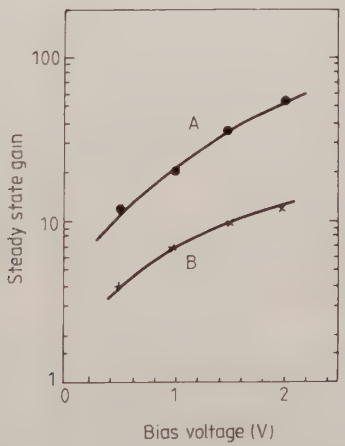

Figure 5.17 Steady-state gain G of the GaInAs–GaAs photoconductor versus its bias voltage V using (A) a CW 1.3 μm wavelength laser diode and (B) a CW 1.06 μm wavelength YAG laser ($P_L = 0.2$ μW).

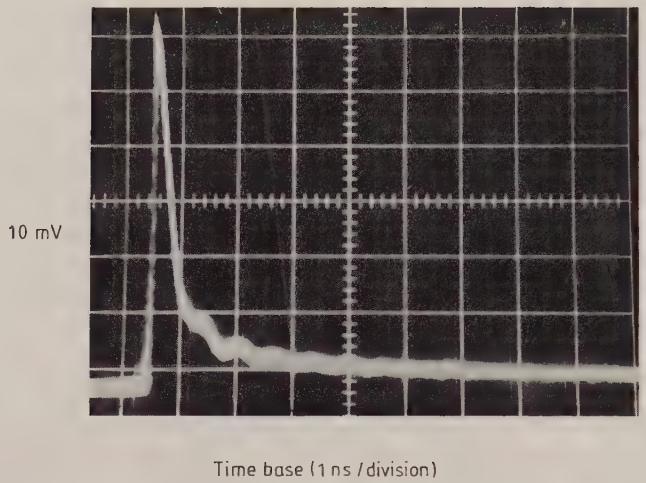

Figure 5.18 Picosecond response using a mode-locked dye laser; $\lambda = 0.580\ \mu m$, $P_L = 0.25$ mW. The light has been focused on the photosensitive area of the photoconductor using a microscope objective, to be sure that the light impinging on the device creates electron–hole pairs only in the $Ga_{0.47}In_{0.53}As$ of the photoconductor and not in the GaAs of the FET. The voltage measurements have been performed using a 10 dB attenuator.

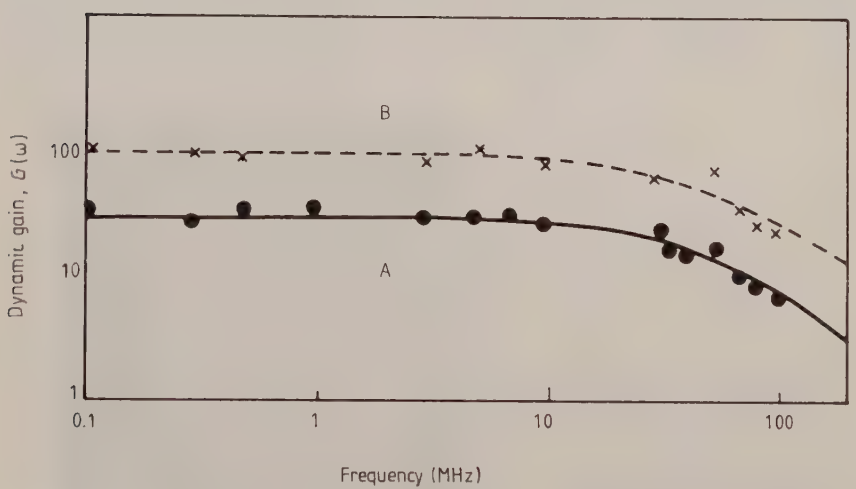

Figure 5.19 Dynamic gains versus frequency using a sinusoidally modulated 1.3 μm laser diode: (A) photoconductor, bias voltage 2 V; (B) integrated circuit, $V_{GS} = -2$ V, $V_{DS} = 2$ V.

results can be described by the expression $G(\omega) = \tau_r/\tau_t(1 + \omega^2\tau_r^2)^{1/2}$ corresponding to an assumption of a generation–recombination process governed by a Poisson law. The gain–bandwidth product is close to 1 GHz, a value related to the 20 μm electrode spacing. Obviously, this performance can easily be improved by using a shorter electrode spacing. The FET has been characterized separately. Its transconductance is close to 90 mS mm^{-1} corresponding to the gate size (2×900 μm). A current amplification of 2 has been achieved on the picosecond response (figure 5.18) and the same typical amplification factors are obtained for the low-frequency response (figure 5.19).

The noise properties of the photoconductor and of the integrated circuit have also been investigated in the 10 MHz–1.5 GHz frequency range. The experiments (figure 5.20) show a high $1/f$ photoconductor noise for frequencies lower than 100 MHz. For frequencies higher than 100 MHz this $1/f$ noise is greatly reduced, as is commonly observed in III–V photoconductors [18, 19]. The noise of the integrated circuit is higher; its value can be explained by the FET amplification plus the noise of the FET itself (figure 5.20). It can be noted that the noise under illumination is very close to the noise in darkness. This result can be explained by the low value of the gain of the photoconductor, according to the expression for the noise due to illumination of such a device [18].

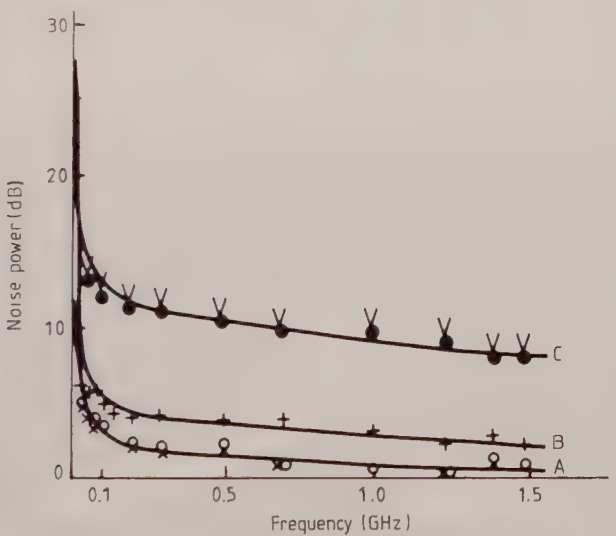

Figure 5.20 Noise power versus frequency for CW 1.06 μm YAG laser illumination at $P_L = 0.2$ mW. (A) Photoconductor; bias voltage 0.5 V: (X) without illumination and (○) with illumination. (B) Field-effect transistor; $V_{GS} = -0.5$ V; $V_{DS} = 2$ V. (C) Integrated circuit; $V_{GS} = -0.5$ V; $V_{DS} = 2$ V; (•) without illumination and (□) with illumination.

Several improvements can be proposed to obtain better performances:

(1) An interdigitated photoconductive detector would lead to a larger photosensitive area with a shorter electrode spacing, and obviously a higher gain–bandwidth product.

(2) An increase in the dark resistance of the photoconductor by growing the $Ga_{0.47}In_{0.53}As$ photosensitive area directly on the GaAs buffer would constitute the main improvement of this device.

(b) Monolithic integration of a Schottky photodiode and a FET using a $Ga_{0.49}In_{0.51}P/Ga_{0.47}In_{0.53}As$ strained material

For the realization of optoelectronic integrated circuits (OEIC) suitable for long-wavelength optical communications systems (1.3–1.55 μm), $Ga_{0.47}In_{0.53}As$ lattice-matched to InP is a potentially important material.

Razeghi *et al* [20] have grown different epilayers by MOCVD on an Fe doped InP substrate. The $Ga_{0.47}In_{0.53}As$ epilayer ($N_D \simeq 2 \times 10^{17}$ cm^{-3}; 2000 Å thick) is suitable for long-wavelength (1.3–1.55 μm) photodetection and FET channel fabrication. The $Ga_{0.49}In_{0.51}P$ epilayer is undoped (residual n-type) and is 1000 Å thick. A photodiode, a FET and an OEIC have been realized on the same chip. The photodiode has a 40×40 μm photosensitive area. The Schottky contact has been realized by the deposition of a 200 Å thick Ti–Pt electrode. A responsivity close to 0.1 A W^{-1} has been measured for a 1.3 μm wavelength optical signal and the picosecond response is given in figure 5.21.

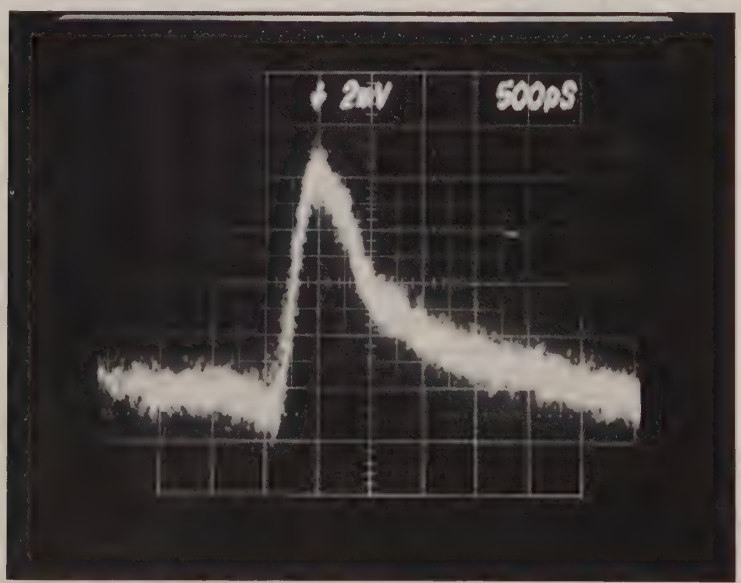

Figure 5.21 Picosecond response of the photodiode.

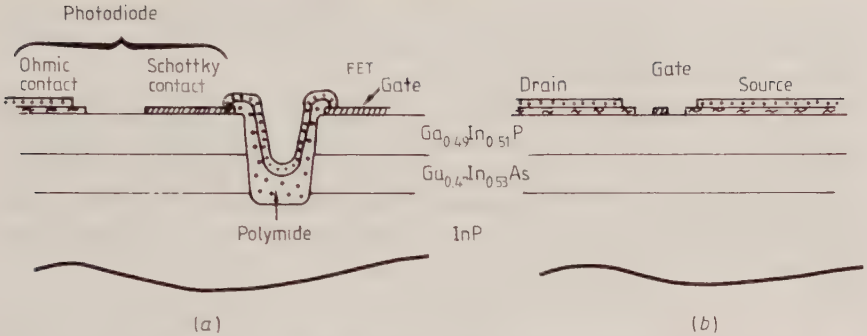

Figure 5.22 Schematic cross sections of the device (OEIC).

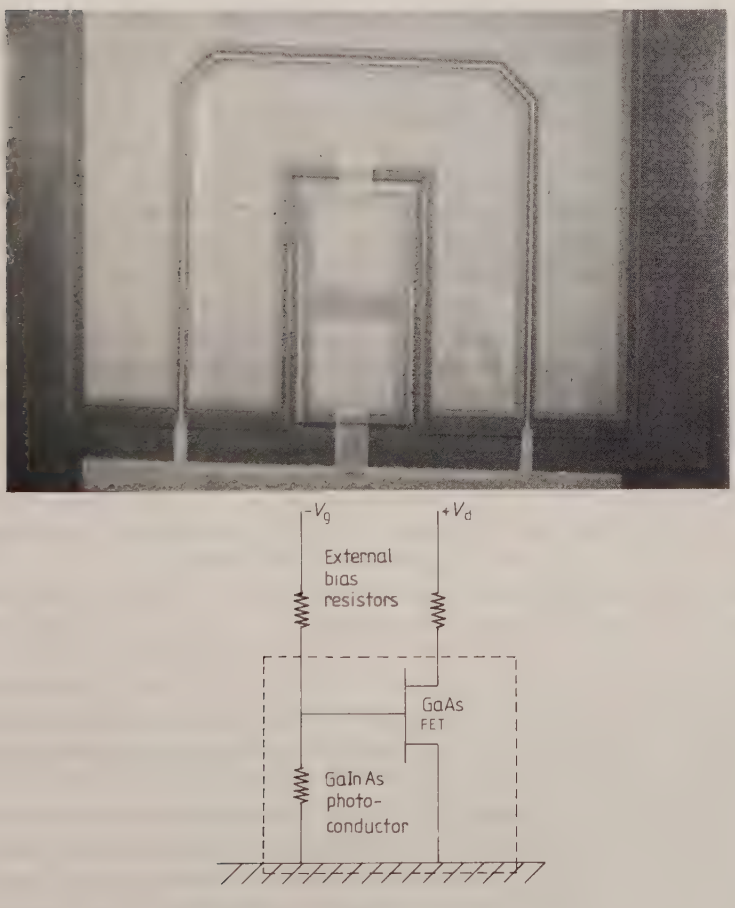

Figure 5.23 SEM photograph and electrical equivalent circuit of the photoreceiver.

The FET gate has a 3 μm length and 300 μm width. The saturation current is about 10 mA and the pinch-off voltage is close to -3 V. The average measured transconductance is 30 mS mm^{-1} [21].

The OEIC (schematic cross sections in figure 5.22) associates the same photodiode and FET (600 μm gate width, in this case) as that previously presented in §5.3.2(*a*). A SEM micrograph and equivalent electrical circuit are shown in figure 5.23. Static, dynamic and noise properties of the IC have been evaluated. As an example, a responsivity of 50 A W^{-1} have been achieved at 1.3 μm for a 1.5 KΩ bias resistor.

5.4 MONOLAYER EPITAXY OF $(GaAs)_n(InAs)_n$–InP BY MOCVD

The atomic-layer epitaxy (ALE) proposed by Suntola [22] and described in §1.3.2 differs completely from the usual growth techniques. His idea is accomplished by alternative adsorption of reactant gas molecules onto the growing surface. So, in ALE, the growth thickness is only determined by the number of adsorptions. Using this method, quantum-well structures, superlattices and modulation-doped heterojunctions can be fabricated with precise thickness control and compositional homogeneity over a large surface of substrate. In modulation-doped GaInAs–InP structures, the enhancement of mobility is limited by the disorder scattering in $Ga_xIn_{1-x}As$ alloys. With monolayer epitaxy of $(GaAs)_n(InAs)_n$, one can provide ordered atomic arrangements in $Ga_{0.5}In_{0.5}As$ alloy, and improvement of the drift velocity is expected. In this section, we describe the successful growth [23] of $(InAs)_n(GaAs)_n$–InP multiquantum-well structures by LP-MOCVD, which exhibited an excellent uniformity of thickness and composition over a large area of InP substrate.

Growth conditions of the different monolayers are detailed in table 5.5. Table 5.6 details the lattice parameter (a), the monoatomic layer thickness (d) and the time necessary to grow this atomic layer (t).

Several growth sequences were first investigated, in order to optimize the quality of the $(GaAs)_n(InAs)_n$ bulk layer.

Type 1 epitaxy

By taking $n = 1$ and 2000 monolayers of InAs and GaAs, a $Ga_{0.5}In_{0.5}As$ bulk layer about 1 μm thick was made, in a continuous growth, without purging between the monolayers.

The epitaxy was initiated by growing an InP buffer layer on an InP ((1 0 0) oriented) substrate. The first InAs layer was realized by switching PH_3 to the waste line and AsH_3 to the reactor. For growing the first GaAs layer, In was then switched to the waste line and Ga to the reactor. The global layer $((GaAs)_1(InAs)_1)$ was then grown, without any purging time between the monolayers.

Table 5.5 Growth conditions.

	InP	InAs	GaAs
Growth temperature (°C)	550	550	500
Growth pressure (mbar)	100	100	100
N_2 flow (l min^{-1})	2	2	2
H_2 flow (l min^{-1})	2	2	2
In flow (N_2) (cm^3 min^{-1})	100	100	–
Ga flow (H_2) (cm^3 min^{-1})	–	–	60
Growth rate (Å min^{-1})	50	50	50
PH_3 flow (cm^3 min^{-1})	200	–	–
AsH_3 flow (cm^3 min^{-1})	–	45	45

Table 5.6 Parameters.

	a (Å)	d (Å)	t (s)
InP	5.86	2.93	2.4
GaAs	5.66	2.83	2.3
InAs	6.06	3.03	2.5

Figure 5.24(a) shows the photoluminescence spectrum at $T = 4$ K of the structure. The recombination peak is located at about 735 meV, at a lower value than the $T = 4$ K gap of the $Ga_{0.47}In_{0.53}As$ material lattice-matched to InP. A full width at half-maximum (FWHM) of 30 meV is determined, which clearly remains higher than the value reported in bulk $Ga_{0.47}In_{0.53}As$ (see chapter 3).

Type 2 epitaxy

This was realized by keeping $n = 1$ with 2000 periods of $(GaAs)_1(InAs)_1$, but purging times were introduced between the layers. After growing the InP buffer layer, PH_3 was switched to the waste line and AsH_3 to the reactor to realize the first InAs monolayer. In was then switched to the waste line, and Ga introduced into the reactor after waiting 1 s during which only AsH_3 was present in the reactor. This has been done to stabilize with As the growing solid surface, in order to prevent mixing between In and Ga.

Figure 5.24(b) shows the $T = 4$ K photoluminescence spectrum of the structure. The recombination peak is located at 766 meV, still at a lower energy than the $T = 4$ K band gap of $Ga_{0.47}In_{0.53}As$. A slight decrease is found in the FWHM parameter, which is about equal to 27 meV.

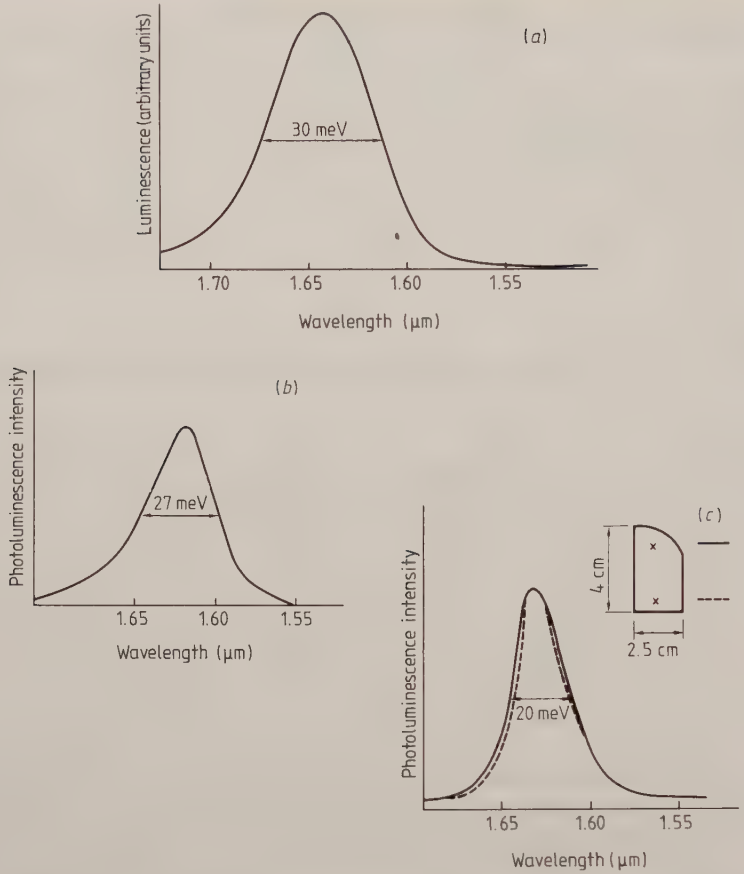

Figure 5.24 Photoluminescence spectra at 4 K of: (*a*) $(GaAs)_1(InAs)_1$ bulk layer grown without purge; (*b*) $(GaAs)_1(InAs)_1$ bulk layer grown with purge; (*c*) $(GaAs)_2(InAs)_2$ bulk layer grown with purge.

Type 3 epitaxy

The purging time is maintained at 1 s, but the time of each GaAs and InAs sequence is multiplied by 2, so that $n = 2$ and the growing material is $(GaAs)_2(InAs)_2$. 1000 periods of $(GaAs)_2$ have been realized, so that the total thickness of this material is kept constant, and equal to nearly 0.6 μm.

Figure 5.24(*c*) shows the $T = 4$ K photoluminescence spectrum of the structure. The peak is located at 758 meV, with a FWHM of 20 meV, which is further lowered, compared to the two previous results.

The quality of the epilayer has been improved by introducing a purging time of 1 s between the InAs and GaAs layers, and by growing two monolayers ($n = 2$) of these compounds at each sequence.

Mobility measurements, performed on this layer, using the classical Van der Pauw technique gave $\mu(300\ \mathrm{K}) = 7000\ \mathrm{cm^2\,V^{-1}\,s^{-1}}$ and $\mu(77\ \mathrm{K}) = 30\,000\ \mathrm{cm^2\,V^{-1}\,s^{-1}}$. Such results are not far away from those of bulk $Ga_{0.47}In_{0.53}As$.

It is worth adding that all these structures showed a remarkable composition uniformity, with no dispersion of the luminescence recombination peak on wafers of about 10 $\mathrm{cm^2}$ area.

5.4.1 Multiquantum wells of $(GaAs)_2(InAs)_2/InP$

This fact was further demonstrated by studying the uniformity of a multiquantum-well structure. The wells were composed of $(GaAs)_2(InAs)_2$, which were grown as described in type 3 epitaxy. The global structure was as follows:

(1) 1000 Å InP buffer layer,
(2) 20 times $(GaAs)_2(InAs)_2$ sequence,
(3) 500 Å InP barrier,
(4) 10 times $(GaAs)_2(InAs)_2$ sequence,
(5) 500 Å InP barrier,
(6) five times $(GaAs)_2(InAs)_2$ sequence,
(7) 500 Å InP barrier,
(8) two times $(GaAs)_2(InAs)_2$ sequence,
(9) 500 Å InP top layer.

Figure 5.25 shows the low-temperature ($T = 4$ K) photoluminescence spectra of the structure, using He–Ne and YAG lasers of wavelengths 0.63 μm and 1.16 μm as excitation sources. The penetration depth of the YAG laser is more important, so that it appears more sensitive than He–Ne to the wells that are situated far away from the surface of the sample.

The thicknesses of the quantum wells, deduced from the growth rate, are about 100, 50, 25 and 12 Å. It is noticeable that a quantum well of $(GaAs)_2(InAs)_2$ as thin as 12 Å shows a clear quantum size effect (figure 5.25). Another interesting feature is the remarkable uniformity in thickness and composition obtained by monatomic layer epitaxy (see figure 5.25). The photoluminescence spectrum has been recorded at two extremities of the sample, with no significant shift in energy in the recombination peaks.

Figure 5.26 shows, for comparison, spectra recorded at the same points of the wafer, in a multiquantum-well structure with wells composed of classical $Ga_{0.47}In_{0.53}As$ material. Shifts of about 20 meV are seen between the peaks attributed to the same quantum wells for all the quantum wells. This indicates that the composition of the GaInAs varies across the wafer. This variation is not found in the case of the monolayer epitaxy (figure 5.25).

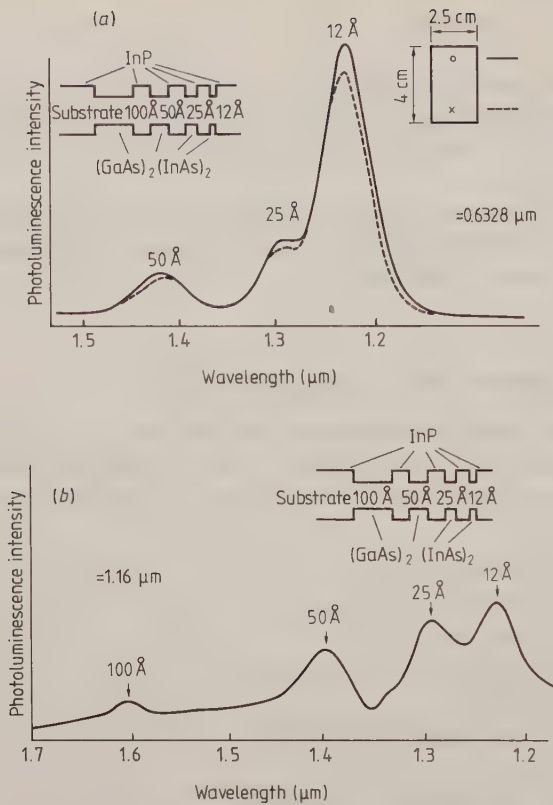

Figure 5.25 Photoluminescence spectra at 4 K of a $(GaAs)_2(InAs)_2$/InP multiquantum well.

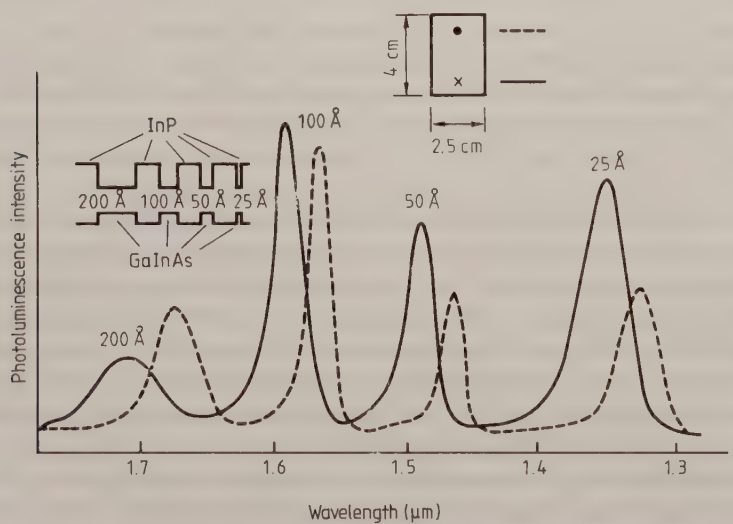

Figure 5.26 Photoluminescence spectrum at 4 K of a GaInAs–InP multiquantum well recorded in two opposite points of the layer.

REFERENCES

[1] Razeghi M, Maurel P, Omnes F and Thorngren E 1987 *Optical Properties of Narrow-gap Low-dimensional Structures* (New York: Plenum) pp 39–53

[2] Gazaux J, Etienne P and Razeghi M 1986 *J. Appl. Phys.*

[3] Razeghi M, Meunier P-L and Maurel P 1986 *J. Appl. Phys.* **59** 2261

[4] Asuka N, Kolodziejski L A, Gunshor R L, Datta S, Bicknell R N and Schetzina J F 1985 *Appl. Phys. Lett.* **46** 860

[5] Cullen G W 1978 *Hetero-epitaxial Semiconductors for Electronic Devices* ed G W Cullen and C C Wang (Berlin: Springer) p 50

[6] Zur A and McGill 1984 *J. Appl. Phys.* **55** 378

[7] Razeghi M, Blondeau R and Duchemin J P 1985 *Gallium Arsenide and Related Compounds, 1984* (Inst. Phys. Conf. Ser. 74) p 679

[8] Barnard J, Ohno H, Wood C E C and Eastman L F 1980 *IEEE Electron. Device Lett.* **EDL-9** 174

[9] Scott M D, Moore A H, Griffith I, Griffith R J M, Sussman R S and Oxley C 1986 *Gallium Arsenide and Related Compounds, 1985* (Inst. Phys. Conf. Ser. 79) p 475

[10] Chen C Y, Cho A Y and Garlinski P A 1985 *IEEE Electron. Device Lett.* **EDL-6** 20

[11] Hilsum C 1964 *Proc. 7th. Int. Conf. Semiconductor Physics* (Paris: Dunod) p 1127

[12] Wada D, Mivra S, Ito M, Fujh T, Sakurai T and Hiyamizu S 1983 *Appl. Phys. Lett.* **42** 380

[13] Kolbas R M, Abrokwah J, Carney J K, Bradshaw D H, Elmre H R and Briard J R 1983 *Appl. Phys. Lett.* **43** 821

[14] Verriele H, Maricot S, Constant M, Ramdani J and Decoster D 1985 *Electron. Lett.* **21** 878

[15] Hata S, Ikeda M, Amano T, Motosugi G and Kurmuda K 1984 *Electron. Lett.* **20** 947

[16] Razeghi M 1985 *Lightwave Technology for Communication* ed W T Tsang (New York: Academic) p 299

[17] Gammel J C, Ohno H and Ballantyne J M 1981 *IEEE J. Quantum Electron.* **QE-17** 269

[18] Vilcot J P, Constant M, Decoster D and Fauquembergue R 1985 *Physica* B **129** 488

[19] Chen C Y, Pang Y M, Alavi K, Cho A Y and Garbinski P A 1984 *Appl. Phys. Lett.* **44** 99

[20] Razeghi M, Ramdani J, Legry P, Vilcot J P and Decoster D 1988 *Gallium Arsenide and Related Compounds, 1987* (Inst. Phys. Conf. Ser. 91) p 781

[21] Razeghi M, Hosseini Therani A, Vilcot J P and Decoster D 1988 *Gallium Arsenide and Related Compounds, 1987* (Inst. Phys. Conf. Ser. 91) p 625

[22] Suntola T 1984 *16th Int. Conf. on Solid State Devices and Materials* Tokyo, Extended Abstracts, p 647

[23] Razeghi M, Maurel P, Omnes F and Nagle J 1988 *Appl. Phys. Lett.* **51** 2216

[24] Huber A M, Razeghi M and Morillot G 1985 *Gallium Arsenide and Related Compounds, 1984* (Inst. Phys. Conf. Ser. 74) p 223

[25] Razeghi M, Ramdani J, Verride H, Decoster D and Constant M 1986 *Appl. Phys. Lett.* **49** 215

Chapter 6 MOCVD Growth of III–V Heterojunctions and Superlattices on Si Substrates and their Applications

6.1 INTRODUCTION

At present, there is a great deal of interest in the growth of GaAs on silicon substrate [1–6]. Devices such as GaAs FET transistors [7] or GaAs lasers [8, 9] have been realized using a silicon substrate. Long-distance optical links use semiconductor lasers emitting at 1.3 and 1.55 μm fabricated using materials such as the GaInAsP–InP lattice-matched system on an InP substrate. Unfortunately, the technology of integrated circuits for signal treatment is more difficult on this material than on GaAs substrates. Since silicon technology is more advanced than that for GaAs- and InP-based materials, the solution is to combine the advantages of InP and GaAs devices with the maturity of Si processing technology, using existing Si integrated circuit equipment.

However, high device quality for InP- and GaAs-based materials has not been obtained by direct growth on Si substrates, since the lattice parameter, crystal symmetry and thermal expansion coefficient of InP, GaAs and Si are all different. Furthermore, nucleation of InP and GaAs on Si substrate is difficult.

At the present stage of III–V/Si technology development, attention is being focused on perfecting the growth of InP, GaAs and related compounds on Si and demonstrating that devices with acceptable operating characteristics can be fabricated in these layers.

The most important problems encountered when III–V semiconductors

are grown on Si substrates are as follows:

(1) the difference in lattice parameter between the III–V semiconductor and the Si substrate;
(2) the difference in lattice symmetry;
(3) the difference in thermal expansion coefficient;
(4) the preparation and chemical etching of the Si substrate to remove the oxide and carbon; and
(5) the cross doping of the III–V epilayer with silicon.

6.1.1 The difference in lattice parameter

An 8% lattice mismatch between InP and Si and 4% between GaAs and Si produces a misfit dislocation at the interface. The formation of misfit dislocations and the introduction of tensile stress in heteroepitaxial InP- and GaAs-based materials on Si are the principal problems besetting the application of these materials for minority carrier devices, such as lasers. The dislocations at the III–V/Si interface do not degrade the III–V epilayer crystalline quality; instead, the propagation of dislocations away from the interface region (the so-called threading dislocation) appears to be primarily responsible for the non-radiative recombination centres. The threading dislocations also reduce minority carrier lifetimes, producing inferior properties for devices fabricated on III–V epilayers on Si substrates. Therefore very low misfit dislocation densities in the III–V epitaxial overlayers are essential for laser applications.

In order to reduce the misfit dislocations in GaInAsP–InP layers grown on Si substrate, using MOCVD, Razeghi *et al* [10] used a two-step growth method. First a thin layer of 200 Å of GaAs is grown at 450°C, using a growth rate of 50 Å min^{-1}. Then the substrate temperature is raised to 550°C. A five-period lattice-matched superlattice of GaInAsP–InP or GaAs–GaInP with $L_z = 100$ Å and $L_B = 100$ Å (L_B is the thickness of InP or GaInP barrier and L_z is the thickness of the GaInAsP or GaAs quantum well) is then grown. These superlattices have been shown to be effective in bending dislocation lines out toward the edges of the crystal, preventing the cross doping of the epilayer with Si, and thus preventing dislocation movement in device operation.

6.1.2 The difference in lattice symmetry

One of the problems in growing a III–V (a polar semiconductor) on Si (a non-polar semiconductor) is the possible occurrence of antiphase domains ($p, g, -a$). In certain regions of the epilayer the cation and anion sublattices have been interchanged. The interface between domains with opposite sublattice allocation forms a two-dimensional structural defect

called an antiphase boundary [11]. Antiphase boundaries in a III–V semiconductor containing III–III and V–V bonds represent an electrically charged defect. The III–III bonds act as acceptors, the V–V bonds as donors (see figure 6.1(*b*)). In general, antiphase boundaries which act as highly compensated doping sheets with very little net doping can also act as non-radiative recombination centres.

In order to eliminate the antiphase domain, in III–V layers grown on Si by MOCVD one can use a 4° off (1 0 0) towards (0 1 1) oriented Si substrate, and then perform the high-temperature annealing (1000°C) under AsH_3–H_2 of the tilted substrate prior to growth, in order to form the double atomic layer steps, which help to eliminate antiphase domains ($p, g, -c$) [11].

In fact, (1 0 0) Si substrates cannot be prepared to have misorientations totally along one direction, e.g., just along the ⟨011⟩ direction, leading to the growth of a surface consisting of steps along the ⟨011⟩ directions and terraces having a (1 0 0) orientation. Two types of double steps can form on the misoriented (1 0 0) Si surface, the so-called 'type A' surface step where the Si dangling bonds point parallel to the step edge, and the 'type B' surface step in which the Si bonds are perpendicular to the step edge [11, 12] (see figure 6.1(*a*), (*c*)). As a result, the possibility exists that two

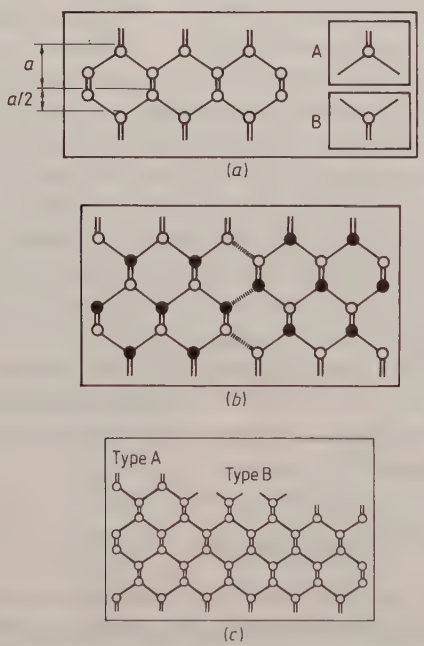

Figure 6.1 (*a*) Two sublattices in diamond structure; (*b*) an antiphase boundary in a III–V semiconductor (○, III; •, V); (*c*) two kinds of step on a Si(100) surface.

distinct domains can result in the heteroepitaxial GaAs film. It has been shown experimentally [11, 13] that for a properly prepared (1 0 0) Si surface, the type A steps form preferentially, leading to the formation of a single-domain GaAs/Si heteroepitaxial layer (see figure 6.1(*c*)). Calculations by Aspnes and Ihm [12] have shown that the production of single-domain regions on such a surface is favoured if the substrate misorientation is within a certain range of directions off the nominal (1 0 0) surface, as determined experimentally for MOCVD GaAs/Si by Akiyama *et al* [14].

Studies of the early stages of MBE GaAs/Si growth on clean (1 0 0) Si substrates slightly misoriented towards the ⟨0 1 1⟩ have shown that the deposition of GaAs begins with the nucleation of GaAs islands on the Si surface [15]. Surface preparation techniques strongly influence this process, probably because of the details of the step density and the Si atom surface mobility. Hull and co-workers have shown that, for Si substrates annealed at low temperatures ($T_{ann} \approx 730^{\circ}C$), the surface reconstruction consists primarily of steps of one or two (2 0 0) monolayers [15]. In contrast, high anneal temperatures ($T_{ann} \approx 900^{\circ}C$) can lead to the formation of large clusters of Si surface steps to form local Si facets about 6–10 (2 0 0) monolayers high. Similar detailed studies of the early stages of the MOCVD growth of GaAs/Si have not yet been reported. However, the $H_2 + AsH_3$ atmosphere used in the Si annealing pre-growth sequence for MOCVD GaAs/Si films is quite different from the high-vacuum environment used in the substrate cleaning step for MBE growth of GaAs/Si and this could influence the surface reconstruction [16].

6.1.3 The difference in thermal expansion coefficient

The difference in thermal expansion coefficients of GaAs, InP and related compounds with Si substrates puts the epilayer under extreme tensile stress. The difference in the lattice parameters parallel and perpendicular to the interface arises from the difference in thermal expansion between the III–V compound and Si, not from misfit accommodation by elastic strain.

Analyses of the tetragonal distortion in III–V on Si would thus be expected to yield information concerning the defect structure in this material.

Some physical parameters of Si, GaAs and InP relevant for the heteroepitaxy of these materials are listed in table 6.1.

6.1.4 Preparation and chemical etching of Si substrate

Preparation of atomically clean surfaces is essential in order to achieve good epitaxial growth. One has to eliminate the oxides and carbon from the Si surface before growth. Several cleaning procedures have been employed

Table 6.1 InP, GaAs and Si properties.

	Si	GaAs	InP
Thermal coefficient of expansion (K^{-1})	2.6×10^{-6}	6.8×10^{-6}	4.56×10^{-6}
Thermal conductivity ($W\,cm^{-1}K^{-1}$)	1.5	0.46	0.68
Lattice parameter (Å)	5.43	5.65	5.86
Crystal symmetry	Diamond	Zinc blende	Zinc blende
Density ($g\,cm^{-3}$)	2.328	5.32	4.787

in the MOCVD growth of III–V/Si layers. One of the most commonly used techniques involves the sequential chemical oxidation and removal of a thin non-stoichiometric oxide film [18]. This relatively volatile oxide layer is subsequently removed by heating to a temperature of 1000°C for 10 min. This procedure, or some variation of it, is generally employed in MOCVD heteroepitaxy on Si.

6.1.5 The cross doping of the III–V epilayer with Si

To eliminate the cross doping of the III–V epilayer with Si using a Si substrate, several types of superlattices have been evaluated. Razeghi *et al* [18] showed experimentally that GaInAsP/InP lattice-matched superlattices can prevent the cross doping of the III–V semiconductor epilayer with Si.

6.2 MOCVD GROWTH OF GaAs ON Si

The growth procedure is as follows. A Si substrate is chemically cleaned by HF dipping, and then loaded into the reactor. The substrate is then heated to approximately 1000°C for 10 min to remove the oxide and the double-atomic-layer steps. This high-temperature cleaning procedure, 4° off substrate, is essential to obtain a single-domain structure. The substrate is then cooled to a relatively low temperature, 400–450°C, and a 200 Å GaAs layer is deposited on the substrate. The initial growth is normally by island formation followed by coalescence. The growth temperature dramatically affects the shape and size of the islands that nucleate. At lower temperatures, the islands are smaller and closer together, resulting in a smoother surface. (However, it is necessary to have decomposition of AsH_3 and TEGa for growth of GaAs to occur. At temperatures lower than 400°C decomposition of alkyls and hydrides is not complete, so with the MOCVD growth technique a temperature of 450°C for the nucleation is adequate.)

After nucleation, the substrate temperature is raised to 550°C for the growth of the rest of the structure. To decrease the threading dislocations, different kinds of interlayers between GaAs and Si, such as a Ge, GaP strained layer superlattice, a GaAs/GaInP superlattice, or a GaInAs/InP or GaInAsP/InP lattice-matched superlattice can be used [19]. Razeghi *et al* [10] showed that the strain fields associated with the lattice-matched superlattice interlayers are effective in leading dislocation lines out toward the edges of the crystal. These superlattices may also prevent dislocation movement in device operation.

GaAs is grown on silicon using GaAs/$Ga_{0.49}In_{0.51}P$ superlattices as buffer layers in order to decrease the mismatch dislocations [30]. They consist of ten periods, 20 Å (GaAs) and 40 Å (GaInP). The superlattices are introduced to prevent the propagation of the dislocations present at the GaAs/Si interface. The GaAs top layer is grown at 550°C with a growth rate of 100 Å min^{-1}.

Figures 6.2 and 6.3 show the typical optical and crystallographic properties of the 0.6 μm thick GaAs epilayer. The $T = 77$ K photoluminescence intensity is as high as that for GaAs grown simultaneously on a GaAs substrate (see figure 6.2). The full width at half maximum (FWHM) is about 20 meV.

The GaAs epilayer has the same (1 0 0) orientation as that of the substrate. Figure 6.3 shows the double x-ray diffraction spectrum of this layer. The good crystallinity of the GaAs is shown by the relatively narrow linewidth ($\simeq$ 150 arcsec).

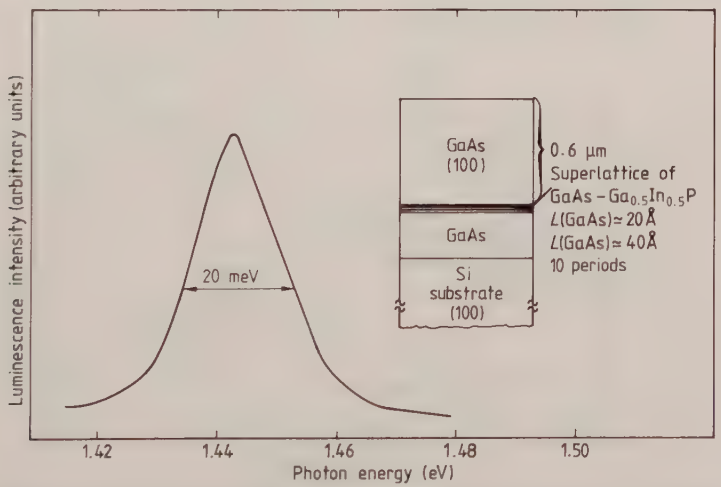

Figure 6.2 Photoluminescence spectrum at $T = 77$ K of bulk GaAs grown on Si, using GaAs–$Ga_{0.49}In_{0.51}P$ superlattices as buffer layers.

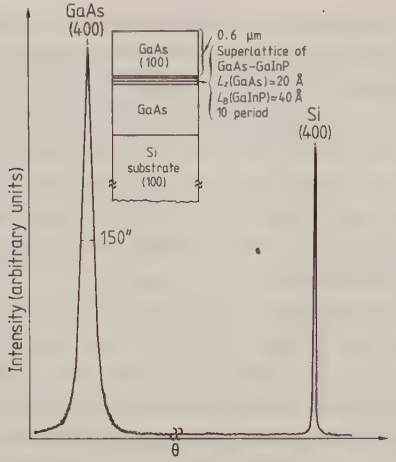

Figure 6.3 Double x-ray diffraction pattern of GaAs grown on Si using GaAs–$Ga_{0.49}In_{0.51}P$ superlattices as a buffer layer.

6.3 InP GROWN ON Si

For the growth of InP on Si Razeghi *et al* [18] used the same preparation and heating for the Si substrate. A thin (≈ 500 Å) layer of GaAs is first directly grown on the silicon substrate. A GaInAsP/InP superlattice is then deposited, to prevent the propagation of misfit dislocations. The InP layer is finally grown at a temperature of 550°C.

The electrochemical profile of such a structure is detailed in figure 6.4.

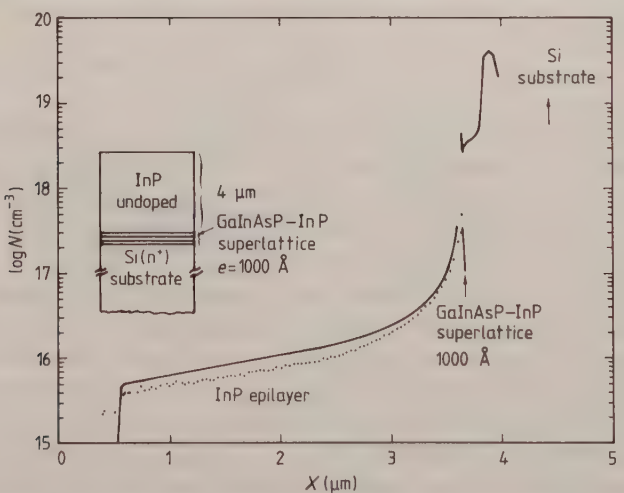

Figure 6.4 Typical electrochemical profile of an InP epilayer grown on Si substrate.

Note that InP has a low n-type residual doping level, about 5×10^{15} cm^{-3}. Measurements in the dark (dotted curve) and illumination (full curve) give essentially the same results, indicating that almost no deep traps are present in the layer. The $T = 2$ K photoluminescence spectrum of a 1.5 μm thick undoped InP layer grown on Si substrate is shown in figure 6.5, together with the corresponding electrochemical profile. The intrinsic (or shallow donor related) peak appears at about 1410 meV, which is 13 meV lower than the low-temperature gap for unstrained InP. The lattice mismatch existing between InP and Si seems to indicate that some strain is present in the layer. The peaks at 1370 and 1326 meV are believed to be due to an electron–neutral acceptor recombination (e–A^0) with an associated one-phonon replica. Extrinsic recombinations attributed to shallower impurities or defect-related excitons appear between 1380 and 1405 meV. Their precise origin is not clearly understood.

The excellent crystallographic properties of the same InP epilayer are shown in the simple crystal diffraction pattern of the structure (figure 6.6). The profile of the InP-related signal appears to be nearly equivalent to that of the Si substrate.

Razeghi *et al* [20] studied the problem of Si autodoping in the following way. InP was grown on a silicon substrate using different buffer layers:

(*a*) a simple GaAs layer;
(*b*) a GaAs/GaInP superlattice; and
(*c*) a GaInAsP/InP superlattice.

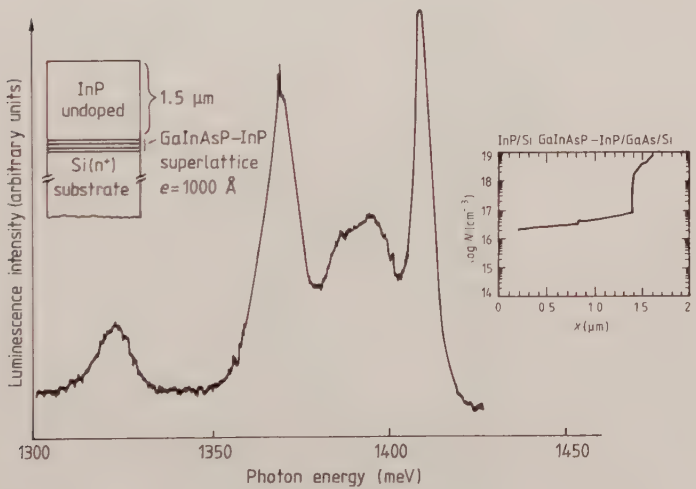

Figure 6.5 Low-temperature PL spectrum of undoped InP grown on Si. The excitation power is around 0.8 W cm^{-2} (642.8 nm). The electrochemical profile of this layer is shown in the inset.

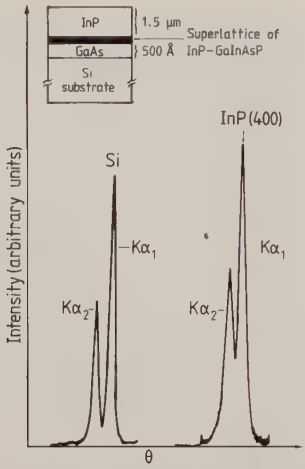

Figure 6.6 X-ray rocking curve of InP grown on Si.

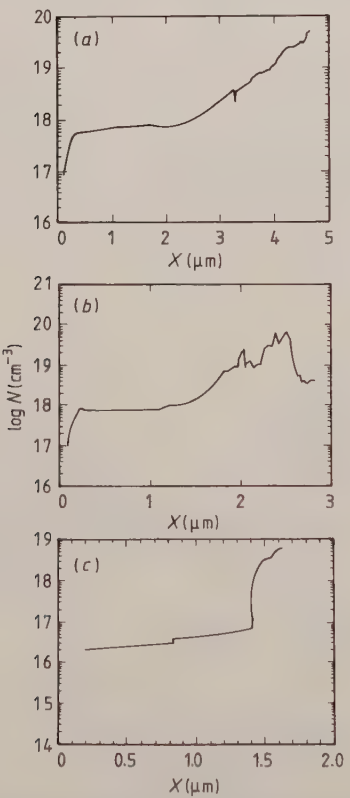

Figure 6.7 Electrochemical profile of InP on Si substrate using different buffer layers: (*a*) GaAs, (*b*) GaAs–$Ga_{0.49}In_{0.51}P$ superlattice, (*c*) GaInAsP–InP superlattice.

They measured the electrochemical profile of a nominally undoped InP layer, following procedures (*a*), (*b*) and (*c*).

In case (*a*) the observed doping interface is very large and has a thickness of about 2 μm, indicating that Si has efficiently diffused through the InP epilayer during growth. For case (*b*) the doping interface between the Si substrate and the InP layer has decreased to 0.5 μm, thus indicating that the GaAs/GaInP superlattice acts as an efficient blocking layer for Si diffusion.

Case (*c*) shows a very abrupt doping interface between Si and InP, with a thickness of less than 500 Å. Thus it seems that the InP/GaInAsP superlattice prevents Si diffusion and cross doping (see figure 6.7).

SIMS measurements were performed on sulphur-doped (2×10^{18} cm^{-3}) InP layers grown simultaneously on InP, GaAs and Si substrates, using GaAs/GaInP superlattices as buffer layers (figure 6.8). Figure 6.8 shows no evidence of silicon substrate doping by P and As, because the growth

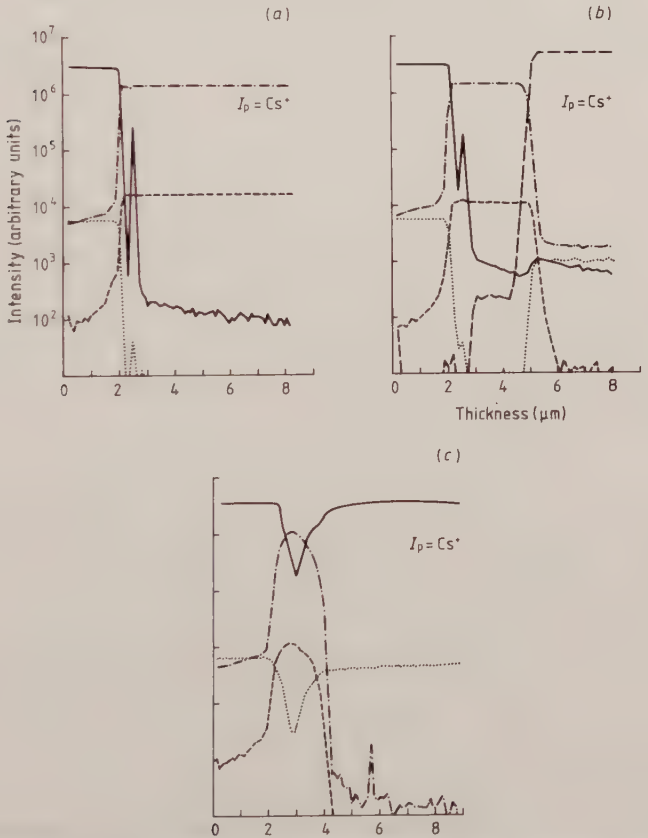

Figure 6.8 SIMS profile of an InP layer grown simultaneously on (*a*) GaAs, (*b*) Si and (*c*) InP substrates: ·····, In; ———, P; —·—, As; ---, Ga; ———, Si.

temperature is low enough to avoid the deterioration of the Si substrate. This is an excellent result in view of monolithic integration of III–V compounds on Si substrate.

The 20 K photoluminescence spectrum of the InP layers doped with S on Si substrate shows [29] a full width at half maximum of about 28 meV, a value essentially the same as that for InP layers grown simultaneously on GaAs and InP substrates (figure 6.9). However, the InP/Si PL peak is shifted to a lower energy by 15 meV relative to the InP/InP PL, indicating that some strain is present in the InP/Si layer.

6.4 GaInAsP–InP GROWN ON Si

Because of the application of long-wavelength components, especially 1.3 and 1.5 μm lasers, quaternary compounds $Ga_xIn_{1-x}As_yP_{1-y}$ ($0 \leqslant x \leqslant 0.47$ and $0 \leqslant y \leqslant 1$) lattice-matched to InP have become very important materials for the optoelectronic industry, and it would be of great interest to combine these materials with Si technology [29].

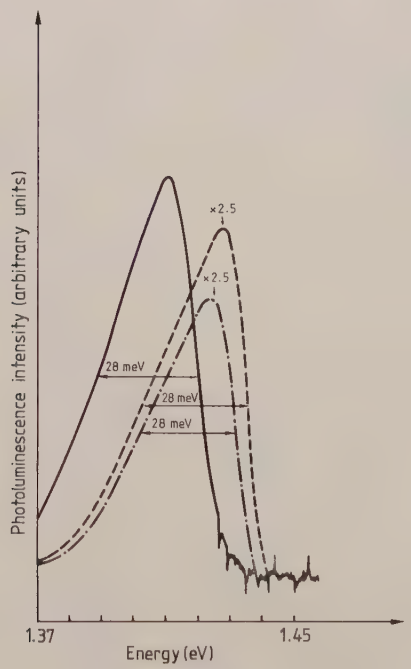

Figure 6.9 PL spectrum at $T = 20$ K of the InP/GaAs–$Ga_{0.49}In_{0.51}P$ structure grown on InP (—·—), GaAs (---) and Si (——) substrates. The excitation power of the 632.8 nm He–Ne laser is around 0.8 W cm^{-2}.

The lattice parameter of the quaternary compounds with a composition $Ga_xIn_{1-x}As_yP_{1-y}$ is given by Sharma and Purohit [21]:

$$a(x, y) = a(\text{GaAs})xy + a(\text{InAs})(1 - x)y + a(\text{GaP})x(1 - y) + a(\text{InP})(1 - x)(1 - y).$$

The coefficient of linear thermal expansion, $\alpha(xy)$, of the quaternary compound may also be calculated using Vegard's law:

$$\alpha(x, y) = [\alpha(\text{GaAs})a(\text{GaAs})xy + \alpha(\text{InAs})a(\text{InAs})(1 - x)y + \alpha(\text{GaP})a(\text{GaP})x(1 - y) + \alpha(\text{InP})a(\text{InP})(1 - x)(1 - y)]/a(x, y).$$

The thermal expansion coefficient of GaP is 5.3×10^{-6}, InAs is 5.16×10^{-6}, InP is 4.56×10^{-6}, GaAs is 6.8×10^{-6} and Si is $2.6 \times 10^{-6}\,K^{-1}$. The difference between the mean linear coefficients of thermal expansion of InP and Si is less than the difference between those of GaAs and Si. In addition, the deposition temperatures for MOCVD growth of GaInAsP–InP are typically 550°C, whereas MOCVD GaAlAs–GaAs layers are grown at 750°C. As a result of the lower thermal expansions and the lower growth temperature, the thermally-induced stress in GaInAsP–InP/Si films due to cooling from the growth temperature is less than for GaAs–GaAlAs/Si layers of comparable thickness.

The preliminary results for GaInAsP–InP/Si lasers [10] show that the solution to the problem of degradation of GaAlAs–GaAs/Si lasers is to use instead GaInAsP–InP/Si lasers. It is known that InP-based long-wavelength lasers are more 'immune' to the deleterious effects of stress than are GaAs-based lasers [22, 23]. As a result, the lifetime of heteroepitaxial GaInAsP–InP lasers grown on Si substrates may be longer than that of GaAlAs–GaAs/Si lasers, although the lattice mismatch of InP/Si is 8% compared to 4% for GaAs/Si.

A double $InP/Ga_{0.25}In_{0.75}As_{0.5}P_{0.5}$ heterostructure has also been grown on a silicon substrate. Figure 6.10 shows the global structure of the layer. The growth was initiated with a 1000 Å GaAs–GaInP buffer layer, followed by 2 μm InP. The $Ga_xIn_{1-x}As_yP_{1-y}$ active layer is about 2000 Å thick. The single diffraction pattern in figure 6.10(*a*) shows the good crystallographic quality of the InP/GaInAsP/InP structure. The $K\alpha_1$ and $K\alpha_2$ peaks also appear to be very well resolved. The GaAs buffer layer remains very thin, so its related signal is difficult to detect. Nevertheless, $K\alpha_1$ and $K\alpha_2$ are separated, even when the epilayer lies near the silicon substrate. The quaternary compound has a wavelength of 1.3 μm. The 300 K photoluminescence spectrum in figure 6.10(*b*) shows the good optical properties of the quaternary. The recombination peak is situated at the expected energy, with a full width at half maximum of 55 meV, which can be

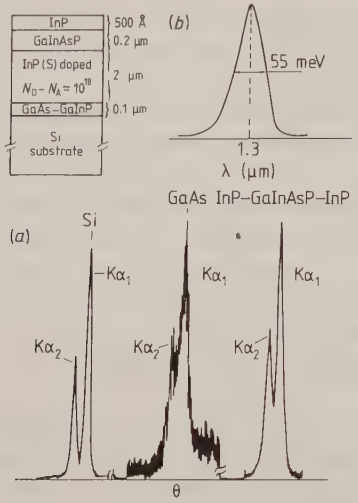

Figure 6.10 (*a*) X-ray diffraction pattern of the double heterostructure InP–GaInAsP–InP on Si; (*b*) 300 K PL spectrum of this sample.

favourably compared with that of the same structure grown on InP substrates.

In addition, a structure with an InP/GaInAsP superlattice as its buffer layer was also studied. The layers are composed as follows:

(1) 500 Å undoped GaAs;

(2) five periods InP–$Ga_{0.25}In_{0.75}As_{0.5}P_{0.5}$ superlattice with barriers of 50 Å and wells of 50 Å;

(3) 3 μm InP sulphur-doped with $N_D - N_A = 2 \times 10^{18}$ cm^{-3} as an n-type confinement layer;

(4) 0.2 μm GaInAsP ($\lambda = 1.3$ μm) as an active layer;

(5) 1 μm InP zinc-doped with $N_A - N_D = 5 \times 10^{17}$ cm^{-3} as a p-type confinement layer; and

(6) 0.5 μm $Ga_{0.47}In_{0.53}As$ zinc-doped with $N_A - N_D = 10^{19}$ cm^{-3} as a contact layer.

The quality of the structure was first derived from its (400) double x-ray diffraction pattern (see figure 6.11). The full width at half maximum (FWHM) of the 400 reflection peak of the epilayer appears only eight times higher than that of the silicon substrate. Transmission electron microscopy (TEM) shows that the superlattice blocking layer prevents most of the dislocations (figure 6.12). Since the InP confinement layer seems to have no dislocations, one can conclude that there are less than 10^5 cm^{-2}, corresponding to the TEM resolution. The optical quality of the quaternary compound active layer was derived by photoluminescence spectra at

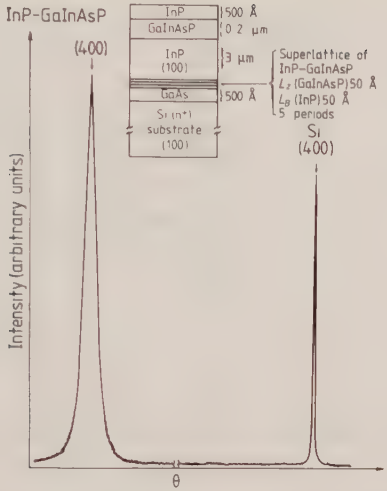

Figure 6.11 Double x-ray diffraction pattern of GaInAsP–InP DH laser on Si substrate.

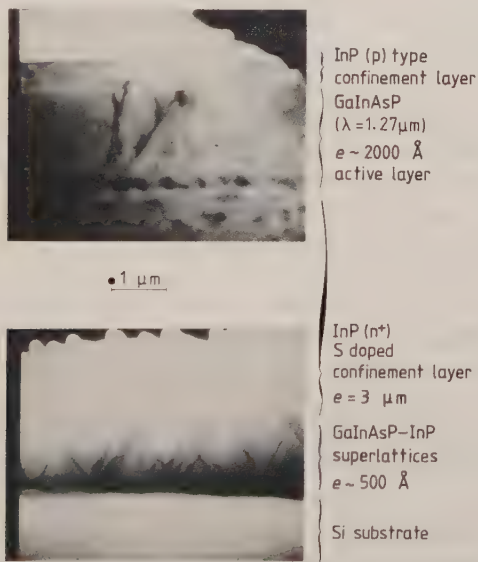

Figure 6.12 TEM cross section of GaInAsP–InP DH laser on Si substrate.

$T = 300$ and 4 K, recorded on a structure with GaInAsP covered by only 500 Å InP. The typical room-temperature photoluminescence spectrum of this layer shows the expected wavelength of GaInAsP of 1.3 μm, with FWHM of about 55 meV, which can be favourably compared with that

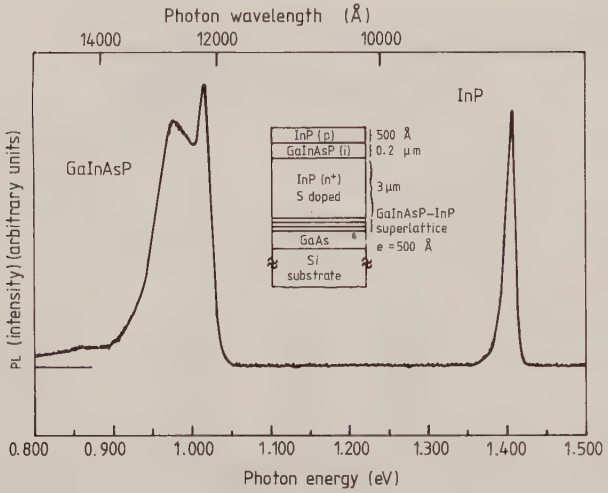

Figure 6.13 4 K PL spectrum of GaInAsP–InP DH laser on Si substrate.

of the same structure grown on an InP substrate. The $T = 4$ K photoluminescence of the structure is shown in figure 6.13. Two different peaks corresponding to extrinsic (975 meV) and intrinsic (1010 meV) recombination in the quaternary compound were noted. Their origins were then confirmed by plotting their respective intensities as a function of the excitation power of the laser. The acceptor ($e-A^0$) related peak saturated, while the other peak linearly increased with the excitation power, as expected from extrinsic and intrinsic recombination.

6.5 APPLICATIONS

6.5.1 Room-temperature CW operation of a GaInAsP/InP ($\lambda = 1.15$ μm) light-emitting diode on silicon substrate

The epitaxial structure was grown by MOCVD on (1 0 0) silicon n^+ substrate misoriented 4° off towards (1 1 0). The growth procedure has been described in §6.4. The structure of the devices includes:

(*a*) 1000 Å GaAs–GaInP superlattice undoped as buffer layer;
(*b*) 2 μm InP sulphur-doped as n-type confinement layer;
(*c*) 2000 Å GaInAsP ($\lambda = 1.15$ μm) undoped active layer;
(*d*) 500 Å InP zinc-doped as p-type confinement layer.

Figure 6.14 shows the room-temperature photoluminescence spectrum of this layer, as well as its double x-ray diffraction pattern. The photolumines-

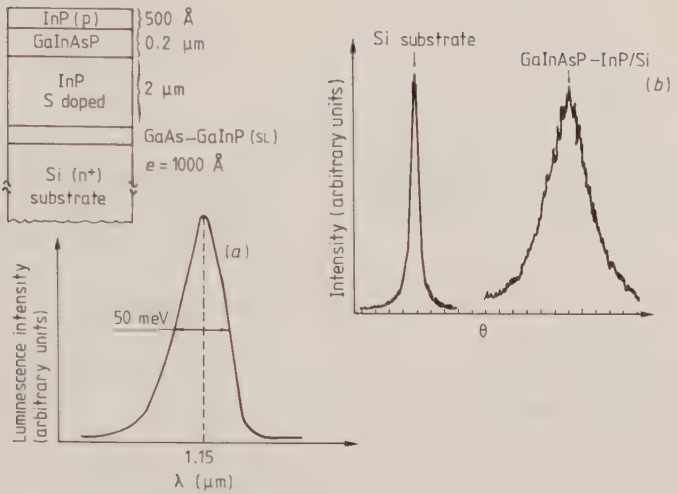

Figure 6.14 (*a*) Room-temperature photoluminescence spectrum of a double heterostructure InP/GaInAsP ($\lambda = 1.15\ \mu m$) grown on silicon substrate by MOCVD. (*b*) X-ray double diffraction pattern of an InP/GaInAsP ($\lambda = 1.15\ \mu m$) heterostructure grown on silicon substrate by MOCVD.

cence (PL) showed a composition of $\lambda = 1.15\ \mu m$ as expected. It exhibits a full width at half maximum of about 50 meV. The PL intensity is ten times lower than high-quality GaInAsP of the same composition grown on InP substrate. Furthermore, the FWHM of the (400) InP reflection peak is only six times that of the Si(400), demonstrating the good crystallographic quality of the epilayer.

Using this structure (figure 6.15(*a*)), Razeghi *et al* [24] have prepared stripes of $1\ \mu m$ width by using photolithography followed by chemical etching. The stripe-to-stripe spacing is about $300\ \mu m$, as shown in figure 6.15(*b*).

In the second growth step, the stripes were covered with $1\ \mu m$ InP Zn-doped as a p-type confinement layer and $0.5\ \mu m$ thick $Ga_{0.47}In_{0.53}As$ Zn-doped as p-type contact layer (see figure 6.15(*c*)).

The diodes were prepared as follows: Pt and gold metallization are used for p-type contacts and gold has been used for n-type contacts on Si substrate (figure 6.15(*d*)). Next, proton implantation was used to localize the injection current through the stripe active layers, as shown in figure 6.15(*e*)). Their length is $50\ \mu m$.

After bonding the contacts, an infrared camera was used to visualize the electroluminescence (figure 6.16). This shows light coming out from both diode sides. These diodes were placed under continuous wave operation for 24 h, with an injection current of 200 mA. No degradation was observed.

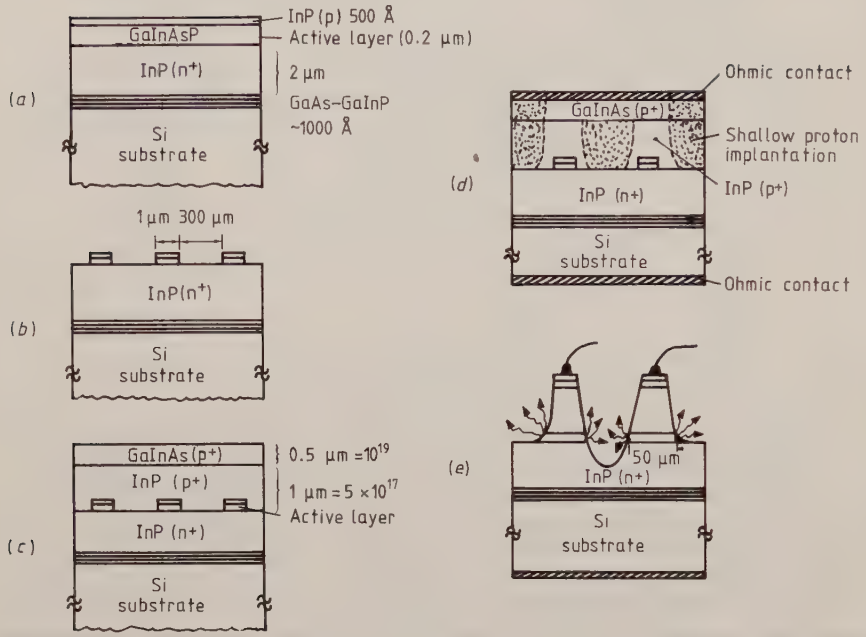

Figure 6.15 Successive technological steps for fabricating a light-emitting diode on a Si substrate.

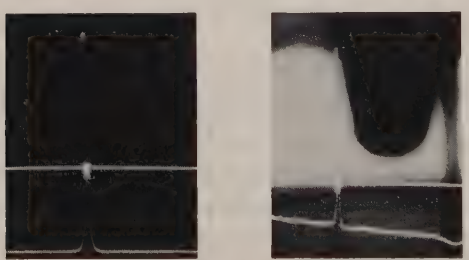

Figure 6.16 Electroluminescence of the InP–GaInAsP ($\lambda = 1.15\ \mu m$) heterostructure grown on a Si substrate.

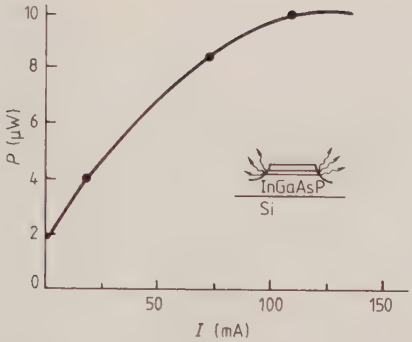

Figure 6.17 Output power against injected current of a stripe-buried heterostructure InGaAsP on Si under CW operation.

Figure 6.17 shows the output power against injection current in continuous wave operation of this stripe-buried heterostructure GaInAsP/InP on an Si substrate.

6.5.2 GaInAsP/InP double heterostructure laser emitting at 1.3 μm on Si

The structure of this device is as follows:

(*a*) Five periods InP/$Ga_{0.25}In_{0.75}As_{0.5}P_{0.5}$ superlattice with an InP thickness of 50 Å and a GaInAsP thickness of 50 Å, for elimination of mismatch dislocations;
(*b*) 3 μm InP S-doped with $N_D - N_A \simeq 10^{18}$ cm^{-3} as an n-type confinement layer;
(*c*) 0.2 μm $Ga_{0.25}In_{0.75}As_{0.5}P_{0.5}$ undoped active layer;
(*d*) 1 μm InP Zn-doped ($N_A - N_D \simeq 5 \times 10^{17}$ cm^{-3}) as a p-type confinement layer;
(*e*) 0.5 μm $Ga_{0.47}In_{0.53}As$ Zn-doped ($N_A - N_D \simeq 10^{19}$ cm^{-3}) as cap layer.

Figure 6.18 shows the electrochemical polaron profile of this structure.

Transmission electron microscopy (TEM) shows the elimination of most dislocations by superlattices of GaInAsP–InP at the interfaces (figure 6.12). Photoluminescence, photoluminescence excitation and double x-ray diffraction show high-quality GaInAsP material. Figure 6.19 shows the SIMS spectrum of this structure.

Gain-guided oxide-defined stripe-geometry lasers were fabricated as follows (see figure 6.20). The injected current profile is defined by a self-aligned technique: Au–Zn is evaporated on the GaInAs cap layer through a photoresist mask, a selective etching is then done of the contact layer and subsequently Al_2O_3 is deposited, and lift-off is realized. After

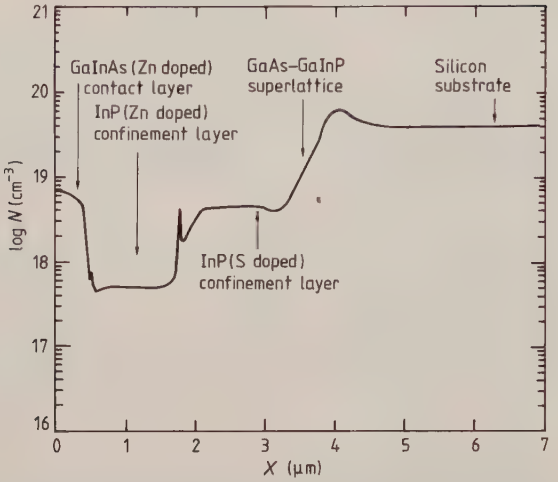

Figure 6.18 Electrochemical polaron profile of a GaInAsP–InP DH laser on Si.

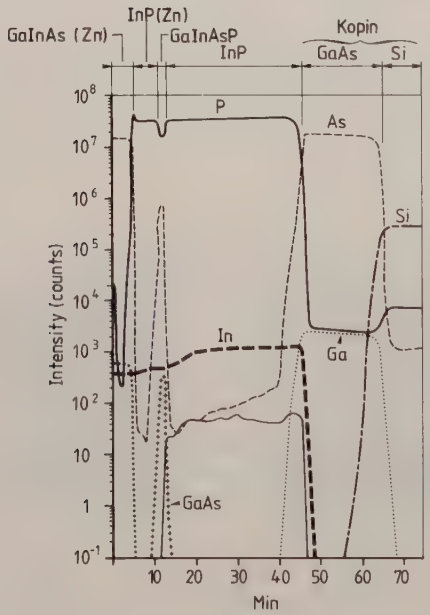

Figure 6.19 SIMS spectrum of a GaInAsP–InP DH laser on a Si substrate.

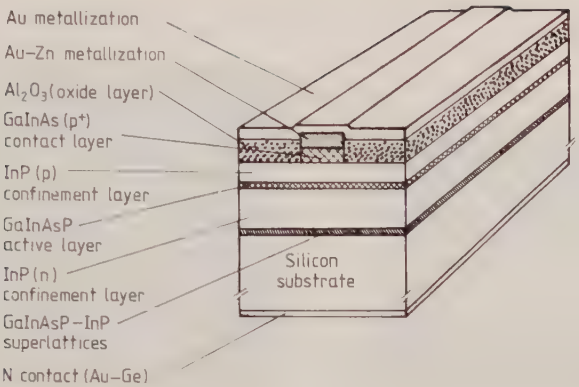

Figure 6.20 Oxide-defined stripe geometry of a GaInAsP–InP DH laser on a Si substrate.

annealing Au–Zn (at $T = 420^{\circ}C$ for 10 s), the silicon substrate is lapped down to 50 μm thickness and Au–Ge is evaporated. The wafer is then cleaved in bars along the (1 1 0) direction, which is a cleavage plane of InP but not of the Si substrate.

Figure 6.21(*a*) shows a typical top view of a wafer cleaving in bars. The cleaved facet of the stripe laser region is presented in figure 6.21(*b*). The interface between the InP and the Si substrate is delineated on this photograph by a continuous line due to different crystal parameters.

Figure 6.22 shows the light–current characteristic in pulse operation of a laser with a cavity length of 250 μm and a stripe width of 12 μm. Measurements show a threshold current $I_{th} = 510$ mA with a differential quantum efficiency $\eta_D = 10\%$ per face and an output power up to 20 mW per facet. Threshold current density for these devices is about $J_s \approx 10\ \text{kA cm}^{-2}$. The improvement in the quality of the epitaxial layers and laser structures will lead to a lower threshold current density and a higher differential efficiency.

The inset of figure 6.22 of the spectral output of these devices shows power output levels of 4 mW using driving pulses of 50 ns at 5 kHz. The behaviour of the lasing spectra as a function of output power is similar to that obtained on InP substrates having a gain-guided structure.

Preliminary ageing tests were run in pulse conditions at room temperature. After an equivalent CW ageing time of 80 s (under driving pulses of 50 ns at 5 kHz), an increase of threshold current $\Delta I_{th}/I_{th} = 7\%$ is measured at an output power of 3 mW, with no degradation of the differential quantum efficiency. Such a rapid increase of threshold current may be due to the mismatch dislocation between the GaInAsP active layer and InP confinement layer. These results are very promising compared to ageing tests of GaAs lasers on silicon [25].

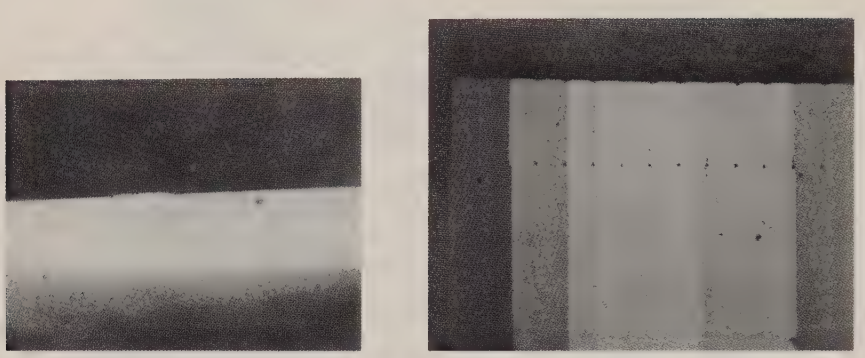

Figure 6.21 (*a*) Top view of the wafer GaInAsP–InP DH laser on Si substrate cleaving in bars. (*b*) The cleaved facet of the stripe laser region.

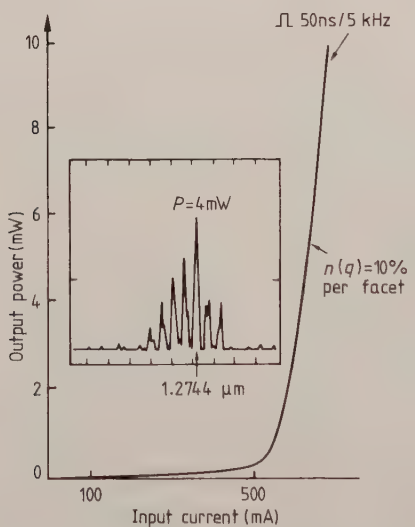

Figure 6.22 Typical characteristics of light output–current input of a GaInAsP–InP DH laser on Si. Inset: spectral output of a gain-guided oxide-defined stripe geometry GaInAsP–InP DH laser on a Si substrate at a power output level of 4 mW.

6.5.3 CW operation of a $Ga_{0.25}In_{0.75}As_{0.5}P_{0.5}$/InP BRS laser on silicon substrate

Figure 6.23 shows a schematic diagram of a $Ga_{0.25}In_{0.75}As_{0.5}P_{0.5}$–InP buried ridge structure (BRS) laser on Si substrate. The structure of devices includes:

(*a*) 1 μm undoped GaAs as a buffer layer;
(*b*) five periods $Ga_{0.47}In_{0.53}As$–InP superlattice with an InP thickness of 100 Å and a GaInAs thickness of 100 Å for decreasing the mismatch dislocations;
(*c*) 3 μm InP S-doped with $N_D - N_A = 10^{18}$ cm^{-3} as an n-type confinement layer;
(*d*) 0.2 μm undoped $Ga_{0.25}In_{0.75}As_{0.5}P_{0.5}$ active layer;
(*e*) 0.1 μm Zn-doped InP with $N_A - N_D = 2 \times 10^{17}$ cm^{-3} as a p-type confinement layer.

The growth temperature was 550°C, with a growth rate of 100 Å min^{-1} for InP, 150 Å min^{-1} for GaInAsP and 200 Å min^{-1} for GaInAs.

The double x-ray diffraction pattern of this structure is shown in figure 6.24. The FWHM of the (400) InP–GaInAsP reflection peak is only about 250 arcsec, evidence for the good crystallinity of the InP–GaInAsP layer grown on Si substrate.

Next the stripes of 2 μm width and stripe–stripe spacing of 350 μm were etched in the 1000 Å InP + 2000 Å GaInAsP active layer through a photolithographic resist mask, followed by chemical etching.

In the next step, after removing the resist mask, the stripes were then covered by a 1 μm thick Zn-doped InP confinement layer (with $N_A - N_D = 5 \times 10^{17}$ cm^{-3}) and a 0.5 μm Zn-doped $Ga_{0.47}In_{0.53}As$ contact layer with $N_A - N_D = 10^{19}$ cm^{-3}. In order to localize the injection in the

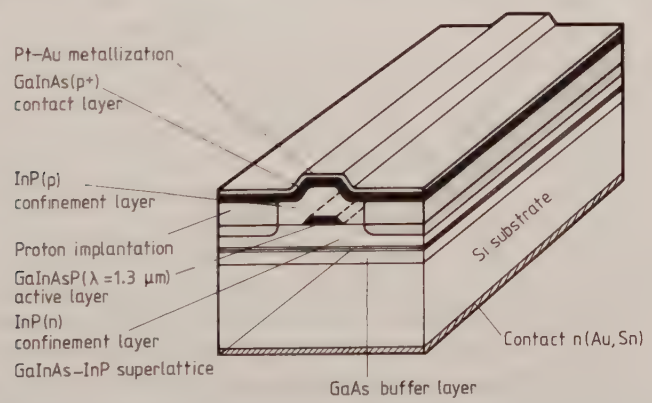

Figure 6.23 Schematic diagram of a GaInAsP–InP BRS laser on a Si substrate.

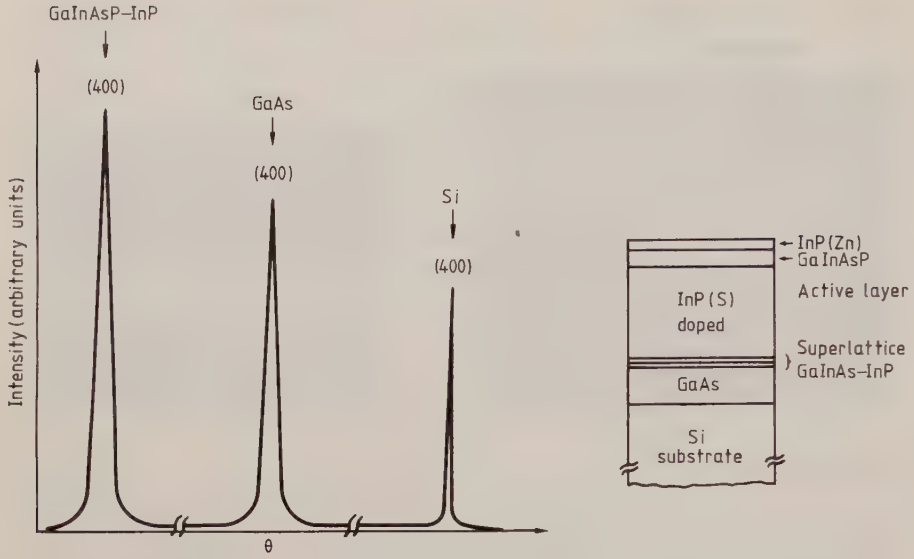

Figure 6.24 Double x-ray diffraction of a GaInAsP–InP BRS laser on Si.

active region, a shallow proton implantation was realized through a 5 μm width photoresist mask after the metallization of the contacts.

Pt and Au are used for the p-type contact, and Au/Sn is used for the n-type contact on the Si substrate. The wafer is then cleaved in bars along the (1 1 0) direction which is a cleavage plane of InP but not of the Si substrate.

After cleaving and scribing into chips 200 μm long and 350 μm wide, the diodes are bonded with In to an Au-plated copper heat sink.

Figure 6.25 shows the light–current characterization under CW operation of a BRS laser with a cavity length of 200 μm and a stripe width of 2 μm. Threshold current $I_{th} = 80$ mA with $\eta(q) = 16\%$ per face, and an output power of 20 mW under CW operation at room temperature have been measured. The inset of figure 6.25 shows the spectral output of these devices at power output levels of 2 mW under CW operation.

On these lasers, a value of $T_0 = 61\,^{\circ}\mathrm{C}$ has been measured. The best threshold current obtained on this structure is $I_{th} = 45$ mA which corresponds to a threshold current density $J_{th} \leqslant 4\ \mathrm{kA\,cm^{-2}}$ (see figure 6.26).

A preliminary ageing test has been processed in CW operation at room temperature, with an injection current of 94 mA corresponding to an output power of 2 mW per facet. The inset of figure 6.26 shows the typical driving current as a function of the ageing time for this device. An increase of the injected current of less than 10% is observed after 10 h ageing time without any decrease in differential quantum efficiency.

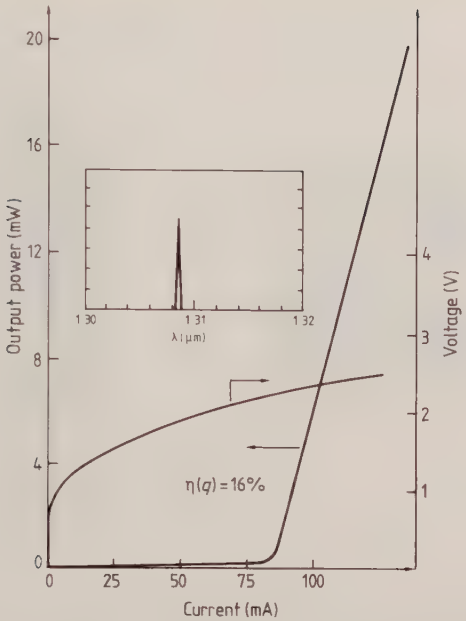

Figure 6.25 Light output–current input of a GaInAsP–InP BRS on a Si substrate under CW operation. Inset: spectral output of this BRS laser at an output power of 2 mW.

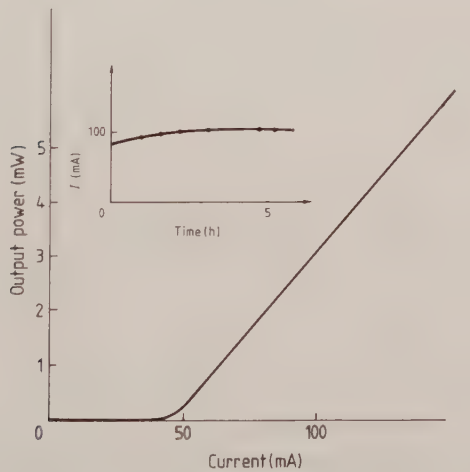

Figure 6.26 Light output–current input before and after ageing test. Inset: typical ageing characteristics of a GaInAsP–InP BRS laser on Si substrate.

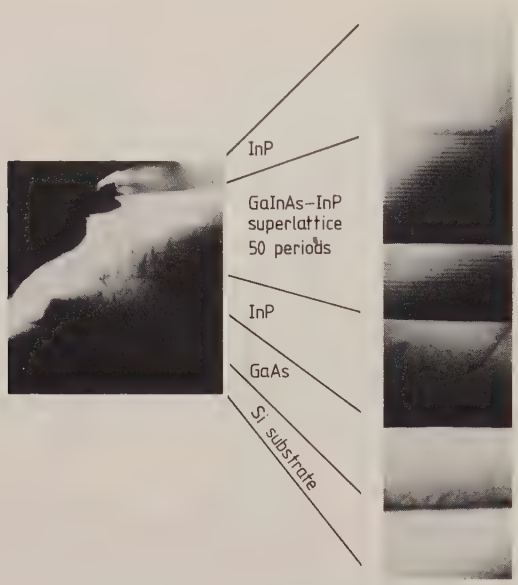

Figure 6.27 Scanning electron transmission micrograph of a GaInAs–InP MQW layer for a 1.5 μm waveguide grown by MOCVD on a Si substrate.

6.5.4 InGaAs–InP MQW on Si substrate

The use of GaInAs–InP multiquantum well (MQW) layers for optical waveguides has been a subject of much interest especially in regard to excitonic dielectric and absorption properties. Figure 6.27 shows the scanning electron transmission micrograph of the GaInAs–InP MQW layers for 1.5 μm waveguides grown by MOCVD on a Si substrate. The structure includes:

(*a*) 1 μm GaAs on Si substrate as a buffer layer [26];
(*b*) 1 μm undoped InP as a confinement layer;
(*c*) 50 GaInAs quantum well layers 30 Å thick, separated by 300 Å InP thick barriers;
(*d*) 1.5 μm InP undoped as a confinement layer;
(*e*) 1 μm InP Zn-doped;
(*f*) 0.5 μm GaInAs Zn-doped as a contact layer.

Most of the dislocations are eliminated by superlattices. The excellent quality of the epilayers is confirmed by the single diffraction pattern of the structure: the $K\alpha_1$ and $K\alpha_2$ components of the (400) reflection peak of Si, GaAs and $InP/Ga_{0.47}In_{0.53}As$ are clearly separated. Near the $InP/Ga_{0.47}In_{0.53}As$ related peak, satellites due to the superperiodicity of the

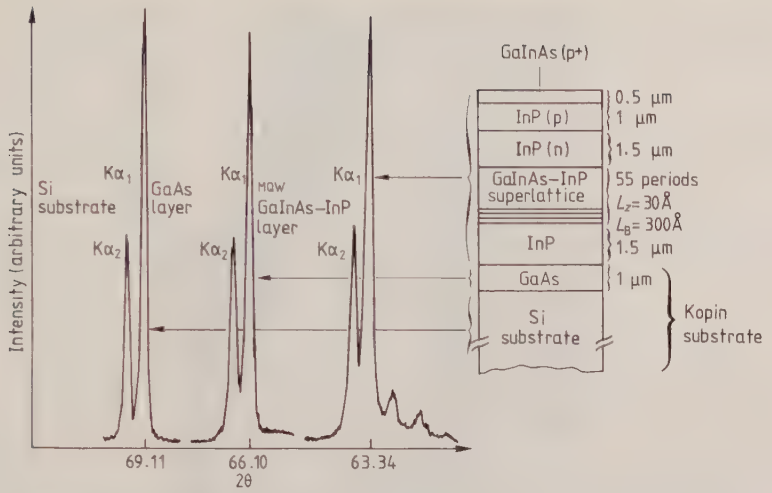

Figure 6.28 Single diffraction pattern of a GaInAs–InP MQW layer for a 1.5 μm waveguide grown by MOCVD on a Si substrate.

55-period superlattice are evidenced. They establish the perfect thickness control of the barriers and the wells in the superlattices (see figure 6.28).

6.5.5 GaInAs–InP PIN photodetector

Razeghi *et al* [27] fabricated a GaInAs–InP PIN photodetector on Si. The growth was carried out in two separate steps. First, 1 μm undoped GaAs with $N_D - N_A = 10^{14}$ cm^{-3} was grown on the (100) 4° off n-type Si substrate [26]. Figure 6.29 shows the transmission electron microscope cross section of the GaAs on the Si substrate used for this structure; most of the dislocations are stopped at the interface.

Then the InP–GaInAs–InP undoped layers were deposited on the GaAs/Si layer as follows:

(*a*) an InP buffer layer 1 μm thick;
(*b*) a GaInAs absorption layer 4 μm thick;
(*c*) an InP window layer 1 μm thick (in order to enhance the responsivity in the near-infrared spectrum beyond 0.9 μm).

The background impurity concentration deduced from a polaron electrochemical profile was found to be 2×10^{15} and 8×10^{14} cm^{-3} for GaInAs and InP, respectively.

The growth temperature is 520°C and the growth pressure 76 Torr. Figure 6.30 shows the double x-ray diffraction pattern of this GaInAs–InP PIN photodetector on a Si substrate, evidencing the good crystallinity of the GaInAs–InP–GaAs layer grown on the Si substrate.

Figure 6.29 Scanning electron microscope pattern of a GaAs layer on a Si substrate (Kopin material).

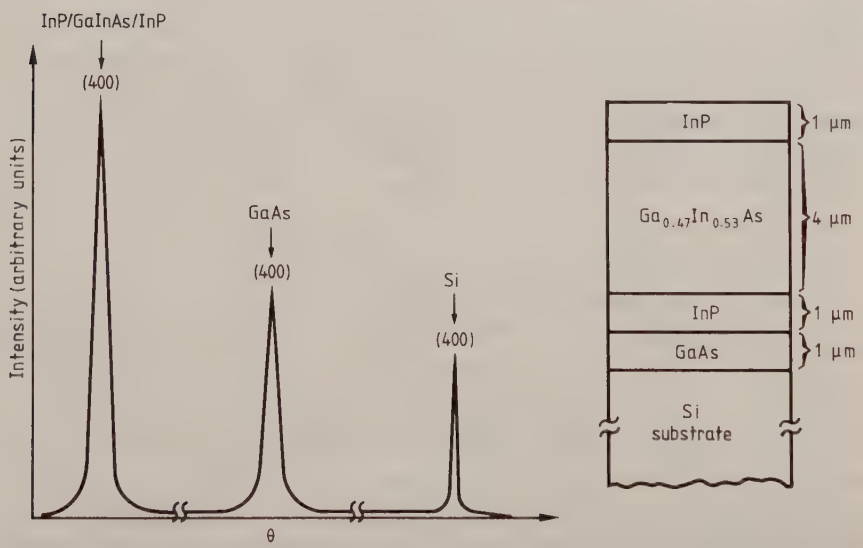

Figure 6.30 Double x-ray diffraction pattern of InP–GaInAs–InP–GaAs on silicon substrate.

The pn junction was formed next by Zn diffusion using the semiclosed box technique, it being located through the InP window in the GaInAs layer (see figure 6.31), using a SiO_2 mask.

The ohmic contacts are made by sputtered Au–Zn alloyed at 450°C for 30 s and then covered with Cr–Au on the p side, and by sputtered Au on the n side (Si substrate) (figure 6.31).

Figure 6.32 shows a photograph of the GaInAs–InP PIN photodiode on Si substrate. Diodes with a diameter of 250 μm have been fabricated. Table 6.2 shows the characteristics of these devices compared with those grown on InP substrates.

Figure 6.33 shows the capacitance–voltage characteristic of the device. The capacitance of the device is low, evidencing the low carrier concentration of the GaInAs layer. For a good receiver performance, capacitance must be low. For PINFET optical receivers the capacitance should be $\leqslant 0.50$ pF, a figure which could be obtained by reducing the junction area. The thickness of the active region of a PIN photodiode is the result of a trade-off between the competing effects of fast transit time requiring a narrow depletion region and the combination of quantum efficiency and low capacitance which requires a wide depletion region. The thickness of the GaInAs active layer of this device is 4 μm, so the responsivity and quantum efficiency are high. Quantum efficiency is the first consideration in a photodiode (i.e. the effective collection of photogenerated carriers by a depleted volume).

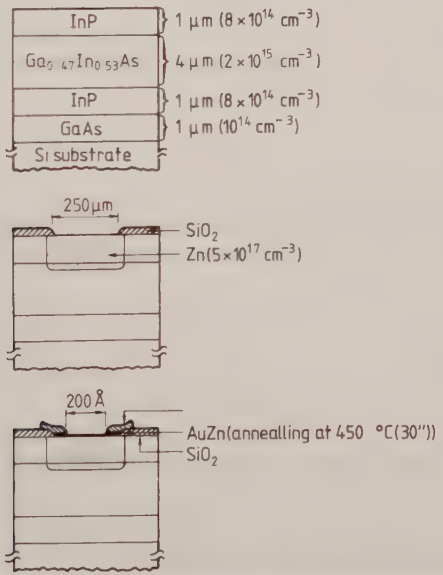

Figure 6.31 Successive technological steps for fabricating a GaInAs–InP PIN photodiode on a Si substrate.

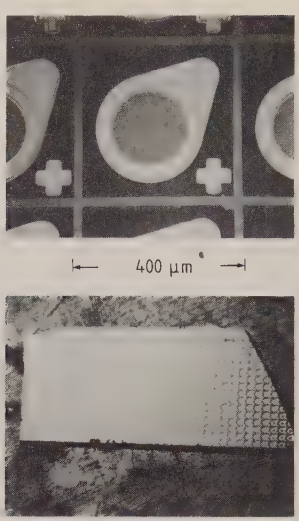

Figure 6.32 Photograph of GaInAs–InP PIN photodiode on a Si substrate.

Table 6.2 Characteristics of GaInAs–InP PIN photodetector on Si and InP substrate

	PIN GaInAs–InP on InP	PIN GaInAs–InP on Si
I_d (−1 V)	8 nA	0.5 μA
I_d (−10 V)	200 nA	100 μA
Capacitance	5 pF	5 pF
Responsivity $R = \eta \frac{q\lambda}{hC} = \eta\lambda/1.24$	with anti-reflection coating	without anti-reflection coating
at $\lambda = 0.8$ μm	0.12	0.27
at $\lambda = 1.3$ μm	0.72	0.71
at $\lambda = 1.55$ μm	0.77	0.75

The dark current of this device is high. Usually the reverse current of the device in the darkness arises from two sources: (i) a generation current in the depleted volume and minority carrier collection at the edge of the depletion region; and (ii) surface leakage.

Current generated in the diode can be kept low by using high-quality dislocation- and defect-free material and using care in processing to avoid

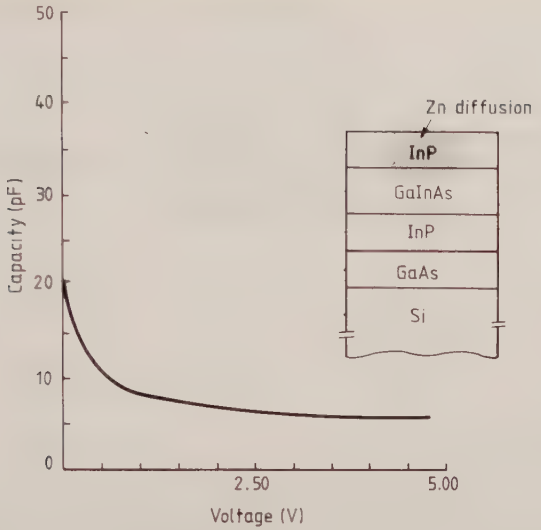

Figure 6.33 The $C(V)$ characteristics of a GaInAs–InP PIN photodiode on a Si substrate.

introducing crystalline defects. In this structure the GaAs and InP buffer layers have very low background carrier concentration (10^{14} cm^{-3}), so the depletion region extends down to the interface which contains a lot of defects and dislocations due to the lattice mismatch between InP, GaAs and the Si substrate. To reduce the dark current one has to dope GaAs and InP buffer layers by up to 10^{16} cm^{-3}.

REFERENCES

[1] Christou A, Wilkins B R and Tsang W T 1985 *Electron. Lett.* **21** 9
[2] Nishi S, Inomata H, Akiyama M and Kaminishi K 1985 *Japan. J. Appl. Phys.* **24** 6
[3] Sheldon P, Jones K M, Hayes R E, Tsaur B Y and Fan J C C 1984 *Appl. Phys. Lett.* **45** 3
[4] Soga T, Hattori S, Sakai S, Takayasu M and Umeno M 1985 *J. Appl. Phys.* **57** 10
[5] Akiyama M, Kawarada Y and Kaminishi K 1984 *J. Cryst. Growth* **68** 21
[6] Wang W I 1985 *J. Vac. Sci. Technol.* B **3** 2
[7] Aksum M I, Morloc H, Lester L F, Duh K H G, Smith P M, Chao P C, Longabone M and Erickson L P 1986 *Appl. Phys. Lett.* **49** 24
[8] Van der Ziel J P, Dupuis R D, Logan R A and Pinzone C J 1987 *Appl. Phys. Lett.* **51** 2
[9] Dupuis R D 1988 *Proc. 4th Int. Conf. on Metalorganic Chemical Vapour Phase Epitaxy, Hakone, Japan*

[10] Razeghi M, Defour M, Omnes F, Maurel Ph and Chazelas J 1988 *Appl. Phys. Lett.* **53** 725
[11] Kroemer H 1986 *Mat. Res. Soc. Symp. Proc.* **67** 3
[12] Aspnes and Ihm 1987 *Heteroepitaxy on Silicon* ed J C C Fan and J M Ponte (Pittsburgh: Materials Research Society) p 45
[13] Sakamoto T and Hashiguchi G 1986 *Japan. J. Appl. Phys.* **25** L57
[14] Akiyama M *et al* 1986 *J. Cryst. Growth* **77** 490
[15] Hull R, Fischer-Collrie A, Rasner S J, Koch S M and Harris J S 1987 *Appl. Phys. Lett.* **51** 1723
[16] Dupuis R D, Van der Ziel J P, Logan R A, Brown J M and Pinzone C J 1987 *Appl. Phys. Lett.* **50** 407
[17] Ota Y 1977 *J. Electrochem. Soc.* **124** 1795
[18] Razeghi M, Defour M, Omnes F, Maurel Ph, Bigan E, Acher O, Nagle J and Brillouet F 1988 *Proc. 4th Int. Conf. on Metalorganic Vapor Phase Epitaxy, Hakone, Japan*
[19] El-Masry N, Hamaguchi N, Tarn J C L, Kasan N, Humphreys T P, Moore D and Bedair S M 1987 *Heterostructures on Si II*, ed J C C Fan
[20] Razeghi M, Defour M, Omnes F, Nagle J, Maurel Ph, Acher O and Mijuin D 1988 *Mtg of Materials Research Society, Reno*
[21] Sharma L and Purohit R K 1974 *Semiconductor-heterojunctions* (Oxford: Pergamon) ch 4
[22] Hayashi I 1980 *Japan. J. Appl. Phys. Suppl.* **19** 23
[23] Thompson G B H 1980 *Physics of Semiconductor Laser Devices* (Chichester: Wiley) p 51
[24] Razeghi M, Blondeau R, Defour M, Omnes F and Maurel Ph 1988 *Appl. Phys. Lett.* **53** 854
[25] Van der Ziel J P, Dupuis R D, Logan R A and Pinzone C J 1987 *Appl. Phys. Lett.* **51** 89
[26] Salerno J P, Lee J W, McCullough R G and Fan J C C 1988 *Proc. MRS Spring Meeting, April 1988, Bally's Reno, Nevada*
[27] Razeghi M, Maurel Ph, Defour M, Omnes F and Acher O 1988 *Proc. 14th European Conf. on Optical Communication, Brighton*
[28] Razeghi M, Omnes F, Defour M and Maurel Ph 1988 *Appl. Phys. Lett.* **52** 209
[29] Razeghi M 1988 *Proc. Solid State Devices and Materials Conf., Tokyo* p 363
[30] Razeghi M, Maurel Ph, Omnes F and Defour M 1988 *J. Appl. Phys.* **63** 4511

Appendix Safety Information about Alkyls

This product safety information sheet is principally directed to managerial, safety, hygiene and medical personnel. The description of physical and chemical properties, human health effects and handling advice is based on experimental results and past experience. It is intended as a starting point for the development of safety and health procedures.

I. Chemical reactivity

This material catches fire if exposed to air. It reacts violently with water and compounds containing active hydrogen. It may react vigorously with compounds containing oxygen or organic halide.

II. Stability

This material is stable when stored under a dry, inert atmosphere and away from heat.

III. Fire hazard

This material is spontaneously flammable in air. It is pyrophoric by the paper char test [1] used to gauge pyrophoricity for transportation classification purposes. The products of combustion may include toxic materials.

IV. Firefighting technique

Protect against fire by strict adherence to safe operating procedures and propert equipment design.

In case of fire, immediate action should be taken to confine it. All lines and equipment which could contribute to the fire should be shut off. As in

any fire, prevent human exposure to fire, smoke, fumes or products of combustion. Evacuate non-essential personnel from the fire area.

The most effective fire extinguishing agent is dry chemical powder pressurized with nitrogen. Sand, vermiculite or carbon dioxide may be used. CAUTION—reignition may occur.

DO NOT USE WATER, FOAM, CARBON TETRACHLORIDE OR CHLOROBROMOMETHANE extinguishing agents, as this material reacts violently and/or liberates toxic fumes on contact with these agents.

When there is a potential for exposure to smoke, fumes or products of combustion, firefighters should wear full-face positive-pressure self-contained breathing apparatus or a positive-pressure supplied-air respirator with escape pack and impervious clothing including gloves, hoods, aluminized suits and rubber boots.

V. Human health

DANGER: Causes severe burns. Do not get in eyes, on skin or clothing (see 'First aid', §VI).

Ingestion
Because of the highly reactive nature of this material with air and moisture, ingestion is unlikely.

Inhalation
Because of the highly reactive nature of this material with air and moisture, inhalation is unlikely.

Skin contact
This material will react immediately with moisture on the skin to produce severe thermal and chemical burns.

Eye contact
This material will react immediately with moisture in the eye to produce severe chemical and thermal burns.

VI. First aid

If contact with this material occurs, immediately initiate the recommended procedures below. Simultaneously contact a poison centre, a physician, or the nearest hospital. Inform the person contacted of the type and extent of exposure, describe the victim's symptoms, and follow the advice given.

Ingestion
Should this material be swallowed, immediately give several glasses of water

but do not induce vomiting. If vomiting does occur, give fluids again. Have a physician determine if condition of patient will permit induction of vomiting or evacuation of stomach. Do not give anything by mouth to an unconscious or convulsing person.

Skin contact
Under a safety shower, immediately flush all affected areas with large amounts of running water for at least 15 min. Remove contaminated clothing and shoes. Do not attempt to neutralize with chemical agents. Get medical attention immediately. Wash clothing before re-use.

Eye contact
Immediately flush the eyes with large quantities of running water for a minimum of 15 min. Hold the eyelids apart during the flushing to ensure rinsing of the entire surface of the eye and lids with water. Do not attempt to neutralize with chemical agents. Obtain medical attention as soon as possible. Oils or ointments should not be used at this time. Continue the flushing for an additional 15 min if a physician is not immediately available.

Inhalation
Exposure to combustion products of this material may cause respiratory irritation or difficulty with breathing. If inhaled, remove to fresh air. If not breathing, clear the victim's airway and start mouth-to-mouth artificial respiration which may be supplemented by the use of a bag-mask respirator or manually triggered oxygen supply capable of delivering one litre per second or more. If the victim is breathing, oxygen may be delivered from a demand-type or continuous-flow inhaler, preferably with a physician's advice. Get medical attention immediately.

VII. Industrial hygiene

Ingestion
As a matter of good industrial hygiene practice, food should be kept in a separate area away from the storage/use location. Smoking should be avoided in storage/use locations. Before eating, hands and face should be washed.

Skin contact
Skin contact must be prevented through the use of fire-retardant protective clothing during sampling or when disconnecting lines or opening connections. Recommended protection includes a full-face shield, impervious gloves, aluminized Nomex [2] polyamide coat, hood and rubber boots.

Safety showers—with quick-opening valves which stay open—should be

readily available in all areas where the material is handled or stored. Water should be supplied through insulated and heat-traced lines to prevent freeze-ups in cold weather.

Eye contact
Eye contact with liquid or aerosol must be prevented through the use of a full-face shield selected with regard for use-condition exposure potential.

Eyewash fountains, or other means of washing the eyes with a gentle flow of tap water, should be readily available in all areas where this material is handled or stored. Water should be supplied through insulated and heat-traced lines to prevent freeze-ups in cold weather.

Inhalation
This material must be used in a tightly closed system. Use in an open (e.g. outdoor) or well ventilated area to minimize exposure to the products of combustion if a leak should occur. In the event of a leak, inhalation of fumes or reaction products must be prevented through the use of an approved organic vapour respirator with dust, mist and fume filter.

Where exposure potential necessitates a higher level of protection, use a positive-pressure, air-supplied respirator.

VIII. Spill handling

Make sure all personnel involved in spill handling follow proper firefighting techniques and good industrial hygiene practices (see 'Industrial hygiene,' §VII).

Any person entering either a significant spill area or an unknown concentration of fumes or combustion products should wear a positive-pressure, supplied-air respirator with escape pack.

Block off source of spill, extinguish fire with extinguishing agent—see §V. CAUTION—reignition may occur. If fire cannot be controlled with extinguishing agent, keep a safe distance, protect adjacent property and allow product to burn until consumed.

IX. Corrosivity to materials of construction

This material is not corrosive to steel, aluminium, brass, nickel or other common metals when blanketed with a dry inert gas. Some plastics and elastomers may be attacked.

X. Storage requirements

Containers should be stored in a cool, dry, well ventilated area. Store away

from flammable materials and sources of heat and flame. Exercise due caution to prevent damage to or leakage from the container.

REFERENCES

[1] Mudry, W L, Burleson D C, Malpass D B and Watson S C 1975 *J. Fire Flammability* **6** 478
[2] Registered trademark of E.I. Du Pont de Nemours & Co. Inc.

Index

Absorbtion, 85, 113
Antiphase domain, 292
Arsine, 17
Atomic layer epitaxy, 26
Auger analysis, 104, 268

Buried ridge structure laser, 215, 311
Buried waveguide, 256

Calorimetric absorption, 173
Chemical beam epitaxy, 24
Chloride atomic layer epitaxy, 26
Coupling coefficient, 237
$C - V$ method, 45
Cyclotron resonance, 140, 188

Deep level transient spectroscopy, 50, 94
Deep traps, 91
Diethylzinc, 18, 22
Diffraction, 81, 102
Diffusion, Zn, 188
Distribution feedback laser, 233, 239
Double barrier, 113
Double heterostructure laser, 205, 307

Effective mass, 32, 147
Electrochemical profile, 47
Ellipsometry, 193
Energy,
  band structure, 29
  gap, 4
Etch-pit, 52, 105, 269
Excitation spectra, 109, 112
Exciton, 82

Field effect transistor, 155, 282
Flow dynamics, 13

GaInAs, 69
GaInAsP, 165
GaInP, 276, 282
GGG (Garnet), 269

Hall mobility measurement, 47
Heterojunction, 99, 184, 290
Hole gas, 123
Hydrogen sulphide, 17
Hydrostatic pressure effect, 135

Implantation, 96
InP,
  growth and characterization, 29
  physical parameters, 10
Interfaces, 51

Landau level, 117
Laser, 205
Lattice parameter, 4
Light emitting diode, 304
Liquid phase epitaxy, 5

Magnetophonon resonance, 145
Magnetotransport, 117, 177
MESFET, 276
Metallorganic atomic layer epitaxy, 26
Metallorganic chemical vapour deposition, 8

Migration-enhanced epitaxy, 27
Modulator, 257
Molecular beam epitaxy, 7
Monolayer epitaxy, 284

Negative differential resistance, 113

Optical
  confinement factor, 252
  waveguide, 157
Opto-electronic integrated circuits (OEIC), 277
Organometallics, 18

Persistent photoconductivity, 131
Phase-locked laser, 247
Phosphine, 17
Photodetector, PIN, 153, 315
Photodiode, Schottky, 282
Photoluminescence, 37, 104, 108, 111, 171
  imaging, 225
Polaron coupling, 150

Quantum Hall effect, 117, 131, 184
Quantum well, 101, 173, 188, 314
  laser, 251
Quaternaries, 4, 165

Rayleigh number, 14
Reactor, 10
Resonnant tunnelling, 113
Reynolds number, 13

Scanning electron microscope, 235
Secondary-ion mass spectrometry, 38, 103, 266
Shubnikov–de Haas effect, 117, 181
Silane, 17
Silicon substrate, 291
Strained heterostructure, 77, 263
Substrates, 33, 169

Thermal expansion coefficient, 293
Threshold current density, 212, 215, 242
Transmission electron microscopy, 106
Triethylgallium, 18, 21
Triethylindium, 18, 21
Trimethylgallium, 18, 23
Trimethylindium, 18, 22

Vapour phase epitiaxy, 5
Vapour pressure, 20

Wavelength dispersion, 243

X-rays 81, 102, 167

3 1175 01337 0302

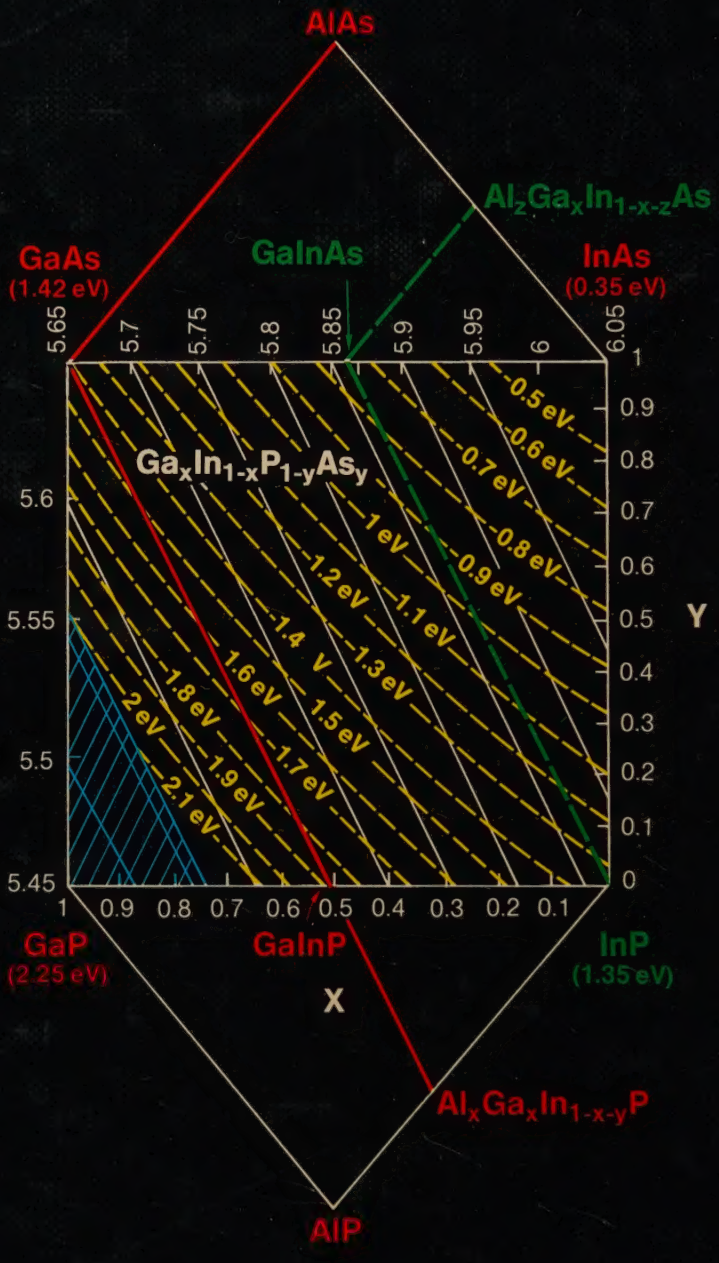
AlAs
GaAs
(1.42 eV)
GaInAs
InAs
(0.35 eV)
$Al_zGa_xIn_{1-x-z}As$
5.65
5.7
5.75
5.8
5.85
5.9
5.95
6
6.05
$Ga_xIn_{1-x}P_{1-y}As_y$
-0.5 eV
-0.6 eV
-0.7 eV
-0.8 eV
-0.9 eV
-1 eV
-1.1 eV
-1.2 eV
-1.3 eV
-1.4 V
-1.5 eV
-1.6 eV
-1.7 eV
-1.8 eV
-1.9 eV
-2 eV
-2.1 eV
5.6
5.55
5.5
5.45
Y
Y
1
0.9
0.8
0.7
0.6
0.5
0.4
0.3
0.2
0.1
0
GaP
(2.25 eV)
GaInP
InP
(1.35 eV)
X
$Al_xGa_xIn_{1-x-y}P$
AlP